Shimmy of Aircraft Main Landing Gears

Citation for published version (APA):
Besselink, I. J. M. (2000). *Shimmy of Aircraft Main Landing Gears*. [Phd Thesis 4 Research NOT TU/e / Graduation NOT TU/e), Delft University of Technology]. Technische Universiteit Delft.

Document status and date:
Published: 01/01/2000

Document Version:
Publisher’s PDF, also known as Version of Record (includes final page, issue and volume numbers)

Please check the document version of this publication:

• A submitted manuscript is the version of the article upon submission and before peer-review. There can be important differences between the submitted version and the official published version of record. People interested in the research are advised to contact the author for the final version of the publication, or visit the DOI to the publisher's website.
• The final author version and the galley proof are versions of the publication after peer review.
• The final published version features the final layout of the paper including the volume, issue and page numbers.

Link to publication

General rights
Copyright and moral rights for the publications made accessible in the public portal are retained by the authors and/or other copyright owners and it is a condition of accessing publications that users recognise and abide by the legal requirements associated with these rights.

- Users may download and print one copy of any publication from the public portal for the purpose of private study or research.
- You may not further distribute the material or use it for any profit-making activity or commercial gain
- You may freely distribute the URL identifying the publication in the public portal.

If the publication is distributed under the terms of Article 25fa of the Dutch Copyright Act, indicated by the “Taverne” license above, please follow below link for the End User Agreement:

www.tue.nl/taverne

Take down policy
If you believe that this document breaches copyright please contact us at:

openaccess@tue.nl

providing details and we will investigate your claim.

Download date: 23. Aug. 2022

Shimmy of Aircraft Main Landing Gears

I.J.M. Besselink

Shimmy of Aircraft Main Landing Gears

PROEFSCHRIFT

ter verkrijging van de graad van doctor
aan de Technische Universiteit Delft,
op gezag van de Rector Magnificus prof.ir. K.F. Wakker,
voorzitter van het College voor Promoties,
in het openbaar te verdedigen op dinsdag 26 september 2000 om 13:30 uur

door

Ignatius Jozef Maria BESSELINK

werktuigkundig ingenieur
geboren te Hengelo (Gelderland)

Dit proefschrift is goedgekeurd door de promotor:
Prof.dr.ir. H.B. Pacejka

Samenstelling promotiecommissie:

Rector Magnificus	voorzitter
Prof.dr.ir. H.B. Pacejka	Technische Universiteit Delft, promotor
Prof.dr.ir. J.P. Pauwelussen	Technische Universiteit Delft / TNO
Prof.dr.ir. P. Meijers	Technische Universiteit Delft
Prof.dr.ir. J.A. Mulder	Technische Universiteit Delft
Prof.Dr.Ing. W. Kortüm	Munich Technical University / DLR, Germany
Prof.dr.ir. D.H. van Campen	Technische Universiteit Eindhoven
Prof.dr.ir. D.J. Rixen, MSc.	Technische Universiteit Delft

ISBN 90-9014104-9

Copyright ©2000 by I.J.M. Besselink

All rights reserved. No part of the material protected by this copyright notice may be reproduced or utilised in any form or by any means, electronic or mechanical, including photocopying, recording or by any information storage and retrieval system, without the prior written permission of the author.

The author makes no warranty that the methods, calculations and data in this book are free from error. The application of the methods and results are at the user's risk and the author disclaims all liability for damages, whether direct, incidental or consequential, arising from such application or from any other use of this book.

Those who cannot remember the past are condemned to repeat it.

George Santayana (1863-1952)

voor papa en mama

Notation

symbol	**description**
a	half of the tyre contact length
a_i	coefficient of the characteristic equation; general coefficient
c	stiffness
c_a	shaft torsional stiffness (co-rotating wheels)
c_c	tyre lateral carcass stiffness per unit of length
c_{eq}	equivalent stiffness
c_y	landing gear lateral stiffness
c_{sd}	shimmy damper spring stiffness
c_v	tyre lateral stiffness
c_z	tyre vertical stiffness
c_β	tyre yaw stiffness
c_ψ	landing gear yaw stiffness
c_ϕ	landing gear roll stiffness
$C_{f\alpha}$	cornering stiffness
$C_{f\kappa}$	longitudinal slip stiffness
$C_{f\phi}$	turn slip stiffness of the lateral force
$C_{f\gamma}$	camber stiffness of the lateral force
$C_{m\alpha}$	self aligning stiffness
$C_{m\phi}$	turn slip stiffness of the aligning moment
$C_{m\gamma}$	camber stiffness of the aligning moment
e	mechanical trail
f	frequency
F_x	tyre longitudinal force
F_y	tyre lateral force
F_z	tyre vertical force
H_i	i-th Hurwitz determinant
$H_{y,x}(s)$	transfer function: input x, output y
I	moment of inertia
I_z, I_t	yaw moment of inertia
I_p	wheel polar moment of inertia
j	complex variable, $j^2 = -1$
k	linear damping constant
k_{eq}	equivalent linear damping constant
k_v	tyre lateral damping constant
k_{sd}	shimmy damper damping constant
k_y	landing gear lateral damping constant
k_β	tyre yaw damping constant

k_ψ	landing gear yaw damping constant
l	(effective) gear length
l_b	overlap, distance between bearings
m	mass
M_x	tyre overturning moment
M_y	tyre rolling resistance moment
M_z	tyre self aligning moment
p	tyre pressure
p_r	rated tyre pressure
$p_\alpha, p_\beta, p_\gamma$	coefficients of the Keldysh tyre model
q	position of the centre of gravity with respect to the wheel centre
R	loaded tyre radius
R_c	curvature radius
R_0	unloaded tyre radius
R_e	effective rolling radius
s	Laplace variable
s_t	travelled distance
t	time
t_p	tyre pneumatic trail
T	oscillation period, $T = \frac{1}{f}$
v	lateral deformation of the tyre string
v_1	lateral deformation of the tyre string at the leading contact point
v_2	lateral deformation of the tyre string at the trailing contact point
V	forward velocity
V_x	forward velocity projected on the wheel plane and parallel to the ground
V_{cy}	lateral sliding velocity of the contact centre C
V_{sx}	longitudinal sliding velocity of the imaginary slip point S
V_{sy}	lateral sliding velocity of the imaginary slip point S
w	half of track width
w_t	tyre width
W	work
x	longitudinal coordinate; degree of freedom
y	lateral coordinate
y_c	lateral position of the tyre contact centre C
y_1	lateral position of the tyre string at the leading contact point
y_2	lateral position of the tyre string at the trailing contact point
α	side slip angle
α'	tyre deformation angle
α_1	side slip angle at the leading contact point
β	twist angle of the contact patch: $\beta = -\alpha'$
δ	tyre deflection
ε	turn slip coefficient (Rogers tyre model)
ε_a	torsion angle of the shaft (co-rotating wheels)
κ	longitudinal slip
κ_m, κ_t	relative damping
γ	inclination angle

λ	wavelength: $\lambda = \frac{V}{f}$; root of the characteristic equation
η	amplitude ratio lateral/yaw motion of the wheel plane at road level
μ	friction coefficient
ψ	yaw angle
ψ_a	yaw angle of the wheel axle
σ	relaxation length
τ	time constant of the Moreland tyre model
ϕ	turn slip
ϕ_a	roll angle of the wheel axle
θ	landing gear cant angle
ξ	phase lead of the lateral motion over the yaw motion of the wheel plane at road level
ω	radial frequency, $\omega = 2\pi f$
Ω	wheel angular velocity
x^*	parameter x made dimensionless using reference variables, see section 1.5
$\dot{x}$	first time derivative of x
$\ddot{x}$	second time derivative of x
$\mathrm{sgn}(x)$	signum function: if $x \geq 0$ then $\mathrm{sgn}(x) = 1$, if $x < 0$ then $\mathrm{sgn}(x) = -1$
$\mathbf{A}, \mathbf{B}, \mathbf{C}, \mathbf{D}$	system matrices, state space representation
$\mathbf{I}$	unity matrix
$\mathbf{M}$	mass matrix
$\mathbf{K}$	damping matrix
$\mathbf{C}$	stiffness matrix
$\mathbf{T}$	transformation matrix
$\mathbf{n}$	normal vector
$\mathbf{x}$	state vector
$\mathbf{A}^{-1}$	inverse of matrix $\mathbf{A}$
$\mathbf{A}^T$	transpose of matrix $\mathbf{A}$

Contents

Notation 5

1 Introduction 11
1.1 Design requirements 11
1.2 Landing gear shimmy, a review 15
1.3 Objectives and scope 17
1.4 Outline of the thesis 18
1.5 Non-dimensional parameters 19

2 Shimmy fundamentals 21
2.1 Trailing wheel model 22
2.2 Lateral flexibility of the support 26
2.3 Energy flow and mode shapes 33
2.4 Damping and gyroscopes 39
2.5 A frequency domain view 44

3 Landing gear application 53
3.1 Equations of motion 53
3.2 Baseline characteristics 57
3.3 Improving stability by design modifications 61
3.4 Strut cant angle 70
3.5 Bob mass - tuned mass 73
3.6 Shimmy damper 78
3.7 Co-rotating wheels 84
3.8 Bogie configuration 86

4 Tyre modelling 89
4.1 Slip definitions, sign convention 89
4.2 Stretched string model and derivatives 94
4.3 Point contact tyre models 102
4.4 Model comparison 106
4.5 Impact on shimmy stability 121
4.6 Tyre parameters 127

5 Detailed modelling and validation 135
5.1 Shock absorber 135
5.2 Landing gear flexibility 139
5.3 Free-play 146

5.4 Friction 147
5.5 Eigenfrequencies and mode shapes 150
5.6 Non-linear behaviour of the shimmy damper 157
5.7 Model development 161
5.8 Test programme and parameter assessment 165

6 Evaluation of a shimmy event 173
6.1 Analysis of recorded data 173
6.2 Model results 183

7 Conclusions and recommendations 189
7.1 Conclusions 189
7.2 Recommendations for future research 190

References 193

Summary 197

Curriculum vitae 199

Document history 201

Chapter 1

Introduction

This introductory chapter starts with a discussion on the design requirements and operating conditions of a landing gear. The available literature on the shimmy phenomenon, with particular reference to aircraft landing gears, will be reviewed. Next, the objectives and scope of this thesis will be defined and an outline will be presented. Finally the usage of non-dimensional parameters will be explained.

1.1 Design requirements

Among the various components that make up an aircraft, the landing gear is an important and complex system. A recent study indicates that the landing gear continues to be the most failure prone system of Western-built commercial jet transports [11]. According to this study there were 1408 system related accidents between 1958 and 1993 in total; about one third (456) of these accidents were related to landing gears. This is more than twice as many as the next most failure prone category engines, which accounted for 192 accidents. Apparently the landing gear design and maintenance procedures may still require improvements to enhance flight safety.

The demands on the landing gear system are numerous and conflicting. The next list is not complete, but gives an impression of the operating conditions of the landing gears on a civil aircraft. For a detailed overview on design requirements reference is made to [19], [27].

- In flight the landing gear is just dead weight. Therefore its mass and volume should be as small as possible in order not to degrade the performance of the aircraft. The mass of the landing gears, including wheels and tyres, typically amounts 6 to 10 % of the aircraft mass (Manufacturing Empty Weight, MEW). The aerodynamics of the aircraft should not be disturbed by the landing gear; generally the gear is retractable and the size of the fairing should be small in order to minimise aerodynamic drag. This implies that a complicated retraction mechanism is required to retract and lower the landing gear. In retracted position the gear should interfere as little as possible with the cargo compartment.

- In order to allow sufficient rotation of the aircraft during take-off, generally about 10 to 15 degrees in pitch, a boundary for the location of the wheels can be established. Furthermore the jet engines or propellers should have sufficient clearance with respect to the runway when the aircraft is on the ground. For many aircraft these requirements result in a wing mounted main landing gear with a considerable length. The main wheels will be located rather close to the centre of gravity of the aircraft in the longitudinal direction. Sufficient load on the nose landing gear has to be provided, in order to prevent aft-tipping of the aircraft. In addition, requirements may exist regarding the aircraft static attitude in order to provide the correct angle of attack during take-off.

- The landing gear should be able to absorb the energy of landing impact up to descent velocities of 3.66 m/s (12 fps). This requires a shock absorber with a considerable stroke in order to limit the loads occurring during landing impact. For a civil jet aircraft the ground speed during landing is in the range of 200 to 300 km/h. On touch down the wheels have to be accelerated and this spin-up phenomenon results in very high loads on the landing gear structure. The vertical loads generated during landing impact may be decisive for the design of several parts of the fuselage. Also during ground operations (e.g. towing, jacking, braking) the loads applied through the landing gear may be highly significant.

- The life of an aircraft is expressed in the number of flights; the current design requirement for a new aircraft may be as much as 90000 safe flights, which corresponds to an operational life of about 30 years. The landing gear should be designed for this period without the replacement of major structural parts. This requirement cannot be met by the brake disks and tyres; they have to be replaced on a regular basis; tyres last for a few hundreds up to several thousands landings. Since many civil aircraft are in use for almost 24 hours a day, there is minimal room for servicing. The reduction of maintenance costs and time is a very important driver in the design of a landing gear.

- The vertical loads, which are allowed for aircraft tyres, exceed by far the values found for truck tyres of similar size. The upper limit on the diameter of aircraft tyres is about 1.2 meter combined with a maximum vertical load capacity of 250 kN for a single tyre. In order to have acceptable ground floatation characteristics and to minimise the damage to the runway, the tyres should have a large contact area and consequently the tyre deflection will be relatively large. The combination of heavy loading, high speeds and high deflection percentages make the operating conditions of aircraft tyres extremely severe.

- The landing gear should be free from excessive vibrations and dynamic instabilities. Ride comfort is in general not a design target, but some minimum requirements have to be met. Vibrations can be induced by the brakes, possibly in combination with the anti-skid system. Normally the tyres are not balanced or only in a very limited way, which also can be a source of vibrations. Shimmy vibrations can occur due to the interaction between the landing gear and tyre dynamic behaviour and are the subject of this thesis.

Generally there is no opportunity to create prototypes during the landing gear design process for a civil aircraft. The design has to be ”the first time right”, because of the high costs involved to create a die and the relatively small production numbers. Various computer models are used in the development stage of the landing gear: calculation of loads, verification of stress levels, fatigue life, retraction analysis, etc. At a later stage of the design process a number of tests are performed to check these calculations. Drop tests are used for example to validate spring and damping characteristics of the shock absorber at high descent velocities. Fatigue tests on the landing gear may run for many years, parallel to operational usage of the first production gears. In order to obtain an airworthiness certificate the landing gear design has to meet the JAR/FAR regulations: the calculation and test methods have to be approved by the airworthiness authorities.

A number of different landing gear configurations are shown in figure 1.1. For nose landing gears a twin-wheeled, cantilevered design is by far the most common design. A twin-wheeled main landing gear is generally used for aircraft weights below roughly 100 tons. The wing mounted cantilevered design is the most common, although there are also some examples of fuselage mounted, levered suspensions. For higher aircraft weights a four-wheeled bogie is employed. If the maximum load capacity of the bogie is reached, a six-wheeled bogie can be introduced or one has to abandon the ”tricycle” lay-out, consisting of one nose and two main gears, and introduce additional landing gears. Some examples: the Boeing 747 has four four-wheeled bogies, the Airbus A-340 has two four-wheeled bogies and a twin-wheeled fuselage mounted centre gear of the cantilevered design type. More exotic wheel arrangements may be employed for military transport aircraft; examples are the Lockheed C-5A and McDonnell Douglas C-17A as shown in figure 1.1.

This thesis will focus mainly on twin-wheeled cantilevered main landing gears. Figure 1.2 gives a detailed illustration; the following components can be distinguished:

- *main fitting*: largest part of the landing gear structure; internally it combines an air spring and hydraulic damper.
- *side stay*: lateral support of the main fitting; consists of two members to allow retraction of the landing gear.
- *sliding member*: translates vertically with respect to the main fitting; since the bearings are circular it also has a rotational degree of freedom with respect to the main fitting.
- *torque links*: transfer moments between main fitting and sliding member and prevent rotation of the sliding member with respect to the main fitting.
- *shimmy damper*: hydraulic damper in series with the torque links, which provides additional damping for the yaw motion of the wheel axle. The shimmy damper is installed at the *apex joint* and its stroke is limited to a few degrees in yaw.
- *wheel axle*: often has a mechanical trail with respect to the vertical rotation axis between sliding member and main fitting.
- *back-up structure*: local structure in the aircraft wing to which the landing gear is attached.

Figure 1.2 also shows some details on the retraction mechanism and doors, which cover the landing gear in retracted position.

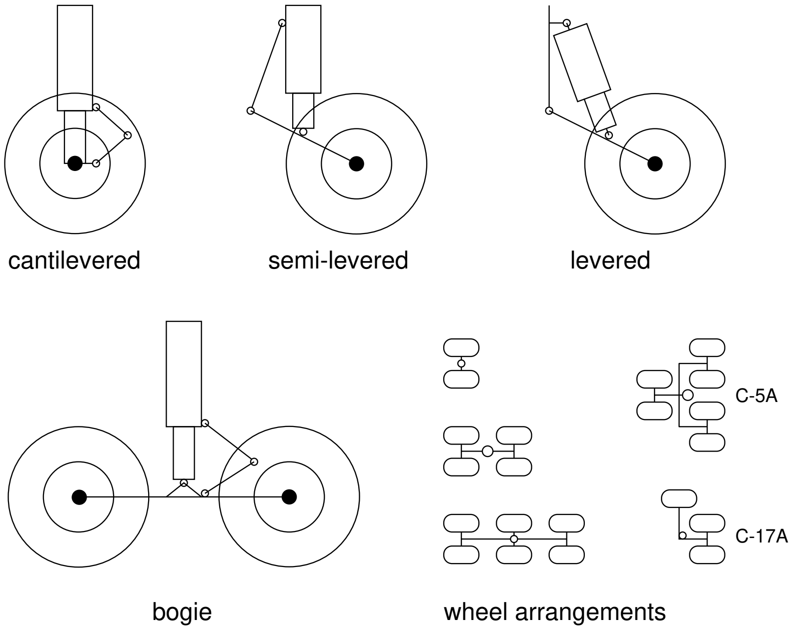
cantilevered
semi-levered
levered
C-5A
C-17A
bogie
wheel arrangements

Fig. 1.1: Schematic overview of different landing gear configurations.

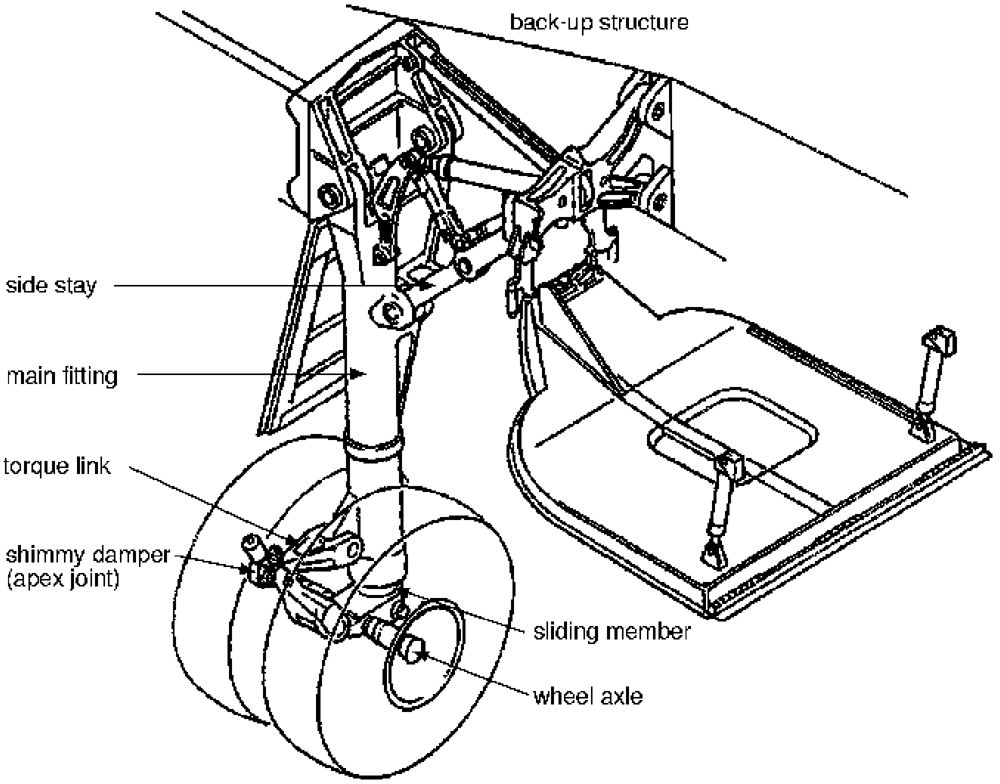
back-up structure
side stay
main fitting
torque link
shimmy damper (apex joint)
sliding member
wheel axle

Fig. 1.2: Main components of a cantilevered main landing gear.

1.2 Landing gear shimmy, a review

Shimmy is an oscillatory, combined lateral-yaw motion of the landing gear caused by the interaction between dynamic tyre behaviour and landing gear structural dynamics. The motion typically has a frequency in the range of 10 to 30 Hz. The amplitude may grow to a level of annoying vibrations affecting the comfort and visibility of the pilot, or can even result in severe structural damage and landing gear collapse. Shimmy can occur on both nose and main landing gears, although the latter case is more rare. Most publications on shimmy found in the open literature typically deal with twin-wheeled cantilevered landing gears, which apparently are more susceptible to shimmy vibrations compared to other landing gear configurations. Shimmy does not only occur on aircraft but has also been encountered on the steerable wheels of cars, trucks and motorcycles.

Theoretical research in the field of shimmy has already a long history. Initially the main focus was on finding a correct description of the tyre dynamic behaviour. Examples from this early period, which are still relevant today, are the tyre models of Von Schlippe (1941, [45]), Keldysh (1945, [22]) and Moreland (1954, [32]). Smiley (1956, [46]) reviewed existing theories of linearised tyre motion and developed a summary theory. Pacejka (1966, [35]) developed the ”straight tangent” approximation to the Von Schlippe tyre model and explored the field of non-linear tyre behaviour. Rogers (1972, [40]) developed an empirical tyre model based on measured transfer functions and provided a theoretical justification using the stretched string approximation.

With the availability of tyre models an increasing need for accurate tyre parameters develops. Smiley and Horne (1961, [47]) compiled an impressive overview of measurements on many different characteristics of aircraft tyres and developed generic, empirical formulas to describe these characteristics. Other sources are for example Collins (1969, [8]) and Ho (1973, [20]). Clark (1974, [6]) performed tests on scale models of aircraft tyres. Black (1982, [4]) provides a systematic approach to obtain parameters for the Moreland model. Traditionally aircraft tyres are of a bias-ply construction. In the last decade radial design aircraft tyres have become available and this has also initiated measurement programmes on tyre characteristics, see e.g. Yager (1990, [52]) and Davis (1991, [9] [10]). A generic, empirical expression for the relaxation length of aircraft tyres was developed by Alsobrook (1996, [1]).

Initially, the models for evaluating shimmy stability remained linear. Pacejka (1966, [35], [36]) used non-linear models for both the tyre and suspension when analysing front wheel shimmy on a light truck. The landing gear model of Leve (1969, [28]) includes a shimmy damper with velocity squared damping force and limited stroke; in addition a number of design guidelines and measures to prevent shimmy are given. The model of Black (1976, [3]) features a detailed model of the yaw stiffness including friction forces, free-play. Grossmann (1980, [15]) demonstrates the use of linearisation techniques to avoid time-consuming non-linear analyses. Van der Valk (1992, [49]) uses a modal representation to describe bending of the main fitting and sliding member. The models created by Baumann (1991, [2]) and Li (1993, [29]) take a similar modelling approach as laid down in the work of Black.

At first sight the amount of literature available over the years on landing gear shimmy may seem to be limited, but one has to be aware that many developments may be in-house proprietary and are not published in the open literature. In a review paper on aircraft ground dynamics Hitch (1980, [19]) states:

> *"Main wheel shimmy is sufficiently rare that it is totally ignored. However the Douglas DC-9, the BAC 1-11 and according to some accounts the Boeing 737 and Fokker F28 all designed to a very similar specification in the same 5 year time span - each suffered main wheel shimmy to varying degrees. This caught the Industry by surprise and, even among rivals, some conferring took place. ... This effort undoubtedly updated the "state-of-the-art" but none of the companies reported their work in the open literature and the especial conditions which these four aircraft represented have never been re-established nor has the problem recurred. The next generation of designers will have to learn the secrets all over again."*

Krabacher (1993, [25]) describes his experiences over a large number of years in the field of landing gear dynamics:

> *"... the actual approach taken in dealing with landing gear dynamics problems frequently is on the level of a primitive science with some engineering conjury thrown in for good measure. ... In the landing gear design phase there seems to be a lack of concern about the design features which could contribute to potential gear problems such as shimmy and gear walk."*

Krabacher proposes to set up working groups to produce a standardised model for landing gear dynamics and to update the work of Smiley and Horne for the aircraft tyres in use today. Norton (1993, [33]) describes the lengthy and troublesome shimmy testing programme of the C-17A military transport aircraft.

In 1995 an AGARD (Advisory Group for Aerospace Research & Development) conference was almost exclusively devoted to landing gear shimmy. A comparatively large number of papers was presented. Krabacher [26] presents the equations of a shimmy model which was developed 17 years ago; parameters and analysis results are given for a number of different landing gears. Woerner [51] discusses the impact of non-linearities on landing gear modal testing and the impact on landing gear stability. Koenig [24] remarks that the mathematical description of the tyre dynamic behaviour is almost 50 years old and questions why no reliable up-to-date theory is available. Glaser and Hrycko [12] report on the past shimmy problems encountered by de Havilland. They state:

> *"... While these problems occurred 10 years ago, it is the authors' contention that little progress has been made in the discipline in the intervening years. It is recommended that advisory material is needed in this important but often neglected subject. ... The authors have reason to believe that the shimmy "problem" is perceived by many to be a "black art" with no basis in sound engineering methods. The authors disagree and are concerned that this "black art" perception has hindered progress in shimmy design unnecessarily. ... What is lacking is the accumulation, integration and dissemination of currently available analytical and experimental experience to support the development of the practical design process."*

The advisory material should include guidelines for modelling, analysis, test procedures, maintenance and practical design information.

As stated before, the landing gear design has to meet the JAR/FAR regulations in order to obtain an airworthiness certificate. Especially with respect to the calculation of load cases the requirements are quite extensive, resulting in a complete procedure to obtain the static design loads. The JAR/FAR regulations to date do not explicitly include dynamic stability of the landing gear or a shimmy analysis in particular. On the other hand a flutter analysis, concerning the dynamic stability of the wings, is required to certify the aircraft. So there seems to be some inconsistency in the regulations for civil air transports. For military aircraft regulations are applicable which explicitly require a shimmy analysis and dedicated tests.

As already indicated by the quotes of a number of experts in the field, shimmy is easily ignored in the design process. That may be partly due to lack of specific knowledge of the shimmy phenomenon, of suitable analysis tools and of reliable data on structural stiffness or tyre characteristics. This situation is complicated by the fact that even with the best available tools, reliable analysis results may not be expected until detailed design of both landing gear and airframe is well advanced. To avoid a development risk in the form of shimmy, at a late stage in the design process while possibly under schedule pressure, will require at least a clear delineation of responsibilities between airframe and landing gear designer/manufacturer, and intensive communication to evaluate the shimmy characteristics as the landing gear design progresses.

As a concluding remark it can be stated that despite a long history, landing gear shimmy remains a relevant problem today.

1.3 Objectives and scope

This research was initiated by a landing gear shimmy event, which occurred on a test aircraft. In the process of studying the shimmy instability, it was felt that the knowledge on the shimmy phenomenon could be improved. The number of publications available in the open literature appears to be relatively small, as already indicated in section 1.2, and was found to be of limited use. This situation marked the starting point of this thesis. The aim is to gain a better understanding of the shimmy phenomenon and possibly develop guidelines for a shimmy-free landing gear design.

The thesis focuses on the shimmy stability of twin-wheeled aircraft main landing gears, in particular the cantilevered design employed on civil jet transports. Three fields of research have been identified:

- *shimmy fundamentals*
  Shimmy is a complex phenomenon and is influenced by many design parameters. Most publications available in the open literature typically deal with detailed models of the landing gear and are generally focussed on solving shimmy problems for this particular configuration. Though sensitivity studies have been performed, the trends may not be generally applicable. The aim of this thesis is to provide a better understanding of the basic mechanisms governing the shimmy stability of landing gears. Relatively simple models will be used to analyse the impact of various parameters on shimmy stability; design guidelines will be extracted when possible.

- *tyre models*
  Over the years a number of different tyre models have been developed for application to the shimmy problem. The question which model is most accurate in predicting shimmy has been a source of disputes. A comparison will be made

between the theories of Von Schlippe, Keldysh, Moreland, Pacejka and others. Furthermore, attention will be paid to obtaining a valid and consistent set of tyre parameters, which is a problem of its own. Accurate tyre data is crucial for making reliable shimmy predictions.

- *dedicated shimmy study*
  Although the simple models are useful for studying the shimmy behaviour in general, more detailed models are required in the design stage or when solving actual shimmy problems. The various issues arising when developing a dedicated model for a particular landing gear will be discussed. Different component tests may be required for validation purposes or to provide characteristics for the model; also the operating conditions and possibilities of full-scale shimmy testing will be discussed.

Since this thesis focuses on main landing gears, no attention will be given to the steering system. The steering system may be an important factor in nose landing gear shimmy vibrations and its characteristics may be tuned to suppress shimmy. Furthermore the possible impact of the brakes on the shimmy stability will be left untouched.

1.4 Outline of the thesis

This thesis covers a variety of shimmy analysis models, ranging from simplified linear models to an elaborate non-linear multi-body/finite element model. The general approach is to start with the most simple models and gradually increase complexity.

In *chapter 2* simplified models of the landing gear structure and tyre are introduced to study the fundamental mechanisms governing shimmy. Analytical expressions will be developed for the stability as a function of the gear and tyre parameters. Based on an energy balance for the tyre, combinations of lateral and yaw motions can be identified which may result in shimmy. Finally it is shown that the Nyquist criterion may be applied to assess system stability in the frequency domain.

Some of these methods will be applied to a twin-wheeled cantilevered landing gear in *chapter 3*. The effect of various parameter changes will be investigated and the base configuration will be optimised for shimmy stability. Special features may be introduced in the landing gear design to suppress shimmy: the shimmy damper, co-rotating wheels, bob mass and tuned mass will be discussed.

A number of different theories to describe tyre behaviour are currently in use to analyse shimmy. In *chapter 4* a description of these theories and their mutual relations are given. A comparison will be made in the frequency domain and using the various step responses. Based on literature, available measurement results and physical considerations, some guidelines will be presented to estimate and judge the parameters of the tyre model.

Various aspects of the landing gear, which must be considered when developing a detailed shimmy analysis model, are described in *chapter 5*. This includes the shock absorber characteristics and the dependency of the gear stiffness on the shock absorber closure. Non-linearities, like free-play and friction, can have a large impact on shimmy stability and may also disturb the results obtained by modal testing. Methods of full-scale shimmy testing and model validation will be discussed.

In *chapter 6* the shimmy vibrations recorded on a test aircraft are analysed and a comparison is made with simulation model results. Finally conclusions and recommendations for future research are given in *chapter 7*.

1.5 Non-dimensional parameters

Although it is possible to obtain some analytical results for shimmy stability, the majority of the results presented in this thesis are based on numerical computations for a given set of parameters. The parameters used in these calculations are presented in a non-dimensional form. This has the advantage that the results will independent of the selected system of units. It will also allow to easily apply the numerical results to similar shimmy problems. The following transformations are applied:

- length is expressed as a fraction of the unloaded tyre radius R_{ref}
- mass is expressed as a fraction of the landing gear unsprung mass m_{ref}
- force is expressed as a fraction of the nominal tyre load F_{ref}
- the unit of time is seconds, $t_{ref} = 1$ s
- the angular unit is radians, $\psi_{ref} = 1$ rad

It is not possible to select R_{ref}, m_{ref}, F_{ref} and t_{ref} independently. For the numerical results presented in this thesis the following relation is applicable:

$$\frac{F_{ref}t_{ref}^2}{m_{ref}R_{ref}} = 500 \tag{1.1}$$

The value of 500 gives the relation between the unloaded tyre radius, landing gear unsprung mass and nominal tyre load. It typically reflects the combination seen on a specific twin-wheeled landing gear, but is believed to be valid for a wider range of twin-wheeled landing gears. This is based on the assumption that the (unsprung) landing gear mass will be a fairly constant fraction of the total aircraft mass. The nominal load on the main tyres will again be almost proportional to the total aircraft mass, the nose landing gear generally carrying only 5 to 10 % of the total aircraft mass. Furthermore it can be noted that the tyre radius is relatively constant for large civil aircraft. These observations seem to justify that equation 1.1 may be valid for a class of twin-wheeled main landing gears.

Using the reference values, it is possible to create dimensionless parameters, which are indicated with a ”*”. Some examples: the relaxation length (unit: length) is expressed as a fraction of the tyre radius:

$$\sigma^* = \frac{\sigma}{R_{ref}} \tag{1.2}$$

The moment of inertia (unit: mass length squared) is made dimensionless using the reference mass and tyre radius:

$$I^* = \frac{I}{m_{ref}R_{ref}^2} \tag{1.3}$$

The expression for the forward velocity (unit: length/time):

$$V^* = \frac{V t_{ref}}{R_{ref}} \tag{1.4}$$

The expression for the cornering stiffness (unit: force/angle):

$$C^*_{f\alpha} = \frac{C_{f\alpha} \psi_{ref}}{F_{ref}} \tag{1.5}$$

An advantage of using non-dimensional parameters is that the numerical results are applicable to any configuration which satisfies equation 1.1. In this way some of the results presented in this thesis could even be relevant to a passenger car suspension. As an example we may choose $m_{ref} = 25$ kg, $R_{ref} = 0.3$ m and $F_{ref} = 3750$ N. If in this case the non-dimensional cornering stiffness $C^*_{F\alpha}$ equals 10, then the cornering stiffness $C_{F\alpha}$ becomes 37500 N/rad; $V^* = 100$ would represent a forward velocity of 30 m/s and $I^* = 0.5$ corresponds to a moment of inertia I of 1.125 kgm^2. These are all fairly realistic values for a passenger car.

Furthermore the reader may transform the non-dimensional parameters to any preferred consistent set of units, with the restriction that the unit of time remains one second and that radians are used for angular dimensions. For example choose $m_{ref} =$ 3 lb·s^2/inch, $R_{ref} = 25$ inch and $F_{ref} = 37500$ lb.

Since the non-dimensional quantities are employed only to facilitate the *presentation* of results, the (differential) equations that govern system behaviour have not been made dimensionless. This is the most common way of presenting equations; it makes the interpretation easier and they can be used directly in numerical calculations without the need to perform transformations.

Chapter 2

Shimmy fundamentals

In this chapter basic knowledge, including various new results, with respect to the shimmy phenomenon is presented. The trailing wheel model, as shown in figure 2.1, is often used to illustrate the shimmy instability and to evaluate differences between tyre models. Examples can be found in the papers of e.g. Von Schlippe [45], Smiley [46] and Pacejka [35]. In this chapter a number of extensions will be made to the trailing wheel model: including a yaw stiffness, a lateral compliance of the support and roll. This model will reflect the actual landing gear more closely.

In this chapter the tyre description is limited to the simple "straight tangent" model. In chapter 4 the influence of using more advanced tyre models on shimmy stability will be discussed, which will be especially important at low forward velocity.

Traditionally, a shimmy stability analysis is performed using either the Hurwitz criterion or an eigenvalue analysis. Using the Hurwitz criterion it appears to be possible to develop analytical expressions for the shimmy stability and ways of presentation, which are new and cannot be found in the available literature.

In addition two new techniques will be introduced, which may be helpful in understanding the cause of the shimmy instability. Based on energy considerations, it is possible to identify stable and unstable combinations of lateral and yaw input to the wheel plane at road level. Furthermore, it will be shown that the Nyquist criterion may be applied to evaluate shimmy stability in the frequency domain.

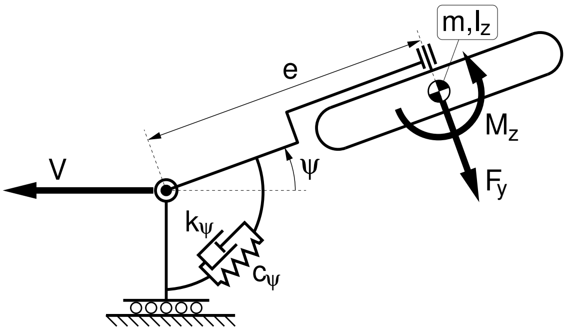

Fig. 2.1: Model of the trailing wheel system (top view).

2.1 Trailing wheel model

The most simple system capable of showing oscillatory unstable shimmy motions is the trailing wheel model shown in figure 2.1. Wheel and tyre are mounted on a trailing arm; this arm can swivel with respect to a vertical rotation axis. A linear stiffness c_ψ and damping constant k_ψ are introduced for the yaw motion. The hinge joint moves forward along a straight line with a constant velocity V.

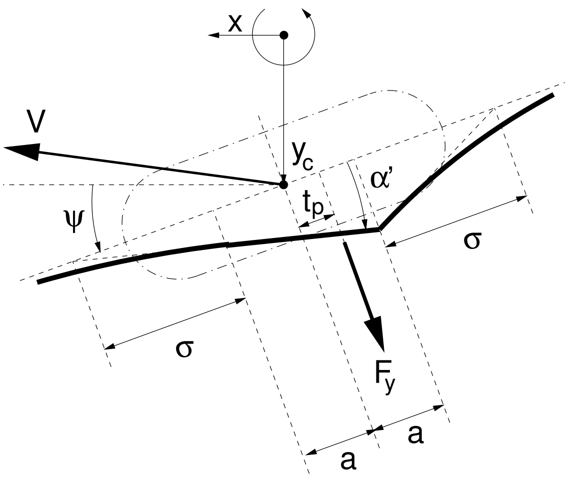

Fig. 2.2: Straight tangent tyre model (top view).

The straight tangent tyre model will be utilised. At this stage it is sufficient to remark that this tyre model is conservative with respect to detecting shimmy; for a detailed discussion on various tyre models reference is made to chapter 4. The next equations are applicable for the straight tangent tyre model when considering small deviations from a straight line motion, see also figure 2.2:

$$\left.\begin{aligned} \sigma\dot{\alpha}' + V\alpha' &= V\psi - a\dot{\psi} - \dot{y}_c \\ F_y &= C_{f\alpha}\alpha' \\ M_z &= C_{m\alpha}\alpha' \end{aligned}\right\} \tag{2.1}$$

In these equations σ is the relaxation length, V the forward velocity and a half of the tyre contact length. The deformation angle α' responds to the lateral velocity $\dot{y}_c$ of the wheel centre, yaw angle ψ and yaw velocity $\dot{\psi}$. The lateral force F_y and self aligning moment M_z generated by the tyre are linearly dependent on the deformation angle. The coefficient $C_{f\alpha}$ is the cornering stiffness; $C_{m\alpha}$ is the self aligning stiffness and this coefficient will be negative following the adopted sign convention (see also section 4.1). They are related by the pneumatic trail t_p:

$$t_p = -\frac{M_z}{F_y} = -\frac{C_{m\alpha}}{C_{f\alpha}} \tag{2.2}$$

As can be seen from figure 2.2 the pneumatic trail t_p has a clear physical interpretation: it represents the moment arm of the lateral force F_y with respect to the tyre contact centre.

The linearised equations of motion for the trailing wheel system in state-space form

($\dot{\mathbf{x}} = \mathbf{A}\mathbf{x}$) read:

$$\begin{pmatrix} \ddot{\psi} \\ \dot{\psi} \\ \dot{\alpha}' \end{pmatrix} = \begin{pmatrix} -\frac{k_\psi}{I_t} & -\frac{c_\psi}{I_t} & -\frac{C_{f\alpha}(e+t_p)}{I_t} \\ 1 & 0 & 0 \\ \frac{(e-a)}{\sigma} & \frac{V}{\sigma} & -\frac{V}{\sigma} \end{pmatrix} \cdot \begin{pmatrix} \dot{\psi} \\ \psi \\ \alpha' \end{pmatrix} \tag{2.3}$$

In these equations e equals the length of mechanical trail, c_ψ the yaw stiffness and k_ψ the yaw damping constant. The total moment of inertia about the swivel axis equals $I_t = I_z + me^2$, with m being the mass and I_z the yaw moment of inertia of the wheel, including the tyre.

If possible, analytical expressions are preferred to describe the shimmy stability. A common way of judging system stability is the calculation of the eigenvalues of the matrix $\mathbf{A}$. Using computational tools, it is even possible to obtain symbolic expressions for the eigenvalues. Unfortunately these symbolic expressions are already very lengthy for this simple third order system, so another method is used to obtain analytical results: the Hurwitz criterion [17], [35].

First the third order system without damper is considered ($k_\psi = 0$). The characteristic equation reads:

$$a_0\lambda^3 + a_1\lambda^2 + a_2\lambda + a_3 = 0 \tag{2.4}$$

where:

$$\left.\begin{aligned} a_0 &= I_t\sigma \\ a_1 &= I_tV \\ a_2 &= c_\psi\sigma + C_{f\alpha}(e-a)(e+t_p) \\ a_3 &= c_\psi V + C_{f\alpha}(e+t_p)V \end{aligned}\right\} \tag{2.5}$$

The Hurwitz criterion can be applied and physically relevant parameters are assumed: I_t, V, $C_{f\alpha}$, t_p, a and σ will all be positive. The system is stable if *all* of the following conditions are met (note: $H_2 = a_1a_2 - a_0a_3$):

$$\left.\begin{aligned} a_0 > 0 &\ :\ I_t\sigma > 0 \\ a_1 > 0 &\ :\ I_tV > 0 \\ a_3 > 0 &\ :\ e > -(t_p + c_\psi/C_{f\alpha}) \\ H_2 > 0 &\ :\ e > \sigma + a \quad \text{or} \quad e < -t_p \end{aligned}\right\} \tag{2.6}$$

The first two conditions are trivial: the relaxation length, velocity and inertia properties will be positive. For slightly negative and limited positive values of the mechanical trail e the system is oscillatory unstable ($H_2 < 0$); independent of inertia, forward velocity, cornering stiffness and yaw stiffness. Furthermore there exists a stable region when the mechanical trail is negative, the size of this region is dependent on the yaw stiffness: if this stiffness equals zero this stable region disappears. For a large negative mechanical trail the system is monotonically unstable ($a_3 < 0$). These results are illustrated by figure 2.5.

The eigenvalues are calculated as a function of the mechanical trail using the following data: $m^* = 1$, $I_z^* = 0.5$, $c_\psi^* = 15$, $k_\psi^* = 0$, $V^* = 120$, $a^* = 0.4$, $\sigma^* = 1.2$, $t_p^* = 0.2$ and $C_{f\alpha}^* = 10$. With these parameters figure 2.3 can be obtained. The real part of one of the eigenvalues is positive for certain regions of the mechanical trail e^*, indicating an unstable

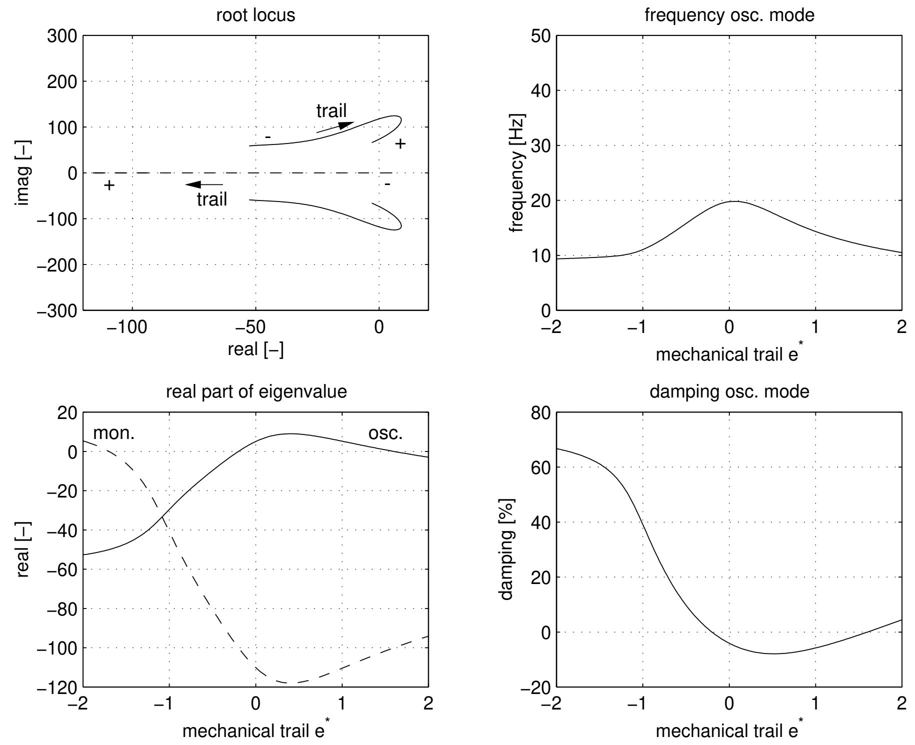

Fig. 2.3: Eigenvalues of the trailing wheel system (c_ψ^*=15, k_ψ^*=0).

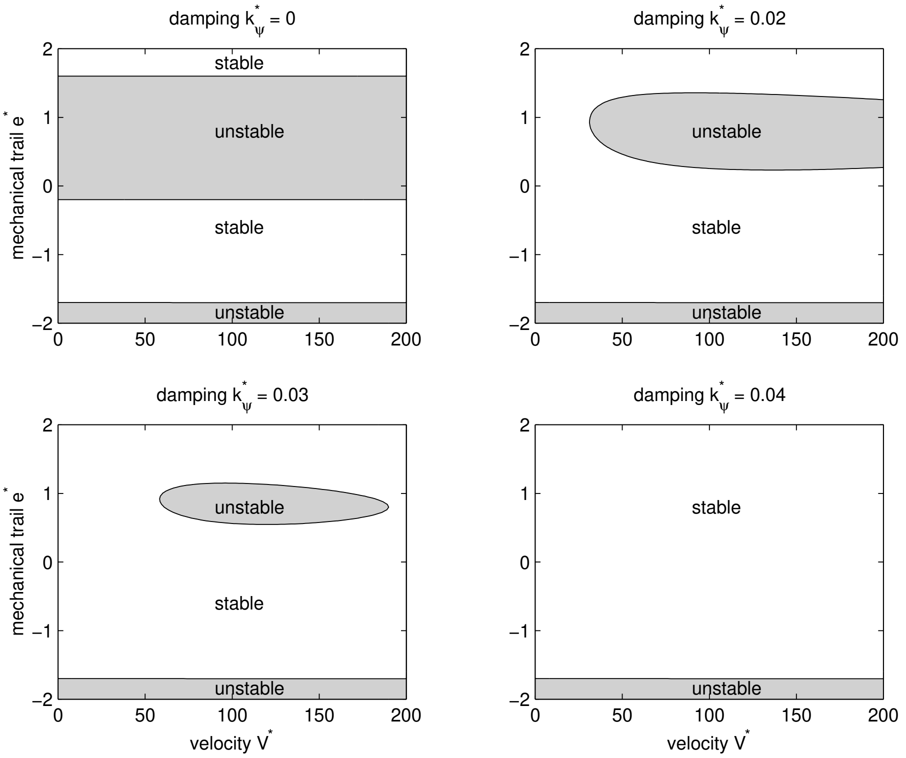

Fig. 2.4: Effect of yaw damping on the stability of the trailing wheel system.

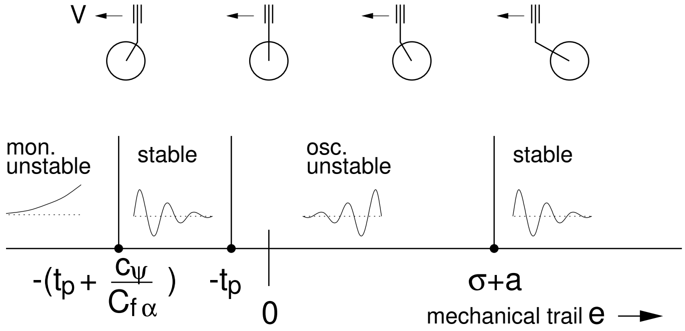

Fig. 2.5: Stability boundaries of the trailing wheel model (k_ψ=0).

system. The system is monotonically unstable for a trail smaller than -1.7 and oscillatory unstable in the region between -0.2 and 1.6; this is consistent with the analytical results.

The effect of introducing yaw damping is shown in figure 2.4. From this figure it can be seen that the oscillatory unstable area is reduced with the introduction of damping and disappears completely when the damping is sufficiently high. Furthermore this figure illustrates the velocity dependency of the (in)stability at moderate values of yaw damping. The transition to the monotonically unstable area does not change with the introduction of damping and remains at $e^* = -1.7$.

Next a closely related system is studied: a bogie consisting of two wheels, see figure 2.6. The required modification of equation 2.3 is simple: only a second deformation angle for the front tyre has to be introduced; the total moment of inertia about the swivel axis now equals $I_t = 2I_z + 2me^2$. The following equation is applicable ($\dot{\mathbf{x}} = \mathbf{A}\mathbf{x}$):

$$\begin{pmatrix} \ddot{\psi} \\ \dot{\psi} \\ \dot{\alpha}'_f \\ \dot{\alpha}'_r \end{pmatrix} = \begin{pmatrix} -\frac{k_\psi}{I_t} & -\frac{c_\psi}{I_t} & \frac{C_{f\alpha}(e-t_p)}{I_t} & -\frac{C_{f\alpha}(e+t_p)}{I_t} \\ 1 & 0 & 0 & 0 \\ -\frac{(e+a)}{\sigma} & \frac{V}{\sigma} & -\frac{V}{\sigma} & 0 \\ \frac{(e-a)}{\sigma} & \frac{V}{\sigma} & 0 & -\frac{V}{\sigma} \end{pmatrix} \cdot \begin{pmatrix} \dot{\psi} \\ \psi \\ \alpha'_f \\ \alpha'_r \end{pmatrix} \tag{2.7}$$

Again the Hurwitz criterion is applied to the characteristic equation for a system without a damper ($k_\psi = 0$). Physically relevant parameters are assumed: I_t, V, $C_{f\alpha}$, t_p, a, e and σ

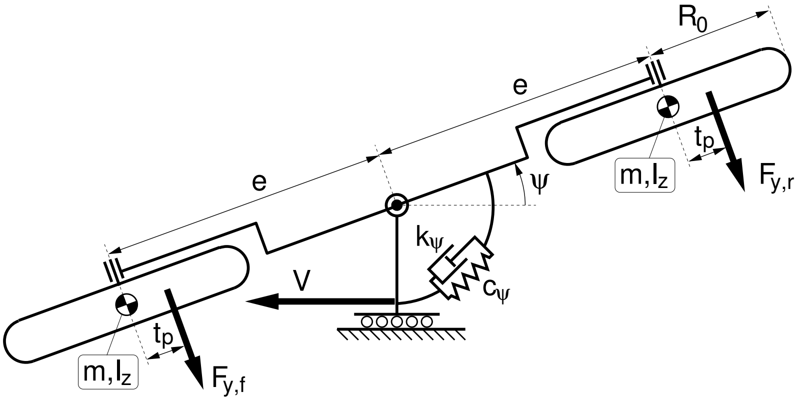

Fig. 2.6: Simple bogie model (top view).

will all be positive. The system is stable if *all* of the following conditions are met:

$$\left.\begin{aligned}
a_0 > 0 &\ :\ I_t\sigma > 0 \\
a_1 > 0 &\ :\ 2I_tV > 0 \\
a_4 > 0 &\ :\ c_\psi + 2C_{f\alpha}t_p > 0 \\
H_2 > 0 &\ :\ e^2 > (\sigma + a)t_p - \frac{I_tV^2}{C_{f\alpha}\sigma} \\
H_3 > 0 &\ :\ e^2 > (\sigma + a)t_p \quad \text{or} \quad e^2 < -\left((\sigma - a)t_p + \frac{c_\psi\sigma}{C_{f\alpha}} + \frac{I_tV^2}{C_{f\alpha}\sigma}\right)
\end{aligned}\right\} \tag{2.8}$$

For a physical system all coefficients will be larger than zero; the stability requirement then reduces to:

$$e^2 > (\sigma + a)t_p \tag{2.9}$$

As a first estimate the following approximations could be used: $a \leq 0.5R_0$, $\sigma \approx 3a$ and $t_p \approx 0.5a$, where R_0 is the unloaded tyre radius. Then the stability requirement becomes: $e \geq \frac{1}{2}\sqrt{2}R_0$. From geometrical considerations, as already indicated by figure 2.6, e will be larger than R_0 and consequently the system will always be stable independent of forward velocity and yaw stiffness. Taking $e^* = 1.4$, $c_\psi^* = 10$ and using the other parameters of the previous numerical example, it can easily be verified that each wheel individually operates in an unstable region (see figure 2.5). Nevertheless the combination is stable: the front tyre apparently suppresses the oscillatory instability of the rear tyre and the rear tyre cancels out the monotonical instability of the front tyre.

2.2 Lateral flexibility of the support

In the trailing wheel model of the preceding section the lateral support of the hinge is rigid, which may not be a reasonable assumption when modelling a realistic landing gear. A landing gear is designed with strength requirements in mind in order to minimise weight; it has to be stress efficient and this may also result in significant flexibility of the structure. For the shimmy phenomenon the dynamic behaviour of this flexible structure has to be considered.

The most simple extension to the base trailing wheel model to illustrate this, is the introduction of a lateral stiffness c_y as shown in figure 2.7. This system has an independent

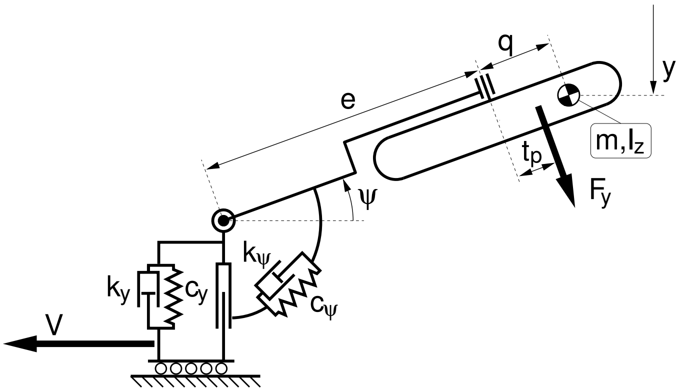

Fig. 2.7: The trailing wheel system with lateral flexibility (top view).

lateral y and yaw ψ degree of freedom. Since the dynamic behaviour will be considered, an additional parameter q is introduced which represents the relative location of the centre of gravity with respect to the wheel centre. The following set of linearised equations is applicable ($\dot{\mathbf{x}} = \mathbf{A}\mathbf{x}$):

$$\begin{pmatrix} \ddot{y} \\ \ddot{\psi} \\ \dot{y} \\ \dot{\psi} \\ \dot{\alpha}' \end{pmatrix} = \begin{pmatrix} -\frac{k_y}{m} & -\frac{k_y e_t}{m} & -\frac{c_y}{m} & -\frac{c_y e_t}{m} & \frac{C_{f\alpha}}{m} \\ -\frac{k_y e_t}{I_z} & -\frac{k_y e_t^2 + k_\psi}{I_z} & -\frac{c_y e_t}{I_z} & -\frac{c_y e_t^2 + c_\psi}{I_z} & \frac{C_{f\alpha}(q - t_p)}{I_z} \\ 1 & 0 & 0 & 0 & 0 \\ 0 & 1 & 0 & 0 & 0 \\ -\frac{1}{\sigma} & -\frac{(q+a)}{\sigma} & 0 & \frac{V}{\sigma} & -\frac{V}{\sigma} \end{pmatrix} \cdot \begin{pmatrix} \dot{y} \\ \dot{\psi} \\ y \\ \psi \\ \alpha' \end{pmatrix} \tag{2.10}$$

where:

$$e_t = e + q \tag{2.11}$$

First the case where wheel centre and centre of gravity coincide is considered ($q = 0$). In this section the damping constants k_y and k_ψ are also taken equal to zero. In addition to the parameters of the numerical example of the previous paragraph a lateral stiffness $c_y^* = 15$ is introduced. The eigenvalues have been calculated as a function of the mechanical trail to investigate shimmy stability, see figure 2.8. A comparison with figure 2.3 makes clear that introducing the lateral stiffness increases the damping of the original mode (”osc. 1”) to a positive value, but now a second mode arises (”osc. 2”), which is unstable for a trail e^* smaller than approximately 0.24. Furthermore it can be observed that maximum obtainable positive damping for the least damped mode at a mechanical trail $e^* \approx 0.5$ is very marginal ($< 1.5\%$); the lateral stiffness had to be selected with care in order to obtain a stable system at all.

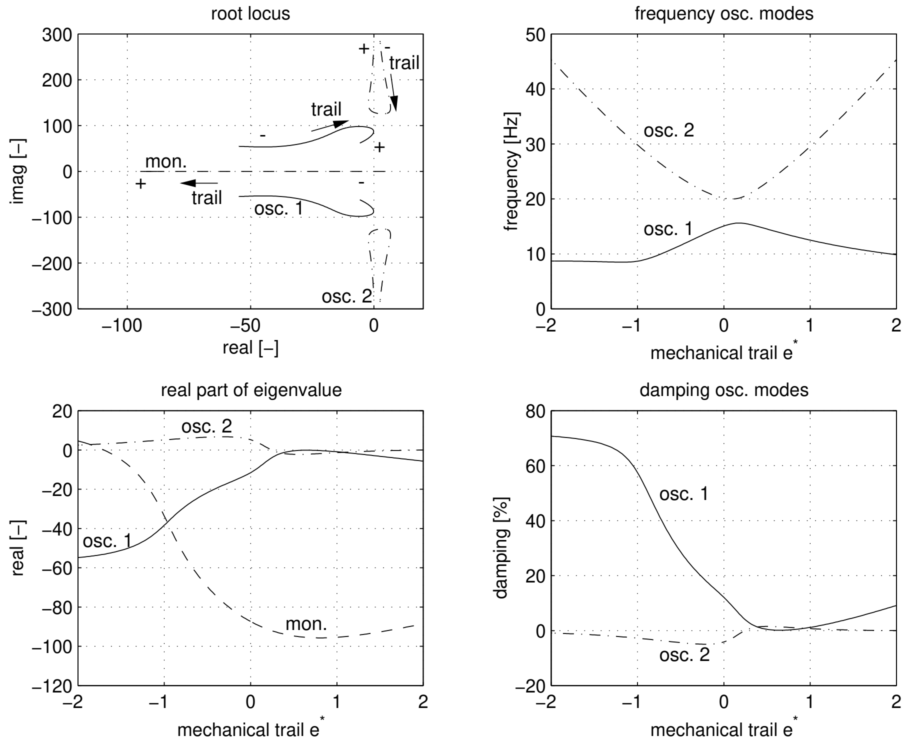

Fig. 2.8: Eigenvalues of the system with lateral flexibility (k_ψ=0, q=0).

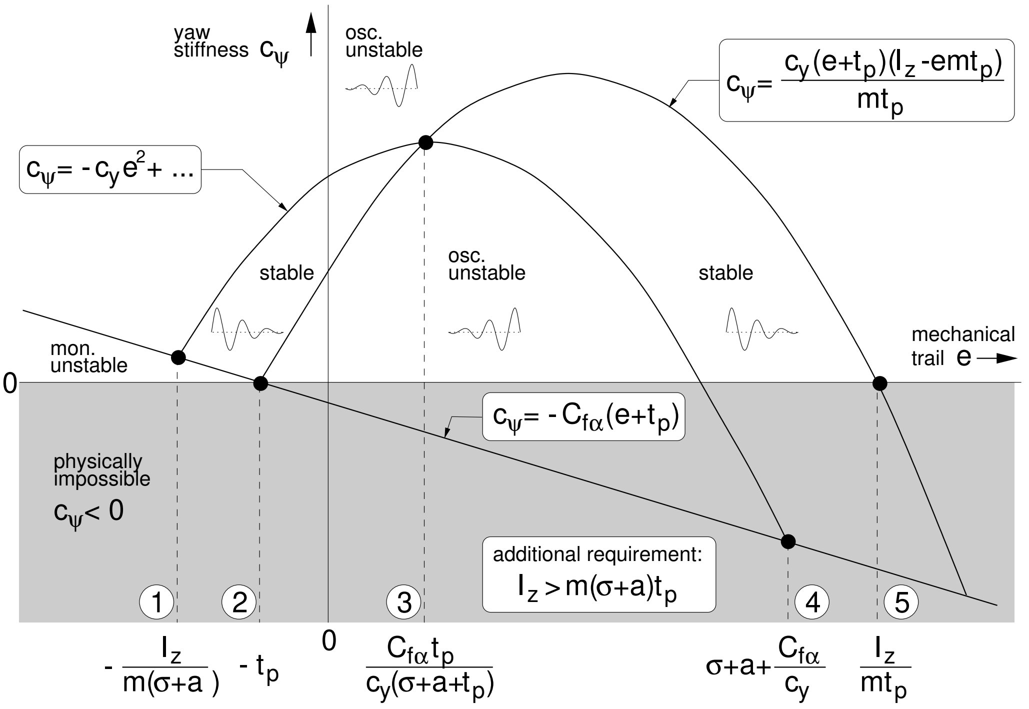
yaw stiffness c_ψ
osc. unstable
$c_\psi = \frac{c_y(e+t_p)(I_z - emt_p)}{mt_p}$
$c_\psi = -c_y e^2 + \ldots$
stable
osc. unstable
stable
mechanical trail e
mon. unstable
0
$c_\psi = -C_{f\alpha}(e+t_p)$
physically impossible
$c_\psi < 0$
additional requirement:
$I_z > m(\sigma+a)t_p$
①
②
③
④
⑤
$-\frac{I_z}{m(\sigma+a)}$
$-t_p$
0
$\frac{C_{f\alpha}t_p}{c_y(\sigma+a+t_p)}$
$\sigma+a+\frac{C_{f\alpha}}{c_y}$
$\frac{I_z}{mt_p}$

Fig. 2.9: Stability of the system with lateral flexibility (q, k_y, k_ψ=0).

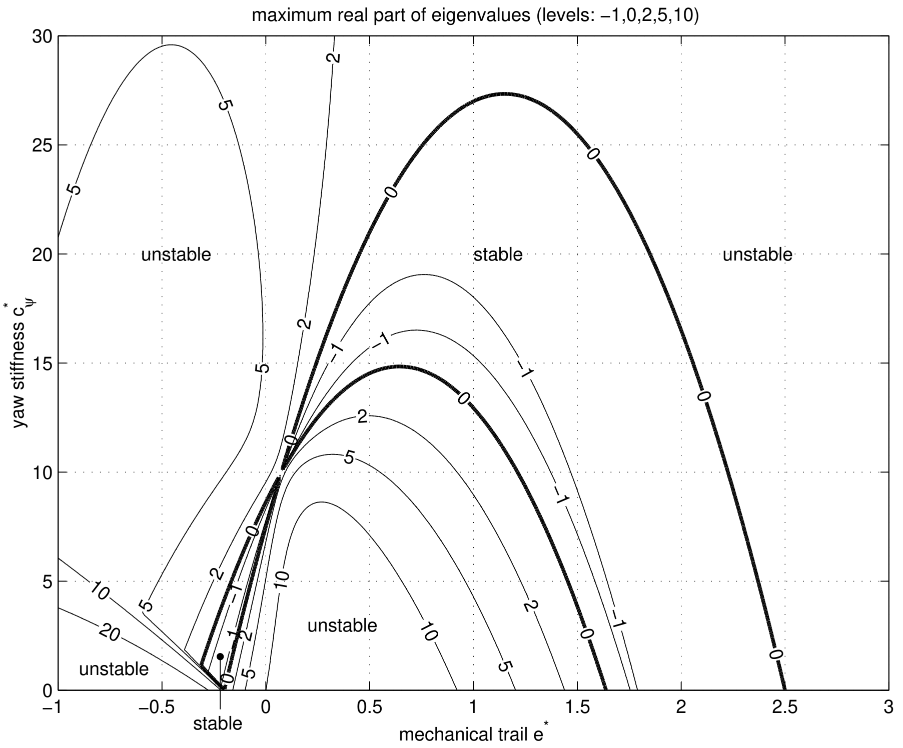

Fig. 2.10: Contour plot of the maximum real part of the eigenvalues for the system with lateral flexibility (q, k_y, k_ψ=0, c_y^*=15).

With the aid of computational tools for the symbolic manipulation of equations, the Hurwitz criterion has been applied to the characteristic equation of the system described by equation 2.10. The parameters q, k_y, k_ψ are taken equal to zero and physically relevant parameters are assumed: m, I_z, V, $C_{f\alpha}$, t_p, a and σ will all be positive. The system is stable if *all* of the following conditions are met ($a_0 = 1$):

$$\left.\begin{array}{lcl}
a_1 > 0 & : & \dfrac{V}{\sigma} > 0 \\
a_5 > 0 & : & c_\psi > -C_{f\alpha}(e+t_p) \\
H_2 > 0 & : & I_z > m(\sigma+a)t_p \\
H_3 > 0 & : & c_\psi < \dfrac{c_y I_z^2}{m^2(\sigma+a)t_p} + \dfrac{I_z(C_{f\alpha}-ec_y)}{m(\sigma+a)} + \dfrac{c_y e I_z}{mt_p} - c_y e^2 - C_{f\alpha}t_p \\
H_4 > 0 & : & \min(r_1,r_2) < c_\psi < \max(r_1,r_2)
\end{array}\right\} \quad (2.12)$$

H_4 is a quadratic function of c_ψ; r_1 and r_2 are the roots of the algebraic equation $H_4 = 0$ with respect to c_ψ:

$$\left.\begin{array}{l}
r_1 = \dfrac{I_z(C_{f\alpha}-ec_y)}{m(\sigma+a)} + \dfrac{I_z c_y}{m} + c_y e(\sigma+a) - c_y e^2 - C_{f\alpha}t_p \\
r_2 = \dfrac{c_y(e+t_p)(I_z-emt_p)}{mt_p}
\end{array}\right\} \quad (2.13)$$

From this equation it can be seen that the two roots (r_1, r_2) are again quadratic functions of e. The requirement for a_1 is trivial and it appears that the condition $H_3 > 0$ is always covered by H_4 (proof will be omitted here). Condition $a_5 > 0$ is a reformulation of condition $a_3 > 0$ for the trailing wheel system with infinite lateral stiffness, see equation 2.6. Apparently this condition is independent of the lateral stiffness. Furthermore a requirement exists representing a lower boundary for the yaw moment of inertia I_z, condition $H_2 > 0$.

It is interesting to note that none of the stability criteria are velocity dependent. The stability boundaries are given schematically in figure 2.9. In this figure also analytical expressions are given to identify a number of characteristic values for the mechanical trail. Basically the stability boundaries in the e-c_ψ plane can be described by two shifted parabolas with a lower boundary for c_ψ based either on physical considerations or the monotonical instability for negative trail values in excess of the pneumatic trail t_p.

For the previously defined numerical example, a stability plot similar to figure 2.9 will be constructed. The actual method employed is to calculate the eigenvalues using a fine grid in the e-c_ψ space. The system is on a stability boundary if the maximum of the real parts of the eigenvalues equals zero, which again corresponds to the results obtained with the Hurwitz criterion. The eigenvalue analysis has the advantage that it is also possible to produce additional contour lines corresponding to a certain stability level. The result is given in figure 2.10 and confirms the parabolic shape. Furthermore it can be noticed that the shimmy stability may be rather sensitive to changes in yaw stiffness, if the value of the mechanical trail is close to zero. It should be noted that large portions of the graph are merely of academic interest, since for a cantilevered landing gear the mechanical trail length e^* is expected to be in the range of -0.4 to 0.6.

The influence of changing the lateral stiffness c_y is shown in figure 2.11; the case where $c_y = \infty$ has been calculated using the model of section 2.1. It appears that the

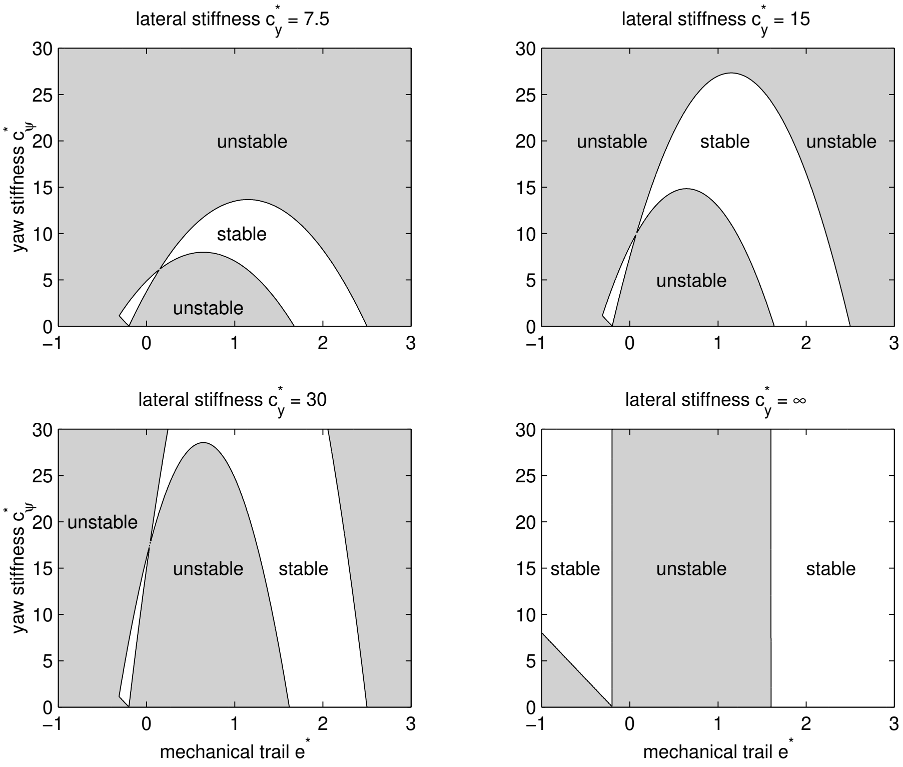

Fig. 2.11: Stability as a function of lateral stiffness (q, k_y, k_ψ=0).

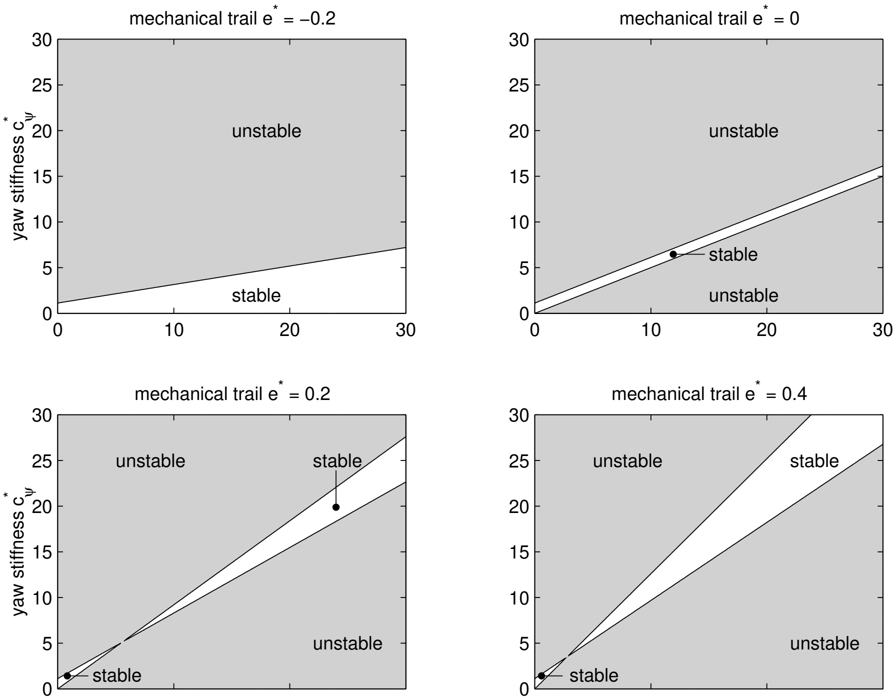

Fig. 2.12: Stability as a function of lateral and yaw stiffness (q, k_y, k_ψ=0).

system is only stable for specific stiffness combinations, depending on the choice of the mechanical trail e. A different representation is given in figure 2.12, which clearly shows that the stiffness *ratio* may be decisive for shimmy stability. The fact that the boundaries are linear is not surprising: the roots (r_1, r_2), as given by equation 2.13, are linear functions of the lateral stiffness c_y.

So far it has been assumed that the centre of gravity coincides with the wheel centre $(q = 0)$. For a twin-wheeled main landing gear the wheels, tyres and brakes determine to a large extent the total mass of the gear, so this appears to be a reasonable first estimate. But the location of the centre of gravity is also affected by the location of the main fitting, sliding member and torque links and therefore an offset may exist from the exact wheel centre. Again the Hurwitz criterion is applied to equation 2.10, now including an offset of the centre of gravity $(q \neq 0)$, but still keeping the damping k_y, k_ψ zero. Similar to the equations 2.12, *all* of the following conditions have to be met in order to obtain a stable system:

$$\left.\begin{array}{rcl} a_1 > 0 & : & \frac{V}{\sigma} > 0 \\ a_5 > 0 & : & c_\psi > -C_{f\alpha}(e+t_p) \\ H_2 > 0 & : & I_z > m(\sigma+a+q)(t_p-q) \\ H_3 > 0 & & \\ H_4 > 0 & & \end{array}\right\} \tag{2.14}$$

The expressions for H_3 and H_4 are rather lengthy and have been omitted here. Nevertheless it appears to be possible to construct a modified version of figure 2.9, and determine a number of characteristic points for the mechanical trail, see figure 2.14. This figure applies to the case where $q < t_p$: the centre of gravity is in front of the point of application of the lateral force F_y. It can be seen that the location of the characteristic points 2 and 4 and the shape of the parabola connecting 1 and 4 remain unchanged when moving the centre of gravity.

Some calculations have been made for the numerical example used so far, to show the effect of large changes in the location of the centre of gravity. The results are given in figure 2.13; it also shows the behaviour when $q \geq t_p$ ($q^* \geq 0.2$ in the numerical example). For the system under study, moving the centre of gravity forward reduces the stable area but the required yaw stiffness to actually stabilise the system at a positive mechanical trail (say $e^* = 0.5$) is smaller in comparison to moving the centre of gravity rearwards with respect to the wheel centre. If q^* equals -0.2 the system is unstable for any combination of yaw stiffness and mechanical trail. It can also be shown that it is possible to obtain a stable system again for very large negative values of q ($q^* \approx -1.3$), but this is only of academic interest.

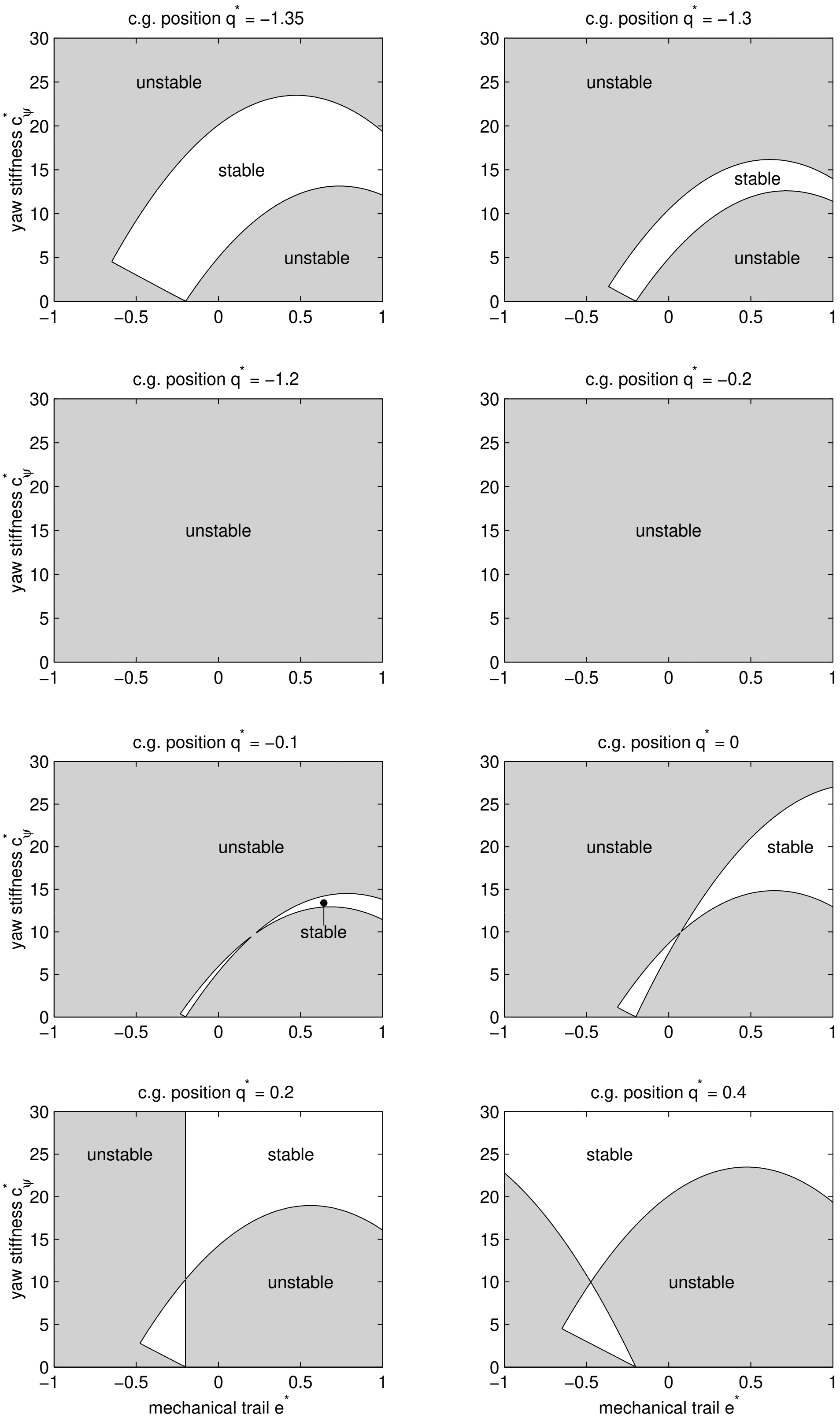

c.g. position $q^* = -1.35$

c.g. position $q^* = -1.3$

c.g. position $q^* = -1.2$

c.g. position $q^* = -0.2$

c.g. position $q^* = -0.1$

c.g. position $q^* = 0$

c.g. position $q^* = 0.2$

c.g. position $q^* = 0.4$

Fig. 2.13: Influence of c.g. position on stability (k_ψ=0).

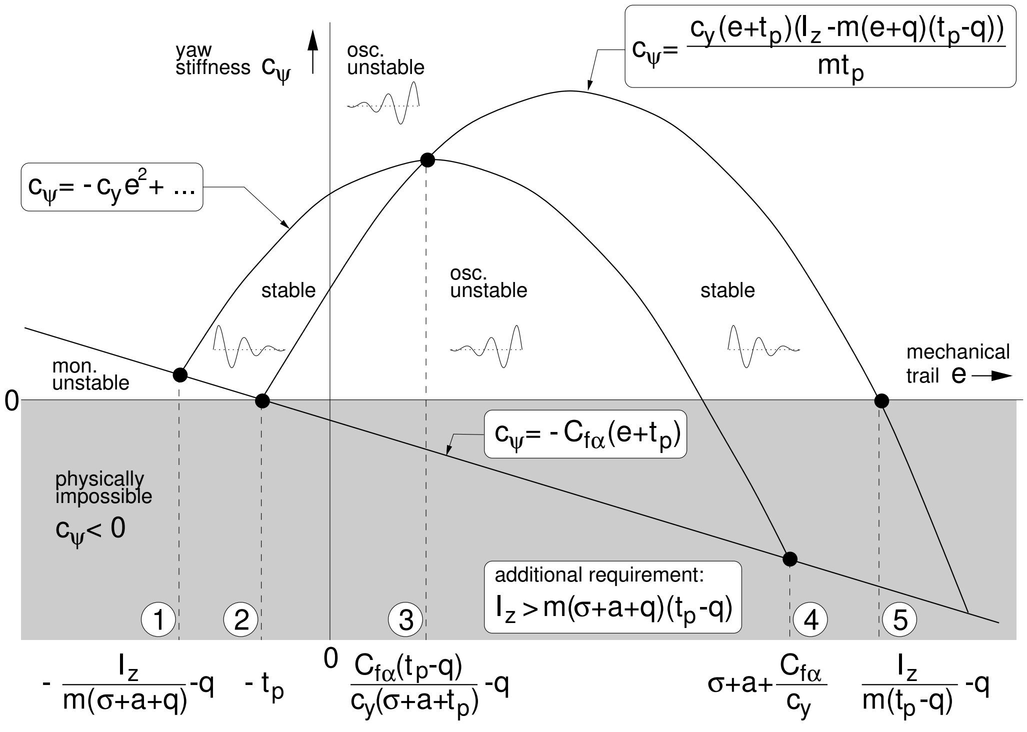

Fig. 2.14: Stability of the system with lateral flexibility (k_y, k_ψ=0, $q < t_p$).

2.3 Energy flow and mode shapes

So far a trailing wheel system without viscous damping has been studied; the structural part is a conservative system and does not dissipate energy. This has to imply that the tyres are responsible for the dissipation of energy in case the total system is positively damped, or vice versa that energy is provided through the tyres to drive the unstable vibration. The underlying mechanism, which describes in detail how energy is extracted from the aircraft forward motion and fed into the lateral/yaw motion of the landing gear in case of an instability, will not be discussed here. In this section the tyre is treated as a ”black box” which, at a given constant forward velocity, produces forces and moments in response to motions of the wheel plane.

The energy balance for the tyre during one vibrational cycle will now be considered. From equations 2.1 it can be seen that the straight tangent tyre model has two inputs: the lateral velocity $\dot{y}_c$ and the yaw motion (ψ and $\dot{\psi}$). The resulting output is the lateral force F_y and self aligning moment M_z. Sinusoidal inputs with a radial frequency ω are considered; a_m is a measure for the amplitude of the motion:

$$\begin{aligned} y_c(t) &= a_m \eta \sin(\omega t + \xi) \\ \psi(t) &= a_m \sin(\omega t) \end{aligned} \tag{2.15}$$

If the amplitude ratio η is zero, only a yaw input is considered; with increasing η the relative magnitude of the lateral motion increases. The relative phase angle ξ indicates the phase lead of the lateral motion with respect to the yaw motion. The energy balance is calculated for one cycle, with a period $T = \frac{2\pi}{\omega}$:

$$W = \int_0^T (F_y \dot{y}_c + M_z \dot{\psi})\, dt \tag{2.16}$$

If W is negative, energy is fed into the tyre. In order to calculate the integral, first the differential equation 2.1, combined with equation 2.15, has to be solved. Since the long-term behaviour will be studied, only the steady-state periodic solution is considered. The following expression is obtained for the deformation angle $\alpha'(t)$:

$$\left.\begin{array}{l} \alpha'(t) = \dfrac{a_m}{V^2+\sigma^2\omega^2}\Big(\; -(\sigma+a)V\omega\cos(\omega t) - \eta V\omega\cos(\omega t+\xi) \\ \qquad\qquad\qquad\quad +(V^2 - a\sigma\omega^2)\sin(\omega t) - \eta\sigma\omega^2\sin(\omega t+\xi)\Big) \end{array}\right\} \tag{2.17}$$

With expressions 2.1 and 2.2 for F_y and M_z integral 2.16 becomes:

$$W = \int_0^T \Big(C_{f\alpha}\alpha'\omega a_m \eta\cos(\omega t+\xi) - C_{f\alpha}t_p\alpha'\omega a_m\cos(\omega t)\Big)dt \tag{2.18}$$

Substitution of 2.17 and solving the integral yields:

$$\left.\begin{array}{l} W = \dfrac{a_m^2 C_{f\alpha}\pi V\omega}{V^2+\sigma^2\omega^2}\Big(\; -\eta^2 + (\sigma+a)t_p + (t_p - a - \sigma)\eta\cos\xi \\ \qquad\qquad\qquad\qquad +(a\sigma\frac{\omega}{V} - \frac{V}{\omega} + t_p\sigma\frac{\omega}{V})\eta\sin\xi\Big) \end{array}\right\} \tag{2.19}$$

First a fixed rotation centre will be considered: in this case the yaw and lateral motion are in phase ($\xi = 0$) and η represents the distance between wheel centre and rotation centre. The expression for the energy reduces to:

$$W = \frac{a_m^2 C_{f\alpha}\pi V\omega}{V^2+\sigma^2\omega^2}(-\eta + t_p)(\eta + \sigma + a) \tag{2.20}$$

Since the leading factor in this equation will always be positive, it can be seen that $W > 0$ if $\eta < t_p$ and $\eta > -(\sigma+a)$. Following the adopted sign convention the rotation centre will have a trail $e = -\eta$. Then it can be verified that these results are identical to the stability criterion $H_2 > 0$ as derived for the trailing wheel model, see equation 2.6. Thus it is shown again that oscillatory instability occurs when $-t_p < e < \sigma + a$. Note that the energy method does not detect the monotonous instability which occurs if $e < -(t_p + c_\psi/C_{f\alpha})$, because not all solutions of 2.1 are considered, but only the steady-state periodic solutions as defined by equation 2.15.

Now the general case will be studied including a phase difference between lateral and yaw motion. It appears to be convenient to switch to polar coordinates:

$$x_p = \eta\cos\xi, \quad y_p = \eta\sin\xi \tag{2.21}$$

Then the expression for the energy becomes:

$$W = -\frac{a_m^2 C_{f\alpha}\pi V\omega}{V^2+\sigma^2\omega^2}\left(x_p^2 + y_p^2 + (\sigma + a - t_p)x_p + \Big(\frac{V}{\omega} - \frac{\sigma\omega}{V}(t_p + a)\Big)y_p - t_p(\sigma + a)\right) \tag{2.22}$$

We will now focus on the $W = 0$ case, which marks the boundary of stability. Furthermore the wavelength λ is introduced:

$$\lambda = \frac{2\pi V}{\omega} \tag{2.23}$$

Equation 2.22 then reduces to:

$$x_p^2+y_p^2+(\sigma+a-t_p)x_p+\left(\frac{\lambda}{2\pi}-\frac{2\pi\sigma}{\lambda}(t_p+a)\right)y_p-t_p(\sigma+a)=0 \tag{2.24}$$

This equation is actually the description of a circle in the x_p-y_p plane. The coordinates of the origin of the circle are given by:

$$(x_{pc},y_{pc})=\left(-\frac{1}{2}(\sigma+a-t_p),-\left(\frac{\lambda}{4\pi}-\frac{\pi\sigma}{\lambda}(t_p+a)\right)\right) \tag{2.25}$$

An expression for the radius of the circle can also be derived, but it is more convenient to consider 2.24 as a circle bundle with the basis points $(-(\sigma+a),0)$ and $(t_p,0)$. As a result, a polar plot can be constructed, where the distance to the origin is the amplitude ratio η and the angle to the positive x-axis represents the relative phase angle ξ. It is important to notice that these $W=0$ circles are only a function of a, σ, t_p and λ; they do not depend on the forward velocity V. Figure 2.15 shows the results for $\sigma=3a$, $t_p=0.5a$ and $\lambda=20a$, $40a$, $60a$ and $80a$. Instability occurs inside the circles, where $W>0$.

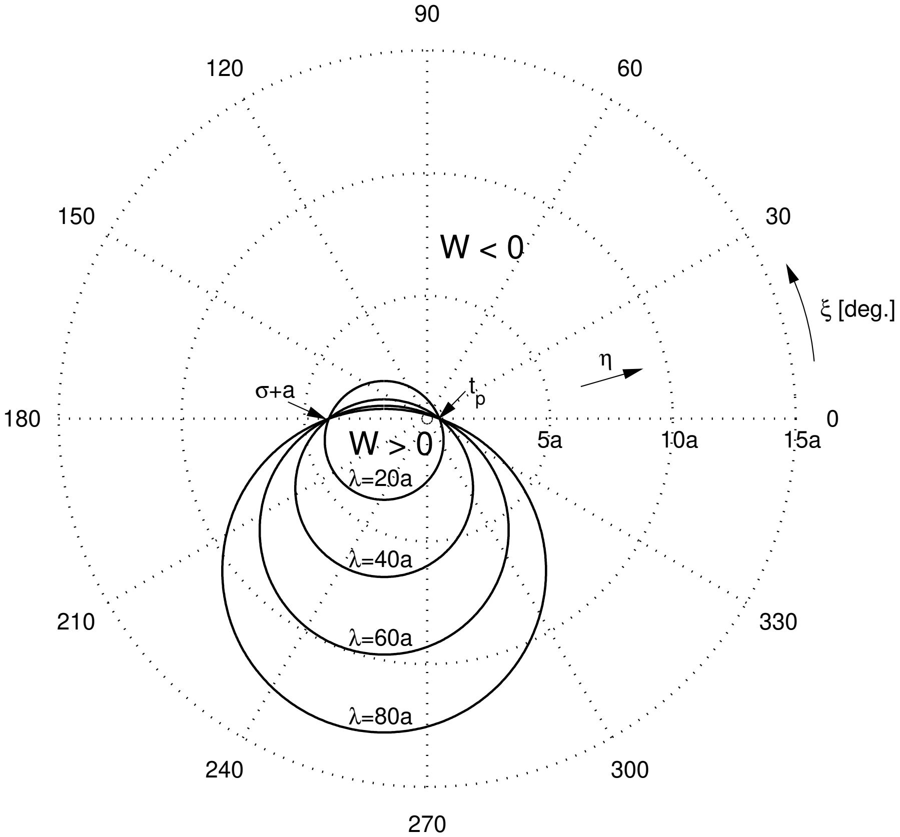

Fig. 2.15: Zero energy dissipation per cycle as function of amplitude ratio η and relative phase angle ξ between lateral and yaw input to the wheel plane at road level (σ=3a, t_p=0.5a).

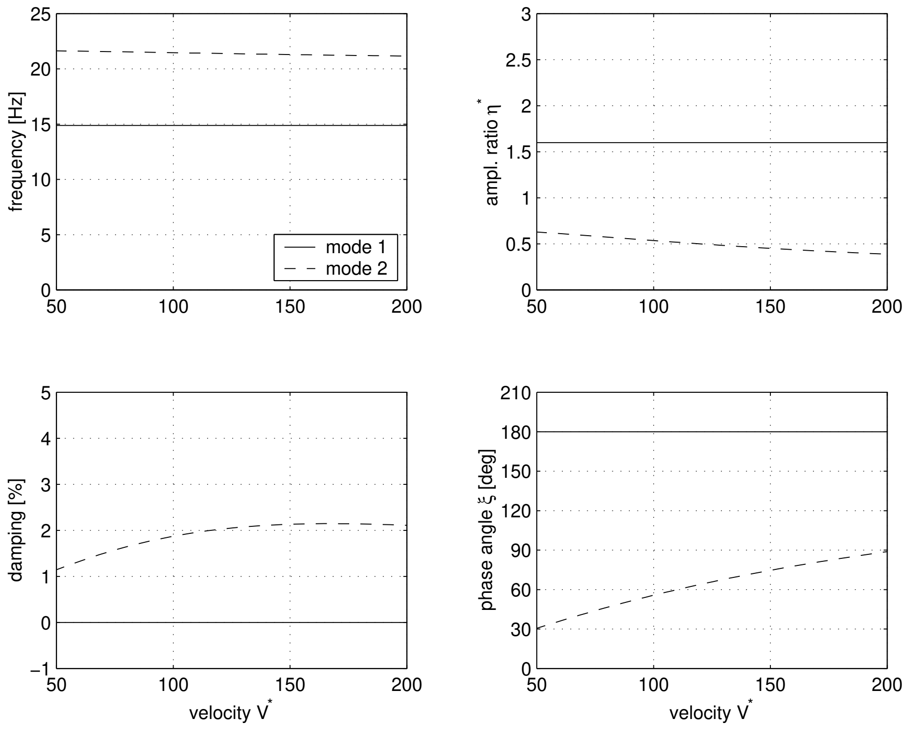

Fig. 2.16: Eigenfrequencies and mode shapes as function of forward velocity (c^*_ψ=13.95, k_y, k_ψ, q=0).

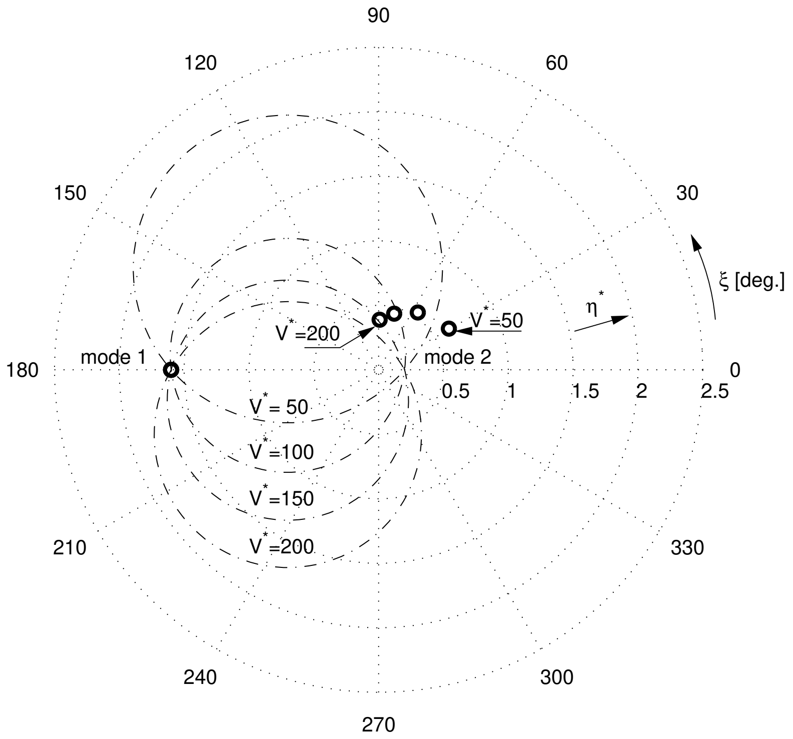

Fig. 2.17: Polar plot of the mode shapes at different forward velocities, W=0 circles are given for mode 2 (c^*_ψ=13.95, k_y, k_ψ, q=0).

Figure 2.15 may be helpful in understanding that:

- a landing gear may become oscillatory unstable if certain conditions are met regarding the mode shape and wavelength. The "unstable" area inside the circle moves and changes in size with wavelength; therefore the stability may become dependent on frequency (stiffness, mass) and forward velocity.
- the stability boundaries of the base trailing wheel system (without damper and lateral flexibility) are the basis points of the $W = 0$ circle bundle. In this special case stability is only a function of the length of the mechanical trail.
- if only the lateral degree of freedom is available ($\eta = \infty$) the system will not become oscillatory unstable.

The next example illustrates the mode shape analysis based on the energy considerations. The trailing wheel model with lateral flexibility is only stable within a certain range of the yaw stiffness, as was shown in the previous section. An upper and lower value of the yaw stiffness can be selected, representing a system with one eigenvalue with a zero real part. For this specific condition the mode shape will be analysed as a function of the forward velocity. In the numerical example $e^* = 0.4$ and $q^* = 0$ are selected. Using the parameters of page 23, taking $c^*_y = 15$ and using equation 2.13, the lower and upper value for the yaw stiffness can be assessed. We obtain: $c^*_\psi = 13.95$ and $c^*_\psi = 18.90$; these values may also be checked in figure 2.10.

For the low value of the yaw stiffness figure 2.16 can be obtained. The damping of the least damped mode ("mode 1") is exactly zero over the velocity range, as expected. Also the frequency and mode shape of this particular mode do not change. Figure 2.17 gives the polar plot with a point representation of the mode shape of "mode 1", indicated with the symbol **o**. Since "mode 1" lies on a basis point of the $W = 0$ circle bundle, it will have zero damping. It can also be seen that at each forward velocity the second mode ("mode 2") is always outside the accompanying $W = 0$ circle and is therefore positively damped.

The diagrams of figure 2.18 have been calculated for the high value of the yaw stiffness. Again we find the damping of the least damped mode ("mode 2") to be exactly zero. For "mode 2" both phase and amplitude of the mode shape change with forward velocity: as the velocity increases the lateral motion gets an increasing phase lead over the yaw motion and the amplitude ratio η^* decreases. At each forward velocity this particular mode shape should be represented by a point on the accompanying $W = 0$ circle in the polar diagram. The frequency of "mode 2" is constant, but the wavelength will increase linearly with forward velocity and therefore also the location of the $W = 0$ circle will change. In figure 2.19 the actual mode shapes of "mode 2" have been indicated with the symbol **o**. It can be observed that these points are indeed located on the accompanying $W = 0$ circle, which again illustrates the validity of the stability requirements derived from energy considerations. The other mode ("mode 1") has a phase angle ξ of 180 degrees and an amplitude ratio η^* of 2.5: it will always be located outside of the $W = 0$ circles and is therefore positively damped.

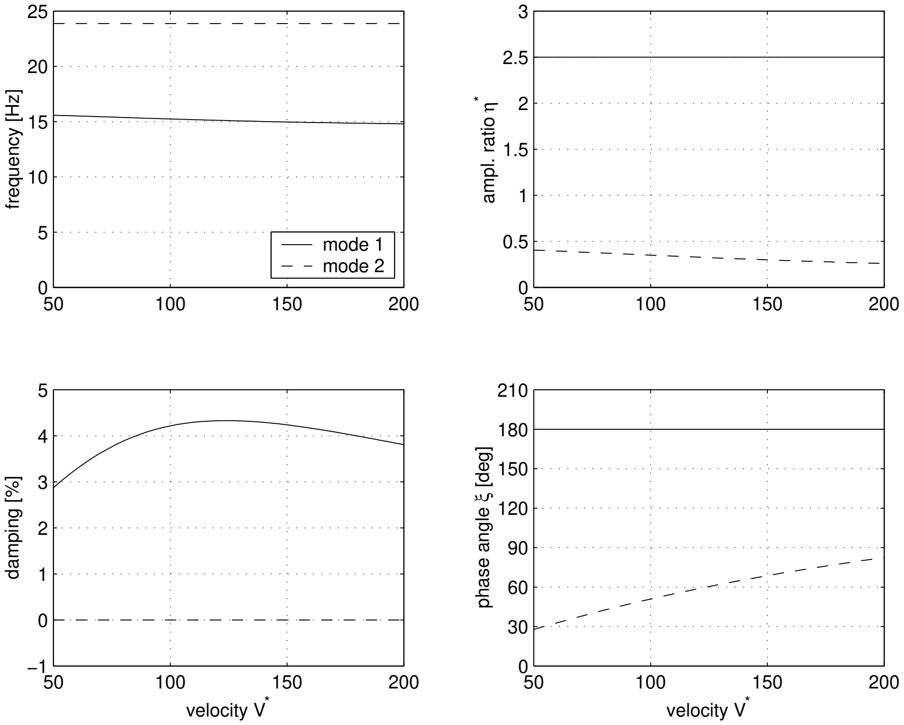

Fig. 2.18: Eigenfrequencies and mode shapes as function of forward velocity (c^*_ψ=18.9, k_y, k_ψ, q=0).

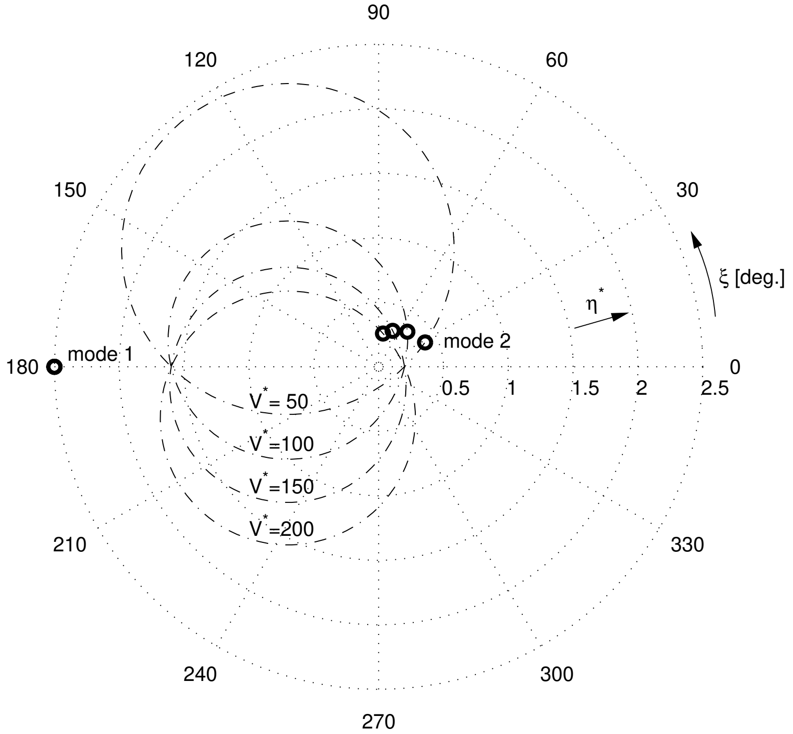

Fig. 2.19: Polar plot of the mode shapes at different forward velocities, W=0 circles are given for mode 2 (c^*_ψ=18.9, k_y, k_ψ, q=0).

2.4 Damping and gyroscopes

In the stability analyses performed so far, both the yaw damping k_ψ and lateral damping k_y have been kept zero for the system with lateral flexibility of the support. The yaw damping is of particular interest because it may represent an approximation to the energy dissipation provided by the friction between main fitting and sliding member. The tyres may also contribute to the yaw damping because of tread width effects, which are not yet considered in the tyre model. For a conventional cantilevered landing gear design the lateral damping will generally be fairly marginal and only consist of structural damping.

One conclusion of the energy considerations for a single tyre, as made in the previous section, is that a yaw degree of freedom motion of the wheel is required to obtain an unstable vibration. A positive yaw damping k_ψ will result in energy dissipation for the yaw motion and may stabilise the system. For the system under consideration this is illustrated by figure 2.20; the parameters of page 23 are used including $V^* = 150$ and $c_y^* = 15$. Note that introducing yaw damping does not change the monotonous instability, which occurs for a combination of a negative mechanical trail and low values of the yaw stiffness c_ψ.

The effect of introducing lateral damping is shown in figure 2.21. It appears that only introducing lateral damping may actually destabilise the gear for small mechanical trail values. This is in contrast to adding yaw damping, which has either no or a positive contribution to the shimmy stability. It is obvious that if the lateral damping is made very large, the system will behave again as the model without flexibility of the lateral support. This system is unstable for any mechanical trail value in the range between $-t_p$ and $\sigma + a$, as was shown in figure 2.5.

A landing gear has to operate up to forward velocities of 300 km/h and the rotating parts, wheels, tyres and brake disks, have a large contribution to the total landing gear mass. Furthermore, the wheel axle will roll about the longitudinal axis when a lateral load is applied at ground level; so it can be expected that gyroscopic effects caused by these rotating parts may be important. A simple extension will be made to the current model to approximately incorporate gyroscopic behaviour, see figure 2.22. The gyroscopes can be introduced in equation 2.10 by replacing two coefficients in the matrix $\mathbf{A}$:

$$\left.\begin{aligned} \mathbf{A}(1,2) &= -\frac{k_y e_t}{m} + \frac{I_p \Omega}{m l} \\ \mathbf{A}(2,1) &= -\frac{k_y e_t}{I_z} - \frac{I_p \Omega}{I_z l} \end{aligned}\right\} \tag{2.26}$$

where I_p is the polar moment of inertia of the rotating parts and l is the effective gear length. The effective rolling radius R_e relates the angular velocity of the wheel Ω with the forward velocity:

$$V = \Omega R_e \tag{2.27}$$

The roll angle of the wheel is taken equal to y_s/l with y_s the lateral position of the swivel axis at ground level. Using this approach, it is assumed that the centre of gravity remains at road level and the lateral stiffness c_y remains independent of l. A more detailed three dimensional model of the landing gear will be introduced in chapter 3. Some results for various values of the effective gear length l are given in figure 2.23. These calculations are made at a constant forward velocity $V^* = 150$; the additional parameters are $I_p^* = 0.2$ and $R_e^* = 1$. It can be observed that the gyroscopes result in a system becoming unstable

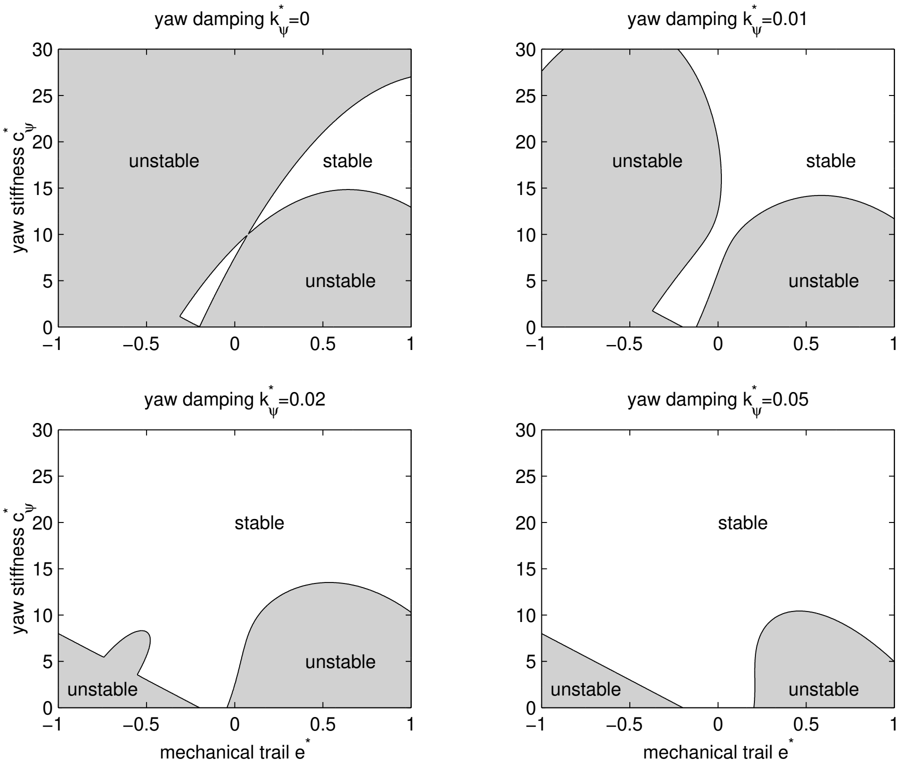

Fig. 2.20: Influence of yaw damping on stability (V^*=150, k_y^*=0, no gyroscopes).

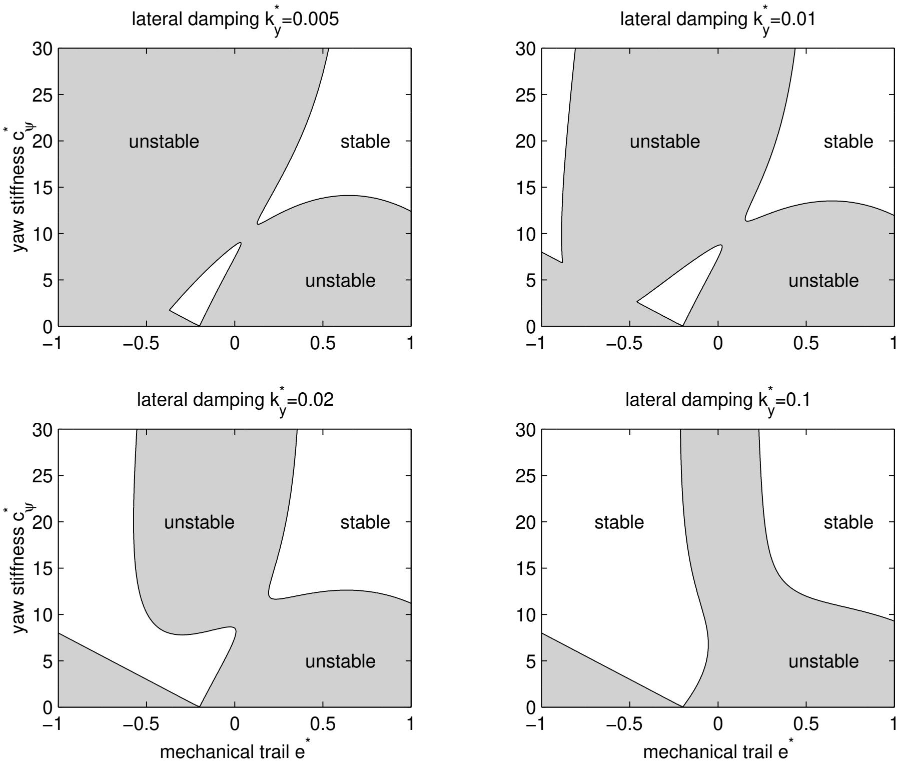

Fig. 2.21: Influence of lateral damping on stability (V^*=150, k_ψ^*=0, no gyroscopes).

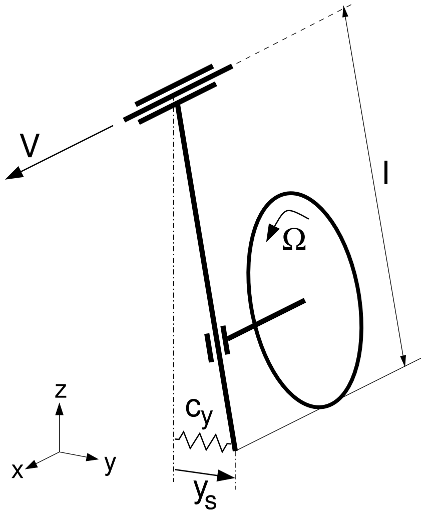

Fig. 2.22: Model of the trailing wheel system with lateral flexibility and roll (front view).

for small positive trail values, irrespective of the value of the yaw stiffness c_ψ. The introduction of gyroscopes will also make the stability boundaries velocity dependent: the effect of increasing the forward velocity is very similar to that of decreasing the gear length l, as is to be expected from equation 2.26. The difference is that changing the velocity also affects tyre dynamic behaviour, but for the landing gear configuration under study this does not give rise to major changes in the e-c_ψ stability plot.

For a given effective gear length, a reduction of the lateral stiffness will result in an increasing contribution of the gyroscopes; this is illustrated by figure 2.24. For the configuration under study, a reduction of the lateral stiffness may have to be combined with a lower yaw stiffness c_ψ and increased positive mechanical trail in order to maintain stability. In particular for small positive values of the mechanical trail e, the yaw damping and gyroscopes seem to have opposite contributions to the stability.

With increasing forward velocity the contribution of the gyroscopes will become more dominant over the damping, making the system unstable for small positive trail and relatively low values of the yaw stiffness as is shown in figure 2.25. If the yaw damping is increased sufficiently, a stable configuration can be obtained again. In the current example, increasing k_ψ^* to 0.08 would result in a stable configuration up to $V^* = 200$ for the whole e-c_ψ plane, with the exception of the monotonous instability at negative mechanical trail values combined with a low yaw stiffness (figure not shown).

In figure 2.25 the combination of a zero mechanical trail e and yaw stiffness c_ψ represents a special case: the system is unstable at low forward velocity and will become unstable again when extrapolating to velocities in excess of $V^* = 200$. This is illustrated in more detail by figure 2.26: at low forward velocity mode 1 is unstable; at high forward velocity mode 2 becomes unstable. This type of behaviour was also noted by Pacejka when studying the shimmy behaviour of the front wheels of a light truck, reference [35]. The instability at the lower forward velocity is known as *tyre* shimmy and the instability at higher forward velocity is named *gyroscopic* shimmy. In the example given here the forward velocity at which gyroscopic shimmy occurs is rather high, a reduction of the lateral stiffness, effective gear length or increase of the polar moment of inertia will considerably reduce this velocity.

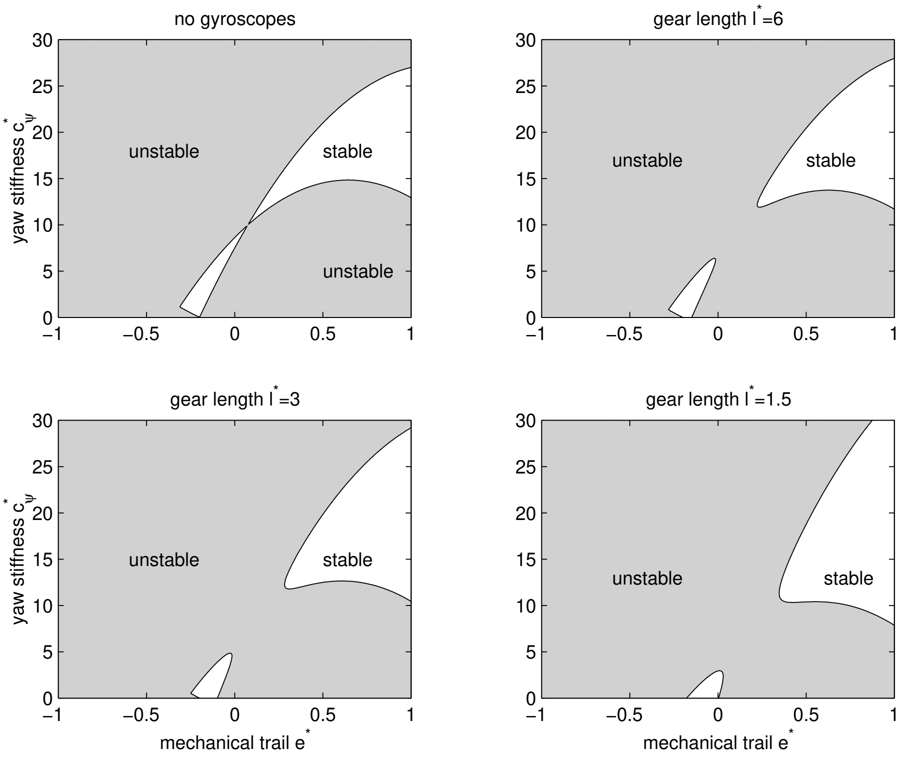

Fig. 2.23: Influence of gyroscopic coupling on stability (V^*=150, k^*_ψ, k^*_y=0).

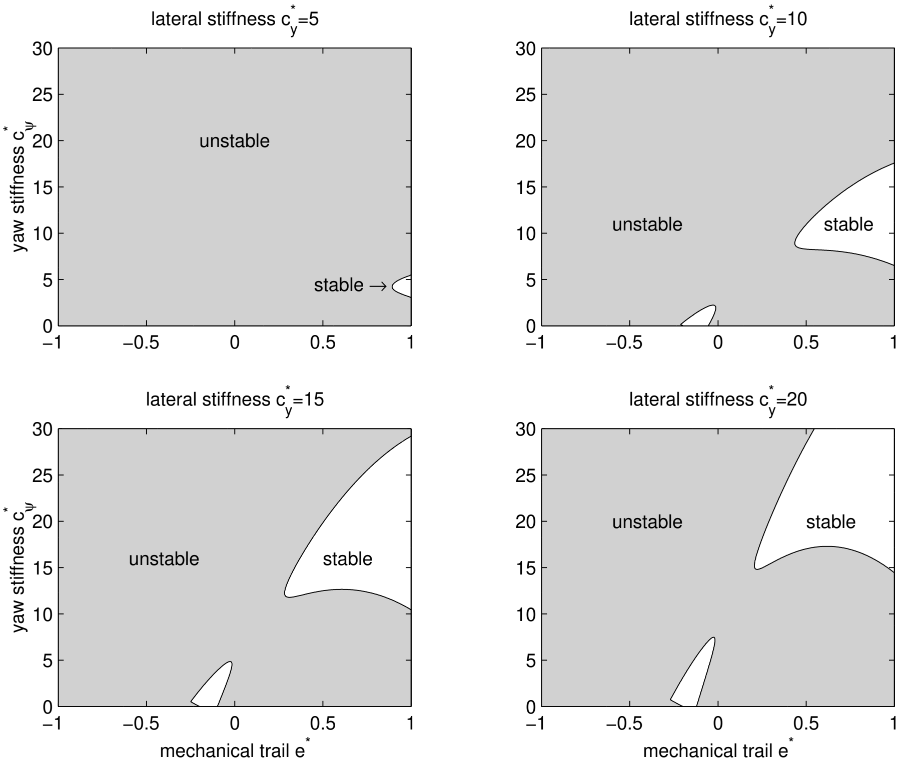

Fig. 2.24: Stability for different values of the lateral stiffness (V^*=150, l^*=3, k^*_ψ, k^*_y=0).

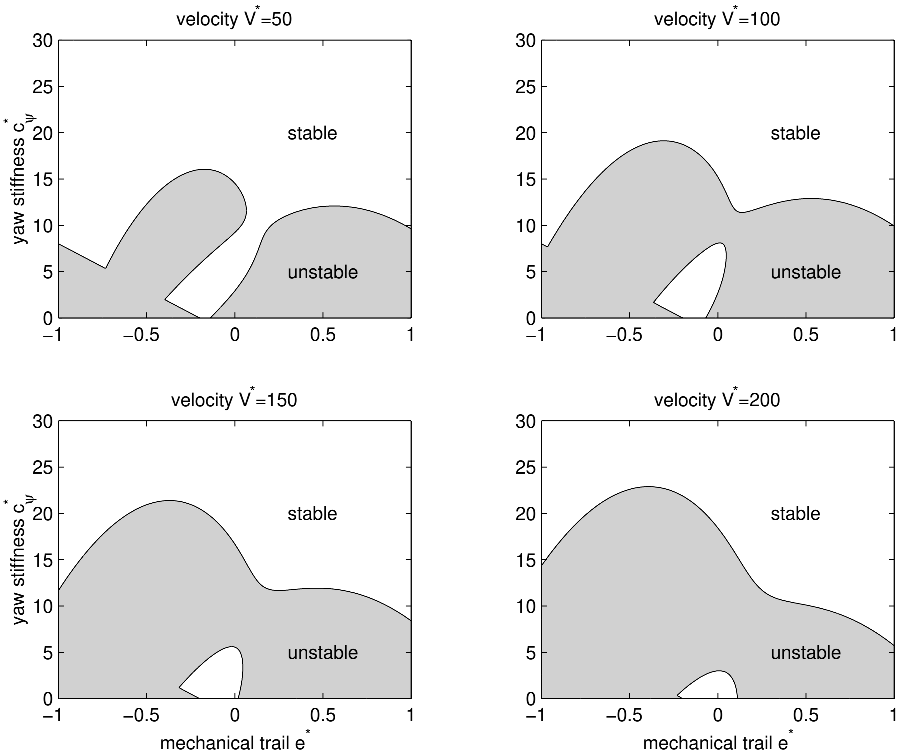

Fig. 2.25: Stability for varying forward velocity (l^*=3, k_ψ^*=0.015, k_y^*=0).

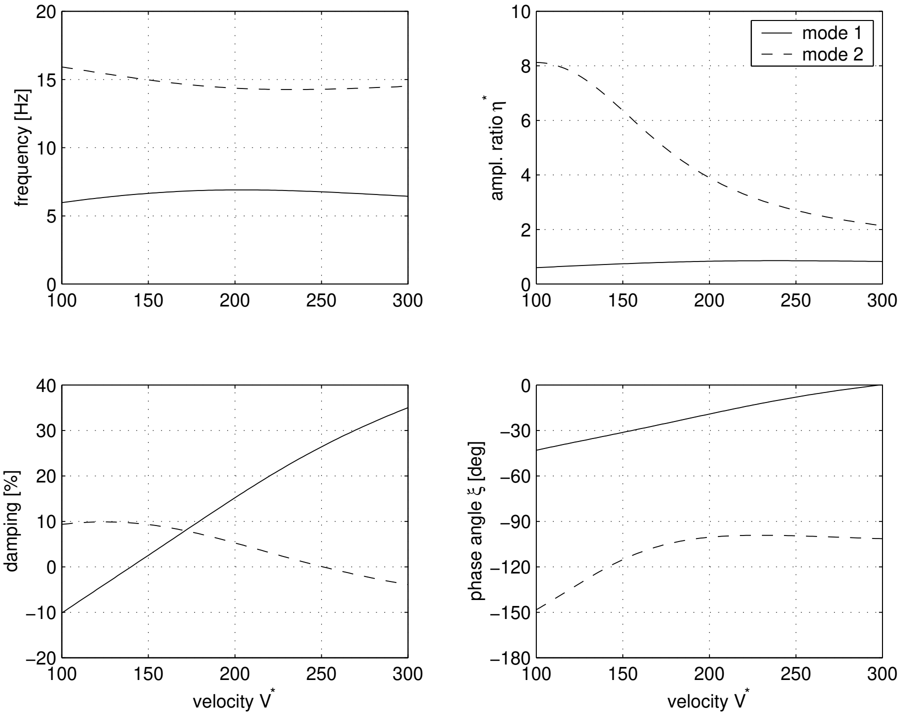

Fig. 2.26: Stability as a function of forward velocity (l^*=3, k_ψ^*=0.015, k_y^*, c_ψ^*, e^*=0).

2.5 A frequency domain view

For an alternative view on the cause of the shimmy instability we may apply some control theory. The landing gear can be considered as a feedback system: the tyre produces lateral forces, which will result in a lateral and yaw motion of the gear structure. At a given forward velocity these motions, combined with the tyre relaxation behaviour, will again result in a lateral force. The closed-loop system may be stable or unstable, depending on the amplitude and phase relation of the open-loop system.

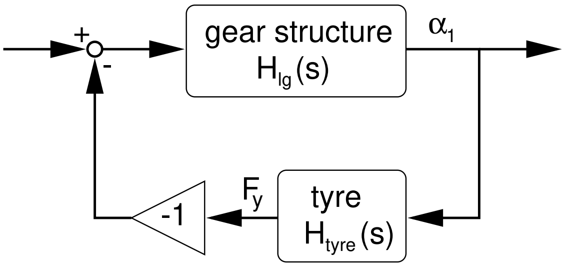

Fig. 2.27: Feedback schematisation of the trailing wheel system.

For the trailing wheel model with lateral flexibility, as presented in section 2.2, the tyre and gear structure will be separated, see figure 2.27. The input for the landing gear structure is the lateral force generated by the tyres acting at the pneumatic trail, the output is the wheel side slip angle α_1 at the leading contact point. For α_1 the following relation holds:

$$\alpha_1 = \psi - a\frac{\dot{\psi}}{V} - \frac{\dot{y}_c}{V} \tag{2.28}$$

The transfer function of the tyre then becomes (see equation 2.1):

$$H_{tyre}(s) = H_{F_y,\alpha_1}(s) = \frac{C_{f\alpha}}{\frac{\sigma}{V}s+1} \tag{2.29}$$

So the straight tangent tyre model behaves as a first order system with a time constant of $\frac{\sigma}{V}$ and the gain equals the cornering stiffness $C_{f\alpha}$.

In general a state space description may be used to define the relations between the input $\mathbf{u}(t)$ and output $\mathbf{y}(t)$ for a linear, dynamic, time-invariant system:

$$\left.\begin{array}{rcccc} \dot{\mathbf{x}}(t) & = & \mathbf{A}\cdot\mathbf{x}(t) & + & \mathbf{B}\cdot\mathbf{u}(t) \\ \mathbf{y}(t) & = & \mathbf{C}\cdot\mathbf{x}(t) & + & \mathbf{D}\cdot\mathbf{u}(t) \end{array}\right\} \tag{2.30}$$

The transfer function of this system is:

$$\mathbf{H}_{yu}(s) = \mathbf{C}(s\mathbf{I}-\mathbf{A})^{-1}\mathbf{B}+\mathbf{D} \tag{2.31}$$

Where s is the Laplace variable, which may be replaced by $j\omega$. For the trailing wheel model with lateral flexibility (sections 2.2 and 2.4) the input $\mathbf{u}(t)$ equals $F_y(t)$ and the output $\mathbf{y}(t)$ equals $\alpha_1(t)$. The definition of the state vector is:

$$\mathbf{x}(t) = \begin{pmatrix} \dot{y} & \dot{\psi} & y & \psi \end{pmatrix}^T \tag{2.32}$$

The matrices **A**, **B**, **C** and **D** read:

$$\mathbf{A} = \begin{pmatrix} -\frac{k_y}{m} & -\frac{k_y(e+q)}{m} + \frac{I_p\Omega}{ml} & -\frac{c_y}{m} & -\frac{c_y(e+q)}{m} \\ -\frac{k_y(e+q)}{I_z} - \frac{I_p\Omega}{I_z l} & -\frac{k_y(e+q)^2+k_\psi}{I_z} & -\frac{c_y(e+q)}{I_z} & -\frac{c_y(e+q)^2+c_\psi}{I_z} \\ 1 & 0 & 0 & 0 \\ 0 & 1 & 0 & 0 \end{pmatrix} \tag{2.33}$$

$$\mathbf{B} = \begin{pmatrix} \frac{1}{m} & \frac{(q-t_p)}{I_z} & 0 & 0 \end{pmatrix}^T \tag{2.34}$$

$$\mathbf{C} = \begin{pmatrix} -\frac{1}{V} & -\frac{(q+a)}{V} & 0 & 1 \end{pmatrix} \tag{2.35}$$

$$\mathbf{D} = \begin{pmatrix} 0 \end{pmatrix} \tag{2.36}$$

Consequently the transfer of the gear structure becomes:

$$H_{lg}(s) = H_{\alpha_1,F_y}(s) = \mathbf{C}(s\mathbf{I}-\mathbf{A})^{-1}\mathbf{B} \tag{2.37}$$

The Nyquist criterion can be used to study the stability of the closed-loop system using the transfer function of the open-loop system. The open-loop transfer function reads:

$$\overset{\circ}{H}(s) = -H_{lg}(s)H_{tyre}(s) \tag{2.38}$$

According to the Nyquist criterion the stability of the closed-loop system is ensured when the point (-1,0) is on the left hand side of the open-loop transfer function in the polar plot, when following this transfer function with increasing frequency. An additional requirement for the Nyquist criterion is that each element of the open-loop transfer function has to be stable, which will always be the case for a physically relevant tyre and gear structure. Another note is that the Nyquist criterion will not detect a monotonical instability, because transfer functions are only defined for steady-state periodic solutions.

A number of applications will be shown. The parameters of the trailing wheel model will be used, with the exception that a small amount of damping is introduced, which corresponds to about 0.5% damping in the gear structure. So we have the following set of baseline parameters: $m^* = 1$, $I_z^* = 0.5$, $I_p^* = 0.2$, $a^* = 0.4$, $\sigma^* = 1.2$, $t_p^* = 0.2$, $q^* = 0$, $R_e^* = 1$, $e^* = 0.4$, $l^* = \infty$, $C_{f\alpha}^* = 10$, $c_y^* = 15$, $c_\psi^* = 15$, $k_y^* = 25 \cdot 10^{-4}$, $k_\psi^* = 5 \cdot 10^{-4}$, $V^* = 150$.

As an introductory example the effect of modifying the cornering stiffness $C_{f\alpha}$ on the shimmy stability will be investigated. Figure 2.28 gives the amplitude and phase relation of the open-loop transfer function. The two peaks in the amplitude ratio correspond to the eigenfrequencies of the structure without tyre (12.26 and 21.92 Hz). The cornering stiffness is just a gain in the open-loop transfer function: the phase relation remains unchanged, but the amplitude ratio increases with the magnitude of the cornering stiffness.

To judge system stability a Nyquist plot of the open-loop transfer function can be created; see figure 2.29. Since damping in the open-loop transfer function is very low, it is difficult to combine the peak of the transfer function and a visual check of the point (-1,0) in one graph. Therefore it was decided to radially plot the *square root* of the amplitude ratio; this transformation leaves the stability conditions for the point (-1,0) unchanged.

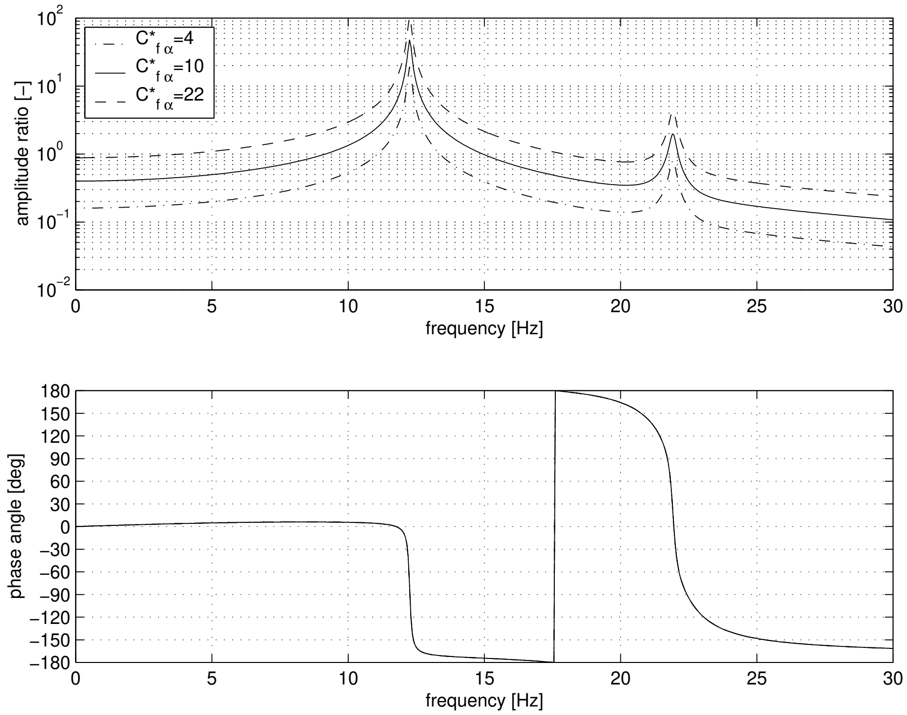

Fig. 2.28: Bode plot of the open loop transfer function; varying cornering stiffness (baseline parameters except for $C_{f\alpha}$).

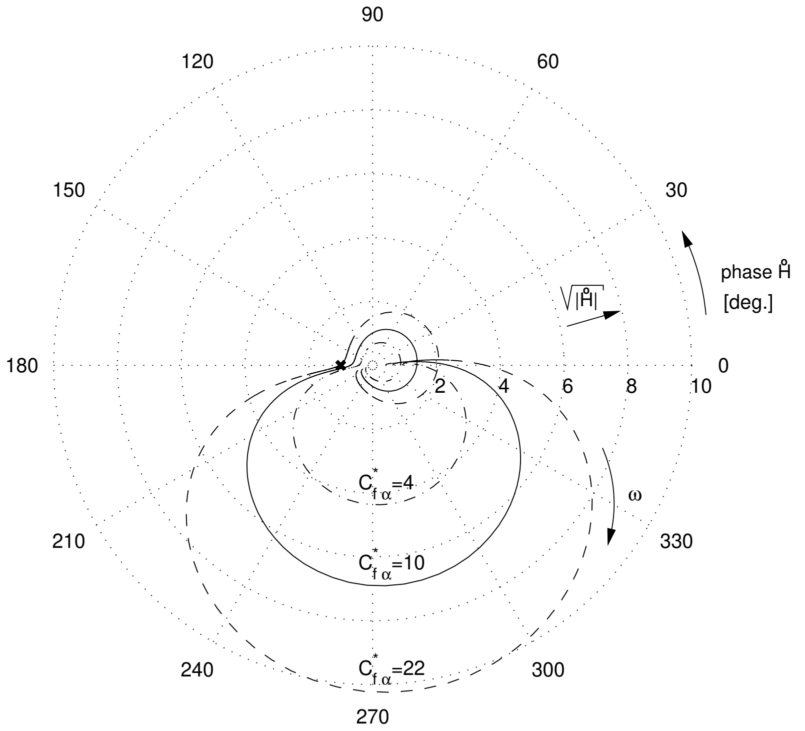

Fig. 2.29: Nyquist plot: varying cornering stiffness (baseline parameters except for $C_{f\alpha}$).

When applying the Nyquist criterion to figure 2.28 or 2.29, it can be observed that the system is unstable for the the highest value of the cornering stiffness: the amplitude just exceeds the value one when the phase angle reaches -180 degrees. This is confirmed by the eigenvalues of the closed system in terms of natural frequency and damping ratio, see table 2.1. This example also illustrates that the actual shimmy frequency may be quite different from the natural frequencies of the gear structure (17.87 Hz versus 12.26 and 21.92 Hz).

condition	mode 1	mode 2
$C^*_{f\alpha}$=4	13.36 Hz (1.27 %)	21.89 Hz (0.99 %)
$C^*_{f\alpha}$=10	14.95 Hz (1.70 %)	21.83 Hz (1.95 %)
$C^*_{f\alpha}$=22	17.87 Hz (-0.58 %)	21.69 Hz (5.84 %)

Table 2.1: Frequency and damping for different values of the cornering stiffness.

Next the influence of the yaw stiffness c_ψ will be investigated; three values are considered: $c^*_\psi = 12$, 18 and 24. The open-loop transfer functions are presented in figure 2.30 and the Nyquist plot is given in figure 2.31. As can be seen from the Nyquist plot, the system is unstable for both the upper- and lower value of c^*_ψ, which is to be expected from figure 2.10 (mechanical trail $e^* = 0.4$). The eigenvalues are listed in table 2.2.

condition	mode 1	mode 2
c^*_ψ=12	14.79 Hz (-2.57 %)	20.26 Hz (4.60 %)
c^*_ψ=18	14.98 Hz (4.25 %)	23.39 Hz (0.66 %)
c^*_ψ=24	15.02 Hz (7.01 %)	26.32 Hz (-0.33 %)

Table 2.2: Frequency and damping for different values of the yaw stiffness.

For the yaw stiffness $c^*_\psi = 18$ it appears that the second resonance peak in the amplitude-ratio of the open-loop transfer function has disappeared. This can be explained by looking at the mode shapes of the gear structure, see figure 2.32. Since the damping in the structure is very low the undamped eigenfrequencies and mode shapes are shown. For the condition $c^*_\psi = 18$ the pole of the second mode shape nearly coincides with the location of the point of application of the lateral force F_y: the pneumatic trail t^*_p which is 0.20 behind the wheel centre in this example. This implies that it will be difficult to "drive" this mode shape with the lateral tyre force F_y. From a control engineers point of view one would state that this particular mode is not *controllable*: it cannot be excited from the input to the system.

The effect of varying the relaxation length is shown in figure 2.33 and 2.34. In addition to the previous nominal parameters the gyroscopic behaviour is included ($l^* = 3$). The main effect of introducing the gyroscopes is an increase of the amplitude of the second resonance peak of the open-loop transfer function and a small phase lead with respect to the system without gyroscopes. Increasing the relaxation length will result in an increased phase lag of the open-loop transfer function: as can be verified from the Nyquist plot the system will become unstable. For this particular system instability appears to occur also

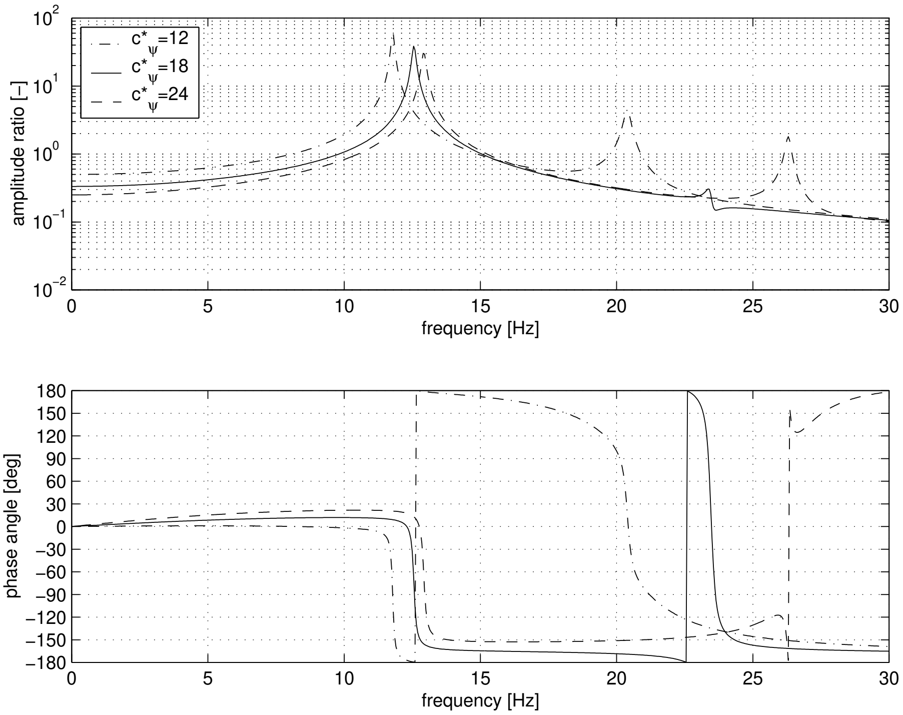

Fig. 2.30: Bode plot of the open loop transfer function; varying yaw stiffness (baseline parameters except for c_ψ).

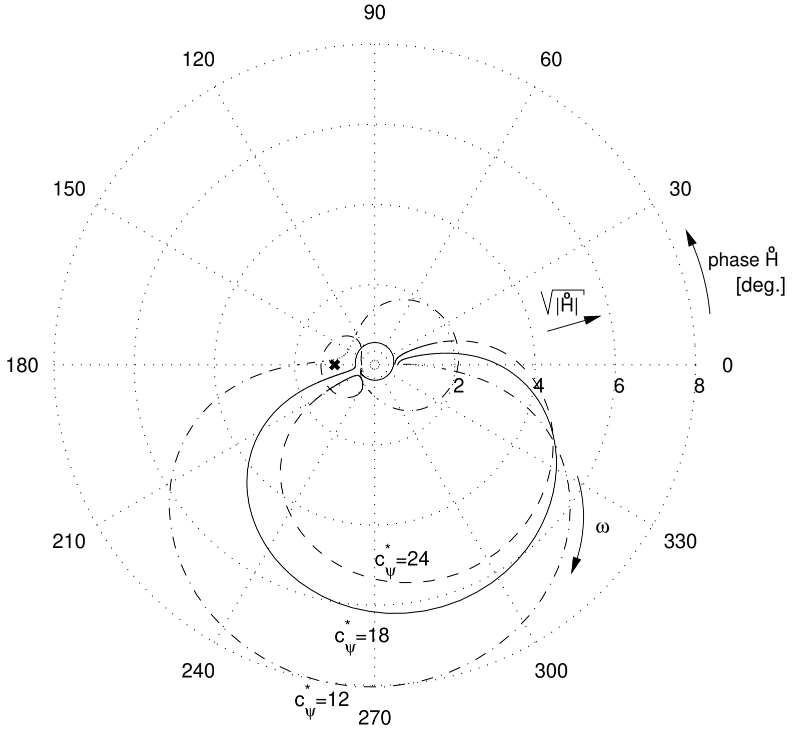

Fig. 2.31: Nyquist plot: varying yaw stiffness (baseline parameters except for c_ψ).

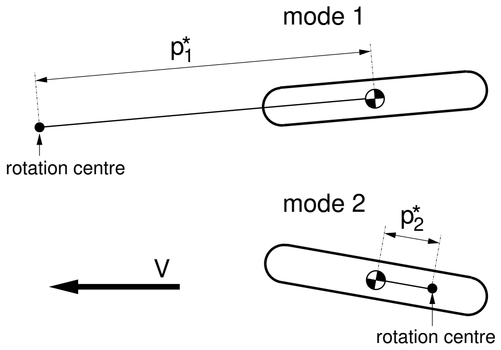

c_ψ^*	p_1^*	freq. [Hz]
12	1.49	11.78
18	2.36	12.56
24	3.30	12.92

c_ψ^*	p_2^*	freq. [Hz]
12	0.34	20.39
18	0.21	23.43
24	0.15	26.30

Fig. 2.32: Mode shapes and resonance frequencies of the gear structure.

at a sufficient decrease of the relaxation length ($\sigma^* = 0.6$), resulting in the other mode (”mode 2”) becoming unstable. This is substantiated by the eigenvalues, see table 2.3.

condition	mode 1	mode 2
σ^*=0.6	15.52 Hz (12.95 %)	21.21 Hz (-0.94 %)
σ^*=1.2	15.44 Hz (4.26 %)	21.40 Hz (1.24 %)
σ^*=2.0	14.71 Hz (-0.80 %)	21.71 Hz (1.59 %)

Table 2.3: Frequency and damping for different values of the relaxation length.

The Nyquist criterion may be quite useful in designing a stable and robust landing gear; with robustness is meant that the system stability is not very sensitive to parameter changes. Figure 2.35 shows the Nyquist diagram of a configuration which was optimised by maximising the *phase margin* and *amplitude margin*.

Starting from the baseline parameters and including gyroscopic behaviour ($l^* = 3$), the modifications consist of selecting a negative trail ($e^* = -0.2$), moving the centre of gravity rearward ($q^* = 0.1$), reducing the yaw stiffness ($c_\psi^* = 6$) and increasing the yaw moment of inertia ($I_z^* = 1$). The eigenvalues are shown in figure 2.36. The damping of both modes is positive for the velocity range under investigation.

Individual parameters have been varied to check the robustness. It was found that for this configuration stability is maintained for any value of the cornering stiffness; the stability actually improves for moderate increases of the cornering stiffness with respect to the nominal value. Stability is also maintained for up to three times the nominal value of the relaxation length. Also the yaw stiffness c_ψ^* may have any value below 10; the shimmy stability increases with the lower values of the yaw stiffness. On the other hand there exists a lower boundary for the lateral stiffness c_y^*: stability is only maintained for values above 11. This requirement can be relaxed if the contribution of the gyroscopes is reduced, e.g. by increasing l^*.

This example illustrates that it is possible to design a landing gear where the tyres may be employed to increase system damping, instead of causing a (shimmy) instability of the gear-tyre combination. A more detailed study will be given in the next chapter.

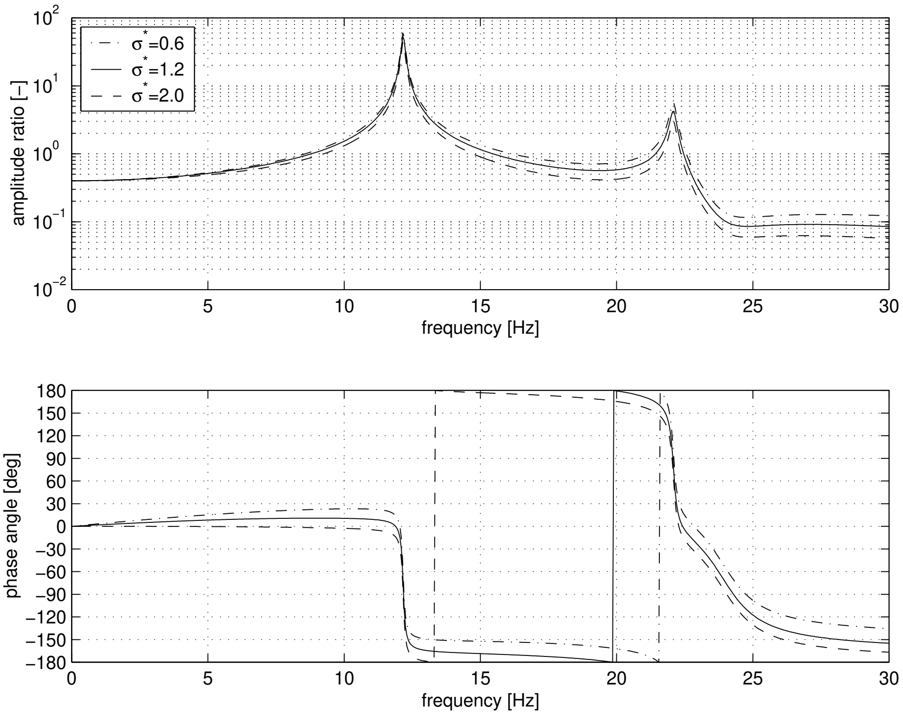

Fig. 2.33: Bode plot of the open loop transfer function; varying relaxation length (baseline parameters except for σ and l=3).*

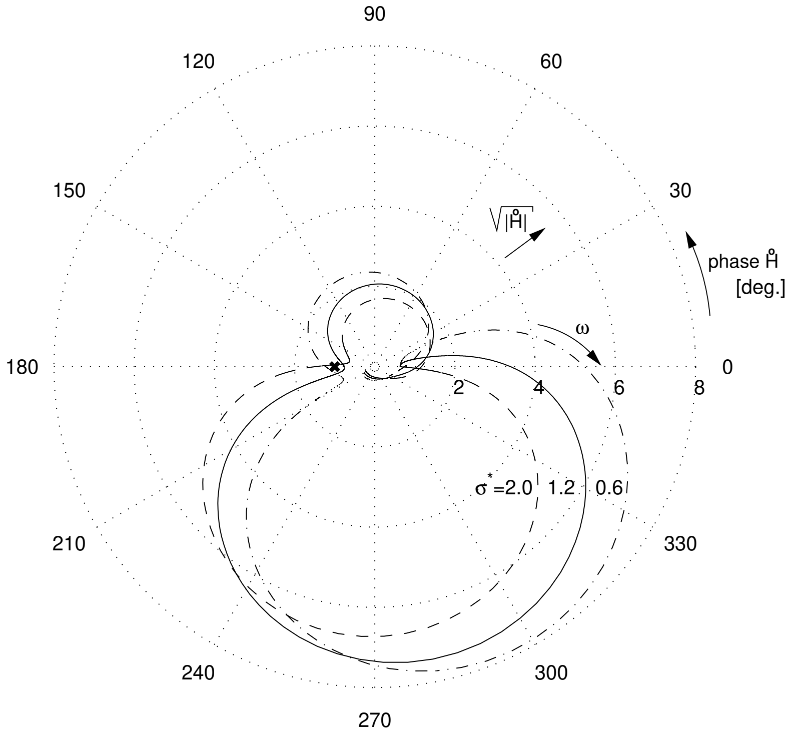

Fig. 2.34: Nyquist plot: varying relaxation length (baseline parameters except for σ and l=3).*

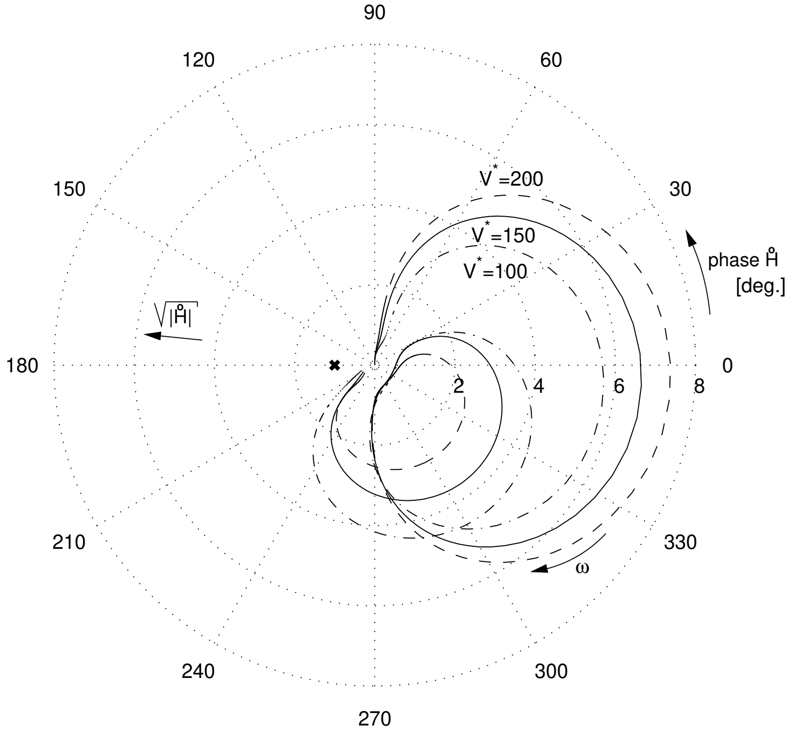

Fig. 2.35: Nyquist plot of the improved gear design.

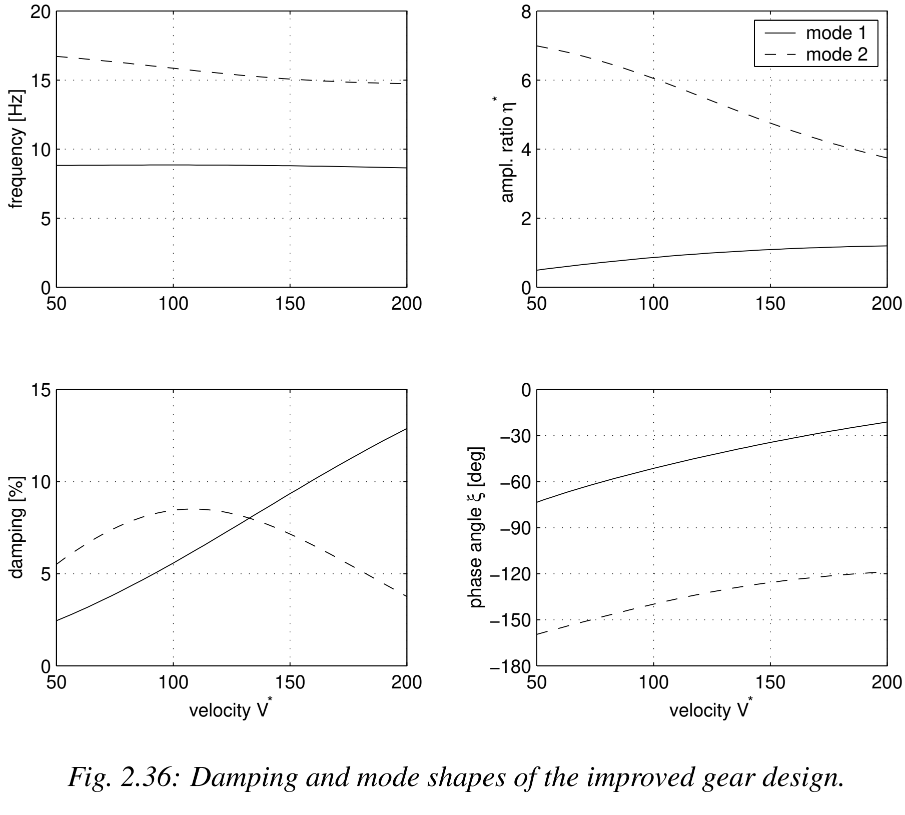

Fig. 2.36: Damping and mode shapes of the improved gear design.

Chapter 3

Landing gear application

The (extended) trailing wheel model, as introduced in the previous chapter, illustrates the basic principles of shimmy stability. In this chapter an enhanced model will be developed to describe the behaviour of a twin-wheeled cantilevered landing gear in more detail. In the available literature a number of suggestions are given to suppress the shimmy instability, but generally numerical results are hardly presented. The aim of this chapter is to systematically explore various methods to eliminate the shimmy instability.

The model employed in this chapter is kept as simple as possible, with a minimal number of degrees of freedom and a small set of parameters. This simplicity will also imply that the model is quite useful for studying general trends in shimmy stability, but may not be suited for a detailed analysis of the shimmy stability of a specific landing gear. The requirements on a more elaborate (multi-body/finite element) model of a landing gear will be discussed in chapter 5.

3.1 Equations of motion

The equations of motion presented here follow the work of Kluiters [23], though some extensions have been made: e.g. an additional roll degree of freedom for wheel axle has been included. The lay-out of the model is illustrated by figure 3.1. The model consists of five bodies (strut, trail, wheel axle and two wheels) which are all connected by hinge joints. Longitudinal, vertical and pitch dynamics are not considered; the forward velocity V is constant. The cant angle θ is taken into account to study different orientations of the landing gear, but it is not a dynamic degree of freedom. The rotational degrees of freedom of both wheels are eliminated by the introduction of a kinematic constraint: the assumption is made that the tyres have zero longitudinal slip. To separate the amount of roll of the strut from the lateral stiffness, the lateral displacement y at wheel axle level is taken as a coordinate rather than the roll angle of the strut. This finally results in a gear representation with three mechanical degrees of freedom represented by the following coordinates: lateral deflection y_a at wheel axle level, yaw angle ψ_a and the absolute roll angle of the wheel axle ϕ_a, as shown in figure 3.1.

Similar to the models presented in the previous chapter, the straight tangent tyre model is used to include the tyre lateral behaviour. Two separate tyres on a rigid axle are taken into account; the track width equals $2w$ and the tyres have a vertical stiffness c_z. The rigid wheel axle has a roll stiffness c_ϕ with respect to the trail body.

Four mass items are considered: the point mass m_s is located at the bottom end of

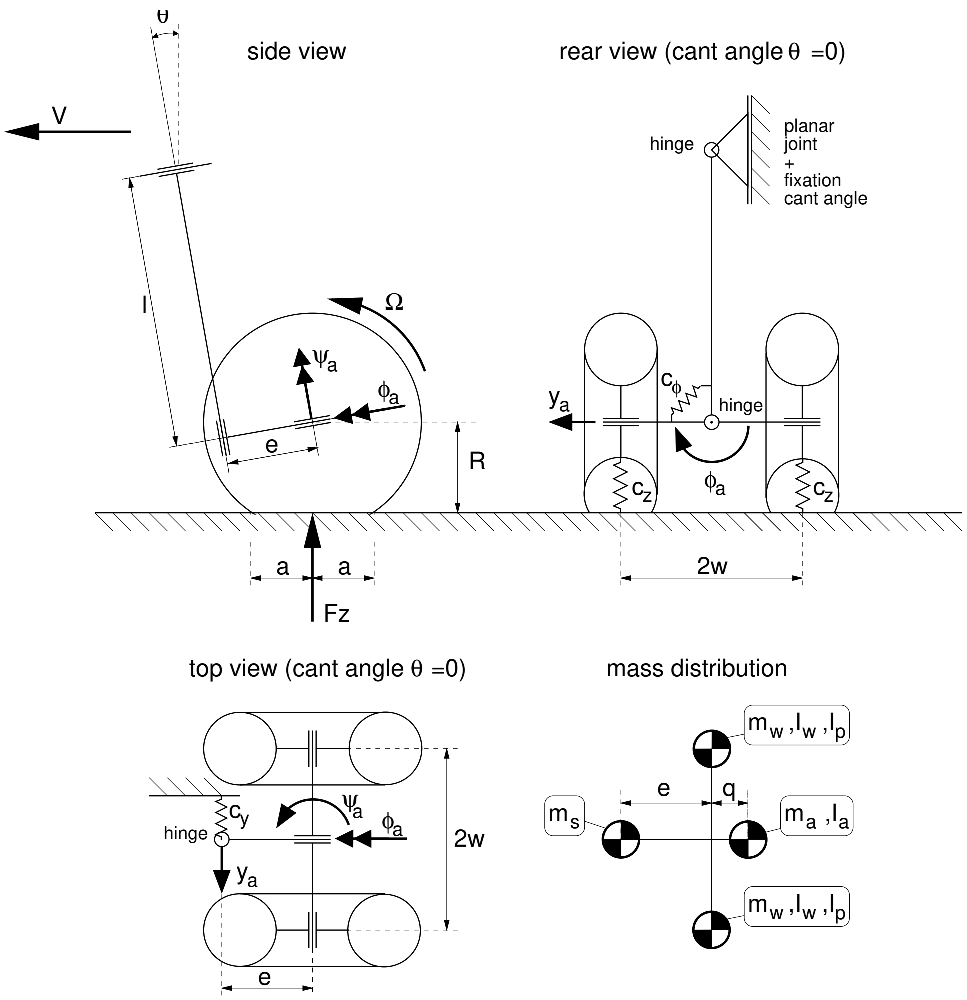
θ
side view
rear view (cant angle θ =0)
V
hinge
planar
joint
+
fixation
cant angle
l
Ω
ψa
φa
e
R
ya
cφ
hinge
cz
φa
cz
a
a
2w
Fz
top view (cant angle θ =0)
mass distribution
mw ,Iw ,Ip
e
q
ms
ma ,Ia
mw ,Iw ,Ip
cy
hinge
ψa
φa
ya
2w
e

Fig. 3.1: Schematic overview of the landing gear model.

the strut, representing the mass of the strut; the wheel mass m_w is located at the wheel centre of each wheel and m_a represents the mass of the wheel axle and brake assembly. The centre of gravity of these point masses is located at wheel axle level. In addition, the moments of inertia of the wheels I_w and axle/brake assembly I_a about the axes parallel to the yaw (ψ_a) and roll (ϕ_a) axes have been taken into account. The polar moment of inertia of the wheels I_p will contribute to the yaw moment of inertia of the rigid axle due to the kinematic constraint on longitudinal slip.

The equations of motion read in state-space form ($\dot{\mathbf{x}} = \mathbf{A}\mathbf{x}$, the dimension of $\mathbf{A}$ equals 7x7):

$$\begin{pmatrix} \ddot{\mathbf{u}} \\ \dot{\mathbf{u}} \\ \dot{\alpha}' \end{pmatrix} = \begin{pmatrix} -\mathbf{M}^{-1}\mathbf{K} & -\mathbf{M}^{-1}\mathbf{C} & \mathbf{M}^{-1}\mathbf{F} \\ \mathbf{I} & \mathbf{0} & \mathbf{0} \\ \mathbf{W_v} & \mathbf{W_p} & -\frac{V}{\sigma} \end{pmatrix} \cdot \begin{pmatrix} \dot{\mathbf{u}} \\ \mathbf{u} \\ \alpha' \end{pmatrix} \tag{3.1}$$

where $\mathbf{u} = \begin{pmatrix} y_a & \phi_a & \psi_a \end{pmatrix}^T$. The matrices contributing to the system matrix $\mathbf{A}$ will be defined, matrix elements not explicitly defined are equal to zero. The matrix $\mathbf{I}$ is a 3x3 unity matrix. The 3x3 mass matrix **M** reads:

$$\left.\begin{aligned}
\mathbf{M}(1,1) &= m_a + m_s + 2m_w \\
\mathbf{M}(1,3) &= -m_a(e+q) - 2m_w e \\
\mathbf{M}(2,2) &= 2m_w w^2 + 2I_w + I_a + 2I_p \tfrac{w^2}{R_e^2}\sin^2\theta \\
\mathbf{M}(2,3) &= -2I_p \tfrac{w^2}{R_e^2}\sin\theta\cos\theta \\
\mathbf{M}(3,1) &= \mathbf{M}(1,3) \\
\mathbf{M}(3,2) &= \mathbf{M}(2,3) \\
\mathbf{M}(3,3) &= m_a(e+q)^2 + I_a + 2m_w(w^2+e^2) + 2I_w + 2I_p \tfrac{w^2}{R_e^2}\cos^2\theta
\end{aligned}\right\} \tag{3.2}$$

The 3x3 damping matrix **K** consists of two parts: $\mathbf{K} = \mathbf{K_g} + \mathbf{K_m}$. The modal damping matrix $\mathbf{K_m}$ will be assessed later (equation 3.9). The gyroscopic matrix $\mathbf{K_g}$ reads:

$$\left.\begin{aligned}
\mathbf{K_g}(2,2) &= 2I_p\Omega \tfrac{w^2}{R_e^2}\tfrac{dR_e}{d\delta}\sin\theta\cos\theta \\
\mathbf{K_g}(2,3) &= -2I_p\Omega + 2I_p\Omega \tfrac{w^2}{R_e^2}\tfrac{dR_e}{d\delta}\sin^2\theta \\
\mathbf{K_g}(3,2) &= 2I_p\Omega + 2I_p\Omega \tfrac{w^2}{R_e^2}\tfrac{dR_e}{d\delta}\cos^2\theta \\
\mathbf{K_g}(3,3) &= -2I_p\Omega \tfrac{w^2}{R_e^2}\tfrac{dR_e}{d\delta}\sin\theta\cos\theta
\end{aligned}\right\} \tag{3.3}$$

The 3x3 stiffness matrix **C** reads:

$$\left.\begin{aligned}
\mathbf{C}(1,1) &= c_y + c_\phi \tfrac{1}{l^2} - 2F_z \tfrac{\cos\theta}{l} \\
\mathbf{C}(1,2) &= -c_\phi \tfrac{1}{l} \\
\mathbf{C}(1,3) &= 2F_z(e - R\sin\theta)\tfrac{\cos\theta}{l} \\
\mathbf{C}(2,1) &= \mathbf{C}(1,2) \\
\mathbf{C}(2,2) &= c_\phi + 2c_z w^2\cos^2\theta - 2F_z R\cos^2\theta \\
\mathbf{C}(2,3) &= 2c_z w^2\sin\theta\cos\theta \\
\mathbf{C}(3,1) &= \mathbf{C}(1,3) \\
\mathbf{C}(3,2) &= \mathbf{C}(2,3) \\
\mathbf{C}(3,3) &= c_\psi + 2c_z w^2 sin^2\theta + 2F_z(e - R\sin\theta)\sin\theta
\end{aligned}\right\} \tag{3.4}$$

The 3x1 matrix **F** reads (related to forces generated by the tyre):

$$\left.\begin{aligned}
\mathbf{F}(1,1) &= 2C_{f\alpha} \\
\mathbf{F}(2,1) &= 2C_{f\alpha}(R\cos\theta + t_p\sin\theta) \\
\mathbf{F}(3,1) &= -2C_{f\alpha}(e - R\sin\theta + t_p\cos\theta)
\end{aligned}\right\} \tag{3.5}$$

The 1x3 matrices $\mathbf{W_v}$ and $\mathbf{W_p}$ read (related to the tyre deformation angle):

$$\left.\begin{aligned}
\mathbf{W_v}(1,1) &= -\tfrac{1}{\sigma} \\
\mathbf{W_v}(1,2) &= -\tfrac{1}{\sigma}(R\cos\theta - a\sin\theta) \\
\mathbf{W_v}(1,3) &= \tfrac{1}{\sigma}(e - R\sin\theta - a\cos\theta) \\
\mathbf{W_p}(1,2) &= -\tfrac{V}{\sigma}\sin\theta \\
\mathbf{W_p}(1,3) &= \tfrac{V}{\sigma}\cos\theta
\end{aligned}\right\} \tag{3.6}$$

Structural damping is introduced in the model by assuming a damping ratio κ_m which is the same for all modes; a value of 0.02 will be used. Let $\mathbf{T}$ be the matrix containing the eigenvectors (columnwise) when determining the eigenvalues of the matrix $\mathbf{M}^{-1}\mathbf{C}$. Then both the mass and stiffness matrix can be diagonalised:

$$\left.\begin{aligned} \mathrm{diag}(m_1,m_2,m_3) &= \mathbf{T}^T\mathbf{M}\mathbf{T} \\ \mathrm{diag}(c_1,c_2,c_3) &= \mathbf{T}^T\mathbf{C}\mathbf{T} \end{aligned}\right\} \tag{3.7}$$

A diagonal damping matrix $\mathrm{diag}(k_1,k_2,k_3)$ can be determined:

$$k_i = 2\kappa_m\sqrt{m_i c_i} \quad i = 1\ldots 3 \tag{3.8}$$

Finally the 3x3 modal damping matrix $\mathbf{K_m}$ is calculated:

$$\mathbf{K_m} = \left(\mathbf{T}^T\right)^{-1}\mathrm{diag}(\mathrm{k}_1,\mathrm{k}_2,\mathrm{k}_3)\,\mathbf{T}^{-1} \tag{3.9}$$

Using this approach each mode of the system consisting of $\mathbf{M}$, $\mathbf{K_m}$ and $\mathbf{C}$ will have a damping ratio of κ_m.

The loaded tyre radius R gives the vertical distance between wheel centre and road; by definition:

$$R = R_0 - \delta. \tag{3.10}$$

where δ is the tyre deflection and R_0 is the unloaded tyre radius. With the assumedly constant vertical stiffness of the tyre the static deflection can be calculated:

$$\delta = \frac{F_z}{c_z} \tag{3.11}$$

The forward velocity V and angular velocity of the wheels Ω are related by the effective rolling radius R_e:

$$\Omega = \frac{V}{R_e} \tag{3.12}$$

The effective rolling radius is again a function of the tyre deflection δ and unloaded tyre radius R_0. According to reference [47] the following empirical equation is applicable:

$$R_e = R_0 - \frac{1}{3}\delta \tag{3.13}$$

The polar moment of inertia of the wheels contributes to the yaw moment of inertia of the wheel axle, due to the zero longitudinal slip constraint for both tyres. In addition the forces generated by changes in effective rolling radius have to be considered. This can be illustrated as follows: when assuming a roll velocity of the wheel axle, the effective rolling radius of the tyre on either side of the wheel axle will change continuously. Since the assumption is made that no longitudinal slip occurs, the wheel angular velocity has to increase or decrease as well. In order to accelerate or decelerate the wheel a longitudinal force is required; the longitudinal forces acting on the tyre at either side of the landing gear have opposite signs and consequently produce a moment about the vertical axis. This gives rise to additional coefficients in the matrix $\mathbf{K_g}$, equation 3.3. The longitudinal forces generated by the tyre are applied at the effective rolling radius; this assumption is supported by the work of Zegelaar [53].

Another factor, which complicates the equations of motion, is the cant angle θ which results in many coefficients depending on $\cos\theta$, $\sin\theta$ or both. Furthermore the static load on the landing gear is the source of geometrical stiffness effects and gives rise to additional terms depending on F_z in the stiffness matrix. This may be of importance for zero or very low values of the yaw stiffness c_ψ and roll stiffness c_ϕ or small values of the effective gear length l.

3.2 Baseline characteristics

In this chapter the behaviour of a realistic landing gear configuration will be investigated and possible counter measures to suppress the shimmy instability will be studied. A baseline configuration will be defined in this section and its stability will be evaluated. The baseline parameter values are listed in table 3.1. With this data the frequency and damping of the mode shapes have been calculated as a function of forward velocity, see figure 3.2. It can be seen that this configuration is only marginally stable at the lower forward velocities: the damping is already lower than the structural damping of 2%. For $V^* \geq 150$ the damping in mode 1 becomes negative, so the system will be unstable; the shimmy frequency is approximately 17.5 Hz.

The mode shapes at the tyre-ground contact point can be plotted in a polar diagram as introduced in section 2.3; the mode shapes are presented in figure 3.3. The wavelength of each mode shape will also increase as the forward velocity increases, since the frequency of the mode shapes remains fairly constant. For the velocity range under investigation, $V^* = 50\ldots200$, the wavelength of mode 1 becomes $\lambda = 7.5a\ldots28a$, mode 2: $\lambda = 5.8a\ldots29a$ and mode 3: $\lambda = 3.5a\ldots13a$. In section 2.3 it was shown that for the straight tangent tyre model a polar plot can be constructed, where at a given wavelength a circle marks the stability boundary. At high forward velocity, mode 1 is clearly within the accompanying circle ($\lambda \approx 30a$) and thus this mode is unstable. Based on figure 3.3 one might expect mode 1 to be already unstable at the lowest forward velocity considered, but the stability criterion as derived in section 2.3 is based on a conservative gear structure (so without energy dissipation). In the current example 2% structural damping is taken into account; it has been verified that mode 1 is unstable over the velocity range under investigation if the structural damping κ_m is set to zero.

Alternatively the Nyquist criterion can be applied to determine system stability, as was shown in section 2.5. The open-loop transfer function for the baseline configuration is presented in figure 3.4. The frequency range has now been extended to 40 Hz to include the third mode of the model, which could be described as the ”roll” mode of the wheel axle. At zero forward velocity and excluding lateral tyre forces (open-loop), the system has three eigenfrequencies: 12.08 Hz, 22.22 Hz and 34.62 Hz. In the graph these three eigenfrequencies of the gear can be recognised. Under the influence of the gyroscopes the frequency of the second mode decreases and the frequency of the third mode increases. It can also be observed that for increasing forward velocity the second peak in the open-loop transfer function increases in magnitude and the amplitude ratio is raised above the value one for frequencies in the neighbourhood of 180 degrees phase lag. This implies that the system may become unstable at high forward velocities as is also illustrated by the Nyquist plot, see figure 3.5.

parameter	description	value
m_s^*	strut mass	0.15
m_a^*	mass axle/brake assembly	0.25
m_w^*	mass wheel/tyre	0.30
I_a^*	moment of inertia axle/brakes	0.05
I_w^*	diametral moment of inertia wheel/tyre	0.07
I_p^*	polar moment of inertia wheel/tyre	0.10
κ_m	modal damping of gear structure	0.02
l^*	effective gear length	2
e^*	mechanical trail	0.4
w^*	half of wheel track	0.6
q^*	offset c.g. axle mass	0
θ	strut cant angle	0
c_y^*	lateral stiffness	15
c_ψ^*	yaw stiffness	15
c_ϕ^*	roll stiffness	30
a^*	half of contact length	0.4
t^*	pneumatic trail	0.2
σ^*	relaxation length	1.2
$C_{f\alpha}^*$	cornering stiffness	5
R_o^*	unloaded tyre radius	1
$dR_e/d\delta$	variation of effective rolling radius with tyre deflection	$-\frac{1}{3}$
c_z^*	tyre vertical stiffness	7
F_z^*	tyre vertical load	1

Table 3.1: Baseline parameters of the landing gear model

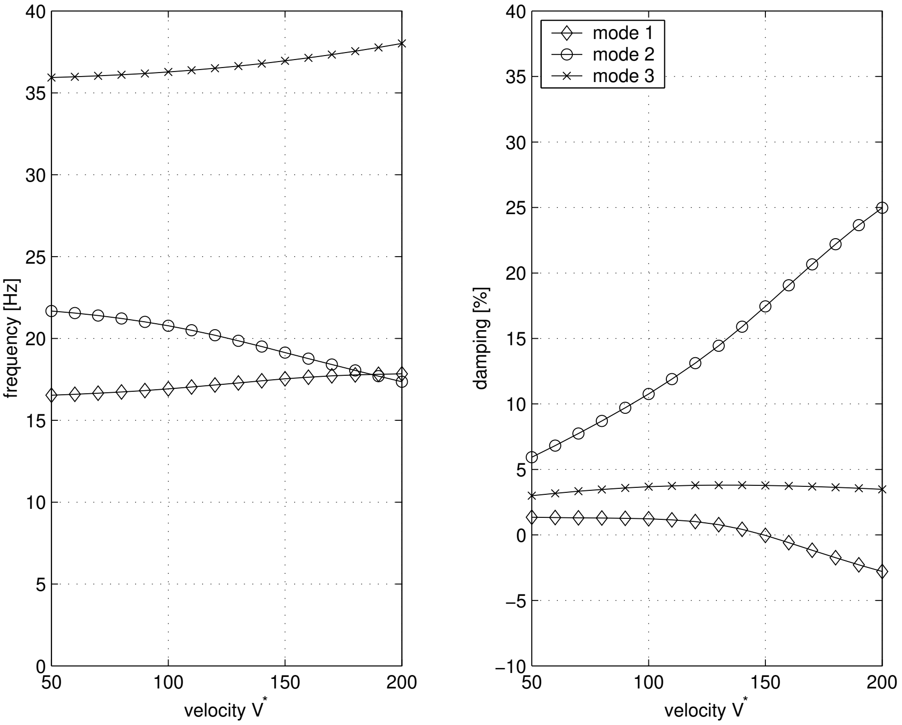

Fig. 3.2: Eigenfrequencies and damping as function of forward velocity (baseline configuration).

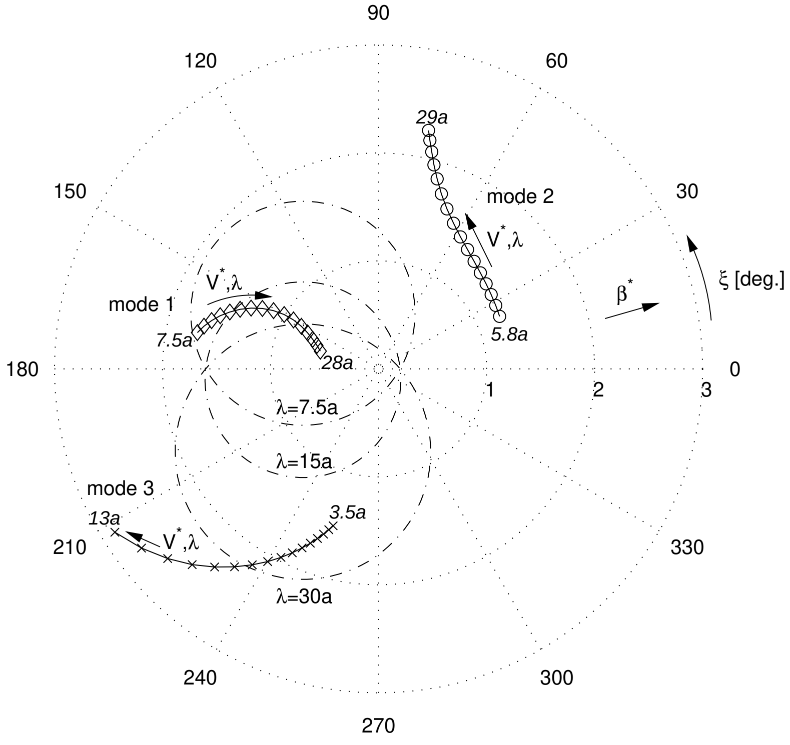

Fig. 3.3: Polar plot of the mode shapes (baseline configuration).

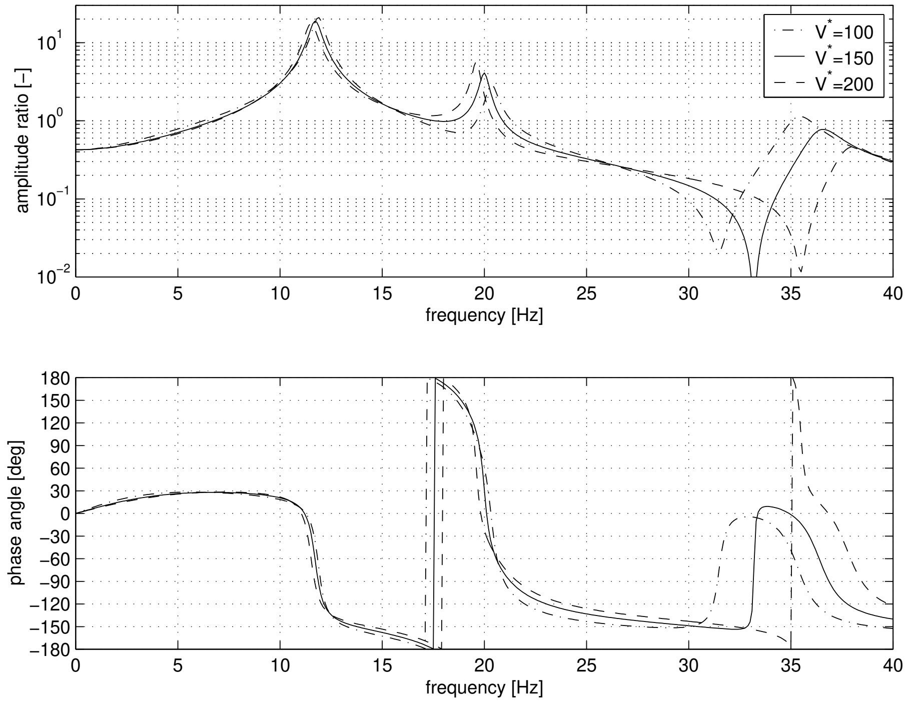

Fig. 3.4: Open-loop transfer function (baseline configuration).

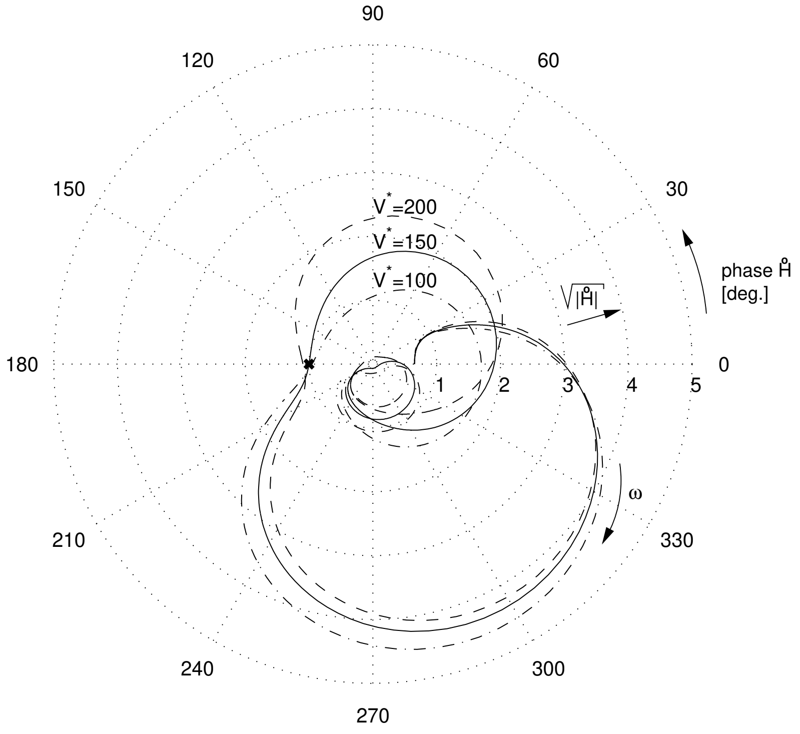

Fig. 3.5: Nyquist plot (baseline configuration).

3.3 Improving stability by design modifications

The configuration introduced in the previous section is unstable if $V^* > 150$. In this section a number of design changes will be investigated to suppress this shimmy instability. In this analysis the tyre parameters will remain constant, since they are outside the control of the designer of a landing gear. Furthermore the total mass is assumed to be constant because wheel, tyre and brake assembly determine to a large extent the landing gear mass.

A first important conclusion from the preceding analysis is that the gyroscopic effect caused by the rotating wheels is an important factor in making the system stability velocity dependent, possibly resulting in a shimmy instability at high forward velocities. This is illustrated by figure 3.6: the shape of the unstable area changes considerably as the velocity V^* is increased from 100 to 200 when gyroscopic effects are included. The baseline configuration is indicated with the symbol "**o**" and is unstable at $V^* = 200$ when gyroscopic effects are included. If the gyroscopic effects are excluded, the stability boundaries are hardly velocity dependent. Under these conditions the baseline system will be stable over the entire forward velocity range and the damping in the two lowest modes is about 4% at $V^* = 50$ and gradually increases to about 7.5% when $V^* = 200$. If gyroscopic effects are not present, the parameters of the system still will have to be selected with care; this was already illustrated for the trailing wheel system in figure 2.9.

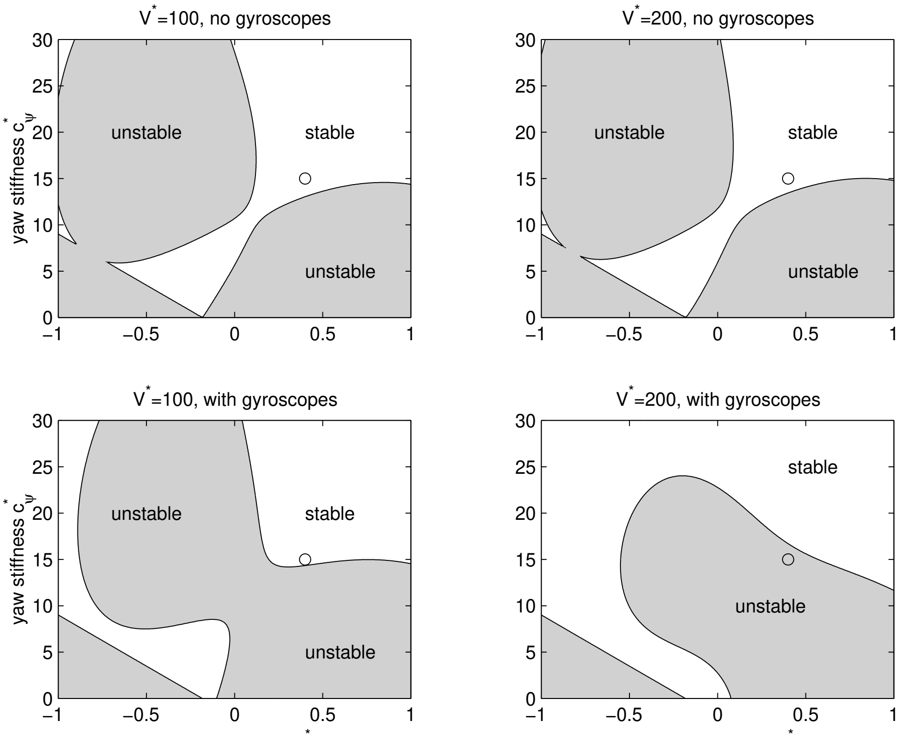

Fig. 3.6: Effect of gyroscopes on stability (o: baseline mechanical trail and yaw stiffness).

In practice it will prove to be difficult to sufficiently reduce the gyroscopic contribution of the rotating wheels. One option is to modify the effective gear length l of the landing gear; some results are shown in figure 3.7 and 3.8. These graphs illustrate that increasing the effective gear length l is beneficial for the stability in case of small positive trail values. It has been verified that the gear will be (marginally) stable for the velocity range $V^* = 50$ to 200 if the effective gear length l^* is increased from 2 to 3. Furthermore it can be noted that the gyroscopes stabilise the system at high forward velocities for the combination of a large effective gear length, high yaw stiffness and negative trail.

As shown in the previous chapter, the lateral and yaw stiffness need to have a certain relation in order to obtain a stable system. Combining figure 3.6 with figure 2.9 seems to suggest that reducing lateral stiffness may improve system stability. Again the results are calculated for two different forward velocities: figure 3.9 gives the results for $V^* = 100$ and figure 3.10 for $V^* = 200$. It can be observed that reducing the lateral stiffness (for the baseline configuration otherwise) gives some improvement of the shimmy stability, but it appears to be difficult to stabilise the baseline gear both at the low and high forward velocity. It is obvious from the graphs that the gear will be stable over the entire forward velocity range if the yaw stiffness and mechanical trail are increased with respect to the baseline configuration in combination with a reduction of the lateral stiffness.

Increasing the wheel track has a large impact on the yaw moment of inertia, since over 50% of the total landing gear mass is located at the wheel centres. Due to the constraint on longitudinal slip the polar moment of inertia also contributes to the yaw moment of inertia. Both contributions are quadratically dependent on half of the track width w. Figures 3.11 and 3.12 show the effects of modifying w on the shimmy stability. For positive values of the mechanical trail increasing the track width results in a less stable gear, but for a negative trail value the opposite is true. It seems to be feasible to design a landing gear with sufficient track width and a negative mechanical trail which is stable for low values of the yaw stiffness.

In the graphs is shown that the baseline system is stable for the lowest value of the track width ($w^* = 0.5$). In practice it may prove to be very difficult to reduce the track width to this value, because both the width of the tyres and the diameter of the main fitting have to be considered. Another interesting case is to reduce the track width of the system with baseline parameters to zero, which could represent the case where there is only one single tyre which has twice the cornering stiffness of the original tyres. Not surprisingly, considering the tendency observed in figures 3.11 and 3.12, it can be shown that this configuration is stable over the forward velocity range under consideration.

The influence of the roll stiffness of the wheel axle with respect to the strut is shown in figure 3.13 and 3.14. Though modifying the roll stiffness c_ϕ^* certainly has its impact on the shimmy stability, it appears to be impossible to select a value which would stabilise the baseline gear at $V^* = 200$. It is difficult to extract generally applicable trends from the graphs; but it is clear that optimising the roll stiffness may result in some gain in stability.

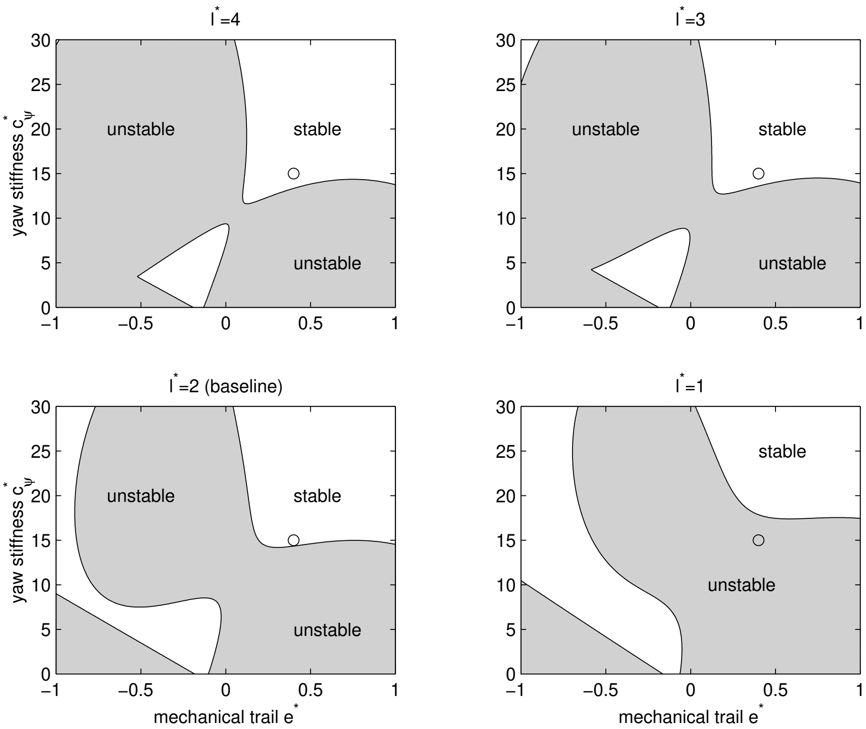

Fig. 3.7: Effect of effective gear length on stability (V^*=100, o: baseline mechanical trail and yaw stiffness).

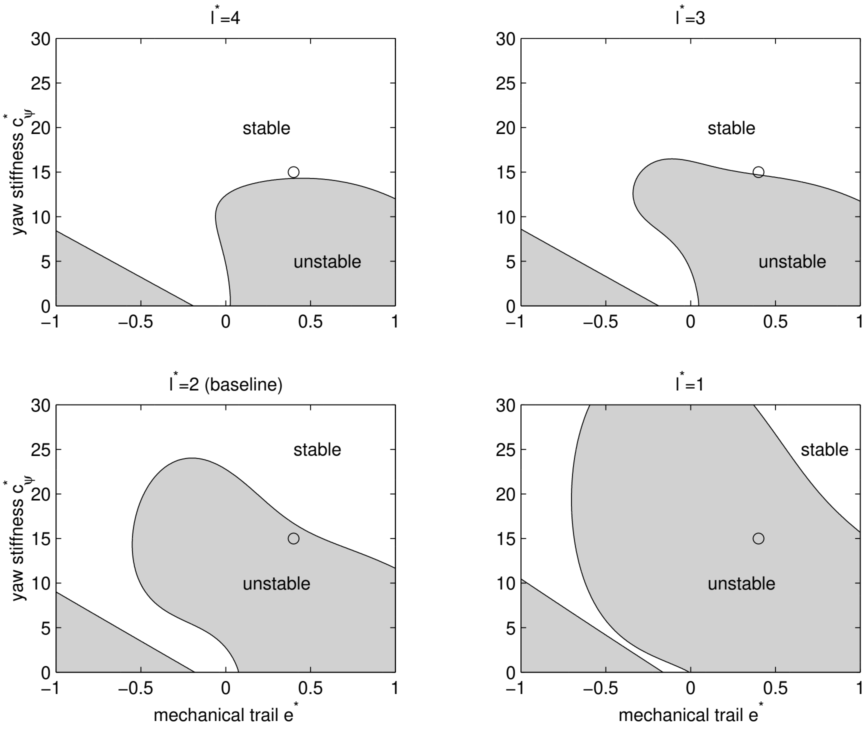

Fig. 3.8: Effect of effective gear length on stability (V^*=200, o: baseline mechanical trail and yaw stiffness).

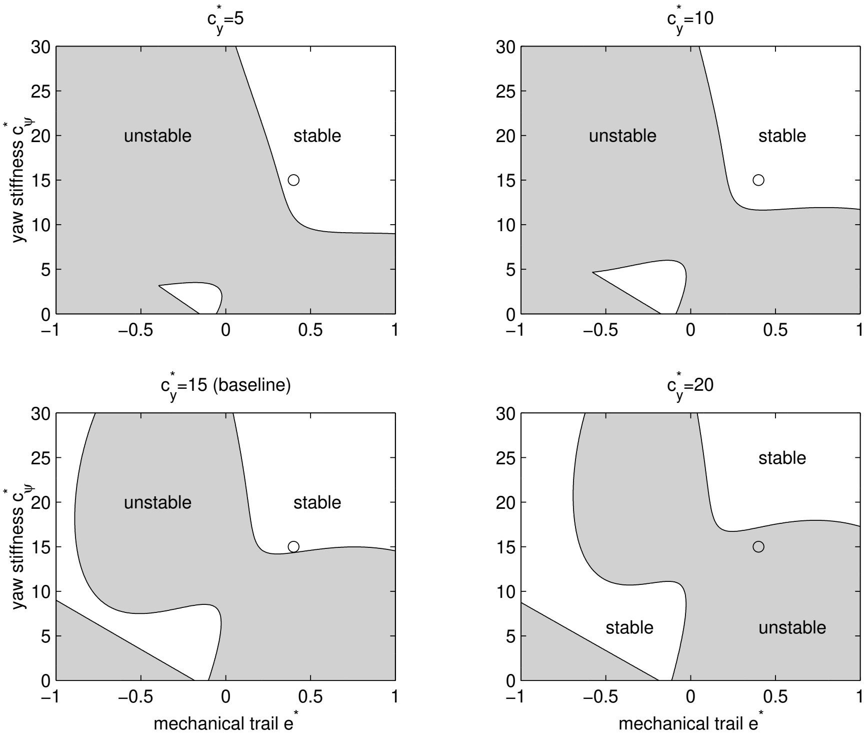

Fig. 3.9: Effect of lateral stiffness on stability (V^*=100, o: baseline mechanical trail and yaw stiffness).

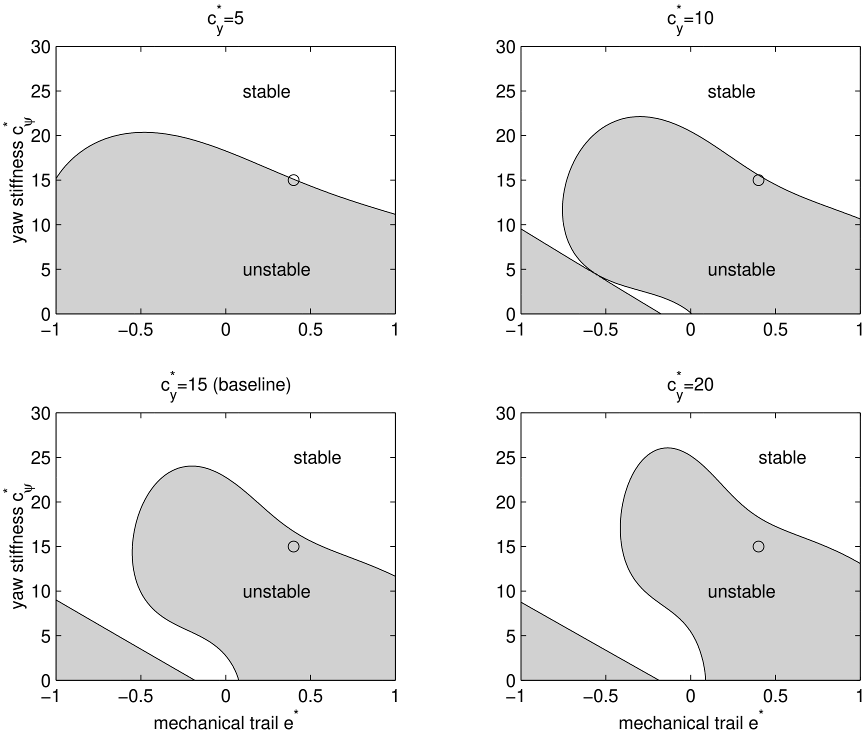

Fig. 3.10: Effect of lateral stiffness on stability (V^*=200, o: baseline mechanical trail and yaw stiffness).

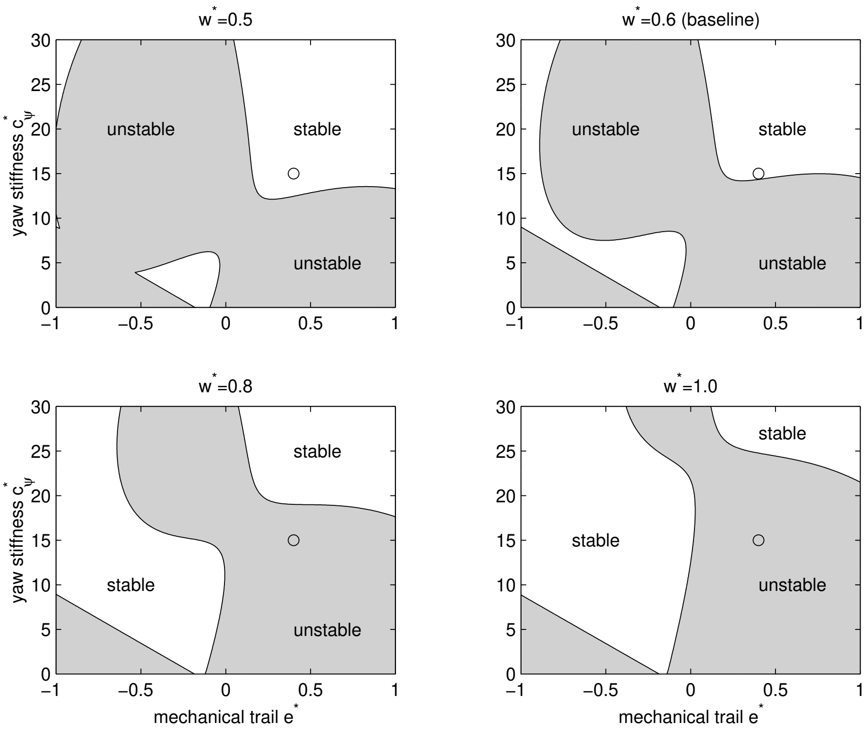

Fig. 3.11: Effect of track width on stability (V^*=100, o: baseline mechanical trail and yaw stiffness).

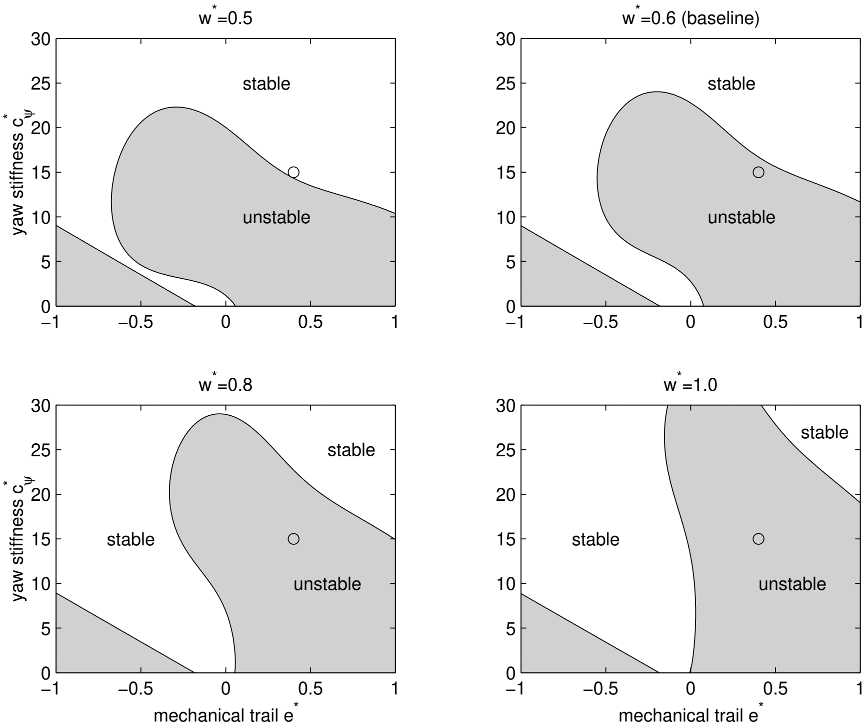

Fig. 3.12: Effect of track width on stability (V^*=200, o: baseline mechanical trail and yaw stiffness).

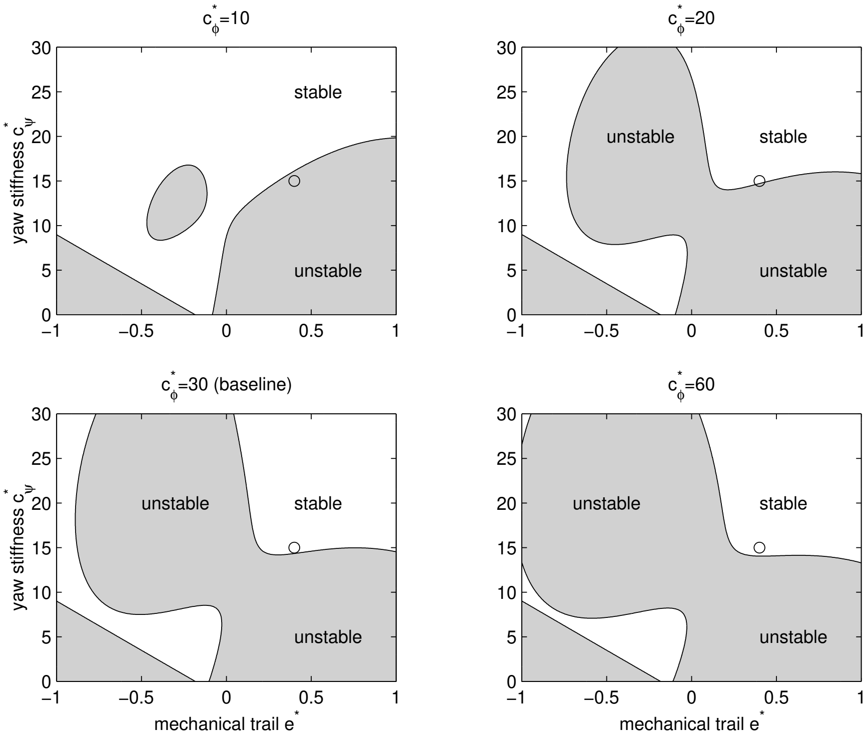

Fig. 3.13: Effect of roll stiffness on stability (V^*=100, o: baseline mechanical trail and yaw stiffness).

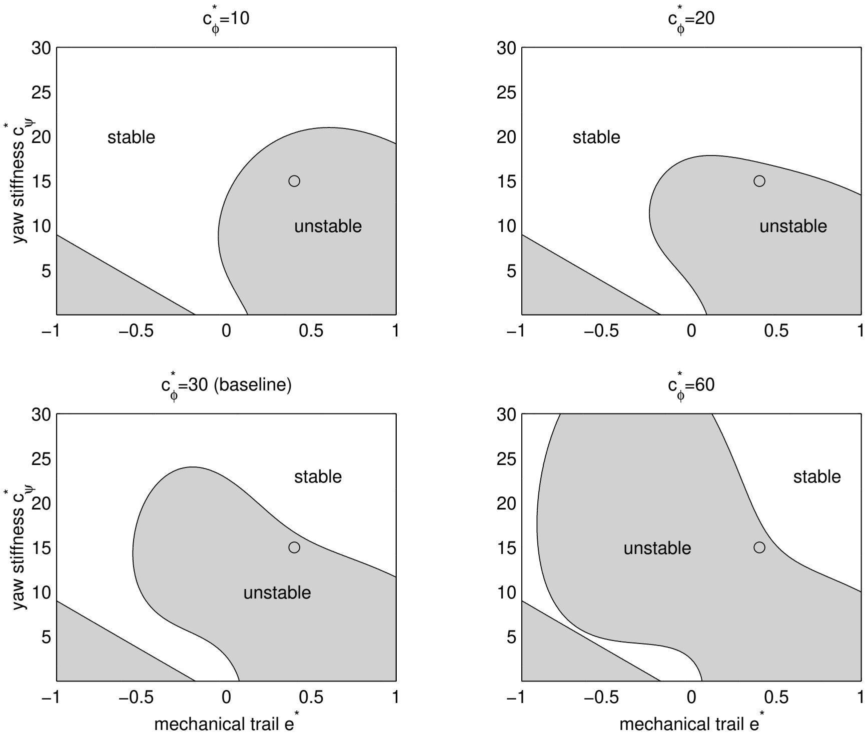

Fig. 3.14: Effect of roll stiffness on stability (V^*=200, o: baseline mechanical trail and yaw stiffness).

parameter	description	configuration 1	configuration 2
e^*	mechanical trail	0.6	-0.2
w^*	half of wheel track	0.6	0.8
c_y^*	lateral stiffness	10	20
c_ψ^*	yaw stiffness	20	10
c_ϕ^*	roll stiffness	20	30

Table 3.2: Parameters of the improved landing gear configurations

Based on this parameter study, two new configurations will be defined, which represent a clear improvement in shimmy stability over the baseline system. The modifications with respect to the baseline system are listed in table 3.2. Basically there are two options:

- *large positive trail* (configuration 1).
  An increase of the mechanical trail and a reduction of the lateral stiffness are required to improve stability at high forward velocity (see figure 3.10). Increasing the yaw stiffness will generally improve the shimmy stability of a gear with a positive mechanical trail provided that some structural damping is present. A limited reduction of the roll stiffness improves the stability at high forward velocities (see figure 3.14). The yaw moment of inertia should be kept as small as possible in case of a large positive mechanical trail (see figures 3.11 and 3.12): the track width remains unchanged with respect to the baseline configuration, which already represents the practical minimum. The frequency and damping of this configuration are shown in figure 3.15, a Nyquist plot of the open-loop transfer function is given in figure 3.16.

- *small negative trail* (configuration 2).
  For a landing gear with a negative trail an upper boundary exists for the yaw stiffness. The actual value of this stiffness may be quite low: for the baseline configuration the yaw stiffness would have to be reduced almost by a factor 3 to obtain a stable configuration with a negative trail. A relatively small increase in track width relaxes this requirement considerably (see figure 3.12). If the absolute value of the negative mechanical trail equals the pneumatic trail, there exists no lower limit for the yaw stiffness to maintain stability. The effect of increasing the lateral stiffness is quite similar to increasing the track width and improves the shimmy stability in case of negative trail. System damping is not very sensitive to the roll stiffness for values of c_ϕ^* in the range of $20 \ldots 60$, so the baseline value was selected. Figure 3.17 shows the frequency and damping of configuration 2, the Nyquist plot is given in figure 3.18.

In comparison to the baseline configuration, see figure 3.2, the proposed modifications result in a major gain in stability. This illustrates that it may be possible to design a stable conventional landing gear, provided that the combination of parameter values is selected correctly.

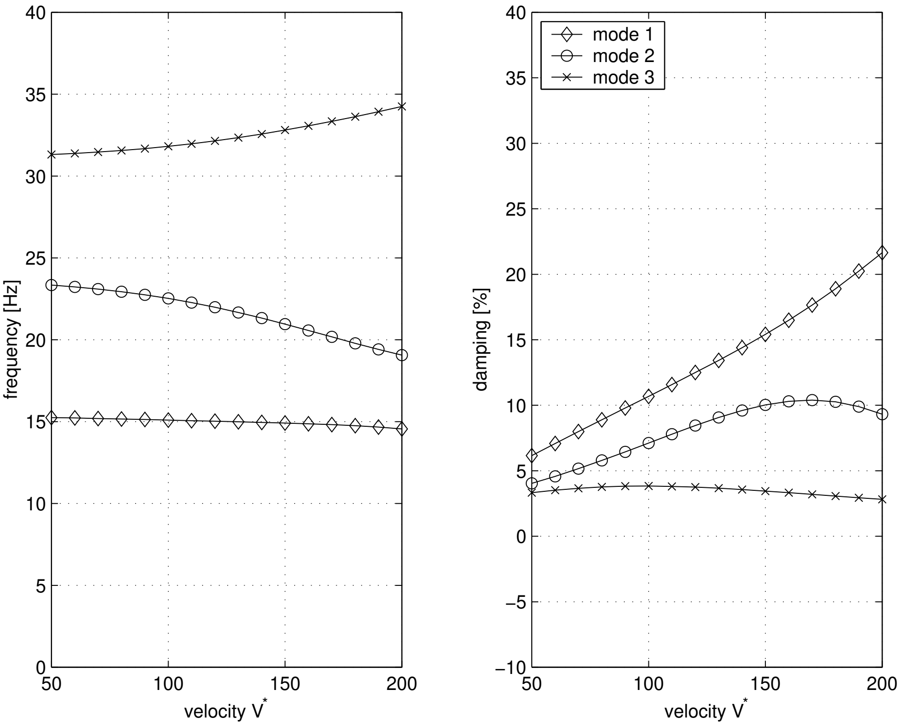

Fig. 3.15: Eigenfrequencies and damping as function of forward velocity (configuration 1: large positive trail).

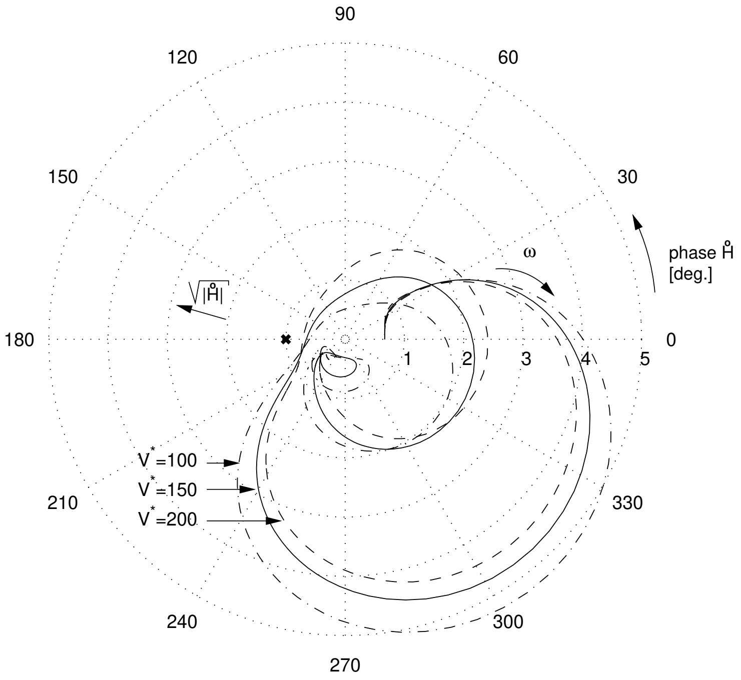

Fig. 3.16: Nyquist plot of the open-loop transfer function (configuration 1: large positive trail).

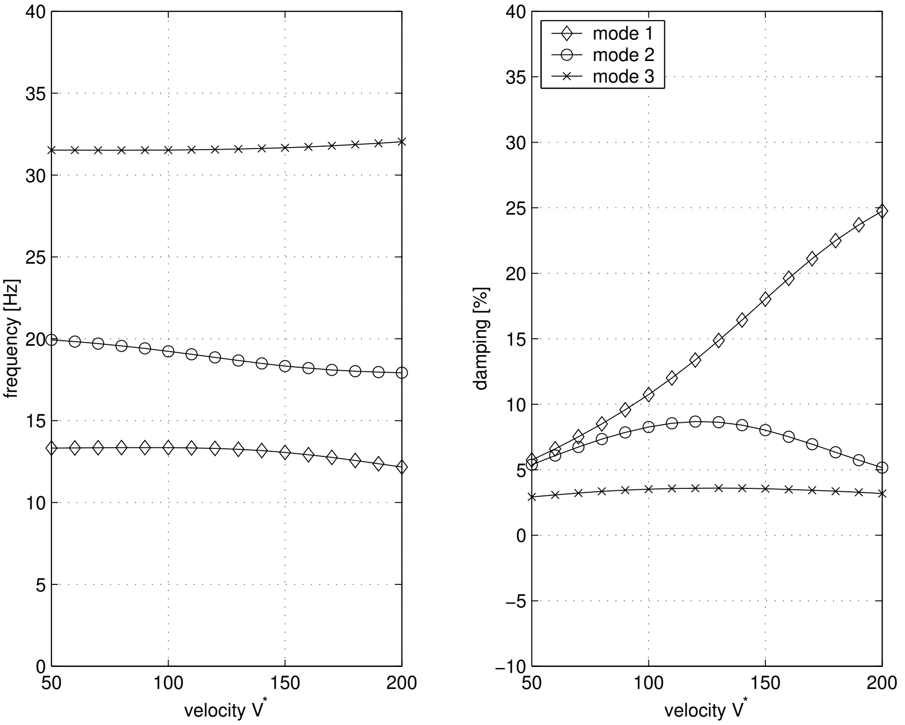

Fig. 3.17: Eigenfrequencies and damping as function of forward velocity (configuration 2: small negative trail).

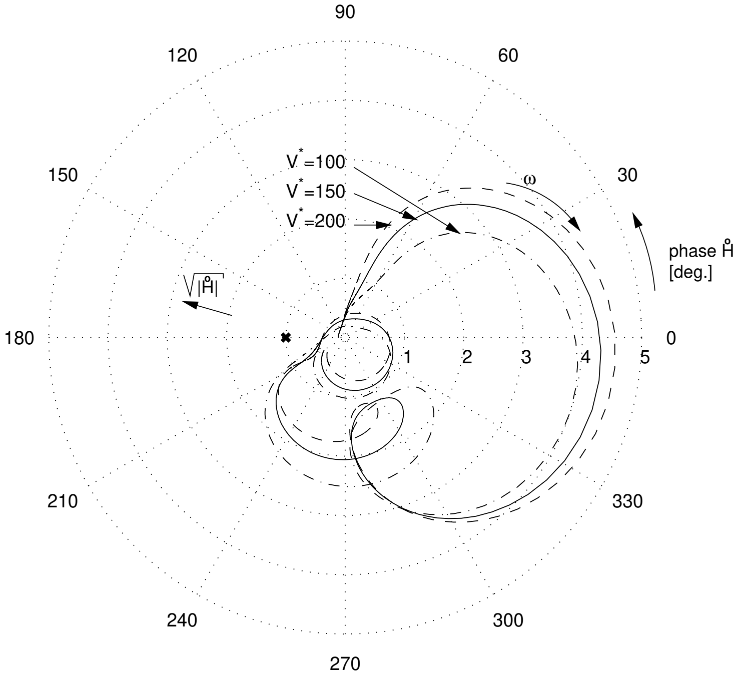

Fig. 3.18: Nyquist plot of the open-loop transfer function (configuration 2: small negative trail).

3.4 Strut cant angle

During take-off and landing the aircraft pitch angle may vary 10 to 20 degrees while the main landing gear tyres are in contact with the runway. This implies that the applicable orientations of the main landing gear have to be checked for stability. Furthermore it is suggested by a number of authors that canting the gear forward (θ negative, see figure 3.1) will improve shimmy stability [28], [29].

For the baseline system the influence of the cant angle is shown in figures 3.19 and 3.20. It can be observed that the stability boundary for monotonical instability changes with the cant angle. For the case of zero yaw stiffness, the minimum trail length to avoid the monotonous instability is determined by the distance of the point of intersection of the swivel axis and ground plane and the application point of the lateral tyre force. When canting the gear forward this distance is increased. For the baseline gear configuration the stability is not improved by either canting the gear forward or backwards as shown in the figures 3.19 and 3.20.

Based on figures 3.19 and 3.20 it appears that canting the gear may allow to design a stable landing gear with zero mechanical trail e, provided that the contribution of the gyroscopes remains limited. This is illustrated by the following numerical example. With respect to the baseline values of table 3.1 the length of the mechanical trail e^* is set to zero, track width w^* is increased to 0.8, the effective gear length l^* is increased to 4 and the yaw stiffness c^*_ψ is reduced to 10. If the cant angle θ is zero, stability of the gear is very marginal as is shown in figure 3.21. For the velocity range considered the damping in the least damped mode is always below the structural damping of 2% and the gear is unstable if $V^* > 170$. When introducing a forward cant angle of 20 degrees the stability can be improved considerably, as is shown in figure 3.22.

This numerical example confirms that it is possible to improve the shimmy stability of a landing gear by introducing a cant angle. On the other hand it has also been shown that introducing a cant angle does not improve the stability of the baseline gear configuration. So it has to be concluded that canting the gear may be beneficial for certain configurations, but this does not apply in general.

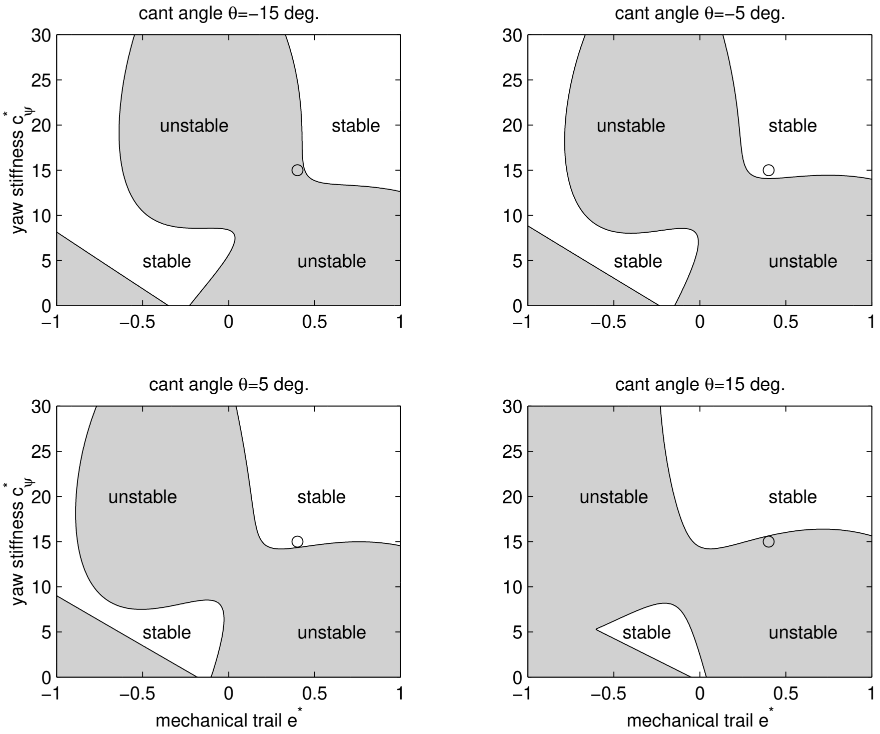

Fig. 3.19: Effect of cant angle on stability (V^*=100, o: baseline mechanical trail and yaw stiffness).

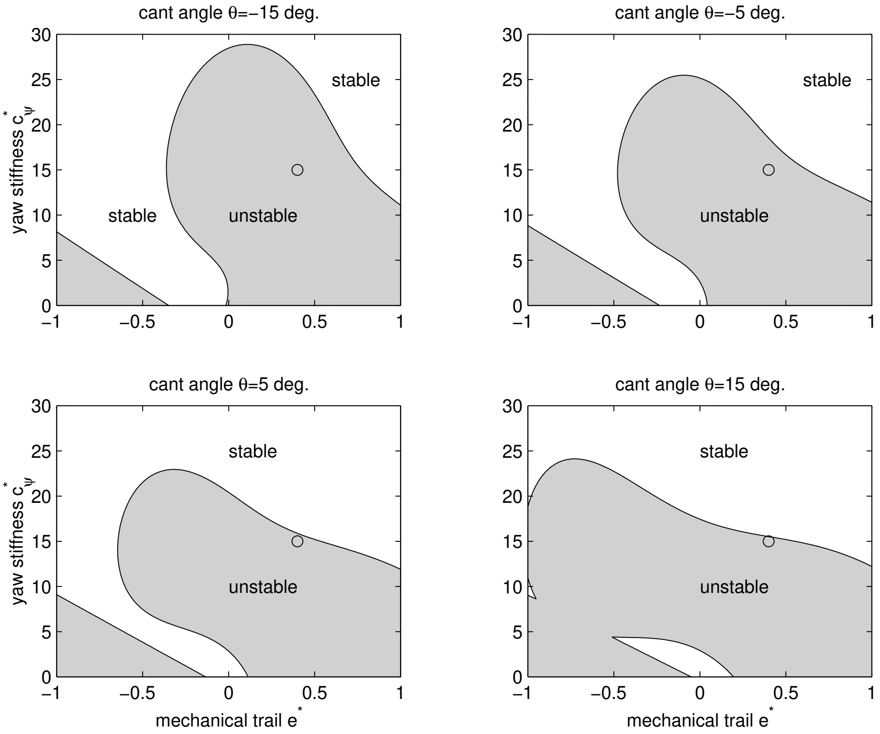

Fig. 3.20: Effect of cant angle on stability (V^*=200, o: baseline mechanical trail and yaw stiffness).

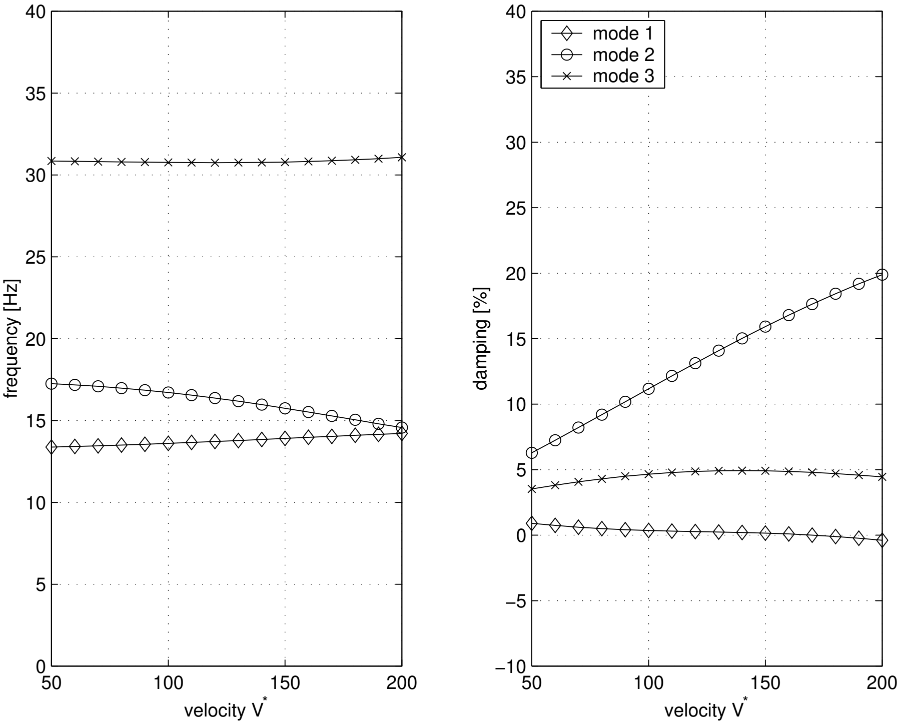

*Fig. 3.21: Eigenfrequencies and damping as function of forward velocity (*θ*=0 deg., zero trail system).*

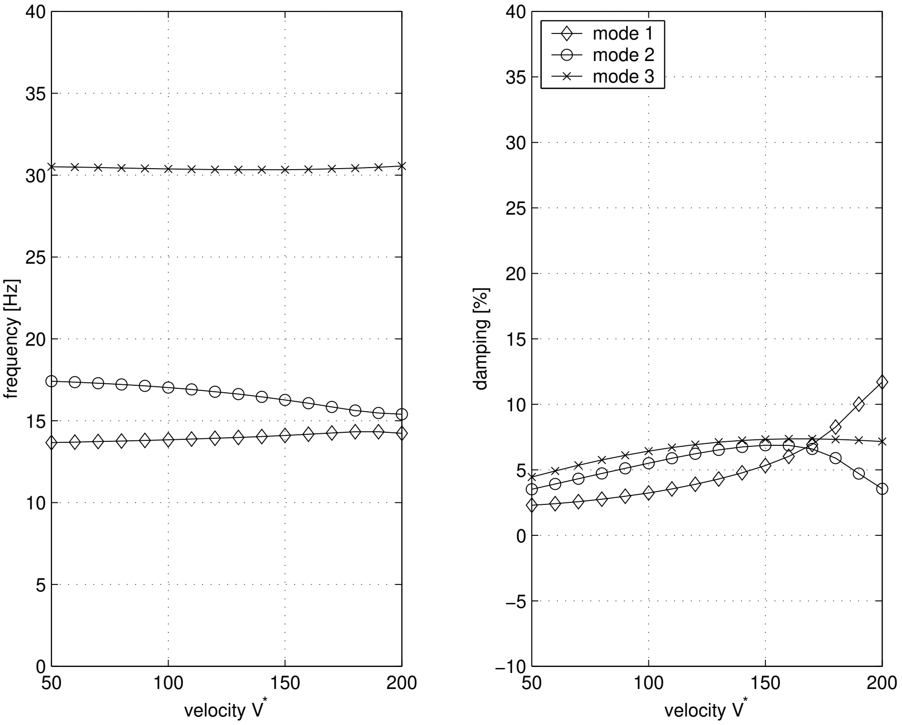

*Fig. 3.22: Eigenfrequencies and damping as function of forward velocity (*θ*=-20 deg., zero trail system).*

3.5 Bob mass - tuned mass

In section 2.2 and figure 2.13 it was already shown that the location of the centre of gravity affects the shimmy stability. Normally, the possibilities of moving the centre of gravity are rather limited, since the brake stack and wheel/tyres determine to a large extent the landing gear mass. On the other hand it is possible to introduce an additional mass item offset of the shock strut centre line to improve stability at the cost of a weight increase.

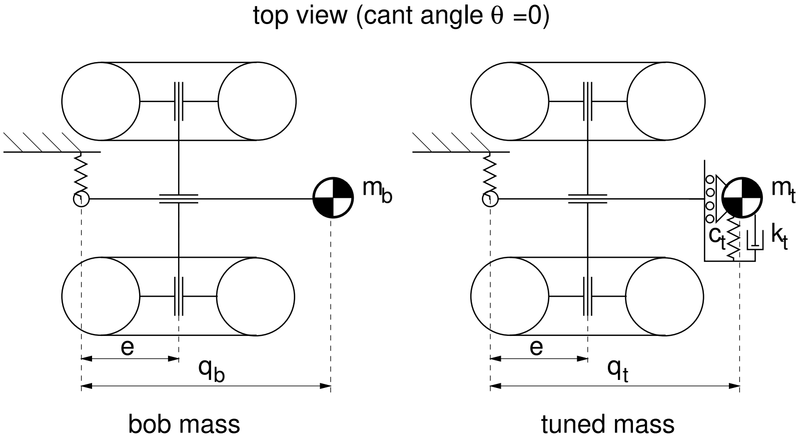

Fig. 3.23: Additional mass items.

bob mass

First, the addition of a mass item rigidly attached to the trail axle is considered, sometimes denoted as "bob mass" (see figure 3.23). Parameter q_b gives the relative location of the mass with respect to the shock strut centre line. The sign convention is the same as for the mechanical trail: a negative value indicates that the mass is in front of the shock strut. In figure 3.24 the stability is given as a function of the location q_b and mass m_b for a number of different forward velocities. In order to stabilise a system at highest forward velocity two combinations are possible: a location in front ($q_b \approx -2$) or aft ($q_b \approx 0.5$) of the strut centre line. Furthermore a significant mass is needed: about 15 to 20% of the total landing gear mass. The impact of the bob mass on the open-loop transfer function is presented in figure 3.25 for two different locations of the bob mass.

For a nose landing gear the weight penalty of the bob mass may still be acceptable: reference [12] describes how a bob mass of 25 lb was added to a nose landing gear to improve the shimmy stability. Reference [2] seems to represent a similar case regarding the nose landing gear of a fighter aircraft. For operation on an aircraft carrier, using the catapult system, the nose landing gear was equipped with a launch bar. At a later stage the aircraft was converted to a land-based configuration and the launch bar was removed; this version proved to be much more susceptible to shimmy. As a remedy, mass was added again to the steering collar and the introduction of a dummy launch bar was considered.

Another reference states that a bob mass in the order of 100 lb per main landing gear is required to produce even a small gain in stability and concludes that it generally will be an unattractive alternative to improve stability [28].

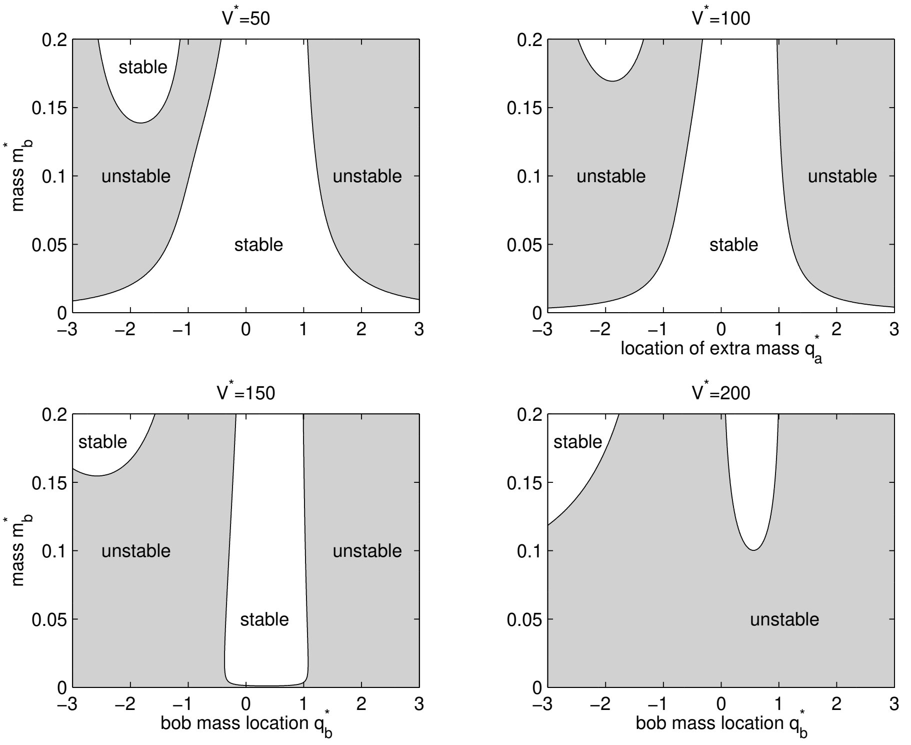

Fig. 3.24: Effect of bob mass magnitude and location on stability for different forward velocities (baseline parameters).

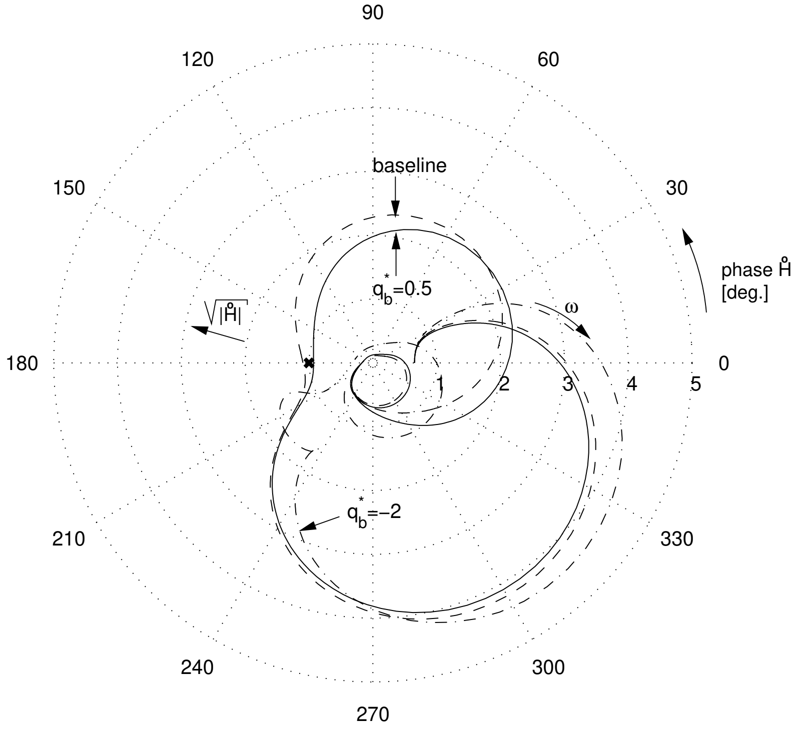

Fig. 3.25: Nyquist plot for various bob mass locations (V^*=200, m_b^*=0.2).

tuned mass

A tuned mass (or dynamic damper) may be used as an alternative to the bob mass; according to Leve, reference [28], this solution will have a lower additional weight. The tuned mass has a lateral degree of freedom and is connected to the trail via a spring-damper combination, see figure 3.23. The required amount of mass will depend on the degree of instability to be compensated for. For the baseline gear parameters used in this example, a relatively small value appears to be sufficient: 2.5% of the total landing gear mass. In order to have a positive contribution to the shimmy stability the stiffness and damping constant have to be tuned appropriately, as is illustrated by figure 3.26. In this graph the well-known expressions for the frequency and dimensionless damping of a single degree of freedom mass-spring-damper system are used:

$$f_t = \frac{1}{2\pi}\sqrt{\frac{c_t}{m_t}}, \quad \kappa_t = \frac{k_t}{2\sqrt{m_t c_t}}. \tag{3.14}$$

Again it can be observed that an offset with respect to the strut centre line is required: either positive or negative. Figure 3.27 gives the stability as function of forward velocity for the following set of parameters $q_t^* = -1.5$, $m_t^* = 0.025$, $k_t^* = 0.002$ and $c_t^* = 0.5$. These parameters correspond to a frequency f_t of 15.9 Hz and dimensionless damping κ_t of 0.2. Particularly at high forward velocity there is a major improvement in stability for the modes below 30 Hz in comparison to the baseline system of figure 3.2.

The open-loop transfer function and Nyquist plot are given in figure 3.28 and 3.29 respectively. It can be observed that the major contribution of the tuned mass is a reduction of the amplitude of the transfer function: the second resonance peak which is related to the yaw vibration of the gear is suppressed almost completely. At -180 degrees phase rotation the amplitude ratio is below one, so stability is obtained again according to the Nyquist criterion.

A final remark is that both the bob and tuned mass generally have to be placed outside of the wheel/tyre contour to be effective; this may result in interference and storage problems while retracting the landing gear.

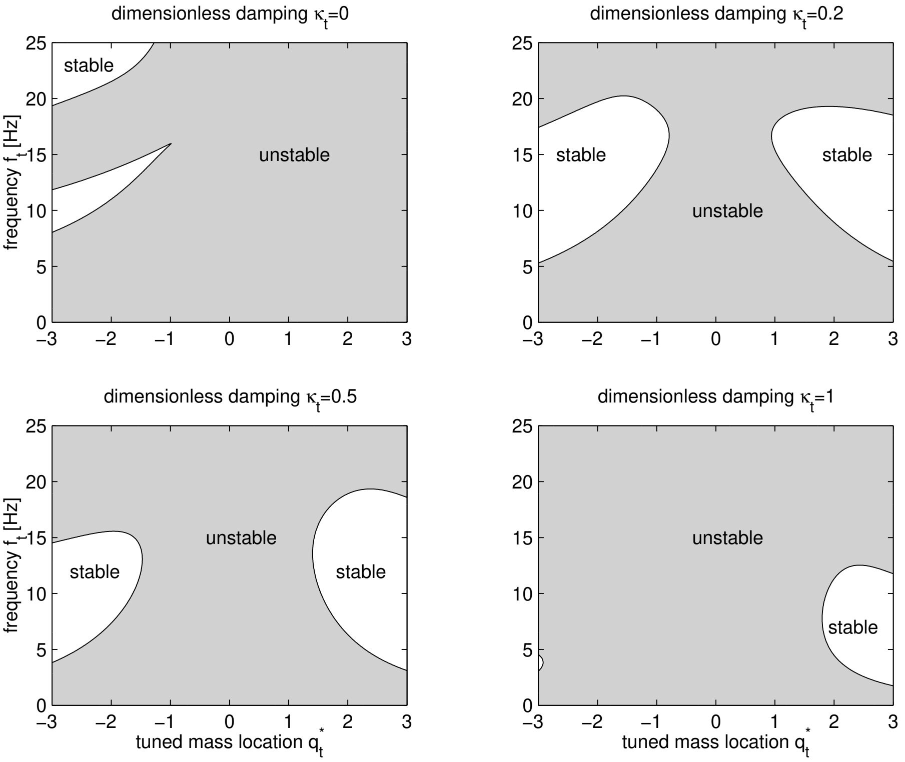

Fig. 3.26: Effect of the spring/damper characteristics of the tuned mass on stability (V^*=200, m_t^*=0.025).

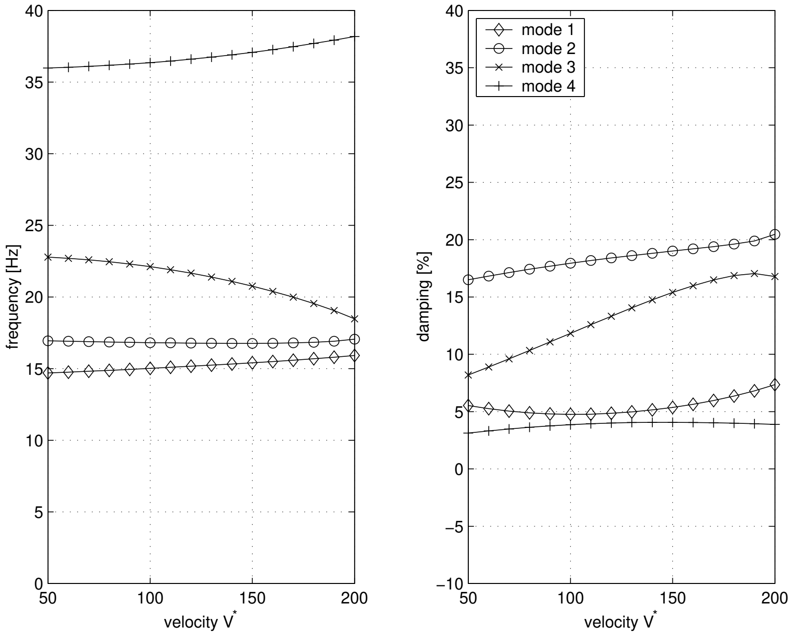

Fig. 3.27: Stability with optimised tuned mass characteristics (q_t^*=-1.5, m_t^*=0.025, k_t^*=0.002, c_t^*=0.5).

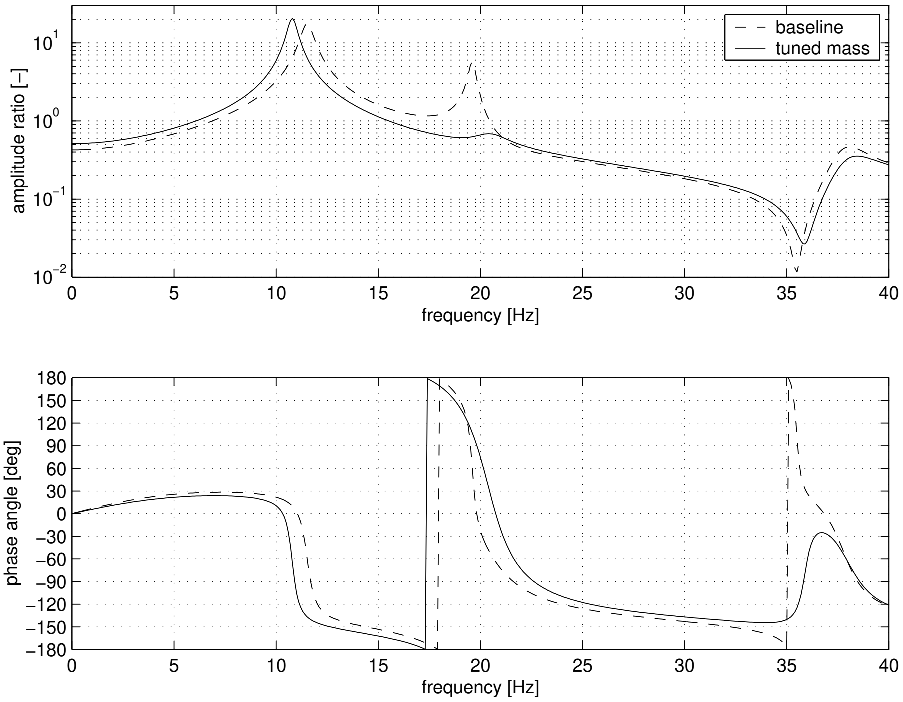

Fig. 3.28: Open-loop transfer function for a landing gear with optimised tuned mass characteristics (V^*=200, q_t^*=-1.5, m_t^*=0.025, k_t^*=0.002, c_t^*=0.5).

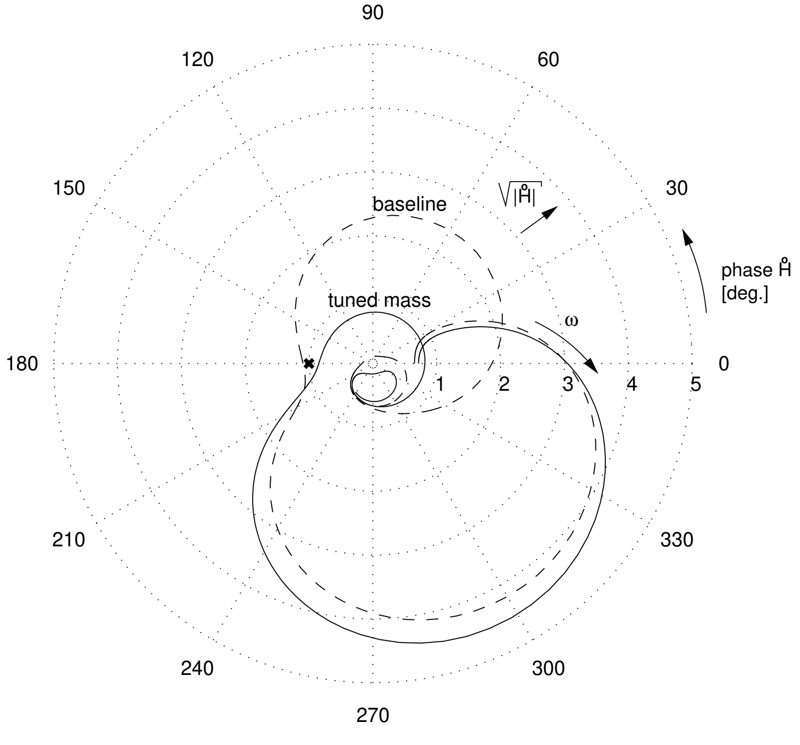

Fig. 3.29: Nyquist plot for a landing gear with optimised tuned mass characteristics (V^*=200, q_t^*=-1.5, m_t^*=0.025, k_t^*=0.002, c_t^*=0.5).

3.6 Shimmy damper

In the previous chapter it was shown for the trailing arm system, with and without lateral flexibility, that yaw damping improves stability (see e.g. figures 2.4 and 2.20). The yaw damping can be increased by introducing a shimmy damper at the apex joint of the torque links, as shown in figure 1.2. Using the distance from the apex joint to the shock strut, it is obvious that the translational characteristics of the shimmy damper can be converted into equivalent torsional characteristics about the strut centre line. In this section only linear spring and damper characteristics will be used to study the fundamentals; non-linear behaviour of the shimmy damper will be discussed in section 5.6.

The shimmy damper operates in series with the stiffness c_ψ of the landing gear as shown in figure 3.30. The shimmy damper consists of a damper and spring in parallel having a damping constant k_{sd} and stiffness c_{sd}. This situation is different from the examples given in the previous chapter, where a damping k_ψ was introduced parallel to the yaw stiffness c_ψ. Since a real landing gear is designed for minimum weight it is not possible to neglect the yaw flexibility of the strut; providing a more stable attachment point for the shimmy damper would be preferable, but also increases the weight of the landing gear. Furthermore the shimmy damper is often introduced as a remedy to solve shimmy problems on an existing main landing gear design; this generally leaves only very limited possibilities to increase the yaw stiffness c_ψ.

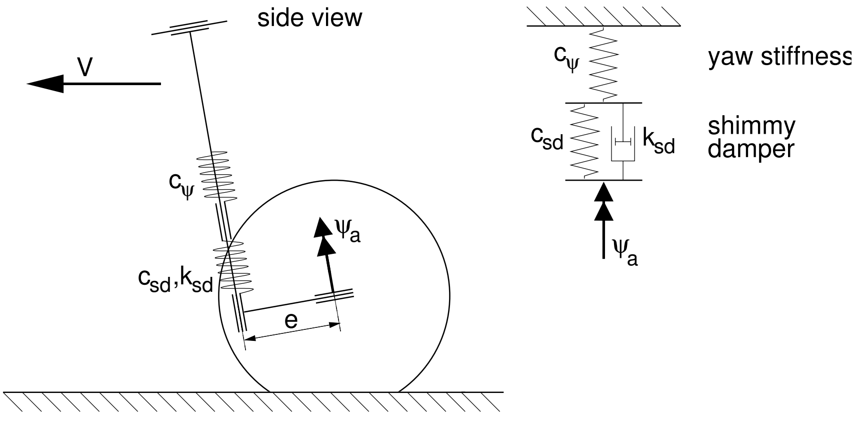

Fig. 3.30: Implementation of the shimmy damper in the landing gear model.

The shimmy damper parameters have to be selected with care, due to the series connection with the yaw stiffness c_ψ of the landing gear. A very high value of the shimmy damper stiffness c_{sd} will block the damper, so no improvement of the shimmy stability is to be expected. Zero stiffness of the shimmy damper would result in maximum utilisation of the damper; but to maintain a proper alignment of the wheels with the fuselage, a minimum value for the stiffness c_{sd} is required to prevent free swivelling of the wheels. Even more importantly, the damping constant has to be tuned: if the damping constant k_{sd} is too small the energy dissipation will be limited. Since the overall yaw stiffness is reduced due to the series connection of springs, a too low damping constant k_{sd} may actually aggravate the shimmy problems. A very high value for the damping constant on the other hand will effectively eliminate the contribution of the shimmy damper in suppressing the shimmy vibrations.

The process of tuning the damping constant is illustrated by figure 3.31. The parameters of the baseline gear are used in combination with a stiffness $c_{sd}^* = 3$. The tuning process is performed at the highest forward velocity considered for this system, $V^* = 200$, because the maximum obtainable gain in stability appears to decrease with forward velocity. The optimum value of the damping constant k_{sd}^*, which maximises the damping in the least damped mode, equals 0.3 in this example. Figure 3.31 also illustrates that if the damping constant is too low ($k_{sd}^* < 0.1$), the landing gear may become highly unstable. The choice of the damping coefficient is also a function of forward velocity: at $V^* = 100$ the optimum value of k_{sd}^* equals 0.15. Nevertheless the gear is also stable at this velocity if k_{sd}^* equals 0.3, as shown in figure 3.32. This figure also illustrates that an additional, highly damped, oscillatory mode may occur at the lower forward velocities (”mode 4”). Since the order of the system including shimmy damper is eight, it is possible that four oscillatory modes are present. This highly damped mode at low forward velocity was also observed by Van der Valk [49].

The contribution of a shimmy damper on the open-loop transfer function, in comparison to the baseline system, is shown in figure 3.33; the corresponding Nyquist plot is given in figure 3.34. It can be seen that the damper is quite effective in suppressing the resonance peaks of both the lateral and yaw vibration. Also a reduction of the amplitude ratio in the neighbourhood of -180 degrees phase lag is obtained, although the improvement appears to be limited in this region.

Next, various combinations of the yaw stiffness c_ψ and mechanical trail e are considered. For each combination of c_ψ and e the damping constant which maximises the stability at the most critical velocity is selected. The results are presented in figure 3.35 and it confirms that the highest forward velocity represents the most critical case with respect to stability. Furthermore it can be observed that already relatively small negative values of the mechanical trail result in a monotonous instability (whole left hand shaded area): the overall yaw stiffness is mainly determined by the shimmy damper with $c_{sd}^* = 3$, which is small in comparison to the gear yaw stiffness $c_\psi^* = 15$. Another important result is that the baseline system can still become unstable if the yaw stiffness c_ψ is too small, particularly at high forward velocity. Figure 3.36 illustrates that for a reduced yaw stiffness of the gear with respect to the baseline configuration ($c_\psi^* = 10$), it appears not to be possible to re-tune the shimmy damper to obtain a stable gear again.

The influence of varying the shimmy damper stiffness c_{sd} is shown in figure 3.37. As is to be expected, the area where monotonous instability occurs decreases in size, when increasing the stiffness of the shimmy damper. If the mechanical trail is positive, increasing the shimmy damper stiffness will generally result in a less stable gear. In this case a trade-off may have to be made between stability and the allowable steering compliance.

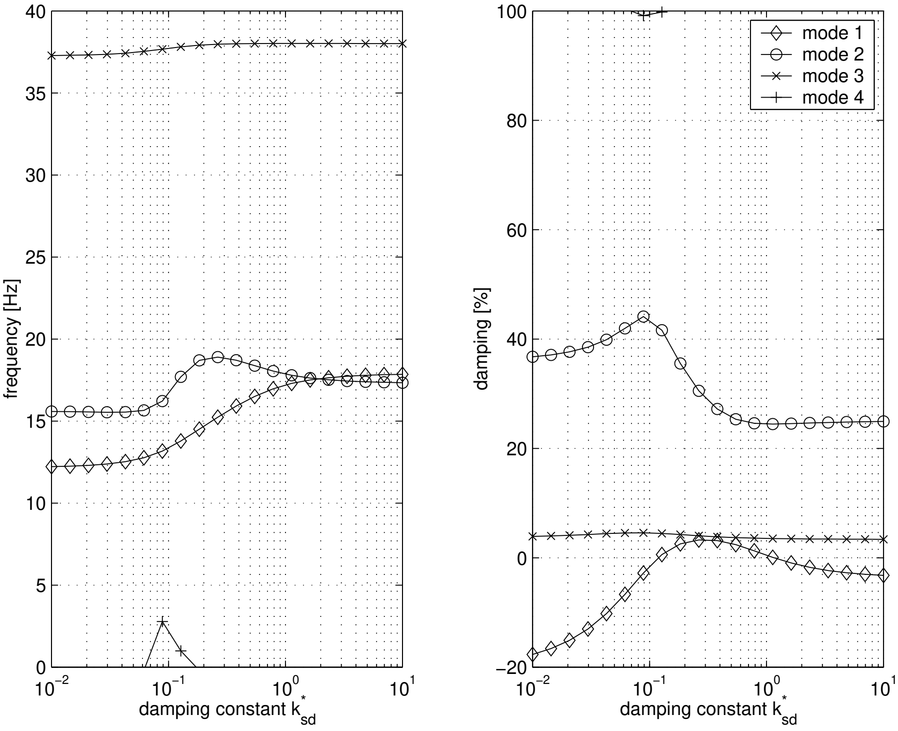

Fig. 3.31: *Tuning of the shimmy damper damping constant k_{sd} (V^*=200, baseline parameters, c^*_{sd}=3).*

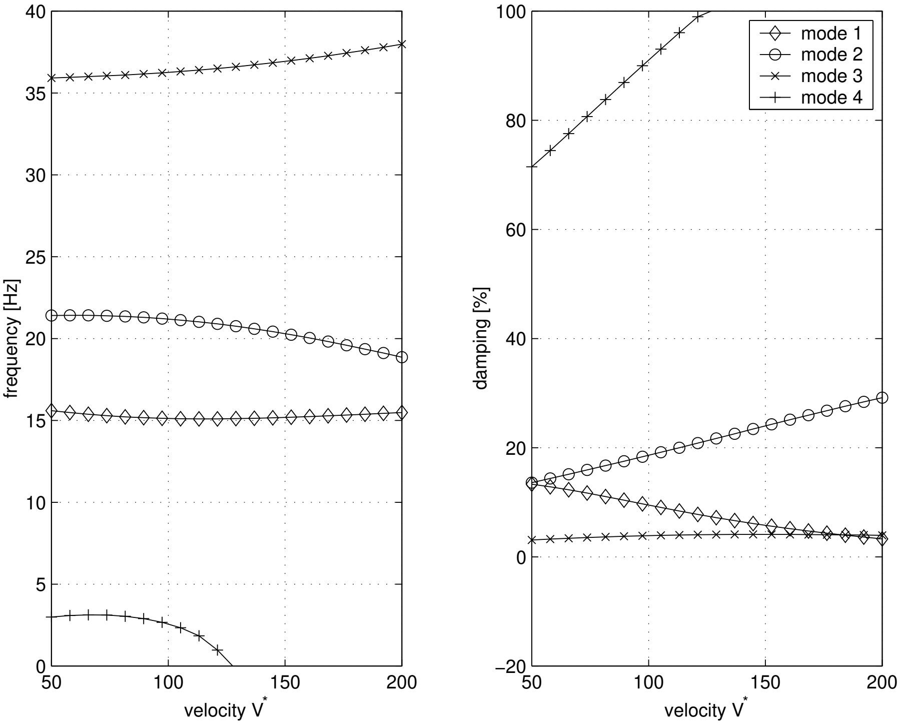

Fig. 3.32: *Stability as function of forward velocity with the optimised damping constant (baseline parameters, k^*_{sd}=0.3, c^*_{sd}=3).*

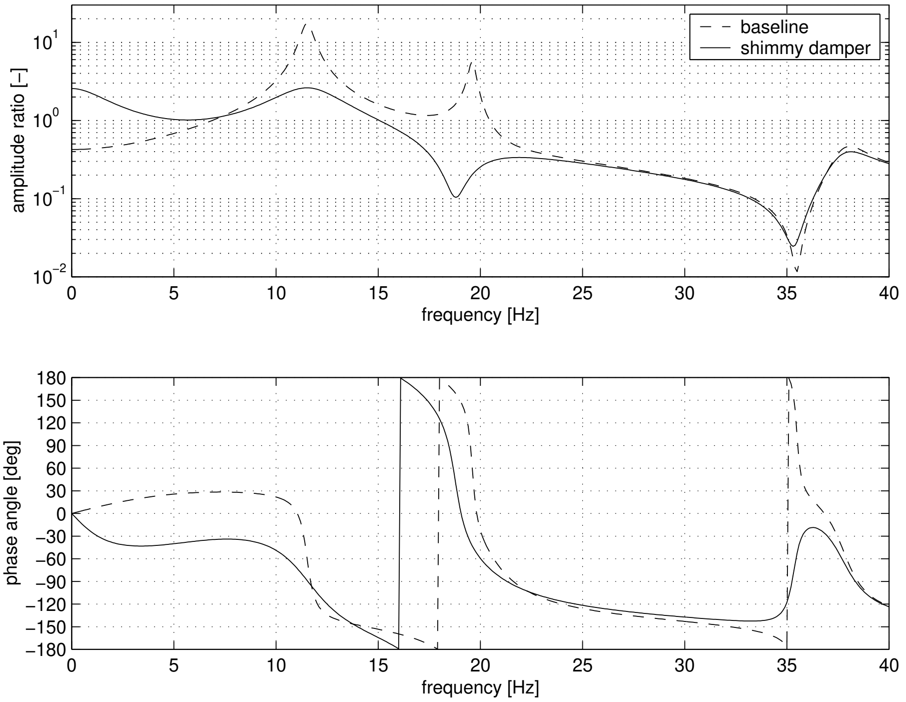

Fig. 3.33: Open-loop transfer function for the baseline system and baseline including shimmy damper (V^*=200, k^*_{sd}=0.3, c^*_{sd}=3).

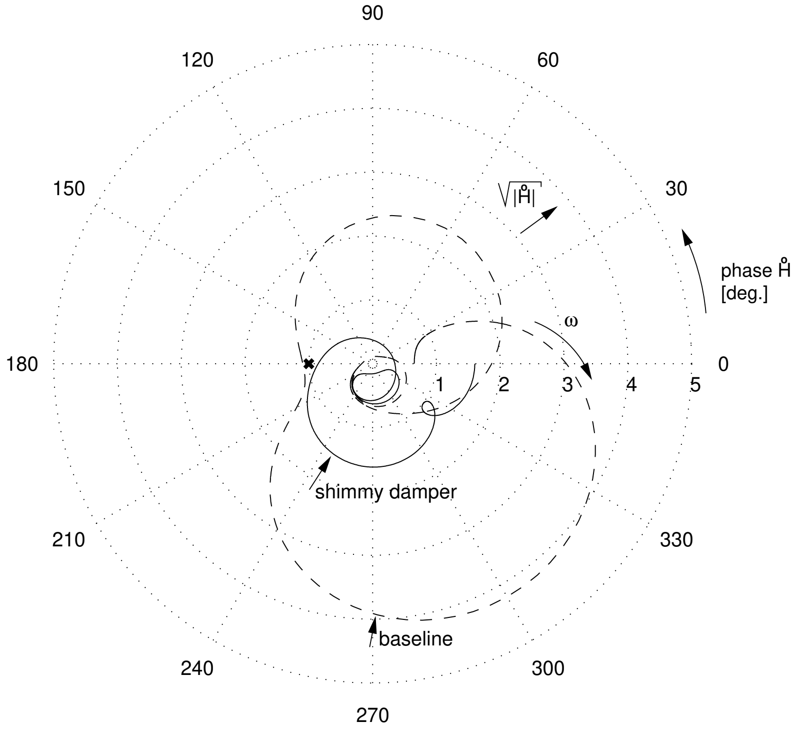

Fig. 3.34: Nyquist plot for the baseline system and baseline including shimmy damper (V^*=200, k^*_{sd}=0.3, c^*_{sd}=3).

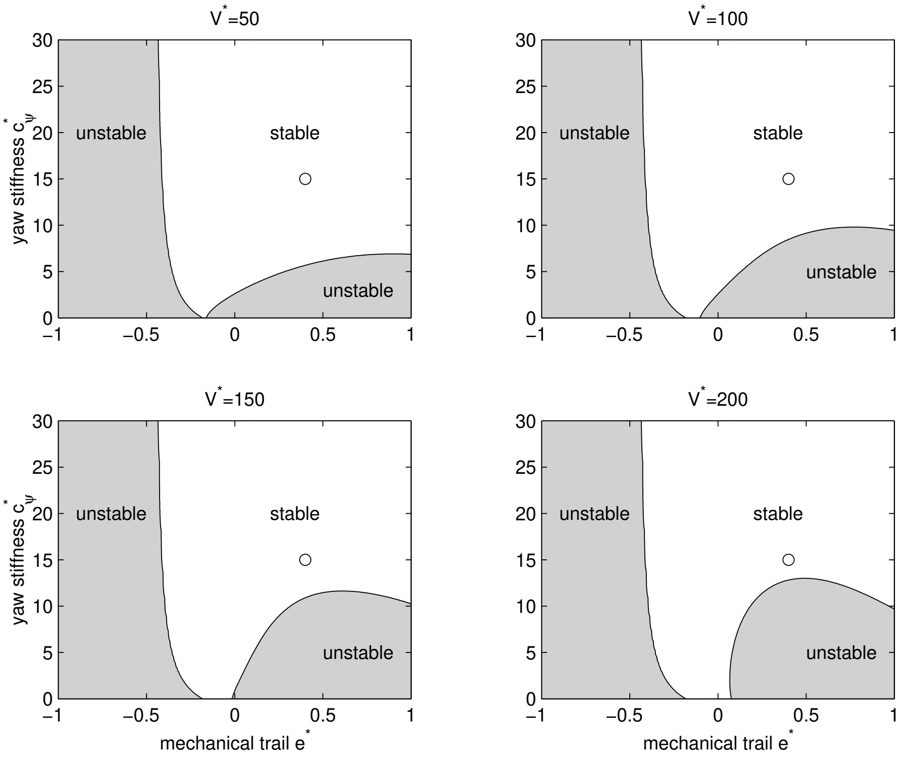

Fig. 3.35: Stability at various forward velocities for systems with optimised shimmy damper damping coefficient k_{sd} (o: baseline values for mechanical trail and yaw stiffness, c^*_{sd}=3).

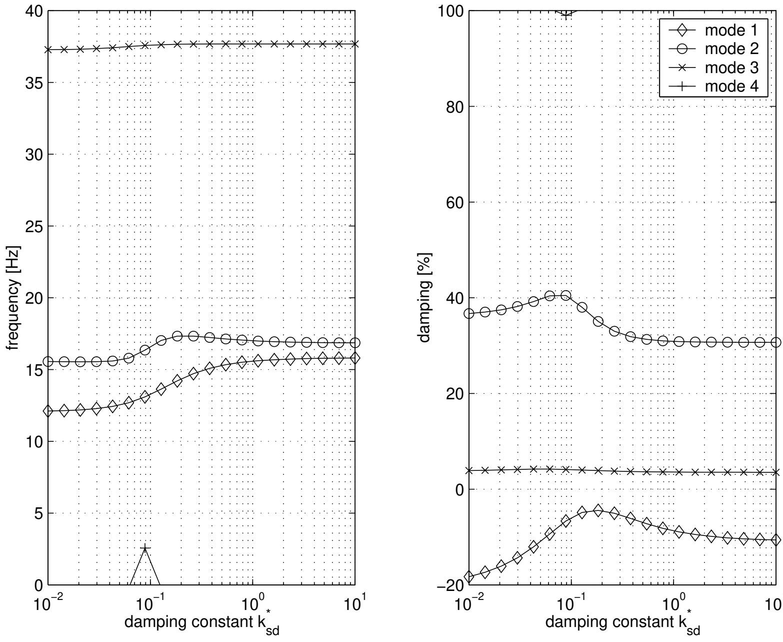

Fig. 3.36: Tuning of the shimmy damper damping constant k_{sd} (V^*=200, baseline parameters except for reduced yaw stiffness: c^*_ψ=10, c^*_{sd}=3).

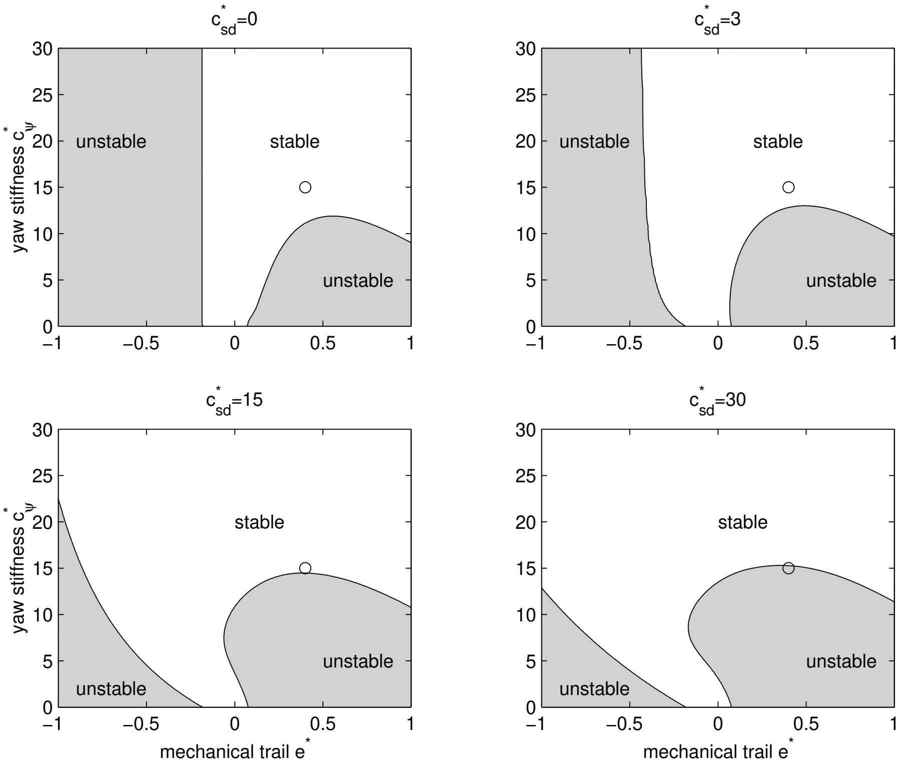

Fig. 3.37: Stability for systems with optimised damping constants k_{sd} and varying stiffness c_{sd} (V^*=200, o: baseline values for mechanical trail and yaw stiffness).

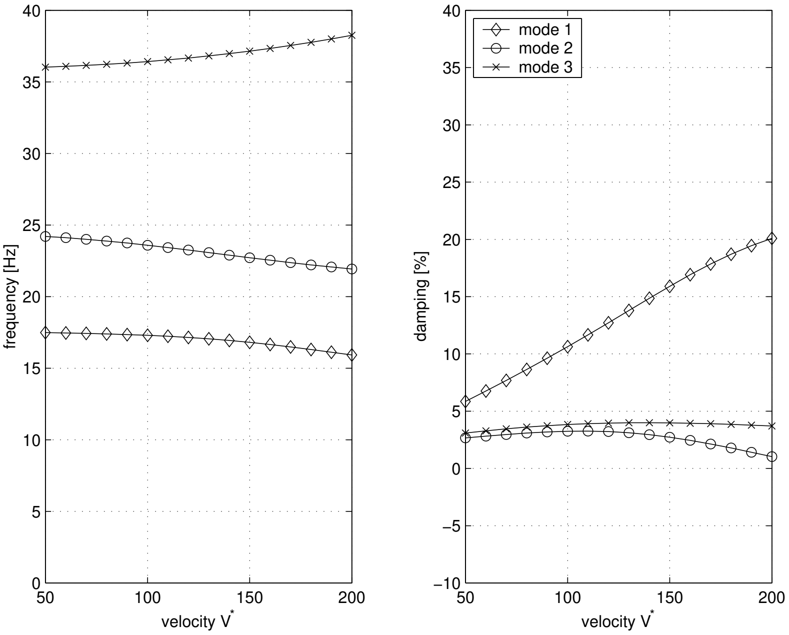

Fig. 3.38: Stability as function of forward velocity, baseline parameters and co-rotating wheels (c_a^*=4).

3.7 Co-rotating wheels

Interconnecting both wheels by means of a shaft will introduce an additional stiffness opposing the yaw motion of the gear. This design is known as dual co-rotating wheels. Referring to German research published in 1943, Moreland [32] already mentions the possible gain in shimmy stability of this design. According to Stevens shimmy free nose landing gear designs have been made using co-rotating wheels, but on a number of occasions shimmy still occurs [48].

To study the contribution of co-rotating wheels a flexible shaft connecting both wheels will be considered. After linearisation, the following expression can be derived for the difference in angular velocity between both wheels:

$$\dot{\varepsilon}_a = \frac{2w}{R_e}\left(\dot{\phi}_a \sin\theta - \dot{\psi}_a \cos\theta + (\phi_a \cos\theta + \psi_a \sin\theta)\Omega \frac{dR_e}{d\delta}\right) \tag{3.15}$$

It is interesting to note that angular velocity difference between the wheels is not only a function of yaw velocity (perpendicular to the road) but also dependent on the roll angle of the axle with respect to the runway. Roll of the wheel axle will result in different effective rolling radii between the left and right side and consequently a different angular velocity of the wheels. The moment in the shaft can be obtained by integration of the angular velocity difference $\dot{\varepsilon}_a$ and multiplication with the torsional stiffness of the shaft c_a. The resulting additional moments about the roll and yaw axis of the gear read:

$$M_\phi = -\frac{2w}{R_e} c_a \varepsilon_a \sin\theta, \quad M_\psi = \frac{2w}{R_e} c_a \varepsilon_a \cos\theta \tag{3.16}$$

By introducing co-rotating wheels the instability occurring at high forward velocity for the baseline system can be eliminated, as is shown in figure 3.38 (compare with figure 3.2). Particularly at high forward velocity the results become sensitive to the value of $dR_e/d\delta$. If this value is zero, the effective rolling radius remains constant, the shaft only increases the yaw stiffness of the system and a clear improvement in stability can be obtained, see figure 3.39. The value $dR_e/d\delta = -\frac{1}{3}$ is typically obtained for bias ply tyres. In case of radial tyres it is expected to be closer to zero, but no experimental data for aircraft tyres is available to support this. The shaft stiffness has to be tuned carefully as is illustrated by figure 3.40 and confirms that simply introducing co-rotating wheels does not guarantee shimmy stability.

In the current analysis longitudinal slip of the tyres is not considered; this assumption may prove to be less accurate depending on the stiffness of the connection shaft and tyre parameters. Some practical considerations concerning the co-rotating wheels design should be recognised: the connecting shaft will experience considerable (fatigue) loading, and it can be expected that the tyre wear will increase. For a main landing gear the shaft may interfere with a proper operation of the anti-skid system, which normally operates on each wheel individually.

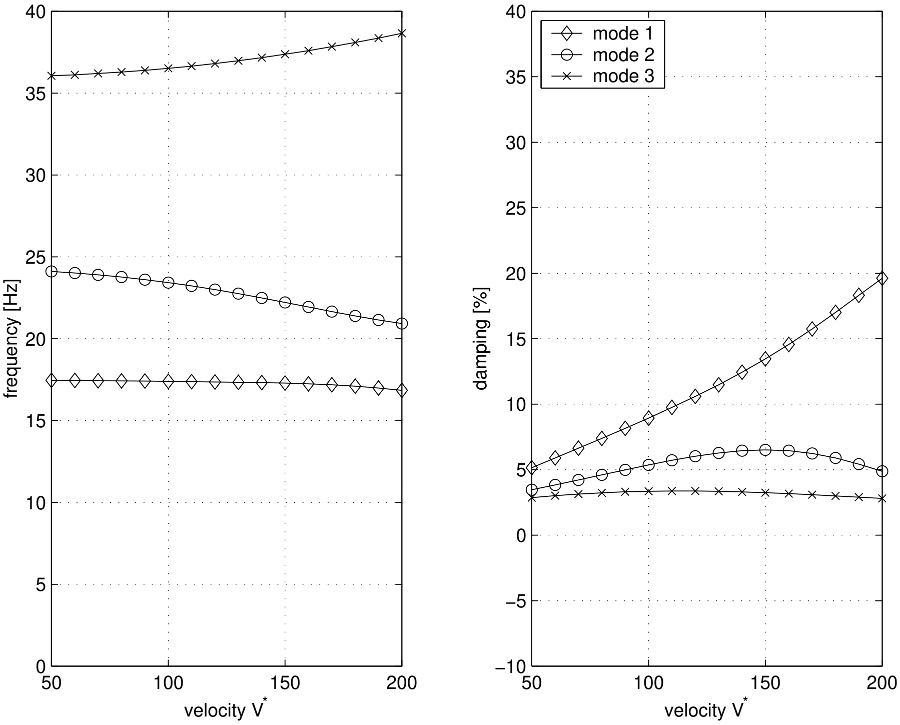

Fig. 3.39: Stability as function of forward velocity, baseline parameters, co-rotating wheels c_a^*=4 and constant effective rolling radius $\frac{dR_e}{d\delta}$=0.

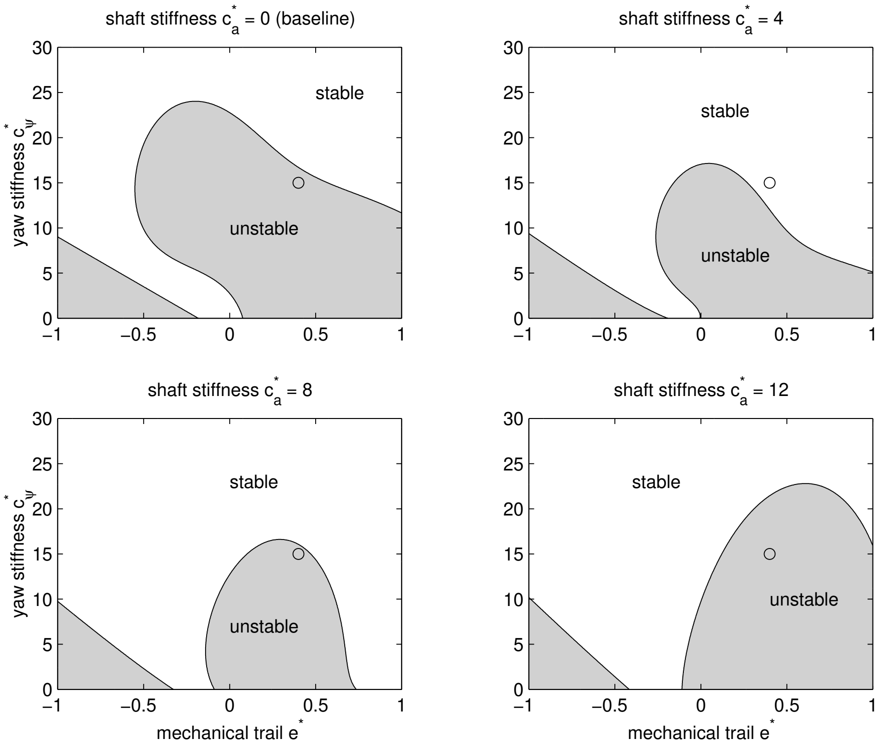

Fig. 3.40: Stability as a function of torsional stiffness and trail for various values of the shaft stiffness (V=200, o: baseline values for mechanical trail and yaw stiffness).*

3.8 Bogie configuration

A bogie is a very common main landing gear configuration for large aircraft. In section 2.1 an analytical expression was derived for this system, indicating that stability can be obtained if the wheelbase is sufficiently large (equation 2.9). The landing gear model introduced in this chapter is extended to a four-wheeled bogie and the effect of lateral stiffness and gyroscopic behaviour of the rotating wheels on system stability is investigated. Independent roll degrees of freedom for the front and rear axle are used in the bogie model. Two first order differential equations for the two tyre pairs are considered. The resulting system is of 10th order.

The baseline parameters are used, with the exception that a distance e^* of 1.2 is selected, see figure 2.6. With these parameters figure 3.41 is obtained. It can be seen that the modes below 30 Hz are damped quite well at the lower and medium forward velocities. At very high velocity the damping of mode 2 starts to decrease; this mode becomes unstable for a velocity V^* in excess of 300. Figure 3.42 shows the impact of lateral and yaw stiffness on the stability at $V^* = 300$; a lower boundary for the lateral stiffness can be established.

Nevertheless it should be noted that this high speed already represents a rather extreme case, far outside the normal operating range of the aircraft. If the maximum velocity V^* is limited to 200 it can be shown that the bogie gear under consideration is stable for any combination of lateral and yaw stiffness, which is in agreement with the results of section 2.1. It can be verified that the gyroscopic moment caused by the rotating wheels is responsible for the instability at very high forward velocity. Consequently, to prevent the instability the focus should be on minimising the roll of the wheel axle under lateral loading. This can be achieved by e.g. increasing the lateral stiffness c_y, track width w or effective gear length l.

A general conclusion from this numerical example is that a bogie landing gear configuration appears to be far less critical with respect to shimmy instability than the twin-wheeled cantilevered design.

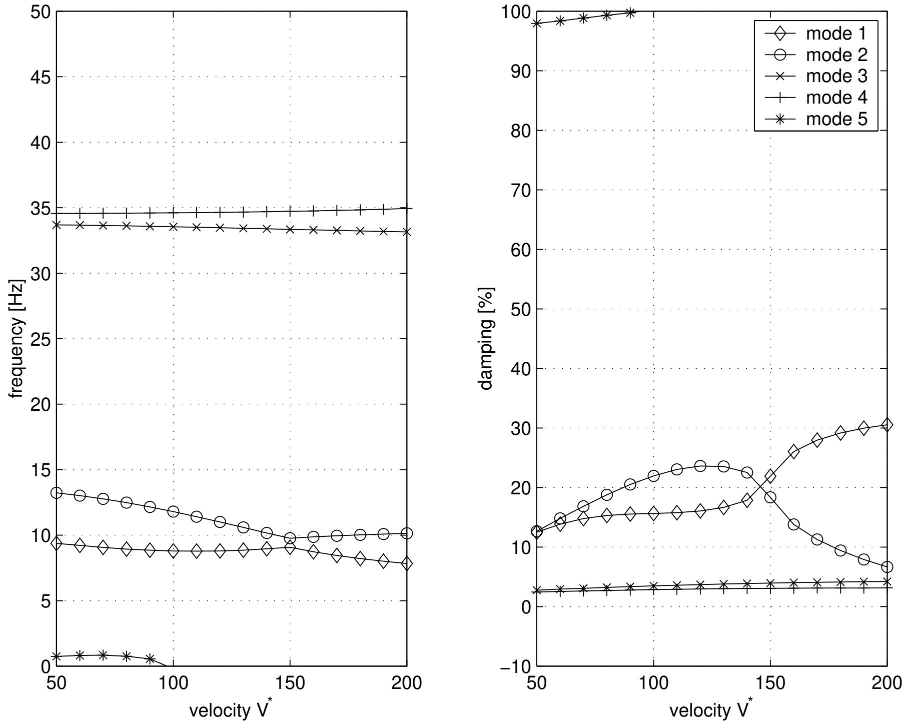

Fig. 3.41: Stability as function of forward velocity, bogie landing gear.

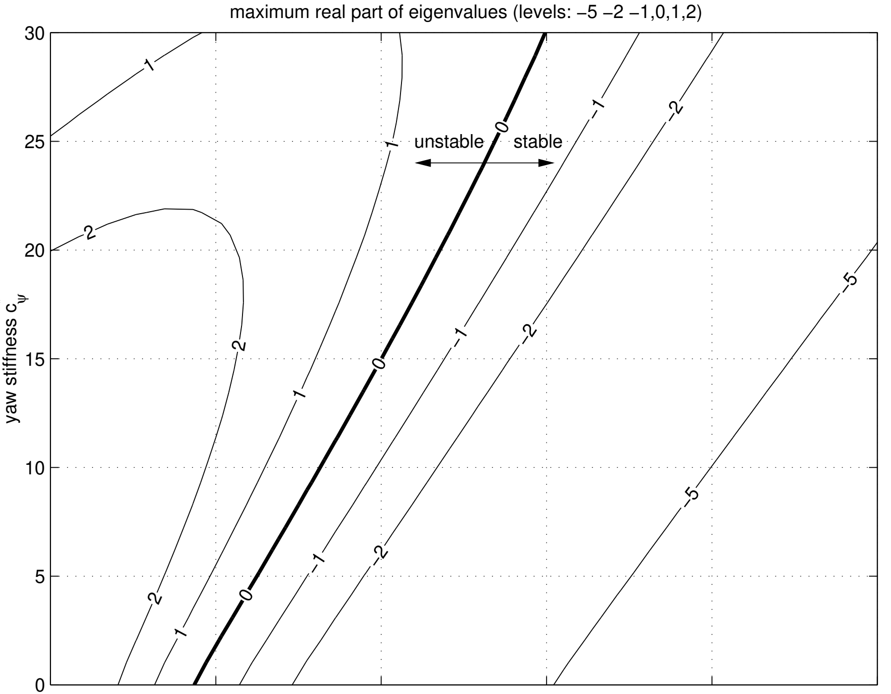

Fig. 3.42: Stability as a function of lateral and yaw stiffness for a bogie landing gear (V^*=300).

Chapter 4

Tyre modelling

The tyres play an important role in causing the shimmy instability. In the previous chapters the straight tangent tyre model, as developed by Pacejka, has been utilised. It appears that the simple straight tangent tyre model becomes less accurate at low forward velocity (short wavelength) and a more advanced tyre model with a proper inclusion of the effect of the finite tyre contact length may be preferred to use.

In the literature various tyre models are available for application to the shimmy problem. Smiley has already investigated different models from the early days of shimmy analysis, reference [46]. In this chapter a comparison will be made between a number of different tyre models, which are still in use today for analysing shimmy. The discussion includes the model of Keldysh and Kluiters' implementation of the Von Schlippe model. These models may be relatively unknown, but are considered to be of importance.

A systematic comparison will be made, based on transfer functions, step response and energy considerations. Using these results and a careful examination of the governing differential equations, it appears to be possible to extract equivalence conditions between some of the tyre models. Furthermore the impact of different tyre models on the shimmy stability will be investigated for a number of relatively simple mechanical systems. Finally some attention will be paid to the parameters of the tyre model. Available measurement data is compared against empirical formulas, as developed by various authors.

4.1 Slip definitions, sign convention

The interaction between tyre and road under various rolling conditions is a complex contact problem. Forces and moments are developed at the contact patch due to the relative motion between wheel and road. Standardised definitions may be used to describe the tyre characteristics; a generally accepted approach is to consider the tyre and wheel as a disk which coincides with the plane of symmetry of the tyre, see figure 4.1. The forces generated by the tyre are assumed to act at the contact centre C. The point C is defined as the point of intersection between wheel plane, road plane and plane through the wheel spin axis and normal to the road. The distance R from the wheel centre to point C is known as the loaded radius.

A local axis system is defined which is used to express the components of the forces, moments and slip velocities: x-axis is parallel to the line of intersection of the road and wheel plane; the y-axis is perpendicular to this line and parallel to the road plane; the

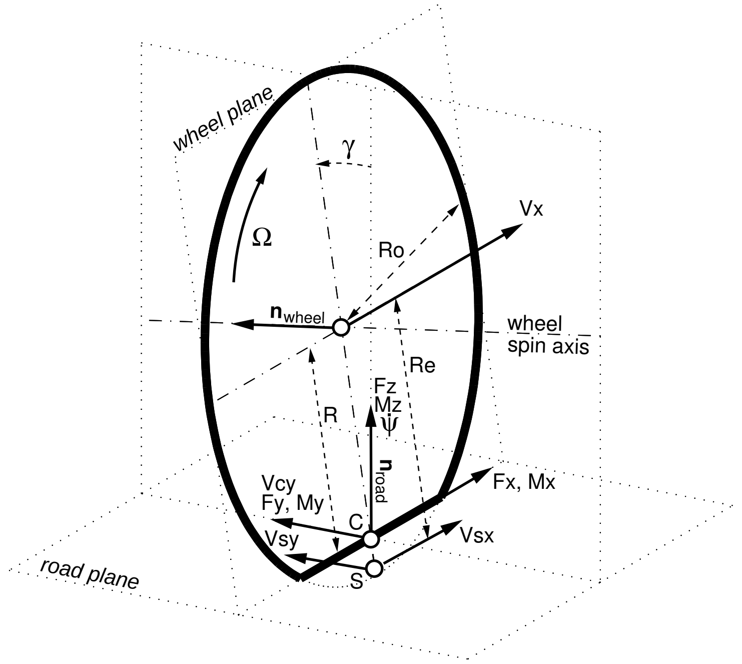

Fig. 4.1: Disk representation of wheel and tyre (rear view).

z-axis is normal to the road. At the contact centre C three forces and moments can be distinguished: longitudinal force F_x, lateral force F_y, vertical force F_z, overturning moment M_x, rolling resistance moment M_y and self aligning moment M_z. These forces and moments are a function of various input quantities: e.g. the vertical force F_z will be a function of the tyre deflection. The other variables considered in this thesis are:

- *longitudinal slip* κ
  The longitudinal slip is defined as:

  $$\kappa = -\frac{V_{sx}}{V_x} \tag{4.1}$$

  In this expression V_{sx} is the velocity of the imaginary slip point S with respect to the road (see figure 4.1). The following equation holds:

  $$V_{sx} = V_x - \Omega R_e \tag{4.2}$$

  By definition both κ and V_{sx} will be zero for a freely rolling wheel. If the wheel is locked ($\Omega = 0$) V_{sx} will be equal to V_x and κ will be -1. Generally the effective rolling radius R_e is larger than the loaded radius R and consequently point S will be located below the road surface. A final note on the definition of longitudinal slip is that some authors prefer to use an expression different from 4.1 to describe the case of driving ($\kappa > 0$).

- *slip angle* α
  The slip angle (or drift angle) is defined as:

  $$\tan(\alpha) = -\frac{V_{cy}}{V_x} \tag{4.3}$$

Instead of V_{cy} one may also use V_{sy} (the lateral component of the velocity of the wheel at the slip point S); the differences will be very small to negligible.

- *turn slip* ϕ
  Turn slip is given by:
  $$\phi = -\frac{\dot{\psi}}{V_x} \tag{4.4}$$
  Turn slip typically occurs when the wheel travels along a circular path with a constant radius, as indicated in figure 4.2.

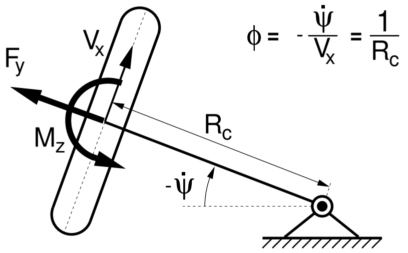

Fig. 4.2: Model showing a pure turn slip condition (top view).

- *inclination angle* γ
  The inclination angle is calculated as:
  $$\sin(\gamma) = -\mathbf{n}_{road} \cdot \mathbf{n}_{wheel} \tag{4.5}$$
  The vector $\mathbf{n}_{road}$ is the normal to the road, the vector $\mathbf{n}_{wheel}$ is the normal to the wheel plane and the "·" denotes the dot product. The variable γ is often referred to as the *camber angle*, but strictly speaking the definition of camber is only applicable in the context of an axle: camber is considered positive when both wheels lean outwards at the top and negative when they lean inwards [41]. This implies that for one value of camber the tyres on either side of the axle will have opposite inclination angles.

It is obvious that using this set of variables to describe tyre characteristics is still a limited representation: the forces generated by the tyre will also be dependent on inflation pressure, road roughness, temperature, etc.

Some of the slip definitions employed in this thesis deviate from the SAE and ISO sign conventions; details are shown in figure 4.3. For the forces and moments the ISO convention is selected: if the tyre is compressed a positive vertical load F_z is obtained. The definition of the slip angle α is reversed with respect to ISO; in this way a positive value for the cornering stiffness $C_{f\alpha}$ is obtained when taking the derivative of the function $F_y(\alpha)$ at zero slip angle; it also enhances the similarity between the longitudinal and lateral slip characteristics. Also the sign of the inclination angle is reversed with respect to ISO: in this way a positive inclination angle produces a positive overturning moment M_x and a positive increase of the lateral force F_y and self aligning moment M_z. Finally the definition of turn slip is reversed with respect to the original definition used by Pacejka [37]: with the current definition a lateral force F_y and positive moment M_z are obtained when the turn slip ϕ is positive.

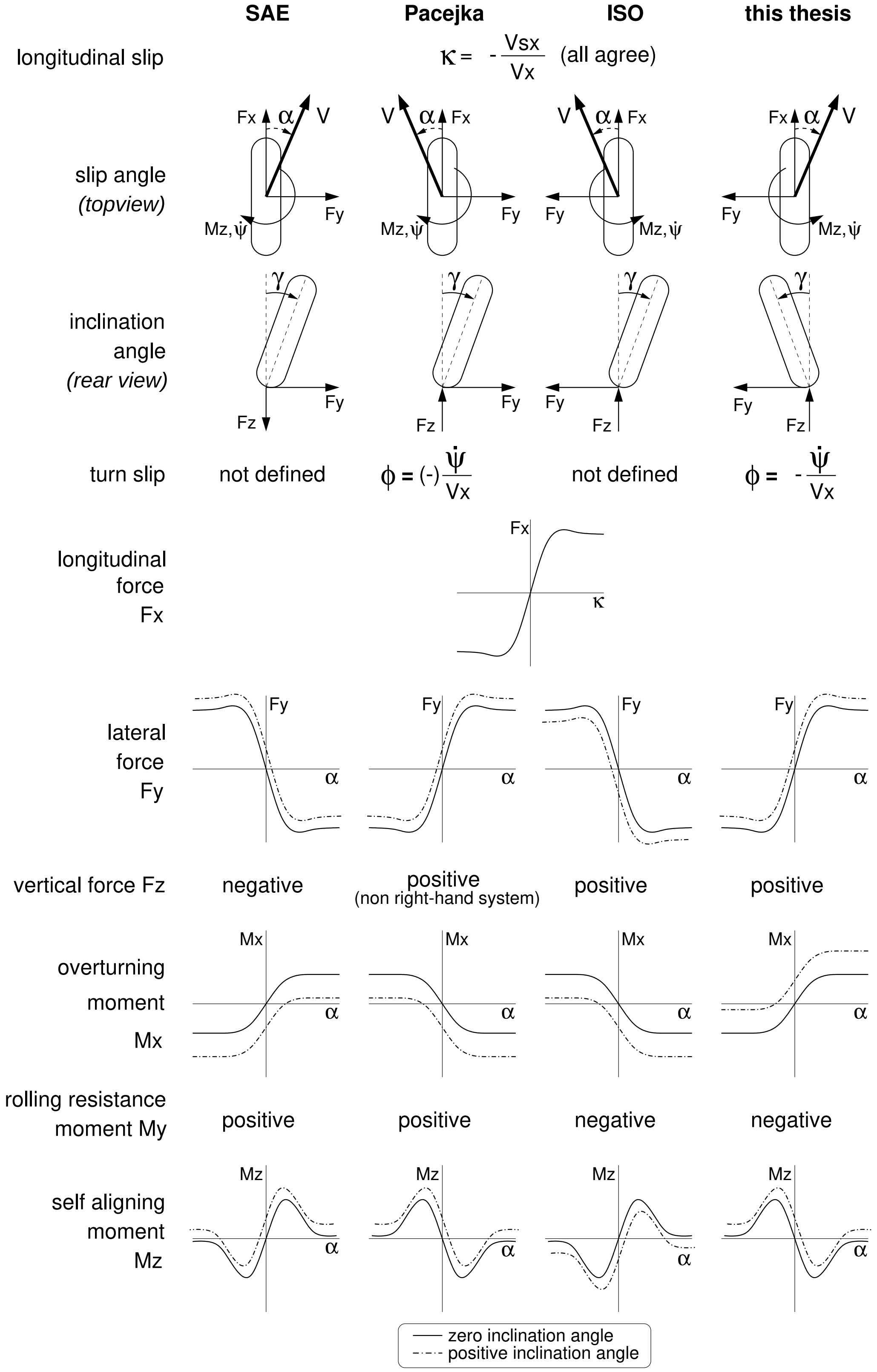
SAE
Pacejka
ISO
this thesis
longitudinal slip
κ = - Vsx/Vx (all agree)
slip angle
(topview)
Fx
α
V
Fy
Mz, ψ̇
inclination
angle
(rear view)
γ
Fz
turn slip
not defined
ϕ = (-) ψ̇/Vx
not defined
ϕ = - ψ̇/Vx
longitudinal
force
Fx
κ
lateral
force
Fy
vertical force Fz
negative
positive
(non right-hand system)
positive
positive
overturning
moment
Mx
rolling resistance
moment My
positive
positive
negative
negative
self aligning
moment
Mz
zero inclination angle
positive inclination angle

Fig. 4.3: Different sign conventions for slip, inclination angle and tyre forces/moments.

Following this approach a minus sign has to be applied consistently to the slip and inclination angle definitions (equations. 4.1, 4.3, 4.4 and 4.5). The slip definitions given here are only valid for a positive value of the forward velocity V_x. In case of backwards driving some corrections are required, but the discussion of these modifications is outside the scope of this thesis and irrelevant for the shimmy phenomenon. The following set of equations could be used to describe the linearised, steady-state behaviour of a tyre operating at small values of the inclination angle and slip:

$$\left.\begin{array}{lcl} F_x & = & C_{f\kappa}\kappa \\ F_y & = & C_{f\alpha}\alpha + C_{f\gamma}\gamma + C_{f\phi}\phi \\ M_z & = & C_{m\alpha}\alpha + C_{m\gamma}\gamma + C_{m\phi}\phi \end{array}\right\} \tag{4.6}$$

With the current definitions of slip and inclination angle all C-coefficients, except $C_{m\alpha}$, will be positive for a regular tyre operating at small values of slip and inclination angle. When considering the full non-linear characteristics as given in figure 4.3, it is clear that the derivative of the self aligning moment M_z with respect to the side slip angle α is negative; consequently also the self aligning stiffness $C_{m\alpha}$ will be negative:

$$C_{m\alpha} = \left.\frac{\partial M_z}{\partial \alpha}\right|_{\alpha=0} \qquad (< 0) \tag{4.7}$$

To accurately describe shimmy, the dynamic behaviour of the tyre has to be included. On page 22 the straight tangent tyre model was introduced: the lateral force F_y and self aligning moment M_z depend on lateral velocity $\dot{y}_c$, yaw angle ψ and yaw velocity $\dot{\psi}$. For small values of $\dot{y}_c$ and ψ the slip angle equals (see figure 4.4):

$$\alpha = \psi - \frac{\dot{y}_c}{V} \tag{4.8}$$

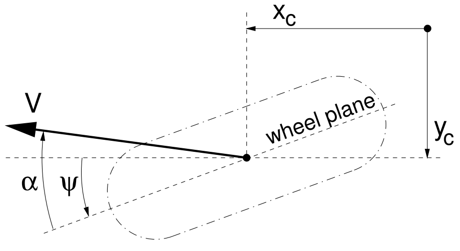

Fig. 4.4: Sign convention of the slip angle α*, yaw angle* ψ *and coordinates* x_c*,* y_c *(road level).*

A formulation using side and turn slip is not restricted to small deviations from a straight line motion of the wheel and thus better suited for a generic implementation of a tyre model in a multi-body program. In the next sections various tyre models will be compared using transfer functions, which relate the lateral force F_y and self aligning moment M_z to side and turn slip. The response of the tyre to pure side slip is given by the transfer functions $H_{F_y,\alpha}(s)$ and $H_{M_z,\alpha}(s)$; for turn slip the transfer functions $H_{F_y,\phi}(s)$ and $H_{M_z,\phi}(s)$ are applicable.

Using equations 2.1, 4.4 and 4.8 the following transfer functions can be obtained for the straight tangent tyre model:

$$H_{F_y,\alpha}(s) = C_{f\alpha}\left(\frac{1}{\sigma\frac{s}{V}+1}\right) \tag{4.9}$$

$$H_{M_z,\alpha}(s) = C_{m\alpha}\left(\frac{1}{\sigma\frac{s}{V}+1}\right) \tag{4.10}$$

$$H_{F_y,\phi}(s) = C_{f\alpha}\left(\frac{a}{\sigma\frac{s}{V}+1}\right) \tag{4.11}$$

$$H_{M_z,\phi}(s) = C_{m\alpha}\left(\frac{a}{\sigma\frac{s}{V}+1}\right) \tag{4.12}$$

Another important response of the tyre can be obtained when the wheel centre is forced to move in a straight line and a steering angle is applied to the wheel. We will refer to this case as pure yaw: $\dot{y}_c = 0$, $\alpha = \psi$, $\phi = -\dot{\psi}/V$. The accompanying transfer functions are a combination of the transfer functions with respect to side and turn slip:

$$\left.\begin{aligned} H_{F_y,\psi}(s) &= H_{F_y,\alpha}(s) - \tfrac{s}{V}H_{F_y,\phi}(s) \\ H_{M_z,\psi}(s) &= H_{M_z,\alpha}(s) - \tfrac{s}{V}H_{M_z,\phi}(s) \end{aligned}\right\} \tag{4.13}$$

The transfer functions with respect to pure yaw have been verified experimentally using a yaw oscillation test stand on top of a drum (see e.g. [20], [39]).

4.2 Stretched string model and derivatives

The first tyre models used in a shimmy analysis were based on a single contact point approach (e.g. Kantrowitz, Wylie [46]). In 1941 Von Schlippe introduced the concept of a stretched string with a finite contact length to describe the mechanics of a rolling tyre [45]. For a detailed discussion on the stretched string model reference is made to [35]. In this section a summary will be given of the mathematics governing the stretched string model and its derivatives.

In the stretched string approach the tyre is considered as a massless string of infinite length under a constant pre-tension force and it is uniformly supported elastically in the lateral direction. Some authors prefer to start their analysis with a string of finite length in a circular shape, which resembles the actual tyre more closely. Nevertheless on deriving the expressions for the forces generated by the tyre, simplifying assumptions are introduced whereby the model is effectively reduced to a plane model of a string with infinite length, see e.g. reference [43]. Furthermore the equilibrium of forces acting on the circular string is somewhat more complicated: Pacejka noted that in the expression for the self aligning torque derived by Von Schlippe a corrective factor was introduced, which would not exist if the point of application of all forces acting on the string had been take into account correctly [35]. Consequently a plane description of the stretched string will be considered.

The region where the string is in contact with the road has a length of $2a$; for points in the contact region the assumption is made that no sliding occurs with respect to the road. Furthermore it is assumed that the angles under consideration remain small. First

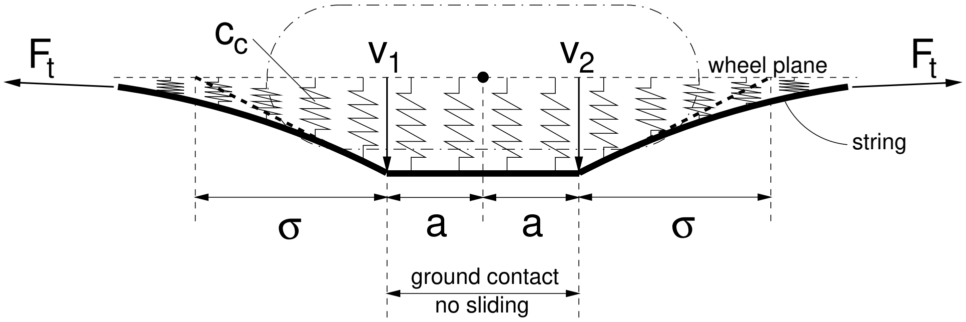

Fig. 4.5: Deflection of the string upon application of a lateral displacement of the wheel centre (non-rolling tyre, top view).

a lateral movement of the rim is considered for a non-rolling tyre. For the free portion of the string (not in contact with the road) the solution to the partial differential equation governing the deflection of the string is an exponential function. The constant σ relates the lateral deflection and slope in the fore and aft point of the contact region, see figure 4.5. The following formula is applicable:

$$\sigma = \sqrt{\frac{F_t}{c_c}} \tag{4.14}$$

where F_t is the tension force in the string and c_c is the lateral carcass stiffness per unit of length.

Next a rolling tyre will be considered: a point on the circumference of the tyre will enter, travel through and leave the contact region. On entering the contact region the zero sliding condition has to be fulfilled. The lateral deflection of the string in the leading contact point with respect to the wheel plane equals v_1; the location y_1 of the leading contact point in the ground frame is given by (see figure 4.6):

$$y_1 = y_c + a\psi + v_1 \tag{4.15}$$

When regarding the boundary condition that the slope of the string deflection remains continuous at the leading edge, the following differential equation can be obtained for the string deflection in the leading contact point with respect to travelled distance s_t:

$$\frac{dv_1}{ds_t} = \psi - \frac{v_1}{\sigma} - \frac{dy_c}{ds_t} - a\frac{d\psi}{ds_t} \tag{4.16}$$

Assuming a constant forward velocity V, we may assume $s_t = Vt$ and the equation for the deflection at the leading edge becomes:

$$\dot{v_1} = V\left(\psi - \frac{v_1}{\sigma}\right) - \dot{y_c} - a\dot{\psi} \tag{4.17}$$

After differentiation of 4.15 with respect to time, while assuming a constant contact length a, and substitution in 4.17, we obtain for the lateral position of the leading edge:

$$\frac{\sigma}{V}\dot{y_1} + y_1 = y_c + (\sigma + a)\,\psi \tag{4.18}$$

As stated before, the assumption is made that no sliding occurs for all points in the contact region: their position with respect to the road will remain unchanged. In his paper

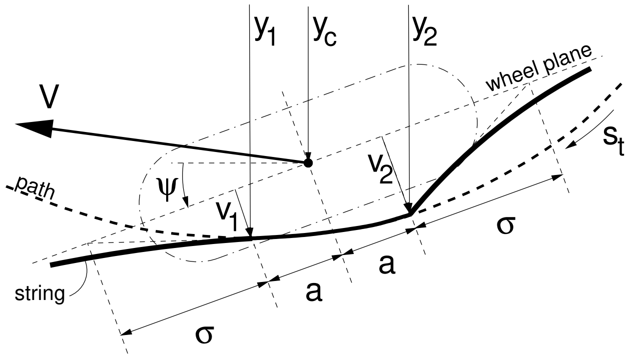

Fig. 4.6: Deflection of the string for a non-stationary rolling condition (top view).

Von Schlippe points out the analogy with a train consisting of a tractor and several trailers: the tractor travels along a certain path and the trailers have to follow it. Similarly the ground contact line follows the leading contact point; the lateral position of the leading point with respect to the ground is governed by equation 4.18. On leaving the contact region the lateral string deflection will gradually tend to zero again. Generally a kink will occur in the deflection of the string at the aft contact point because the string has no bending stiffness. The lateral force and self aligning moment applied to the rim can be determined by integrating the lateral tyre deflection of the string with respect to the rim or by considering the forces acting on the part of the string in contact with the road.

The retardational behaviour of points on the ground contact line (trailing the leading contact point), poses mathematical difficulties which limit the general usage of the stretched string model in shimmy stability analysis studies. Nevertheless it is possible to obtain analytical expressions for the forces and moments developed by the tyre in response to prescribed motions of the rim. Higuchi determined analytical expressions for various step responses of the tyre [18]. Segel derived analytical expressions for the transfer functions of the stretched string tyre model [43], [37]. These transfer functions read:

$$H_{F_y,\alpha}(s) = c_c \left(\frac{2(\sigma+a)}{\frac{s}{V}} - \left(1 + \frac{\sigma\frac{s}{V}-1}{\sigma\frac{s}{V}+1} e^{-2a\frac{s}{V}} \right) \frac{1}{\left(\frac{s}{V}\right)^2} \right) \tag{4.19}$$

$$H_{M_z,\alpha}(s) = -c_c \left(\frac{a\left(1+e^{-2a\frac{s}{V}}\right) + \frac{s}{V}\left(1-e^{-2a\frac{s}{V}}\right)\left(\sigma(\sigma+a) - \left(\frac{s}{V}\right)^{-2}\right)}{\left(\sigma\frac{s}{V}+1\right)\left(\frac{s}{V}\right)^2} \right) \tag{4.20}$$

$$H_{F_y,\phi}(s) = c_c \left(\frac{2(\sigma+a)}{\left(\frac{s}{V}\right)^2} - \left(1 + \frac{\sigma\frac{s}{V}-1}{\sigma\frac{s}{V}+1} e^{-2a\frac{s}{V}} \right) \frac{\sigma+a+\left(\frac{s}{V}\right)^{-1}}{\left(\frac{s}{V}\right)^2} \right) \tag{4.21}$$

$$H_{M_z,\phi}(s) = c_c \left(\frac{2a\left(\sigma(\sigma+a)+\frac{1}{3}a^2\right)}{\frac{s}{V}} \right) + H_{M_z,\alpha}(s) \left(\sigma + a + \left(\frac{s}{V}\right)^{-1} \right) \tag{4.22}$$

The following relations can be obtained when considering steady-state side slip conditions; under these conditions the ground contact line will be straight:

$$\left. \begin{array}{lcl} C_{f\alpha} & = & 2c_c\,(\sigma+a)^2 \\ C_{m\alpha} & = & -2c_c a\left(\sigma\,(\sigma+a)+\frac{1}{3}a^2\right) \end{array} \right\} \tag{4.23}$$

Assuming $\sigma = 3a$ the corresponding pneumatic trail would read $\frac{37}{48}a \approx 0.77a$.

To allow time domain simulation of the stretched string tyre attached to a flexible structure, Sharp developed a discretised string model with about 50 elements in the contact region [44]. This approach may still be considered as being nearly exact; other researchers have used different methods to simplify the mathematics involved. In particular their aim has been to obtain a set of differential equations with constant coefficients; this allows the application of standard stability calculation methods like the eigenvalue analysis. A number of approximations to the stretched string tyre model will now be discussed.

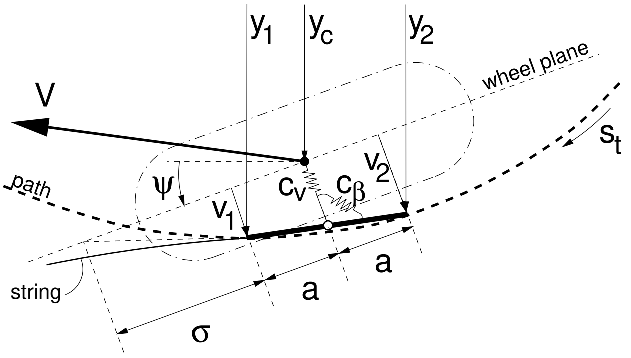

Fig. 4.7: The Von Schlippe approximation (top view).

Von Schlippe

In the Von Schlippe approximation the contact line is considered to be a straight line connecting the leading and aft contact point, see figure 4.7. Due to the retardational (non-sliding) behaviour, the lateral position of the aft contact point will be identical to the leading contact point, once the tyre has moved a distance $2a$ forward. In the time domain this equation becomes:

$$y_2(t) = y_1\left(t - \frac{2a}{V}\right) \tag{4.24}$$

The lateral force and self aligning moment can be determined from the deflection of the contact patch with respect to the wheel plane:

$$\left.\begin{array}{rcccl} F_y & = & c_v\left(\dfrac{v_1+v_2}{2}\right) & = & c_v\left(\dfrac{y_1+y_2}{2} - y_c\right) \\ M_z & = & c_\beta\left(\dfrac{v_1-v_2}{2a}\right) & = & c_\beta\left(\dfrac{y_1-y_2}{2a} - \psi\right) \end{array}\right\} \tag{4.25}$$

In these equations c_v and c_β represent the lateral and yaw stiffnesses of the centre of the contact patch with respect to the rim. For a straight contact line, the relation with the distributed stiffness carcass stiffness c_c of the stretched string is given by:

$$\left.\begin{array}{rcl} c_v & = & 2c_c\,(\sigma + a) \\ c_\beta & = & 2c_c a\left(\sigma(\sigma+a) + \frac{1}{3}a^2\right) \end{array}\right\} \tag{4.26}$$

The lateral position of the leading contact point is governed by equation 4.18. Combined with equations 4.23 to 4.26 the transfer functions can be determined:

$$H_{F_y,\alpha}(s) = C_{f\alpha}\left(\frac{2\sigma\frac{s}{V}+1-e^{-\frac{2as}{V}}}{2(\sigma+a)(\sigma\frac{s}{V}+1)\frac{s}{V}}\right) \tag{4.27}$$

$$H_{M_z,\alpha}(s) = C_{m\alpha}\left(\frac{1-e^{-\frac{2as}{V}}}{2a(\sigma\frac{s}{V}+1)\frac{s}{V}}\right) \tag{4.28}$$

$$H_{F_y,\phi}(s) = C_{f\alpha}\left(\frac{(\sigma-a)\frac{s}{V}+1-\left(1+(\sigma+a)\frac{s}{V}\right)e^{-\frac{2as}{V}}}{2(a+\sigma)(\sigma\frac{s}{V}+1)\left(\frac{s}{V}\right)^2}\right) \tag{4.29}$$

$$H_{M_z,\phi}(s) = C_{m\alpha}\left(\frac{-2a\sigma\left(\frac{s}{V}\right)^2+(\sigma-a)\frac{s}{V}+1-\left(1+(\sigma+a)\frac{s}{V}\right)e^{-\frac{2as}{V}}}{2a(\sigma\frac{s}{V}+1)\left(\frac{s}{V}\right)^2}\right) \tag{4.30}$$

Smiley

Smiley made an extensive overview of the different tyre models used in shimmy analyses and developed a summary theory [46], which will be discussed here. If equation 4.18 is transformed to the distance domain, we obtain:

$$\sigma\frac{dy_1}{ds_t}+y_1 = y_c+(\sigma+a)\,\psi \tag{4.31}$$

Smiley uses a Taylor series to approximate the lateral position of the centre of the contact patch y_0. The following relations can be obtained:

$$y_1 = y_0+a\frac{dy_0}{ds_t}+\frac{a^2}{2!}\frac{d^2y_0}{ds_t^2}+\dots \tag{4.32}$$

$$\frac{dy_1}{ds_t} = \frac{dy_0}{ds_t}+a\frac{d^2y_0}{ds_t^2}+\frac{a^2}{2!}\frac{d^3y_0}{ds_t^3}+\dots \tag{4.33}$$

The following generic formula can be obtained when substituting these series in 4.31:

$$\sum_{i=1}^{n}\frac{(n\sigma+a)a^{n-1}}{n!}\cdot\frac{d^ny_0}{ds_t^n}+y_0 = y_c+(\sigma+a)\,\psi \tag{4.34}$$

The expressions for the lateral force and self aligning torque read:

$$\left.\begin{array}{rcl} F_y & = & c_v\,(y_0-y_c) \\ M_z & = & c_\beta\left(\dfrac{dy_0}{ds_t}-\psi\right) \end{array}\right\} \tag{4.35}$$

It can be noted that the tyre is reduced to a single ground contact point; its position and orientation are governed by 4.34. Once these are known, the lateral force and self aligning moment can be calculated easily from the deflection with respect to the wheel plane (equation. 4.35).

An obvious question is the required order of the Taylor expansion to achieve sufficient accuracy. In his paper Smiley suggests using $n = 3$ when the shimmy wavelength is larger than four times the tyre radius. This value is also used in a recent paper by Krabacher

[26]; confusing is the fact that the model is referred to as ”Von Schlippe”. The transfer functions for this particular case ($n = 3$) read:

$$H_{F_y,\alpha}(s) = C_{f\alpha}\left(\frac{a^2\left(\frac{3\sigma+a}{6(\sigma+a)}\right)\left(\frac{s}{V}\right)^2 + a\left(\frac{2\sigma+a}{2(\sigma+a)}\right)\frac{s}{V} + 1}{a^2\left(\frac{3\sigma+a}{6}\right)\left(\frac{s}{V}\right)^3 + a\left(\frac{2\sigma+a}{2}\right)\left(\frac{s}{V}\right)^2 + (\sigma+a)\frac{s}{V} + 1}\right) \tag{4.36}$$

$$H_{M_z,\alpha}(s) = C_{m\alpha}\left(\frac{1}{a^2\left(\frac{3\sigma+a}{6}\right)\left(\frac{s}{V}\right)^3 + a\left(\frac{2\sigma+a}{2}\right)\left(\frac{s}{V}\right)^2 + (\sigma+a)\frac{s}{V} + 1}\right) \tag{4.37}$$

$$H_{F_y,\phi}(s) = C_{f\alpha}\left(\frac{a^2\left(\frac{3\sigma+a}{6(\sigma+a)}\right)\frac{s}{V} + a\left(\frac{2\sigma+a}{2(\sigma+a)}\right)}{a^2\left(\frac{3\sigma+a}{6}\right)\left(\frac{s}{V}\right)^3 + a\left(\frac{2\sigma+a}{2}\right)\left(\frac{s}{V}\right)^2 + (\sigma+a)\frac{s}{V} + 1}\right) \tag{4.38}$$

$$H_{M_z,\phi}(s) = -C_{m\alpha}\left(\frac{a^2\left(\frac{3\sigma+a}{6}\right)\left(\frac{s}{V}\right)^2 + a\left(\frac{2\sigma+a}{2}\right)\frac{s}{V}}{a^2\left(\frac{3\sigma+a}{6}\right)\left(\frac{s}{V}\right)^3 + a\left(\frac{2\sigma+a}{2}\right)\left(\frac{s}{V}\right)^2 + (\sigma+a)\frac{s}{V} + 1}\right) \tag{4.39}$$

Pacejka

The exponential function occurring in the transfer functions of Segel or the Von Schlippe approximation can be developed in a Taylor series:

$$e^{-\frac{2as}{V}} = 1 - \frac{2as}{V} + \frac{1}{2}\left(\frac{2as}{V}\right)^2 + \cdots + \frac{1}{n!}\left(\frac{-2as}{V}\right)^n \tag{4.40}$$

The transfer functions of the straight tangent approximation are obtained when substituting the exponential functions in the transfer functions of either Segel or Von Schlippe with the $n = 1$ Taylor approximation, as was done by Pacejka [35]. The transfer functions of the straight tangent tyre model are given by equations 4.9 to 4.12.

Pacejka also developed a parabolic approximation by including one additional coefficient in the Taylor expansion ($n = 2$) and using the transfer functions obtained by Segel. The corresponding differential equations read [37]:

$$\left.\begin{aligned}
\frac{\sigma}{V}\dot{F}_y + F_y &= C_{f\alpha}\left(\psi - \frac{a}{V}\dot{\psi} - \frac{1}{V}\dot{y}_c + \left(\frac{a}{V(\sigma+a)}\right)^2\left(\sigma + \frac{2}{3}a\right)\left((\sigma+a)\ddot{\psi} + \ddot{y}_c\right)\right)\\
\frac{\sigma}{V}\dot{M}_z + M_z &= C_{m\alpha}\left(\psi - \frac{a}{V}\dot{\psi} - \frac{1}{V}\dot{y}_c + \frac{a}{V^2}\left((\sigma+a)\ddot{\psi} + \ddot{y}_c\right)\right)
\end{aligned}\right\} \tag{4.41}$$

It can be noticed that if we omit the second derivatives with respect time on the right hand side of this equation again the equations for the straight tangent tyre model are obtained. The transfer functions of the parabolic approximation read:

$$H_{F_y,\alpha}(s) = C_{f\alpha}\left(\frac{-\frac{s}{V}\left(\sigma + \frac{2}{3}a\right)\left(\frac{a}{\sigma+a}\right)^2 + 1}{\sigma\frac{s}{V} + 1}\right) \tag{4.42}$$

$$H_{M_z,\alpha}(s) = C_{m\alpha}\left(\frac{-a\frac{s}{V} + 1}{\sigma\frac{s}{V} + 1}\right) \tag{4.43}$$

$$H_{F_y,\phi}(s) = C_{f\alpha}\left(\frac{a - \frac{a^2}{\sigma+a}\left(\sigma + \frac{2}{3}a\right)\left(\frac{s}{V} + \frac{1}{\sigma+a}\right)}{\sigma\frac{s}{V} + 1}\right) \tag{4.44}$$

$$H_{M_z,\phi}(s) = -C_{m\alpha}\left(\frac{a(\sigma+a)\frac{s}{V}}{\sigma\frac{s}{V}+1}\right) \tag{4.45}$$

Both approximations of Pacejka have a clear geometrical interpretation as shown in figure 4.8. For the parabolic approximation a parabola is used to approximate the string deflection in the ground contact region; the straight tangent approximation only uses the slope in the leading contact point.

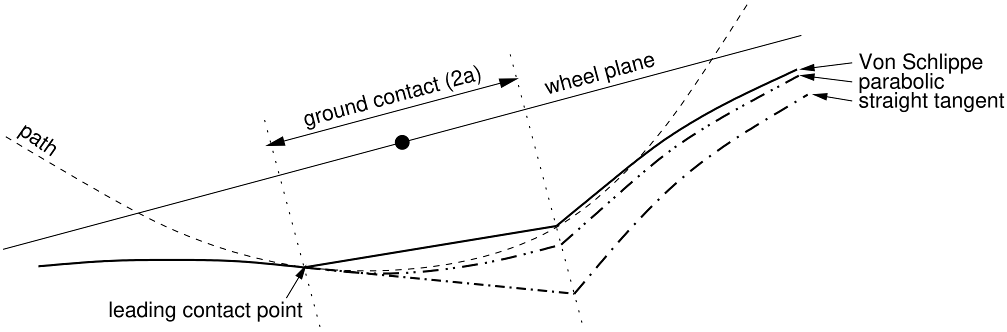

Fig. 4.8: Three approximations to the string deflection (top view).

Kluiters

In his shimmy analysis Kluiters used the Von Schlippe approach, but replaced the pure time delay of the aft contact point (equation 4.24) with a Padé filter [23]. Kluiters made the observation that a Padé filter has better convergence properties when approximating the pure time delay compared to the Taylor expansion employed by e.g. Smiley and Pacejka. The general expression for the transfer function of a Padé filter with a time delay τ and order n is:

$$H(s) = \frac{a_0 - a_1\tau s + a_2(\tau s)^2 + \ldots + a_n(-\tau s)^n}{a_0 + a_1\tau s + a_2(\tau s)^2 + \ldots + a_n(\tau s)^n} \tag{4.46}$$

The following (recursive) formula is applicable for the coefficients:

$$a_k = \frac{(n-k+1)}{(2n-k+1)k}a_{k-1}, \quad a_0 = 1, \quad k = 1\ldots n \tag{4.47}$$

Kluiters investigated the required order of the Padé filter and found that for his problem a second order filter ($n = 2$) was sufficient: increasing the order of the filter did not alter the results significantly. The accompanying transfer function then becomes (note: $\tau = \frac{2a}{V}$):

$$H_{y_2,y_1}(s) = \frac{1 - \frac{as}{V} + \frac{1}{3}\left(\frac{as}{V}\right)^2}{1 + \frac{as}{V} + \frac{1}{3}\left(\frac{as}{V}\right)^2} \tag{4.48}$$

Combining this result with equations 4.18, 4.23, 4.25 and 4.26 the following transfer functions can be obtained:

$$H_{F_y,\alpha}(s) = C_{f\alpha}\left(\frac{\frac{1}{3}\frac{a^2\sigma}{(a+\sigma)}\frac{s^2}{V^2} + \frac{a\sigma}{(a+\sigma)}\frac{s}{V} + 1}{\frac{1}{3}a^2\sigma\frac{s^3}{V^3} + (a\sigma + \frac{1}{3}a^2)\frac{s^2}{V^2} + (a+\sigma)\frac{s}{V} + 1}\right) \tag{4.49}$$

$$H_{M_z,\alpha}(s) = C_{m\alpha}\left(\frac{1}{\frac{1}{3}a^2\sigma\frac{s^3}{V^3} + (a\sigma + \frac{1}{3}a^2)\frac{s^2}{V^2} + (a+\sigma)\frac{s}{V} + 1}\right) \tag{4.50}$$

$$H_{F_y,\phi}(s) = C_{f\alpha}\left(\frac{-\frac{1}{3}\frac{a^3}{(a+\sigma)}\frac{s}{V} + \frac{a\sigma}{(a+\sigma)}}{\frac{1}{3}a^2\sigma\frac{s^3}{V^3} + (a\sigma + \frac{1}{3}a^2)\frac{s^2}{V^2} + (a+\sigma)\frac{s}{V} + 1}\right) \tag{4.51}$$

$$H_{M_z,\phi}(s) = -C_{m\alpha}\left(\frac{\frac{1}{3}a^2\sigma\frac{s^2}{V^2} + (a\sigma + \frac{1}{3}a^2)\frac{s}{V}}{\frac{1}{3}a^2\sigma\frac{s^3}{V^3} + (a\sigma + \frac{1}{3}a^2)\frac{s^2}{V^2} + (a+\sigma)\frac{s}{V} + 1}\right) \tag{4.52}$$

Rogers

Initially, Rogers developed an empirical formula to fit measured transfer functions [39]. At a later stage an analytical model was developed based on the stretched string concept, which substantiated the basic assumptions of the empirical model. For a detailed discussion of this analytical model reference is made to [40], only the results will be presented here. Using a Taylor series expansion to approximate the deflection of the string, Rogers arrived at the following set of differential equations:

$$\left.\begin{array}{rcl} \frac{a\sigma}{V^2}\ddot{F}_y + \frac{a+\sigma}{V}\dot{F}_y + F_y & = & C_{f\alpha}\left(\psi - \frac{1}{V}\dot{y}_c - \frac{a\sigma}{(a+\sigma)V^2}\ddot{y}_c\right) \\ \frac{a\sigma}{V^2}\ddot{M}_z + \frac{a+\sigma}{V}\dot{M}_z + M_z & = & C_{m\alpha}\left(\psi + \frac{\varepsilon}{V}\dot{\psi} + \frac{a\sigma}{V^2}\ddot{\psi} - \frac{1}{V}\dot{y}_c\right) \end{array}\right\} \tag{4.53}$$

The parameter ε could not be justified on a theoretical basis using a single stretched string, but was introduced in the equations to improve turn slip behaviour. Using side and turn slip as inputs to the model, the set of transfer functions becomes:

$$H_{F_y,\alpha}(s) = C_{f\alpha}\left(\frac{\frac{a\sigma}{(a+\sigma)}\frac{s}{V} + 1}{a\sigma\frac{s^2}{V^2} + (a+\sigma)\frac{s}{V} + 1}\right) \tag{4.54}$$

$$H_{M_z,\alpha}(s) = C_{m\alpha}\left(\frac{1}{a\sigma\frac{s^2}{V^2} + (a+\sigma)\frac{s}{V} + 1}\right) \tag{4.55}$$

$$H_{F_y,\phi}(s) = C_{f\alpha}\left(\frac{\frac{a\sigma}{a+\sigma}}{a\sigma\frac{s^2}{V^2} + (a+\sigma)\frac{s}{V} + 1}\right) \tag{4.56}$$

$$H_{M_z,\phi}(s) = -C_{m\alpha}\left(\frac{a\sigma\frac{s}{V} + \varepsilon}{a\sigma\frac{s^2}{V^2} + (a+\sigma)\frac{s}{V} + 1}\right) \tag{4.57}$$

It would also be possible to obtain these results, assuming that $\varepsilon = 0$, using the Von Schlippe approximation (equations 4.18, 4.25) and a first order Padé filter ($n = 1$) which replaces equation 4.24:

$$H_{y_2,y_1}(s) = \frac{1 - \frac{as}{V}}{1 + \frac{as}{V}} \tag{4.58}$$

In section 4.4 a detailed comparison will be made between the responses of the various tyre models discussed above.

4.3 Point contact tyre models

In this section two tyre models will be discussed which are not derived from the stretched string model, but are based on the concept of a single contact point.

Keldysh

Keldysh developed a non-stationary tyre model with the aim of preventing shimmy on an aircraft; the tyre model equations presented here were first published in 1945 [22]. Since the publication is in Russian, the Keldysh tyre model has remained relatively unknown for many years in the Western world. The author became aware of the details of this tyre model through the publications of Goncharenko [13], [14].

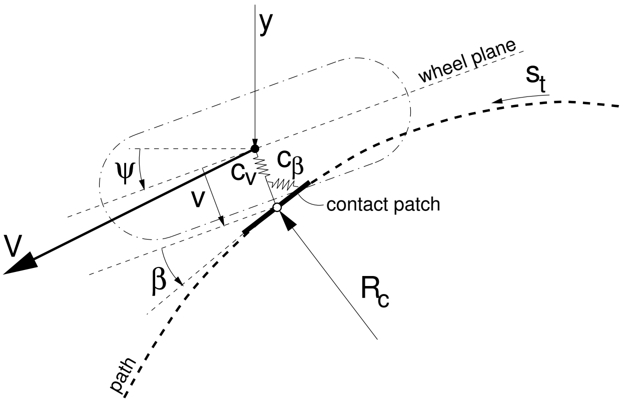

Fig. 4.9: The Keldysh point contact tyre model (top view).

In the tyre model of Keldysh the tyre contact patch has two degrees of freedom with respect to the rim: the lateral degree of freedom v and yaw degree of freedom β, see also figure 4.9. The forces applied on the rim are linear functions of the local deformations:

$$F_y = k_v \dot{v} + c_v v \tag{4.59}$$

$$M_z = k_\beta \dot{\beta} + c_\beta \beta \tag{4.60}$$

No sliding occurs between contact point and road; when assuming small angles the following formula can be obtained:

$$\dot{v} = V(\psi + \beta) - \dot{y}_c = V(\alpha + \beta) \tag{4.61}$$

Path curvature is assumed to be a linear function of lateral deflection and deformation angle of the contact patch and inclination angle of the tyre:

$$\frac{1}{R_c} = \frac{d(\psi + \beta)}{ds_t} = -p_\alpha v - p_\beta \beta + p_\gamma \gamma \tag{4.62}$$

Substituting the equation $s_t = Vt$ results in:

$$\dot{\beta} = V(p_\gamma \gamma - p_\alpha v - p_\beta \beta) - \dot{\psi} \tag{4.63}$$

The following transfer functions can be determined for the Keldysh tyre model:

$$H_{F_y,\alpha}(s) = (c_v + k_v s)\left(\frac{\frac{s}{V} + p_\beta}{\frac{s^2}{V^2} + p_\beta \frac{s}{V} + p_\alpha}\right) \tag{4.64}$$

$$H_{M_z,\alpha}(s) = \left(c_\beta + k_\beta s\right)\left(\frac{-p_\alpha}{\frac{s^2}{V^2} + p_\beta \frac{s}{V} + p_\alpha}\right) \tag{4.65}$$

$$H_{F_y,\phi}(s) = \left(c_v + k_v s\right)\left(\frac{1}{\frac{s^2}{V^2} + p_\beta \frac{s}{V} + p_\alpha}\right) \tag{4.66}$$

$$H_{M_z,\phi}(s) = \left(c_\beta + k_\beta s\right)\left(\frac{\frac{s}{V}}{\frac{s^2}{V^2} + p_\beta \frac{s}{V} + p_\alpha}\right) \tag{4.67}$$

It can be shown that these transfer functions may be equivalent to the model of Rogers (equations 4.54 to 4.57) under the assumption that the damping parameters k_v, k_β, ε and inclination angle γ are equal to zero. The equivalence conditions are:

$$p_\alpha = \frac{1}{a\sigma}, \quad p_\beta = \frac{a+\sigma}{a\sigma}, \quad c_v = \frac{C_{f\alpha}}{a+\sigma}, \quad c_\beta = -C_{m\alpha} \tag{4.68}$$

This is a surprising result: despite following a different approach to modelling the tyre the resulting differential equations may be completely identical.

The model of Keldysh also includes the inclination angle γ; the following transfer functions can be derived:

$$H_{F_y,\gamma}(s) = \left(c_v + k_v s\right)\left(\frac{p_\gamma}{\frac{s^2}{V^2} + p_\beta \frac{s}{V} + p_\alpha}\right) \tag{4.69}$$

$$H_{M_z,\gamma}(s) = \left(c_\beta + k_\beta s\right)\left(\frac{p_\gamma \frac{s}{V}}{\frac{s^2}{V^2} + p_\beta \frac{s}{V} + p_\alpha}\right) \tag{4.70}$$

Considering steady-state operating conditions, some alternative expressions can be derived; they may clarify the nature of the coefficients p_β and p_γ:

$$p_\beta = \frac{C_{f\alpha}}{C_{f\phi}}, \quad p_\gamma = \frac{C_{f\gamma}}{C_{f\phi}} \tag{4.71}$$

Moreland

The first publication of this tyre model appears in the paper "The story of shimmy" by W.J. Moreland in 1954 [32]. Over the years the Moreland tyre model has been quite popular for application in aircraft landing gear shimmy studies (e.g. [2], [3], [15], [28], [29]), though its validity has also been subject of discussion ([12], [39], [46]).

Similar to the model of Keldysh, the contact patch has a lateral v and yaw β degree of freedom with respect to the rim, see figure 4.9. Equations 4.59, 4.60 and 4.61 are applicable; the only exception being that the damping k_β is always taken equal to zero. The main difference with the Keldysh tyre model is that Moreland makes the assumption that the twist angle β responds with some delay to changes in the lateral equilibrium:

$$\dot{\beta} = -\frac{1}{\tau}\left(\frac{F_y}{C_{f\alpha}} + \beta\right) \tag{4.72}$$

In this equation τ is the *tyre time constant*. In the equations presented here the cornering stiffness $C_{f\alpha}$ is used, which is just the inverse of the *tyre yaw coefficient* used by Moreland.

For this tyre model the following transfer functions can be determined (assuming that $C_{m\alpha}$=$-c_\beta$):

$$H_{F_y,\alpha}(s) = C_{f\alpha}\left(\frac{k_v\tau s^2+(k_v+c_v\tau)s+c_v}{\frac{C_{f\alpha}}{V}\tau s^2+(k_v+\frac{C_{f\alpha}}{V})s+c_v}\right) \tag{4.73}$$

$$H_{M_z,\alpha}(s) = C_{m\alpha}\left(\frac{k_v s+c_v}{\frac{C_{f\alpha}}{V}\tau s^2+(k_v+\frac{C_{f\alpha}}{V})s+c_v}\right) \tag{4.74}$$

$$H_{F_y,\phi}(s) = 0 \tag{4.75}$$

$$H_{M_z,\phi}(s) = 0 \tag{4.76}$$

For the self aligning moment a different formula may be used; the lateral force may be applied directly at the pneumatic trail:

$$M_z = -t_p F_y = \left(\frac{C_{m\alpha}}{C_{f\alpha}}\right) F_y \tag{4.77}$$

This formulation, in combination with equations 4.59, 4.61 and 4.72, is known as the *modified Moreland* tyre model. For the modified Moreland tyre model the transfer function of the self-aligning moment with respect to side slip becomes (the other functions remain unchanged):

$$H_{M_z,\alpha}(s) = C_{m\alpha}\left(\frac{k_v\tau s^2+(k_v+c_v\tau)s+c_v}{\frac{C_{f\alpha}}{V}\tau s^2+(k_v+\frac{C_{f\alpha}}{V})s+c_v}\right) \tag{4.78}$$

The Moreland model has always been criticised for the existence of the tyre time constant τ. As was shown with the stretched string model tyre behaviour is essentially path dependent, so the apparent tyre time constant must be a function of the forward velocity. Figure 4.10 gives an overview of Moreland tyre time constants used by a number of researchers; it is obvious from this graph that a wide range of values is being used and apparently it is difficult to determine this parameter experimentally. A similar graph was presented in reference [12].

An interesting result can be obtained when both the tyre time constant τ and lateral tyre damping k_v are taken equal to zero. When $a = 0$ and $\sigma = C_{f\alpha}/c_v$ are introduced for the straight tangent tyre model, it appears that the Moreland and straight tangent tyre model have identical transfer functions. The Moreland tyre model will still show phase lag, despite the fact that the tyre time constant is equal to zero. So the name *tyre time constant* appears to be misleading since it does not reflect the actual (first order) time constant in the force and moment response with respect to side slip variations.

The Moreland and Keldysh tyre models are very similar, apart from the expression for the time derivative of the twist angle β, equations 4.63 and 4.72. The Keldysh model includes contributions of the inclination angle γ and yaw velocity of the wheel $\dot\psi$, which are absent in the Moreland model. Under the restrictions that γ, $\dot\psi$, k_v and k_β are all zero, we may write:

$$\dot\beta = -V(p_\alpha v + p_\beta \beta) = -\frac{1}{\tau}\left(\frac{c_v v}{C_{f\alpha}}+\beta\right) \tag{4.79}$$

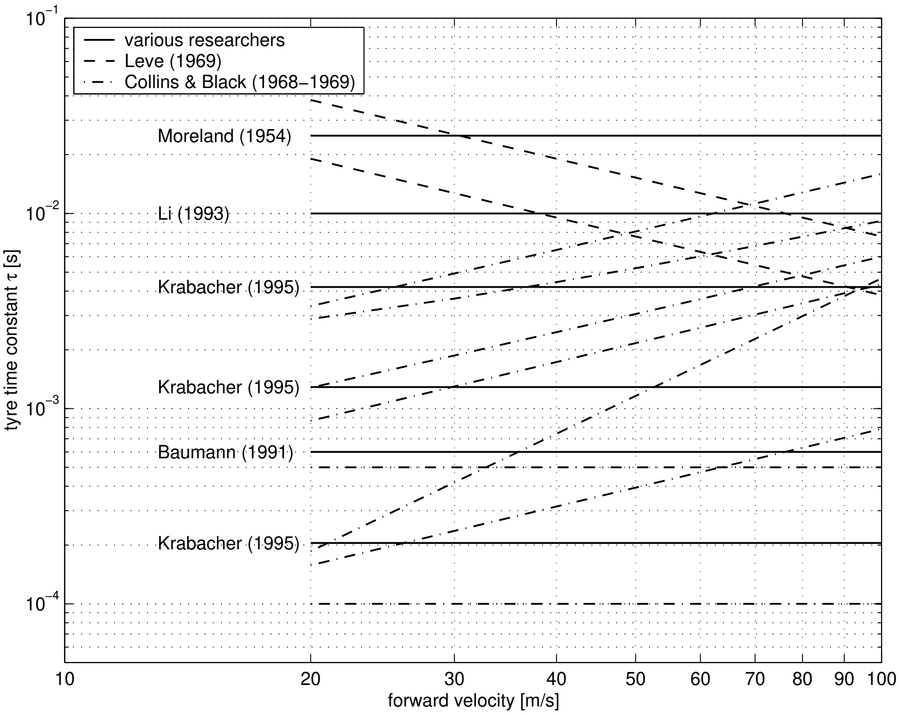

Fig. 4.10: Values for the tyre time constant τ of the Moreland model (based on references [2], [7], [8], [26], [28], [29], [32]).

The aim is to find a value for the tyre time constant τ, which would provide identical results for the Moreland model and Keldysh model, given the restrictions concerning damping and wheel motion. Equation 4.79 results in two conditions for the tyre time constant τ:

$$\left.\begin{aligned} \tau &= \frac{1}{Vp_\beta} \\ \tau &= \frac{c_v}{C_{f\alpha}Vp_\alpha} \end{aligned}\right\} \tag{4.80}$$

It remains unclear if both conditions can be satisfied at the same time. Equation 4.68 provides equivalence conditions between the Keldysh and Rogers tyre models; after substitution of p_α and p_β in equation 4.80 it appears that only one equation remains for the tyre time constant:

$$\tau = \frac{a\sigma}{(a+\sigma)V} \tag{4.81}$$

Using this value for the tyre time constant will give an identical response of the Rogers and Moreland tyre models under the absence of tyre damping and turn slip. This can also be verified directly by substituting equation 4.81 in the expressions for the transfer functions (equations 4.73, 4.74) and additionally using the expressions for the stiffnesses c_v and c_β from equation 4.68; then the transfer functions of Rogers will be obtained (equation 4.54 and 4.55). Equation 4.81 requires the tyre time "constant" not only to be a function of the forward velocity V, but also of the relaxation length σ and contact length a. In the available literature only Leve makes τ inversely proportional to the forward velocity [28], other researchers opting for a constant value or τ increasing with forward velocity.

4.4 Model comparison

Various tyre models have been introduced in the previous sections. A schematic overview is given in figure 4.11, which shows the relations between these tyre models. Another important classification can be made by considering the additional number of states, which are required by the tyre model when a state space description of the mechanical system is used:

- one additional state: straight tangent, Moreland ($\tau = 0$)
- two additional states: parabolic, Rogers, Keldysh, (modified) Moreland
- three additional states: Smiley ($n = 3$), Kluiters ($n = 2$)

Using this classification may be interesting to observe if introducing more states improves the accuracy of the tyre model.

In this section a number of comparisons will be made; in order to limit the number of variants to be studied, only path dependent behaviour will be considered. This implies that damping coefficients k_v, k_β and the tyre time constant τ of the Moreland model are assumed to be zero. Path dependent behaviour can also be obtained for the Moreland tyre model by using equation 4.81, but then the response to side slip will be identical to the model of Rogers. Lacking experimental data on the Keldysh tyre model it is assumed that the equivalence conditions (equation 4.68) apply. The turn slip coefficient ε of the model of Rogers is taken equal to zero; under these assumptions the models of Keldysh and Rogers are equivalent. The Moreland and modified Moreland model will have identical behaviour, because the tyre time constant τ is taken equal to zero.

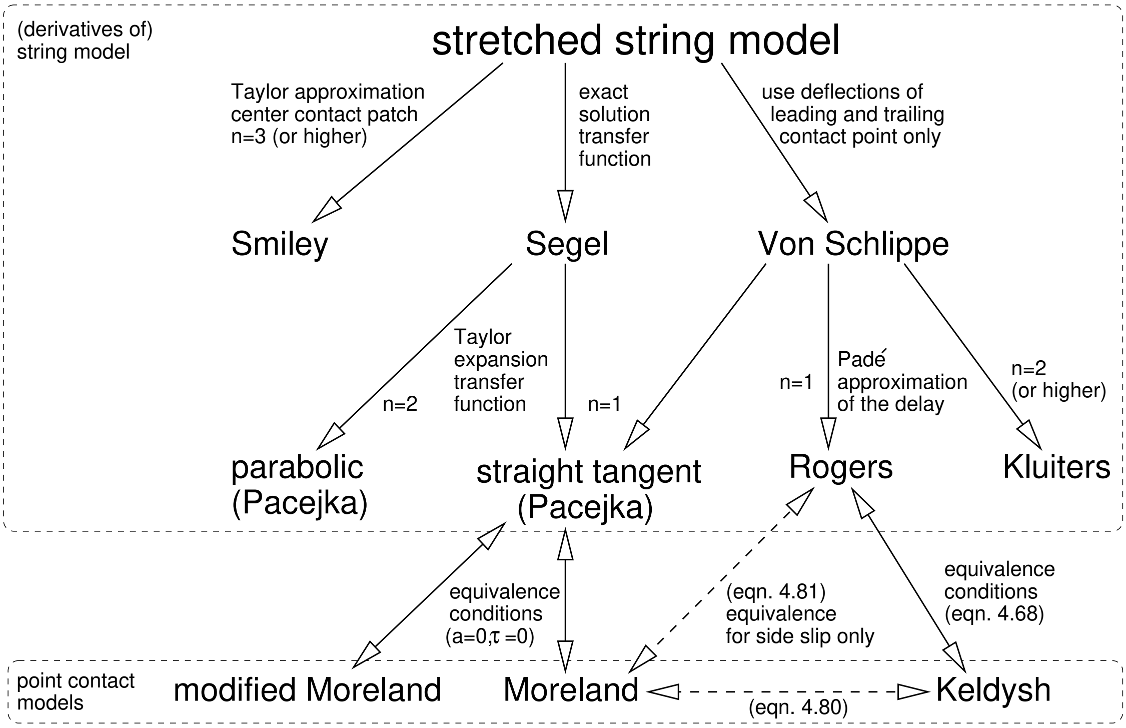
(derivatives of) string model
stretched string model
Taylor approximation center contact patch n=3 (or higher)
exact solution transfer function
use deflections of leading and trailing contact point only
Smiley
Segel
Von Schlippe
Taylor expansion transfer function
n=2
n=1
n=1
Padé approximation of the delay
n=2 (or higher)
parabolic (Pacejka)
straight tangent (Pacejka)
Rogers
Kluiters
equivalence conditions (a=0,τ =0)
(eqn. 4.81) equivalence for side slip only
equivalence conditions (eqn. 4.68)
point contact models
modified Moreland
Moreland
(eqn. 4.80)
Keldysh

Fig. 4.11: Schematic overview of tyre models.

Transfer functions

The transfer functions of the lateral tyre force F_y and self-aligning moment M_z are given for side slip, turn slip and pure yaw excitation of the tyre, see figures 4.12, 4.13 and 4.14 respectively. From the graphs it can be observed that for side slip and yaw all models will have the same steady-state response ($a/\lambda \leq 0.01$). This is not the case for turn slip. The lateral force response of the Moreland model with respect to turn slip excitation is always equal to zero; the steady state turn slip responses of some of the other tyre models are different. Following the adopted sign convention, the steady state coefficient $C_{m\phi}$ should be positive for a regular tyre (see equation 4.6). For most tyre models presented here, with the tread width effect disregarded, the steady state response of the self aligning moment with respect to turn slip is zero and thus $C_{m\phi} = 0$. The behaviour of the self aligning moment of the straight tangent tyre model with respect to turn slip is rather different. For steady state conditions a negative value is obtained. This may result in unexpected behaviour for some specific simulation conditions when turn slip is dominant.

In the neighbourhood of $a/\lambda \approx 0.1$ a dip occurs in the amplitude of the self aligning moment response with respect to yaw, see figure 4.14. The existence of this dip has been verified experimentally. A test can be performed on a drum using sinusoidal steering input signals with a fixed low frequency (e.g. 1 to 3 Hz) and constant steering amplitude; different wavelengths can be obtained by varying the drum angular velocity. A complete description of the test set-up and experimental results can be found in ref. [20]. From the graphs of figure 4.14 it is obvious that the ”simpler” tyre models, straight tangent and Moreland, are not capable of describing this dip; the assumption of a constant pneumatic trail does no longer hold.

For short wavelengths ($a/\lambda > 0.1$) the behaviour of the various models is different, particularly the response to yaw. If our aim is to use differential equations with constant coefficients to describe the dynamic tyre behaviour, then the approach of Kluiters provides a very good match to the exact (Segel) and Von Schlippe approximation up to fairly short wavelengths.

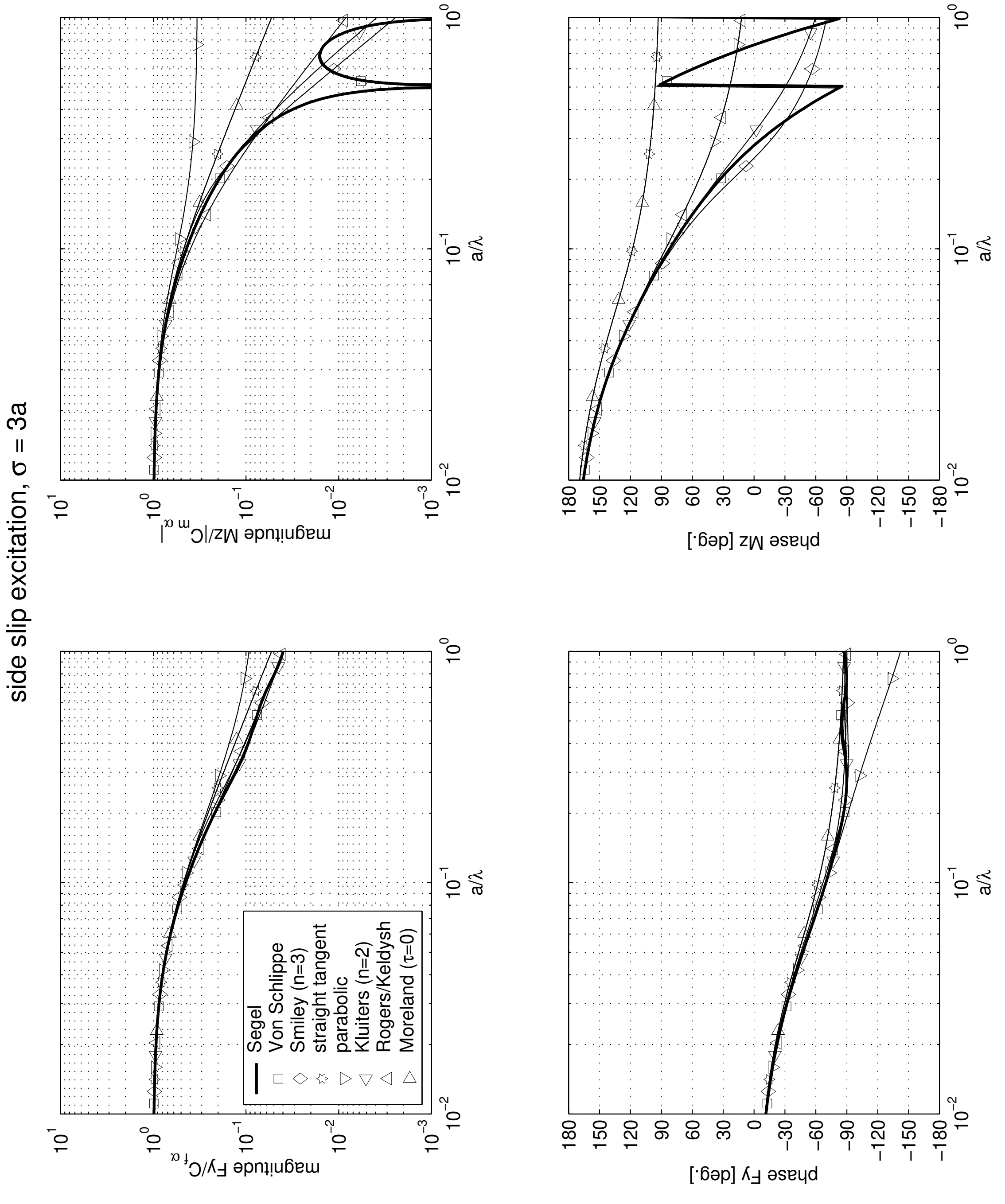

Fig. 4.12: Transfer functions of the lateral force F_y and self aligning moment M_z for various linear tyre models with respect to side slip.

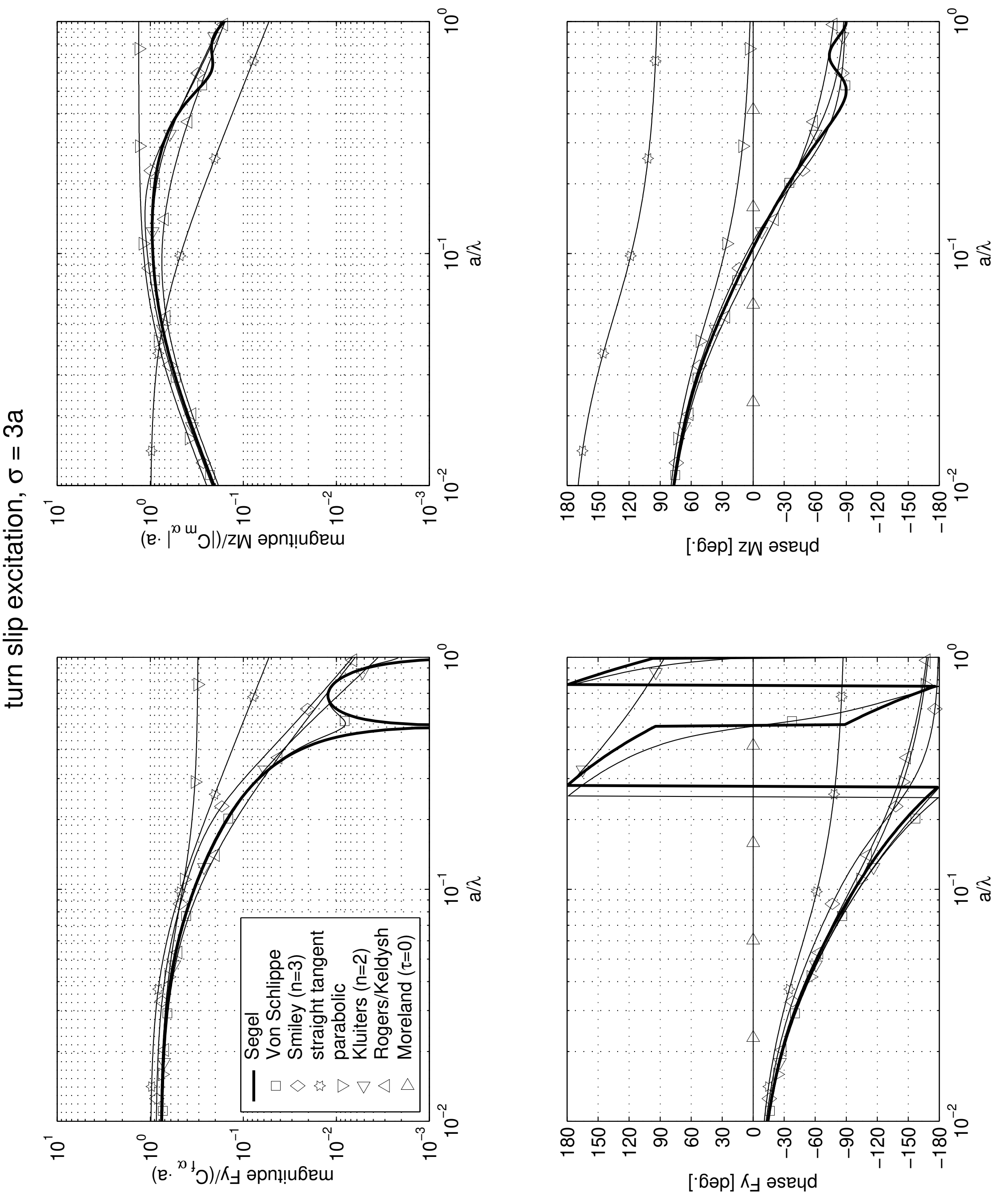

Fig. 4.13: Transfer functions of the lateral force F_y and self aligning moment M_z for various linear tyre models with respect to turn slip.

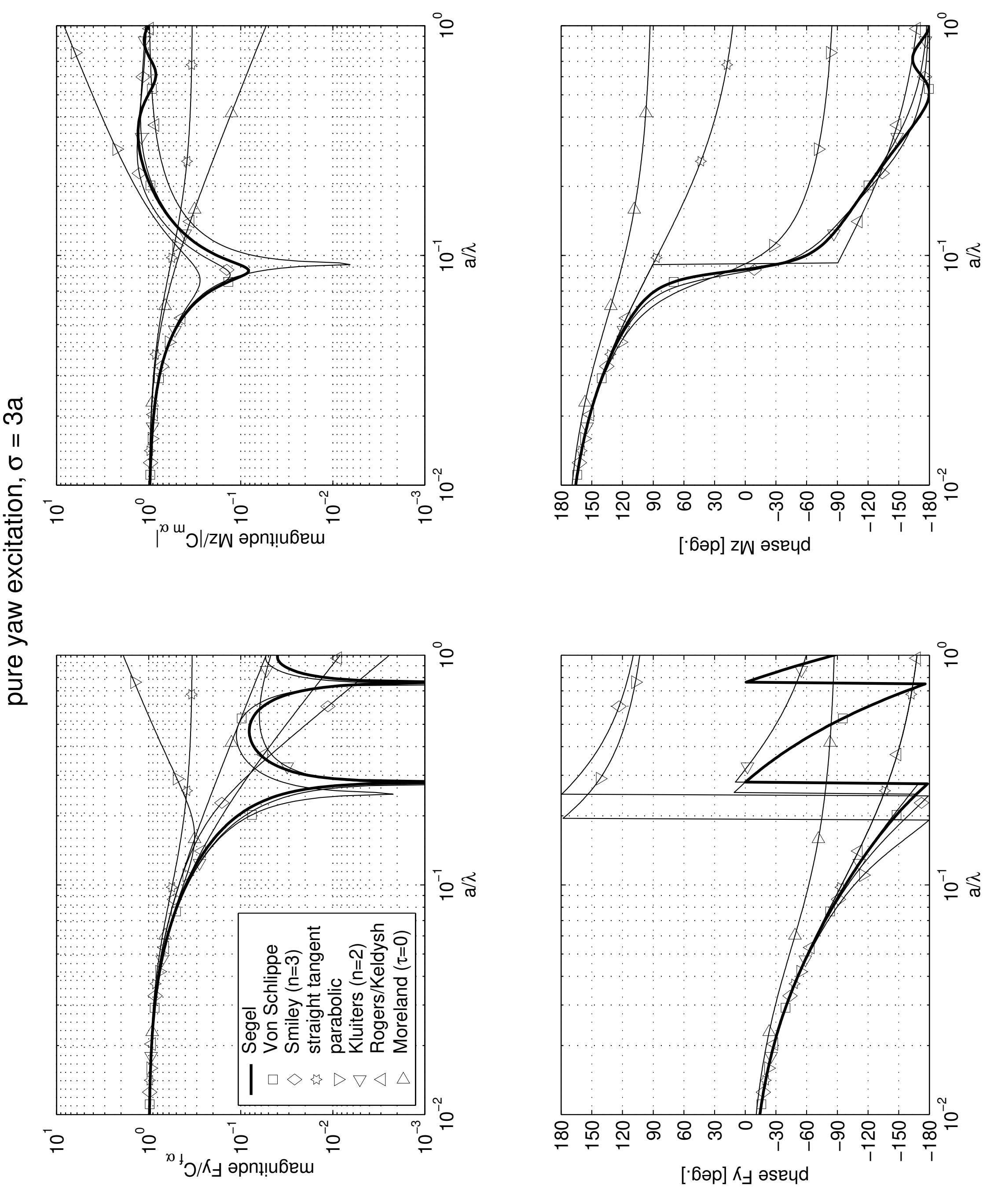

Fig. 4.14: *Transfer functions of the lateral force F_y and self aligning moment M_z for various linear tyre models with respect to pure yaw.*

Step response

The response of the various tyre models has been calculated with respect to three different step inputs: a step in side slip, turn slip and yaw angle. In the graphs the step is applied when the travelled distance equals zero. The results for a step in side slip are given in figures 4.15 and 4.16. From figure 4.15 it is obvious that response of the lateral force F_y of the different tyre models is hardly different. For the self aligning moment M_z two groups can be distinguished: for the models having a constant pneumatic trail the shape of the curve is identical to the lateral force response. The other models display an increased lag with respect to the step input and the slope of M_z on application of the step in side slip is zero.

It is important to note that the additional delay in the self aligning moment M_z is dependent on the relative magnitude of the relaxation length with respect to the contact length. For aircraft tyres the relaxation length may be in the order of three times half the contact length ($\sigma \approx 3a$), whereas for a passenger car tyre the relaxation length may be in excess of ten times half the contact length ($\sigma > 10a$). Consequently the additional M_z delay phenomenon is clearly visible for aircraft tyres, see figures 4.21 and 4.22, but for passenger car tyres this phenomenon may be hardly noticeable, as is illustrated by figure 4.23. Furthermore the experimental data confirms that the first order delay of the lateral force F_y on a step in side slip is correct.

The results for a step in turn slip are given in figures 4.17 and 4.18. As already noted before, the Moreland tyre model has zero response to turn slip and the steady-state values of the some of the models are different. From theoretical considerations and measurements, see figure 4.23, it appears that under steady-state turn slip conditions a positive moment should be generated. So one has to conclude that none of the models discussed so far is capable of describing this condition accurately.

In figures 4.19 and 4.20 the lateral force F_y and self aligning moment M_z to a step in yaw is given. From these graphs it is obvious that the responses of both Moreland and straight tangent are clearly different from the other models, in particular immediately after application of the step input. From a physical point of view the response of the self aligning moment M_z of the Von Schlippe model appears to be quite plausible. The assumption is made that no sliding of the contact points with respect to the road occurs. Then the application of a step in yaw angle on the rim will result in the same deflection of the contact patch with respect to the rim. The yaw stiffness of the contact patch with respect to the rim equals the self aligning stiffness, so on application of the step we may expect the full steady-state moment to be present. As the tyre rolls forward some relaxation phenomena occur in the contact patch area leading to a successive decrease and increase of the moment, before the steady-state condition is reached again.

The experimental results, as shown in figure 4.23, confirm that the response of the lateral force F_y on a step in yaw has a small delay with respect to the step response on side slip. The measured response of the self aligning moment M_z on a step in yaw shows the same trends a the theoretical models, though the initial peak is clearly different from the steady state value.

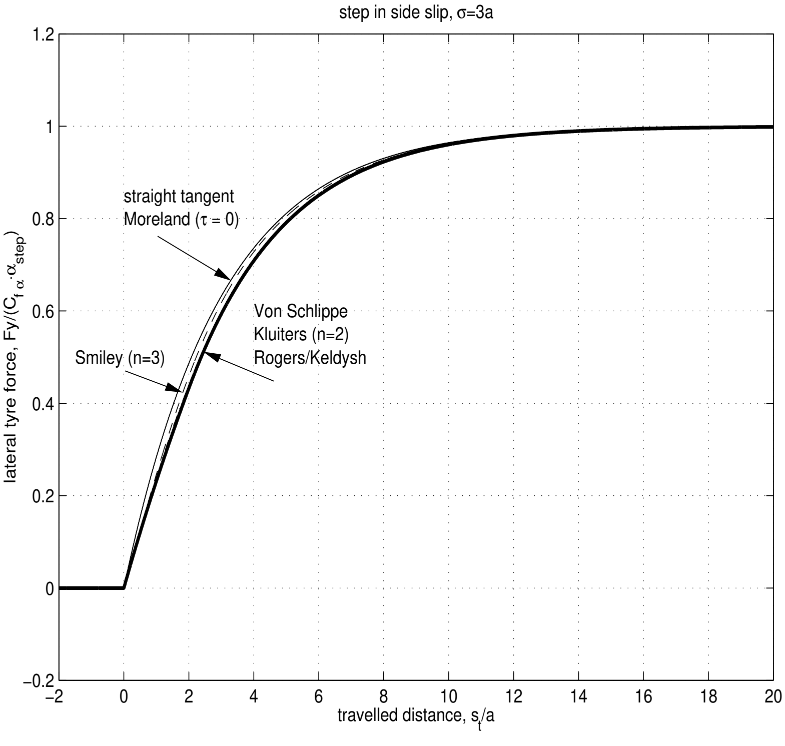

Fig. 4.15: Step response of lateral tyre force F_y to side slip (σ=3a).

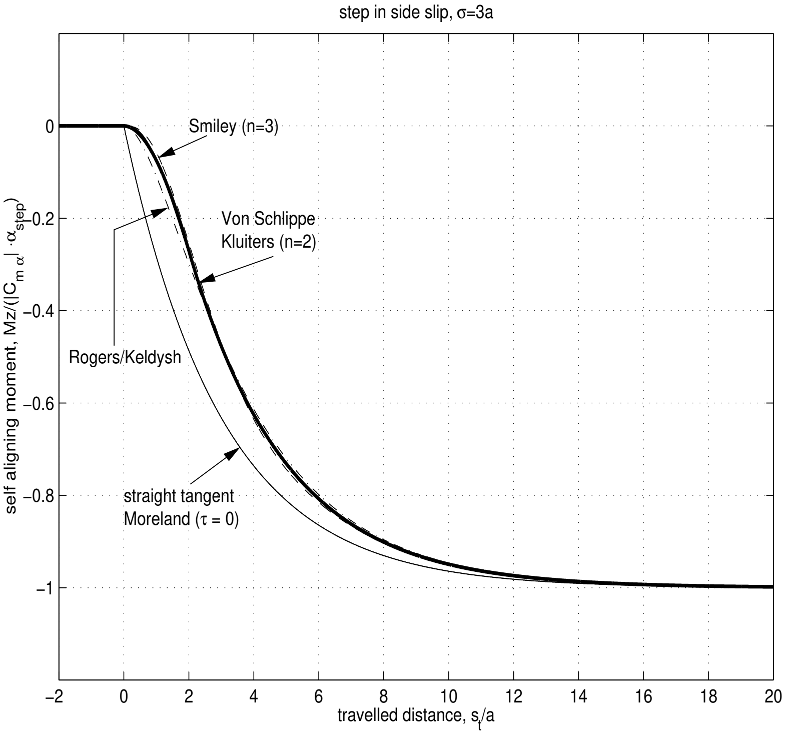

Fig. 4.16: Step response of self aligning moment M_z to side slip (σ=3a).

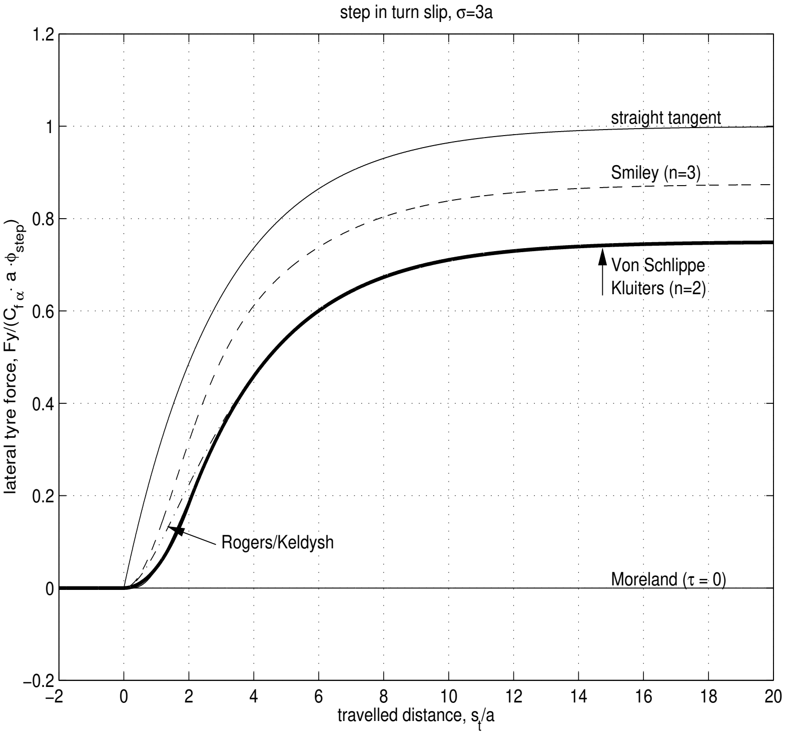

Fig. 4.17: Step response of lateral tyre force F_y to turn slip (σ=3a).

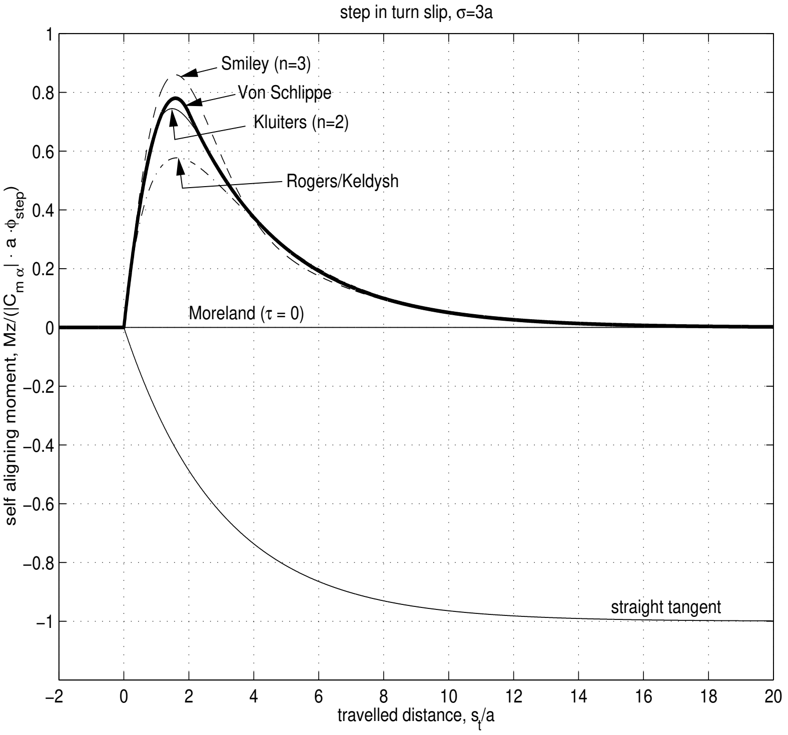

Fig. 4.18: Step response of self aligning moment M_z to turn slip (σ=3a).

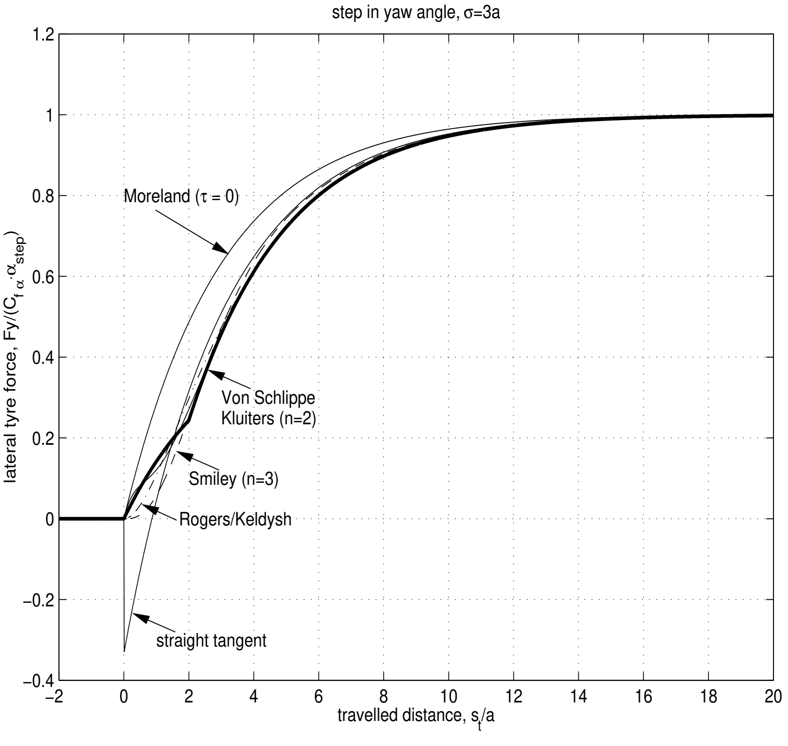

Fig. 4.19: Step response of lateral tyre force F_y to yaw (σ=3a).

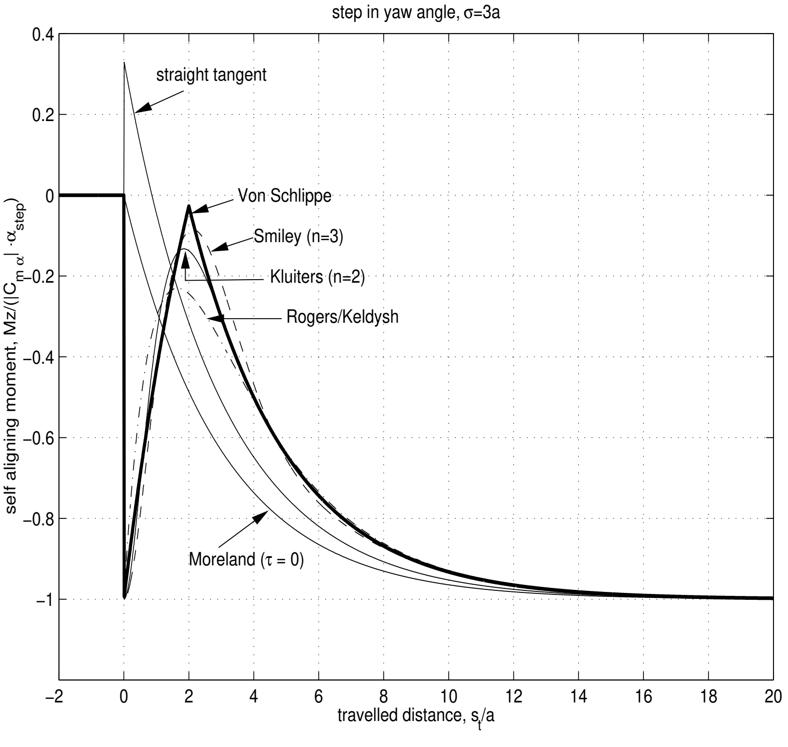

Fig. 4.20: Step response of self aligning moment M_z to yaw (σ=3a).

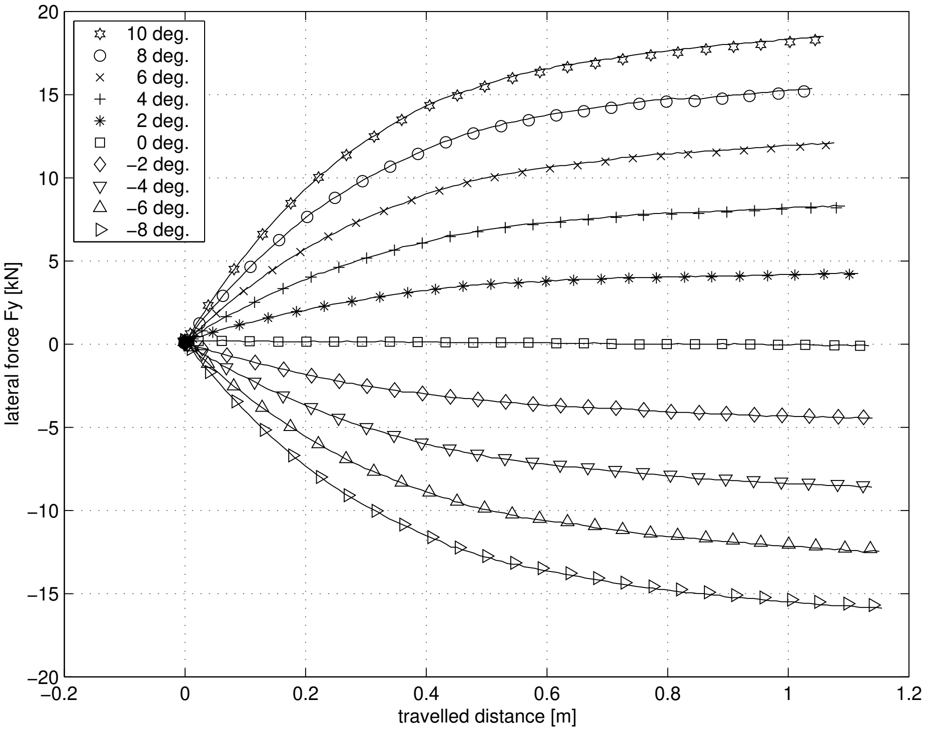

Fig. 4.21: Measured step response of lateral tyre force F_y on various side slip angles (F_z=35 kN, data provided by the Michelin Aircraft Tire Corporation).

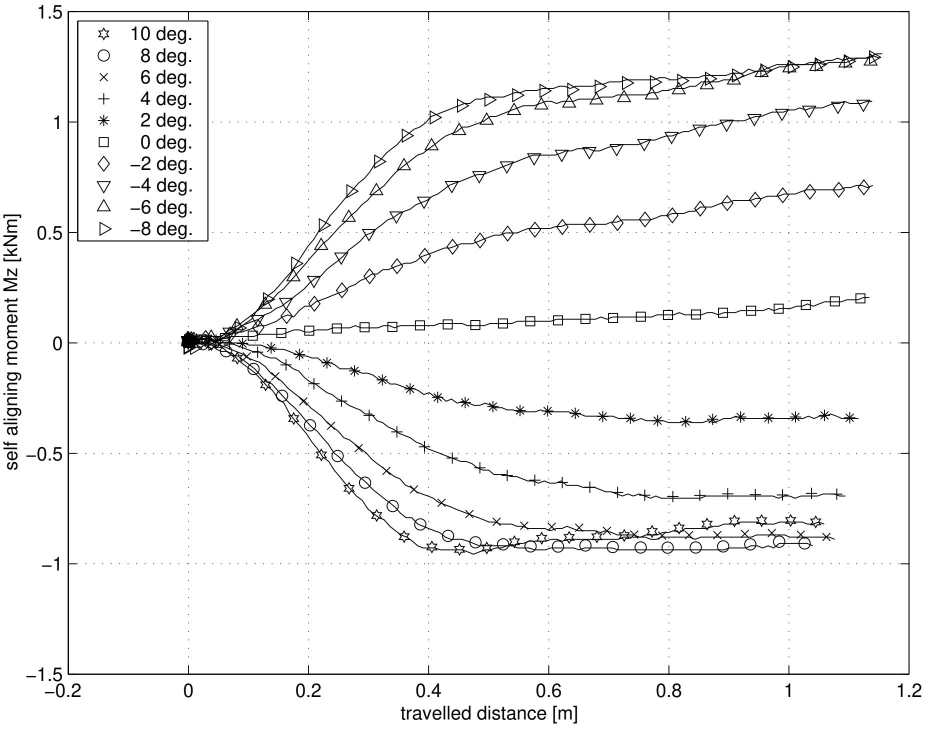

Fig. 4.22: Measured step response of self aligning moment M_z on various side slip angles (F_z=35 kN, data provided by the Michelin Aircraft Tire Corporation).

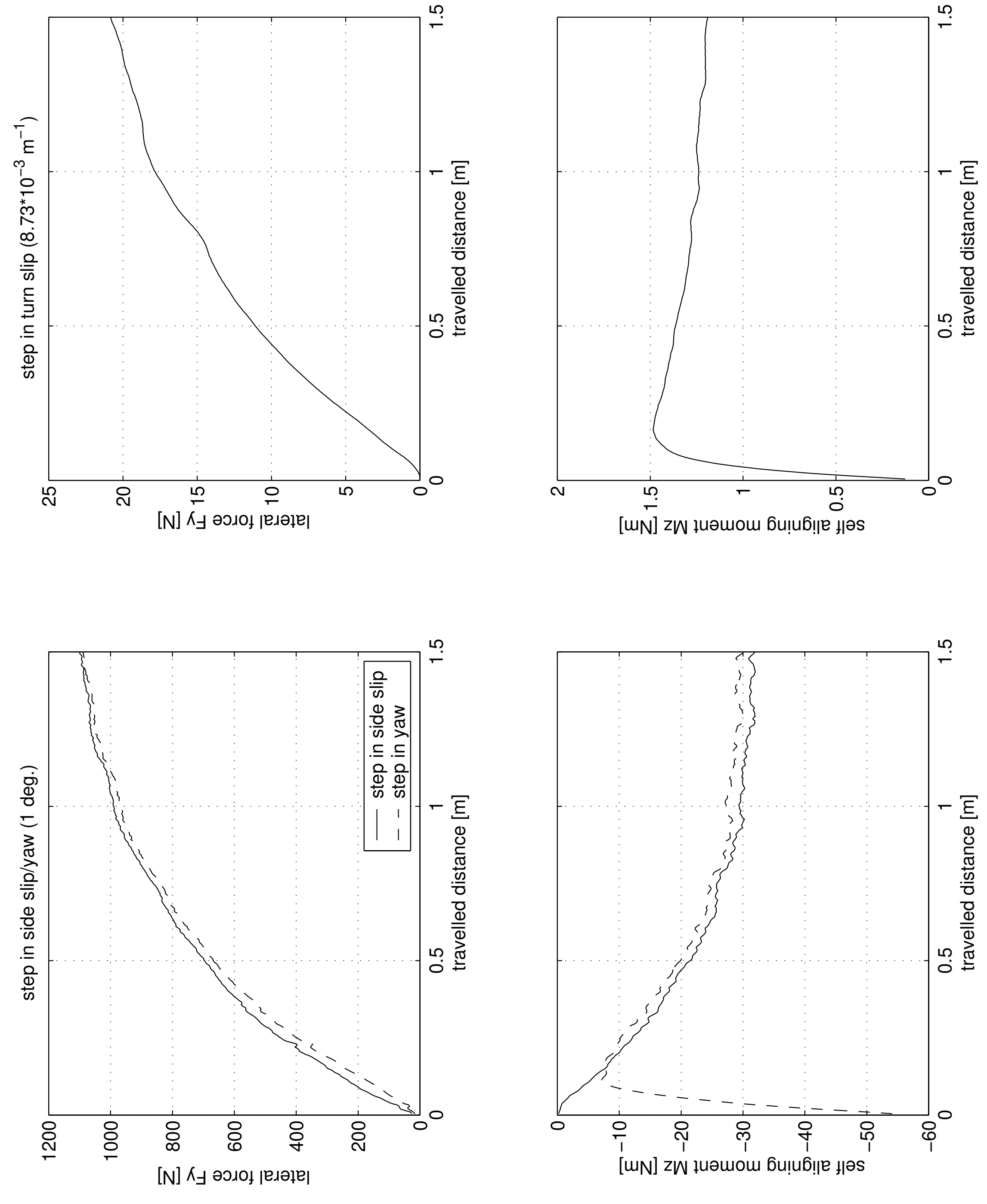

Fig. 4.23: Measured step responses of a passenger car tyre; results for turn slip were obtained by integration of the measured impulse response (F_z=4 kN, data provided by Akira Higuchi [18]).

Energy

In section 2.3 the energy balance for a single tyre was considered. Sinusoidal variations of the lateral and yaw motion were considered on top of a straight line motion with a constant forward velocity. An amplitude ratio η and phase angle ξ between lateral and yaw motion of the tyre were introduced. It was shown that for the straight tangent tyre model a circle represents the zero energy dissipation condition when creating a polar plot using η and ξ. The location of this circle is a function of the wavelength λ of the sinusoidal motion.

This technique can also be used to identify differences between the various tyre models, which have been introduced in the previous sections. Four different wavelengths have been considered: λ = 80a, 20a, 10a and 5a; the results are given in figures 4.24, 4.25, 4.26 and 4.27 respectively. Firstly it can be noted that for all tyre models considered the zero energy dissipation case is represented by a circle in the polar diagram. When the wavelength is sufficiently long all models, with the exception of the Moreland model, agree. As the wavelength is reduced differences start to develop; it can be noted that the models of Smiley and Kluiters remain relatively close to the Von Schlippe approximation and exact solution of the straight tangent tyre model (Segel). It can be observed that three points exist in the polar diagram, which are invariant with respect to changes in λ: $(-(\sigma+a),0)$, $(-\sigma,0)$ and $(t_p,0)$. For all tyres, except the Moreland tyre model, the zero energy dissipation circles will include the basis point $(-(\sigma+a),0)$. The straight tangent model will have an additional basis point: $(t_p,0)$. The two basis points of the Moreland model are: $(-\sigma,0)$ and $(t_p,0)$.

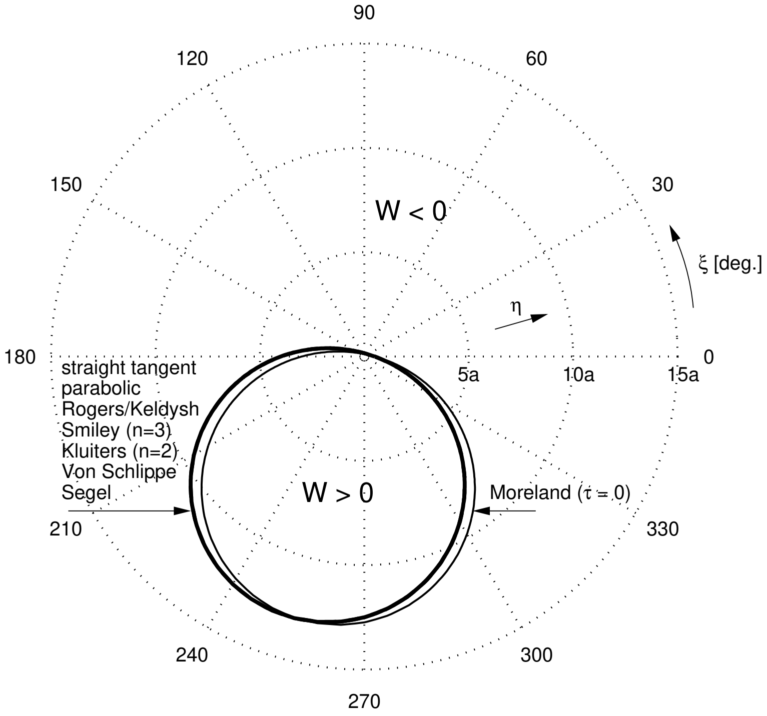

Fig. 4.24: Polar plot showing zero energy dissipation for various tyre models, sinusoidal excitation (λ=80a, σ=3a, t_p=0.5a).

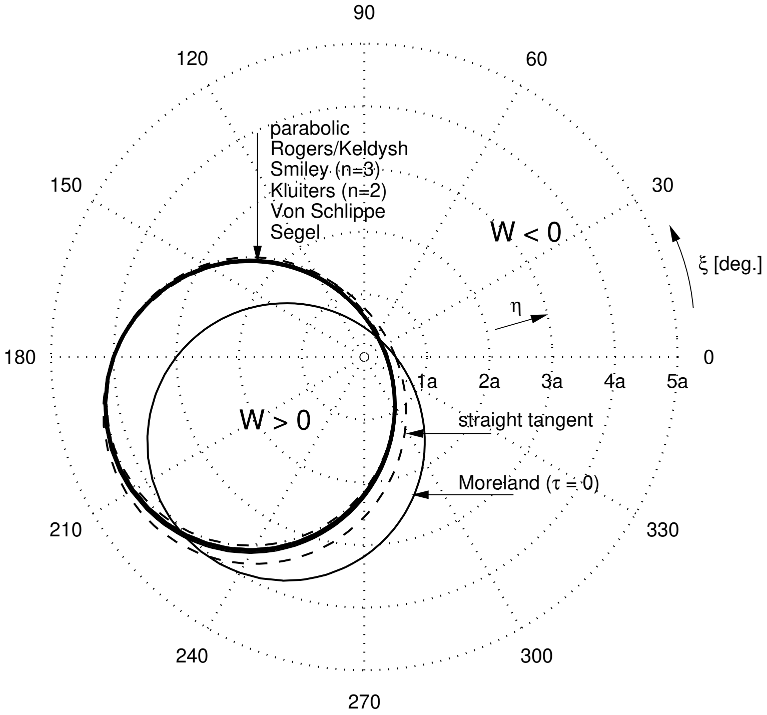

Fig. 4.25: Polar plot showing zero energy dissipation for various tyre models, sinusoidal excitation (λ=20a, σ=3a, t_p=0.5a).

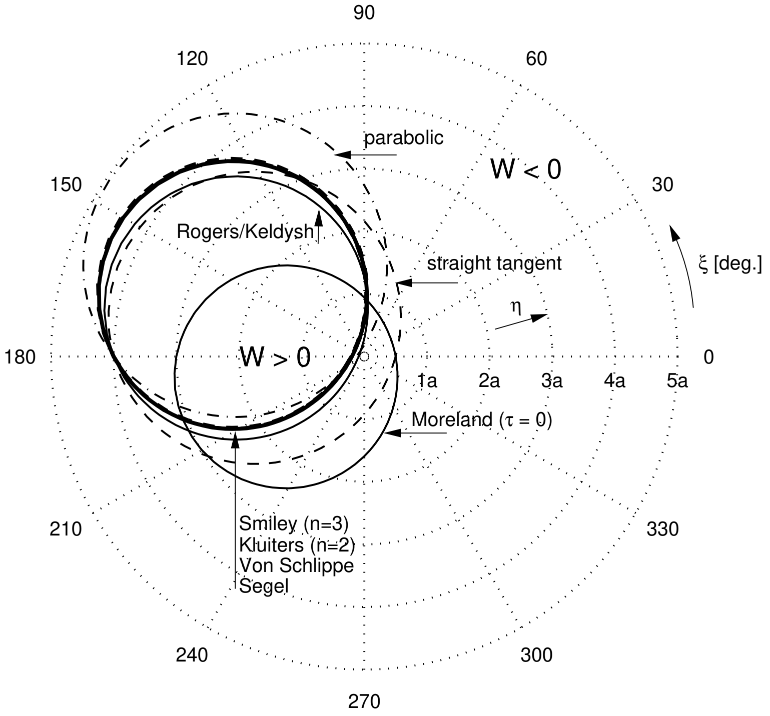

Fig. 4.26: Polar plot showing zero energy dissipation for various tyre models, sinusoidal excitation (λ=10a, σ=3a, t_p=0.5a).

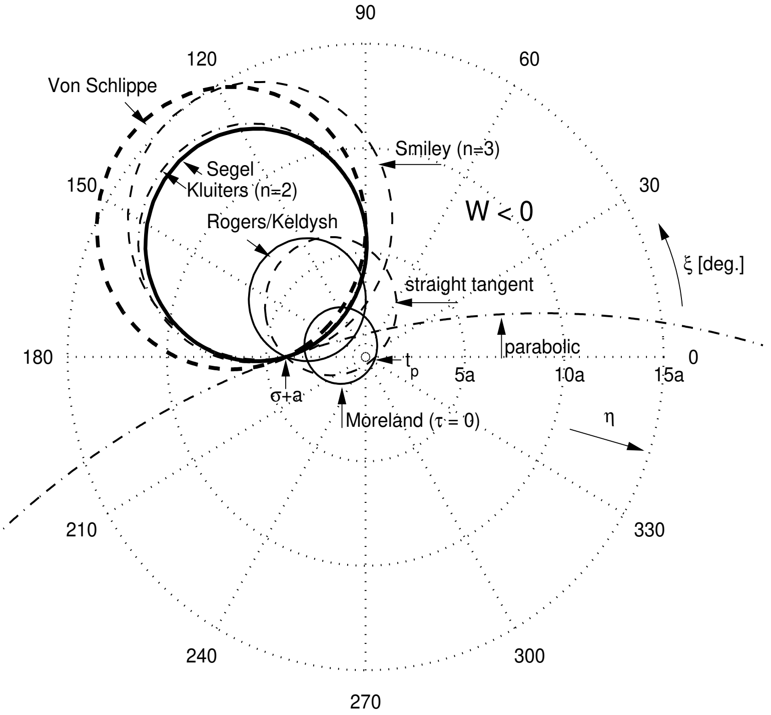

Fig. 4.27: Polar plot showing zero energy dissipation for various tyre models, sinusoidal excitation (λ=5a, σ=3a, t_p=0.5a).

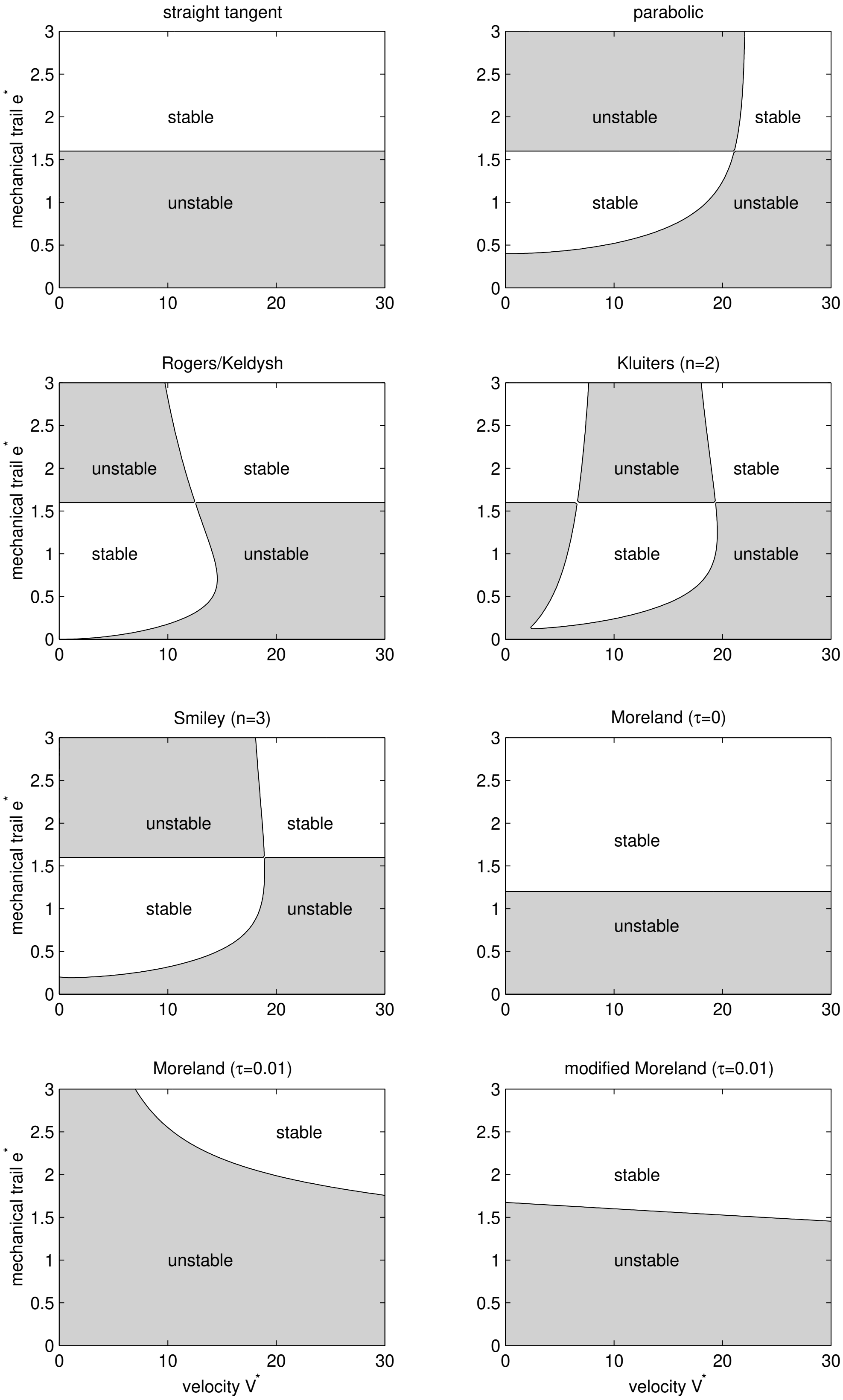

straight tangent

parabolic

Rogers/Keldysh

Kluiters (n=2)

Smiley (n=3)

Moreland (τ=0)

Moreland (τ=0.01)

modified Moreland (τ=0.01)

Fig. 4.28: Stability for the free swivelling trailing wheel system with a rigid lateral support.

4.5 Impact on shimmy stability

In the previous section a comparison was made between various tyre models based on transfer functions, step response and energy considerations. Though these results are very useful to understand the differences between the tyre models, the actual impact on shimmy stability may remain unclear. In this section a number of simple mechanical systems will be employed to compare the shimmy stability of the different tyre models while using the same tyre parameters.

In this comparison the damping of the tyre (k_v, k_β, ε) is taken equal to zero. The tyre time constant τ of the Moreland tyre model is included. After introducing $\sigma = C_{f\alpha}/c_v$ equation 4.72 may be replaced by:

$$\dot{\beta} = -\frac{1}{\tau}\left(\frac{v}{\sigma} + \beta\right) \tag{4.82}$$

The value of the tyre time constant τ is taken equal to 0.01 seconds; this relatively large value will enhance the visibility of possible differences in stability.

Trailing wheel system without lateral flexibility

In chapter 2 the trailing wheel model was introduced to investigate shimmy fundamentals, see figure 2.1 on page 21. Its stability will now be studied for different tyre models. First a free-swivelling system with a positive mechanical trail will be considered (k_ψ and c_ψ equal to zero); the other parameters remain unchanged with respect to section 2.1. The results in the velocity-trail plane are shown in figure 4.28. The behaviour of the straight tangent and Moreland model is rather different from the other tyre models at low forward velocity ($V^* < 20$); in particular the stable area for small positive mechanical trail values combined with a low forward velocity is absent.

The existence of this area could already have been deducted from the energy balance, see e.g. figure 4.27. For the trailing wheel system without lateral flexibility, the lateral and yaw motion are fixed and have a 180 degrees phase difference following the adopted sign convention (ξ =180 degrees); the mechanical trail is proportional to the amplitude ratio η. As the wavelength is decreased, similar to decreasing forward velocity, the zero energy circle starts to rotate around the basis point ($-(\sigma + a)$,0) for the "advanced" models; the energy dissipation may become positive in the range $0 < \eta < \sigma + a$. This behaviour is in contrast to the "simpler" Moreland and straight tangent tyre models which include two basis points and will remain unstable for short wavelengths and small values of the amplitude ratio η.

Next a yaw stiffness is introduced, $c_\psi^* = 15$. The results are given in figure 4.29. With respect to figure 4.28 the velocity range has been extended considerably: due to the introduction of the yaw stiffness the shimmy frequency is much higher. The differences between the tyre models, which are typically a function of wavelength, will still be present at higher velocities. Negative values for the mechanical trail are included, because by introducing a yaw stiffness the boundary for monotonous instability is shifted towards increasing negative values of the mechanical trail. This boundary appears to be the same for the majority of tyre models. Again we find that at the lower forward velocities combined with small positive mechanical trail that the straight tangent and Moreland model yield unstable results, whereas the other tyre models result in a stable system.

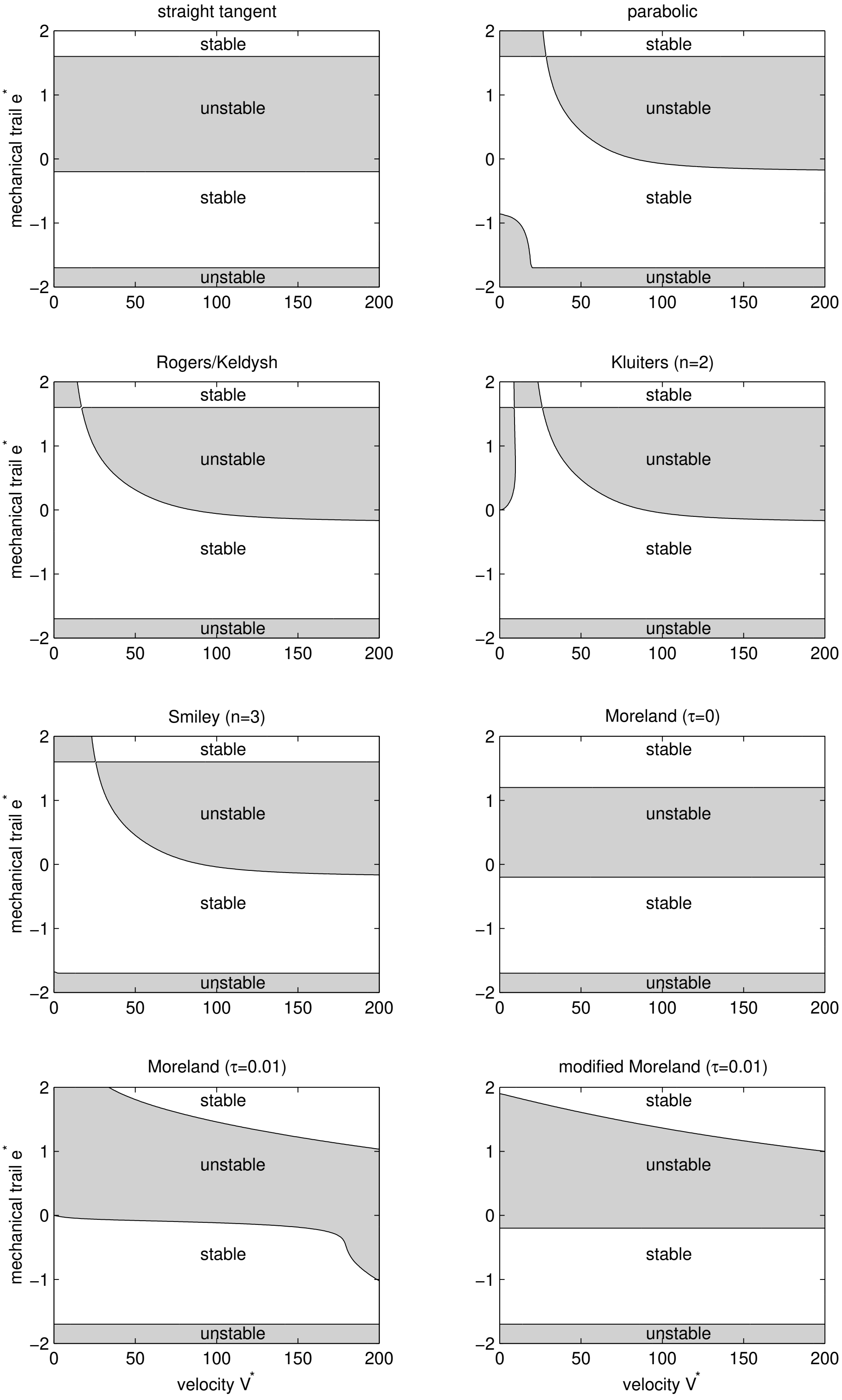

Fig. 4.29: Stability for the trailing wheel system with rigid lateral support, yaw stiffness c_ψ^*=15.

Trailing wheel system with lateral flexibility

The trailing wheel system with lateral flexibility of the support is shown in figure 2.7. An analytical expression for the stability can be derived when a straight tangent tyre model is used, see figure 2.9. Using the parameters of section 2.2 we will now study the impact of different tyre models. Already when the lateral support is rigid the stability is a function of forward velocity for the majority of the tyre models, so the results in the mechanical trail versus yaw stiffness plane have been determined at two forward velocities: $V^* = 50$, see figure 4.30, and $V^* = 150$ as shown in figure 4.31.

The differences between the various models remain limited, except for the straight tangent and Moreland tyre model. As shown before, the results of the straight tangent tyre model in a system without damping are independent of forward velocity. The models of Rogers/Keldysh, Kluiters, Smiley and parabolic approximation indicate that for the lower forward velocity stability will improve for high values of the yaw stiffness. It can be noted that the boundary which separates the stable from the unstable area at positive trail values is the same for all models (except Moreland).

The results of the various Moreland tyre models are clearly different from the others. The inclusion of a time constant generally seems to make the model more unstable. But if the time constant is excluded the results are not conservative with respect to the other tyre models: e.g. the required yaw stiffness to obtain a stable gear with a positive mechanical trail is too low. Furthermore the Moreland model seems to get more unstable at the lower forward velocities, which is opposite to the majority of the other models.

As the velocity is decreased the wavelengths will get shorter; from the polar plots concerning the energy dissipation (e.g. figure 4.27) it is already obvious that the differences between the various tyre models will get larger. Also the location of stable and unstable areas may change rather dramatically with the wavelength (or velocity) in this low speed or short wavelength regime. This is illustrated in figure 4.32, where the velocity range V^*=5 up to 40 is covered. There hardly seems to be any configuration which would be stable for all forward velocities in this range.

Nevertheless the results may be less dramatic in reality. Probably the most important factor to stabilise the system at these low velocities is the damping moment generated by the tyre due to turn slip. This moment is not present in the tyre models discussed in this thesis, but is also commonly ignored in most shimmy analyses available in literature. The apparent damping constant associated with this yaw motion is inversely proportional with the forward velocity, and may be sufficient to stabilise the system. Nevertheless an important conclusion form this exercise is that one may have to be cautious with the interpretation of the results at low values of forward velocity.

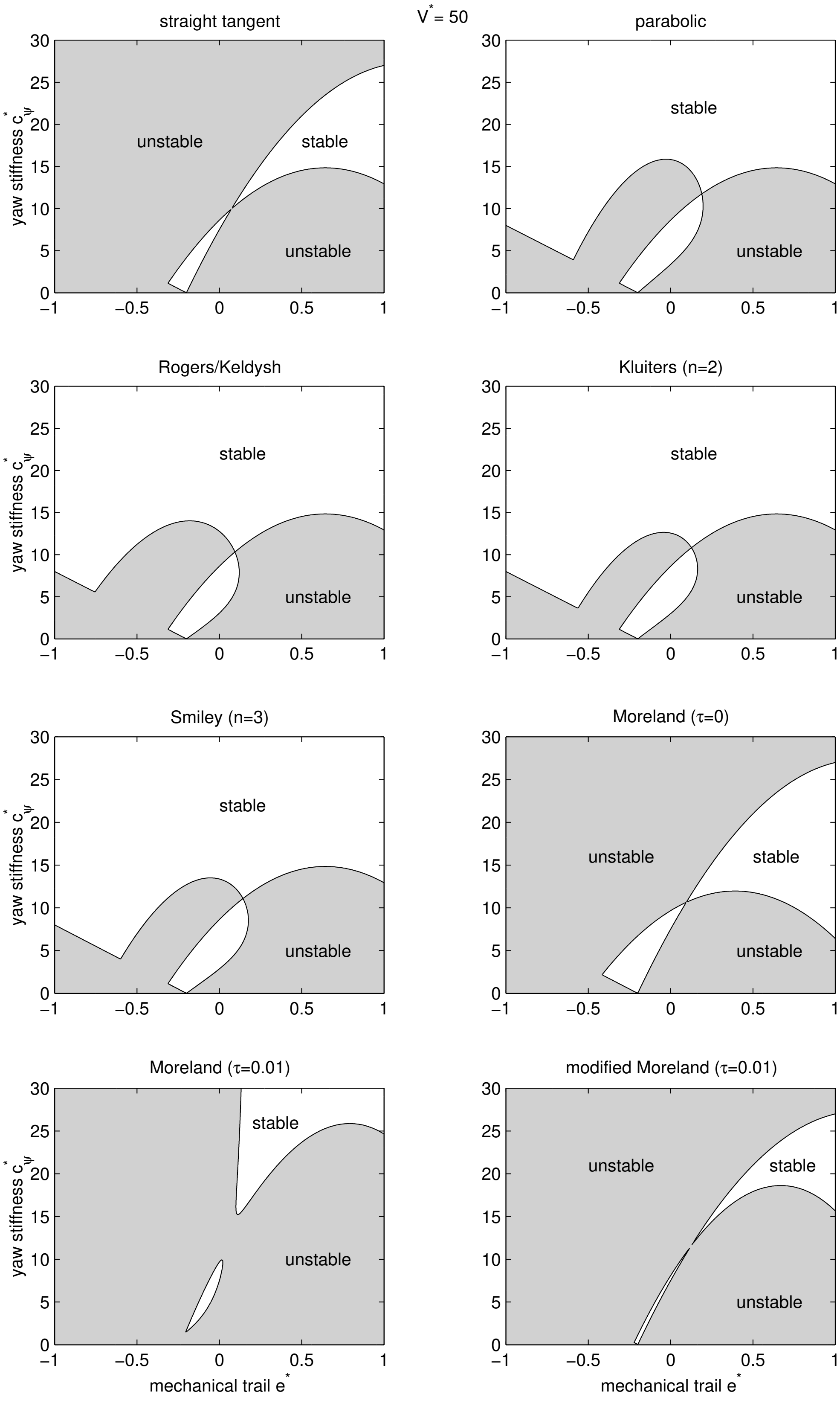

Fig. 4.30: Stability for the trailing wheel system with lateral flexibility, V^*=50.

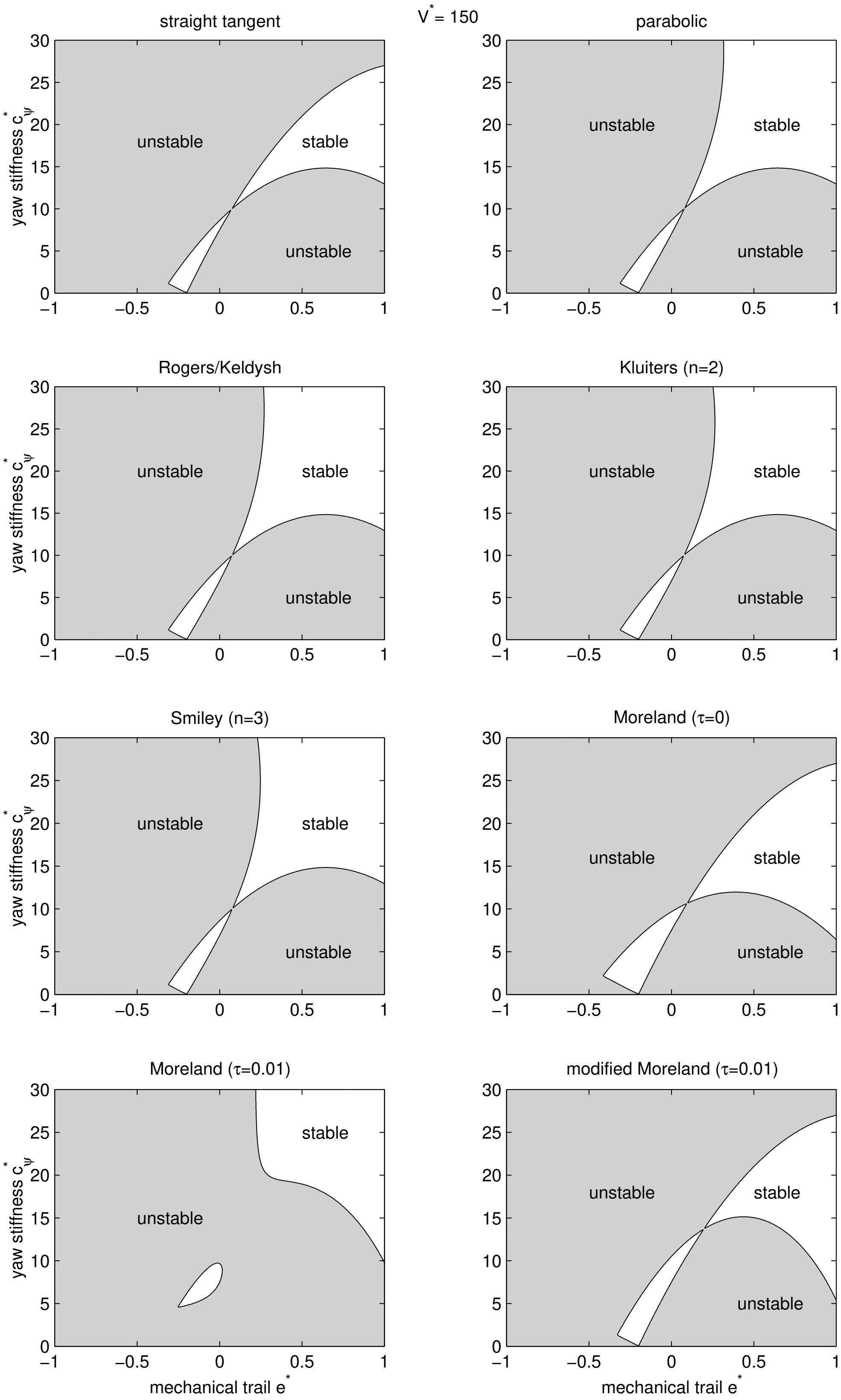

Fig. 4.31: Stability for the trailing wheel system with lateral flexibility, V^*=150.

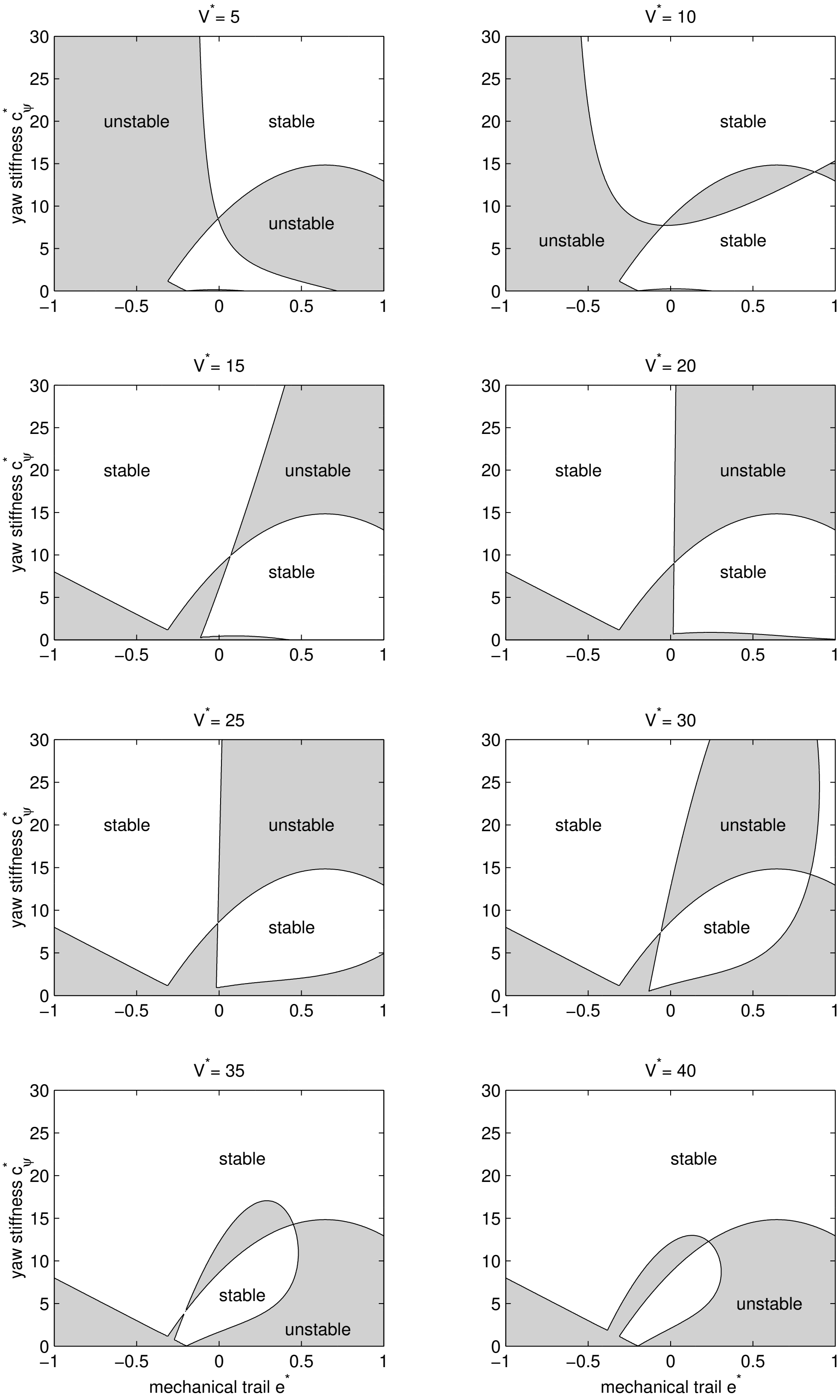

Fig. 4.32: Stability for the trailing wheel system with lateral flexibility as a function of forward velocity, Kluiters (n=2) tyre model.

4.6 Tyre parameters

For the tyre models discussed in this chapter four characteristics are required:

- half of the contact length a
- relaxation length σ
- cornering stiffness $C_{f\alpha}$
- self-aligning stiffness $C_{m\alpha}$

In addition, a tyre-time constant τ is needed for the Moreland model. Figure 4.10 gives an impression of the values used by various researchers, but it is recommended to use equation 4.81.

Obtaining valid tyre data is a problem on its own. Physical models of the tyre are not (yet) accurate enough to provide the required tyre characteristics, so these have to be determined experimentally. Experience has shown that accurate measurement of tyre characteristics is rather difficult. In a recent study differences over 30% in cornering stiffness were found between various tyre testing facilities, while using the same car tyres from a single production batch [34]. Measurements performed on an external drum generally result in a shorter contact length, lower cornering stiffness and a much lower self aligning stiffness compared to measurements on a flat surface.

On the other hand one could argue if it actually is possible to measure *the* tyre characteristics for a particular tyre: the behaviour will be a function of inflation pressure, wear, road roughness, forward velocity, temperature, production tolerances, ageing, etc. For commercial aircraft the use of retreaded tyres is common practice: the tread surface may be replaced multiple times. It is unclear to which extent this affects the tyre characteristics.

The following analysis is intended to provide some rules of thumb and to prevent major errors in the tyre parameters. In this respect the work of Smiley and Horne [47] remains important. Data from numerous experiments on aircraft tyres was collected and empirical formulas were developed to describe the tyre behaviour. In this way a reference frame is provided which can be used e.g. to check the experimental data supplied by a tyre manufacturer or to get an estimate for a missing parameter. Unfortunately, the work of Smiley and Horne was never updated since its creation in 1960. Some of the data may be out of date and could prove to be less accurate in describing the characteristics of tyres currently in use, in particular for radial aircraft tyres.

We will now discuss the required parameters and "check" the empirical expressions available from literature, using experimental data for a number of different makes of aircraft tyres, all having the same dimensions.

contact length

Smiley and Horne provide the following formula for half of the contact length of the tyre:

$$a = 1.7R_0\sqrt{\frac{\delta}{2R_0} - \left(\frac{\delta}{2R_0}\right)^2} \tag{4.83}$$

where δ is the vertical deflection of the tyre and R_0 the unloaded tyre radius. Zegelaar uses the following formula in his thesis [53]:

$$a = q_{a1}\sqrt{F_z} + q_{a2}F_z \tag{4.84}$$

Measurements are required to fit the coefficients q_{a1} and q_{a2}. A disadvantage of this formula is that it will be limited to only one specific inflation pressure and tyre radius; the formula of Smiley and Horne is of a much more generic nature.

Using the experimental data available it appears that the contact length predicted by Smiley and Horne is generally somewhat too large, see figure 4.33. In order to get a better representation of the contact length a modified formula is suggested:

$$a = r_{a1}R_0\left(\frac{\delta}{R_0} + r_{a2}\sqrt{\frac{\delta}{R_0}}\right) \tag{4.85}$$

As can be seen from figure 4.33 this formula gives a fair representation of the contact length for aircraft tyres when taking the coefficient r_{a1} equal to 0.4 and r_{a2} equals 2.25. An additional check on the new formula is made using some passenger car data measured on a drum and flat road surface, see figure 4.34. From this graph it can be concluded that different tyre pressures can be described quite well using the same coefficients. Furthermore it confirms again that on an external drum the contact length, at a given vertical deflection, will be smaller compared to measurements on a flat surface. It appears that for a passenger car tyre slightly different coefficients are needed to match the data. Obviously, to really substantiate the expressions for the contact length more experimental data is required, preferably a wide range of tyres with different dimensions. A final remark is that the contact patch may have the shape of an ellipsoid or a somewhat more boxy shape. This leaves us with the problem how to exactly define the contact length; in this respect also its application within the tyre model has to be considered.

cornering stiffness

Smiley and Horne provide the following empirical formula for the cornering stiffness:

$$\left.\begin{array}{ll} C_{f\alpha} = 57w_t^2\,(p+0.44p_r)\left(1.2\frac{\delta}{2R_0} - 8.8\left(\frac{\delta}{2R_0}\right)^2\right) & \frac{\delta}{2R_0} \leq 0.0875 \\ C_{f\alpha} = 57w_t^2\,(p+0.44p_r)\left(0.0674 - 0.34\frac{\delta}{2R_0}\right) & \frac{\delta}{2R_0} \geq 0.0875 \end{array}\right\} \tag{4.86}$$

where w_t is the width of the tyre, p tyre pressure and p_r rated tyre pressure.

For road vehicles the Magic Formula is a widely used empirical model to describe the steady-state tyre characteristics under various slip conditions [38]. Within the Magic Formula the next expression is used to describe the cornering stiffness (the contribution of the inclination angle is not considered):

$$C_{f\alpha} = p_{Ky1}F_{z0}\sin\left(2\arctan\left(\frac{F_z}{p_{Ky2}F_{z0}}\right)\right) \tag{4.87}$$

The coefficients p_{Ky1} and p_{Ky2} are fitted using measured data, F_{z0} is the nominal (rated) load of the tyre.

Figure 4.35 shows experimentally determined cornering stiffness as a function of vertical load together with the results from Smiley and Horne for this particular tyre size and inflation pressure. In addition two characteristic shapes using a Magic Formula approach have been included. It is clear that Smiley and Horne provides a reasonable first guess for an average tyre, but on the other hand it can be concluded that a large range exists which leaves a fair amount of uncertainty about the actual value. The main deficiency of the Magic Formula approximation appears to be that the slope after reaching the peak value is not sufficiently degressive. This could be modified by increasing the factor 2 in the sin – arctan expression and possibly make it a variable in the fitting process.

A crude first estimate for the cornering stiffness can be obtained by dividing the maximum occurring cornering stiffness ($C_{f\alpha,max}$) with corresponding vertical load ($F_{z,max}$). For passenger car and motorcycle tyres this number is about 10 rad^{-1}; for truck and aircraft tyres it is closer to 5 rad^{-1}; this is illustrated by figure 4.36

relaxation length

Smiley and Horne developed the following formula for the yawed relaxation length:

$$\left.\begin{array}{ll} \sigma = w_t\left(2.8-0.8\frac{p}{p_r}\right)11\left(\frac{\delta}{2R_0}\right) & \frac{\delta}{2R_0}\leq 0.053 \\ \sigma = w_t\left(2.8-0.8\frac{p}{p_r}\right)\left(64\left(\frac{\delta}{2R_0}\right)-500\left(\frac{\delta}{2R_0}\right)^2-1.4045\right) & 0.053\leq\frac{\delta}{2R_0}\leq 0.068 \\ \sigma = w_t\left(2.8-0.8\frac{p}{p_r}\right)\left(0.9075-4\left(\frac{\delta}{2R_0}\right)\right) & \frac{\delta}{2R_0}\geq 0.068 \end{array}\right\} \tag{4.88}$$

Recently Alsobrook developed a different formula [1]:

$$\sigma = 3.106R_0\left(100\frac{\delta}{\delta_{max}}\right)^{0.624} \tag{4.89}$$

Where δ_{max} equals the maximum tyre deflection, where bottoming of the tyre occurs.

Figure 4.37 shows the experimental data combined with the empirical formulas. The relaxation length calculated with the formula of Alsobrook appears to be too large and the formula of Smiley and Horne has a marked kink at a tyre deflection of 0.12; beyond this value the formula appears to be less accurate. As indicated in the graph, the measured relaxation length is approximately within a range of $2a$ to $3.5a$. It should be noted that this is quite different to passenger car tyres; the experimental results of e.g. Higuchi indicate that for these tyres the relaxation length may be in excess of five times the contact length ($\sigma \geq 10a$) [18].

Using the expressions of the stretched string model, equations 4.23 and 4.26, the following formula can be obtained for the relaxation length:

$$\sigma = \frac{C_{f\alpha}}{c_v} - a \tag{4.90}$$

Since the measured lateral stiffness c_v is also available, it is possible to perform a redundancy check on the relaxation length. First the measured lateral stiffness is shown in figure 4.38. Also the empirical formula of Smiley and Horne for the tyre lateral stiffness is plotted; this formula reads:

$$c_v = 2w_t\left(p+0.24p_r\right)\left(1-0.7\frac{\delta}{w_t}\right) \tag{4.91}$$

It appears that the tyre lateral stiffness obtained by Smiley and Horne is somewhat too large, but correctly identifies that in general the lateral stiffness decreases with increasing tyre deflection. The relaxation length can be calculated using formula 4.90 and a comparison can be made with the relaxation length determined in a yawed rolling test of the tyre. For the limited experimental data available it appears that the calculated relaxation length tends to be too small, as is shown in figure 4.39.

self-aligning stiffness

The self aligning stiffness $C_{m\alpha}$ can be calculated by multiplying the cornering stiffness and pneumatic trail. Smiley and Horne suggest a pneumatic trail equal to $0.8a$ for small side slip angles. This compares quite well to the value of $0.77a$, which can be calculated for the stretched string model under the assumption that $\sigma = 3a$, see page 96. The available experimental data for aircraft tyres is shown in figure 4.40; it is clear that a large range exists, varying between $0.3a$ to $0.9a$. It was confirmed that the tyre having the smallest pneumatic trail (indicated with a triangle) was tested on a drum having a diameter of approximately three times the tyre diameter.

For small slip angles (and ignoring the contribution of an inclination angle) a polynomial is used to describe the pneumatic trail in the Magic Formula [38]:

$$t_p = F_z \left(q_{Dz1} + q_{Dz2} \left(\frac{F_z - F_{z0}}{F_{z0}} \right) \right) \tag{4.92}$$

Considering the measurement data, physical modelling consideration and extrapolation properties, another feasible solution would be to use the formula for the contact length (e.g. equation 4.84 or 4.85) as a basis for the calculation of the pneumatic trail.

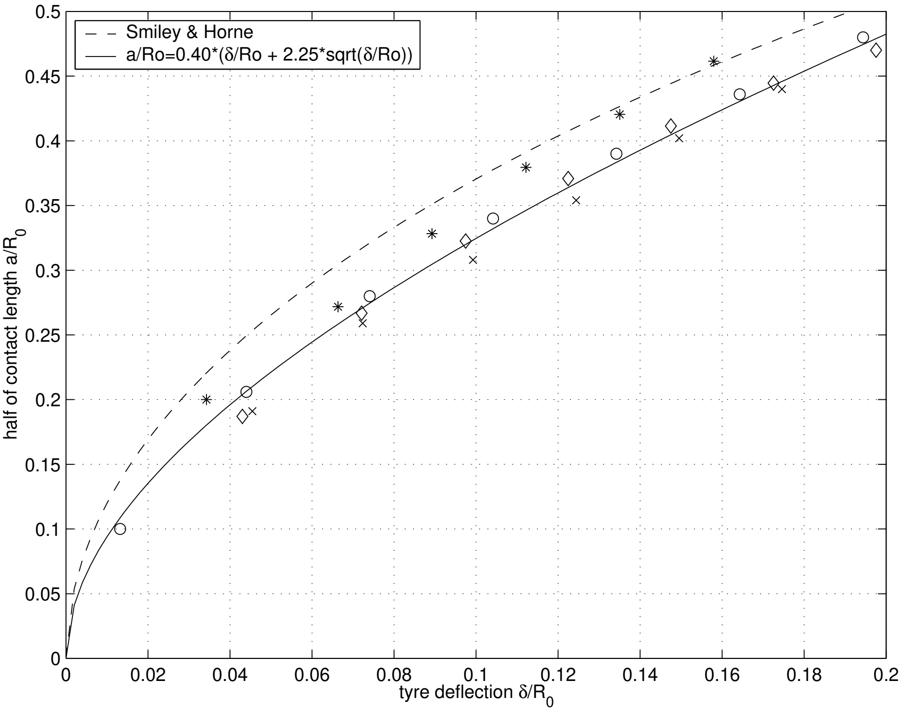

Fig. 4.33: Measurement and empirical formulas for half of the contact length as a function of tyre deflection, aircraft tyres.

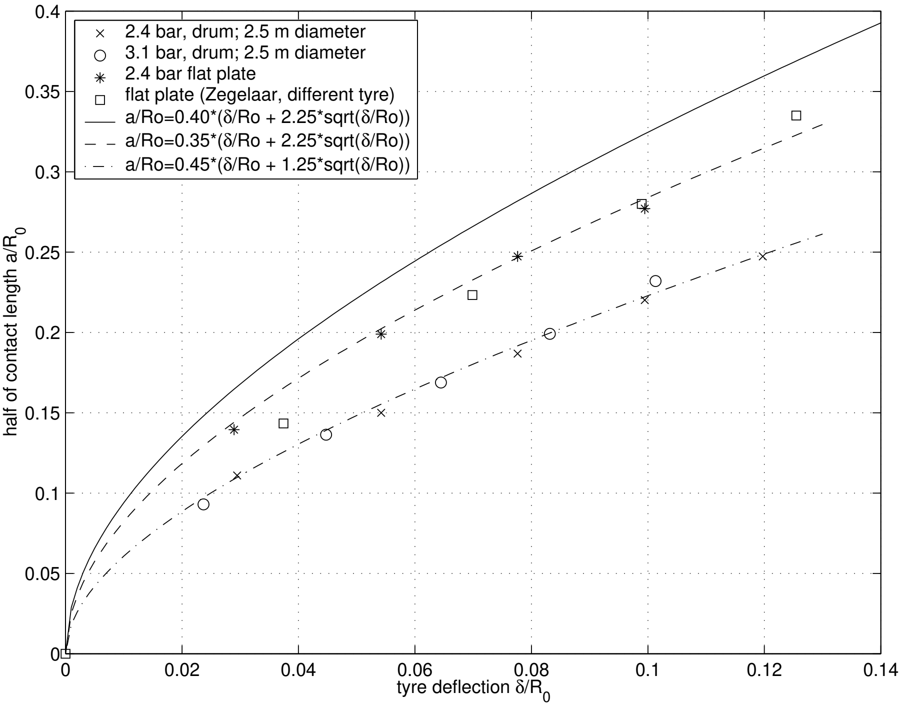

Fig. 4.34: Measurement and empirical formulas for half of the contact length as a function of tyre deflection, passenger car tyres.

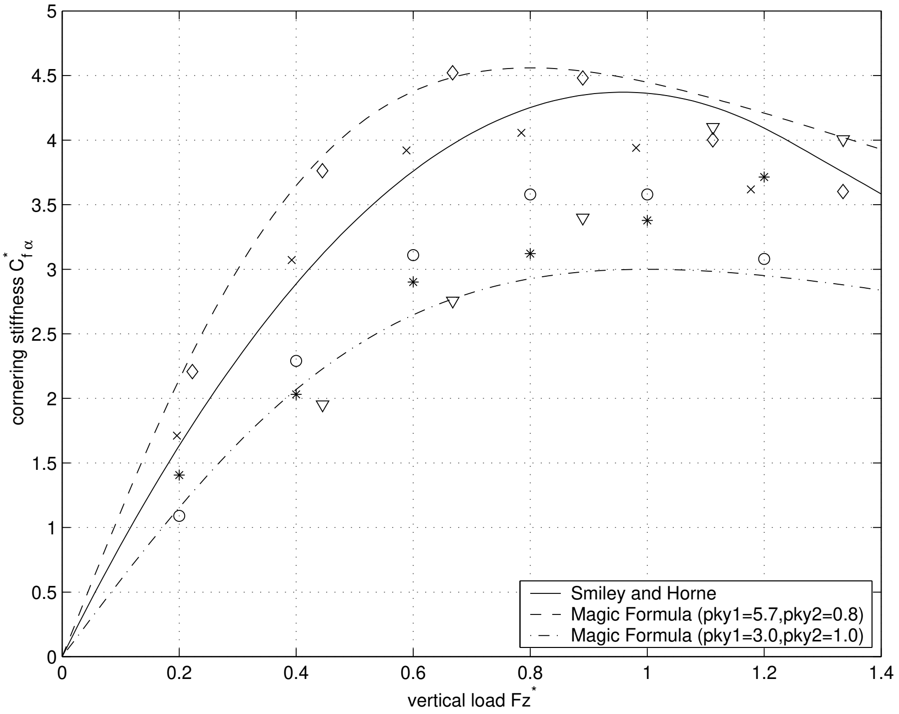

Fig. 4.35: Measurement and empirical formulas for the cornering stiffness, aircraft tyres.

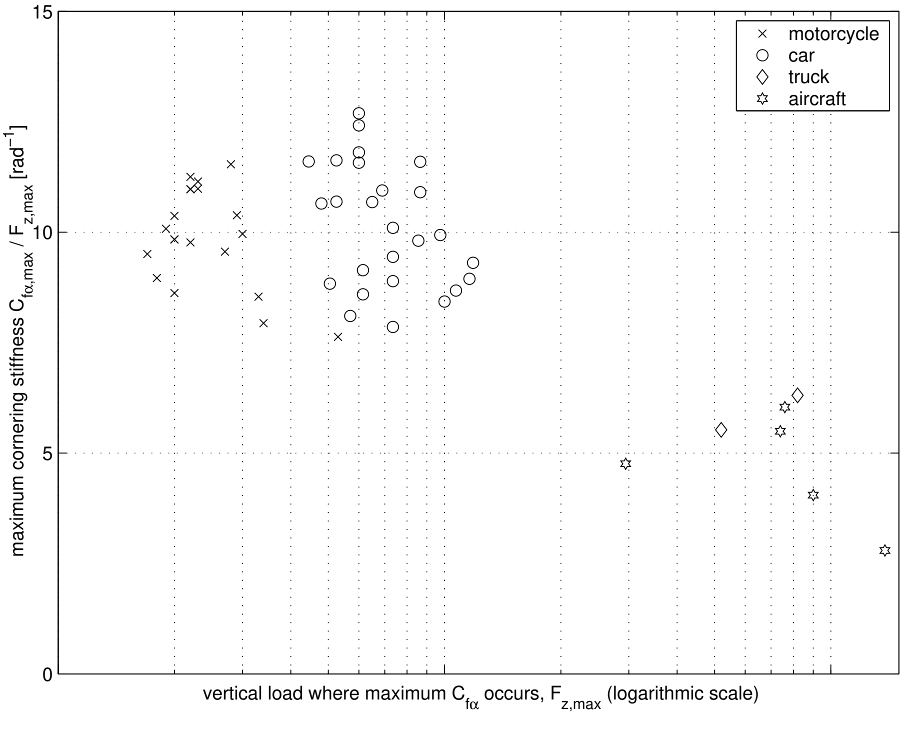

Fig. 4.36: Normalised peak cornering stiffness as a function of the vertical load.

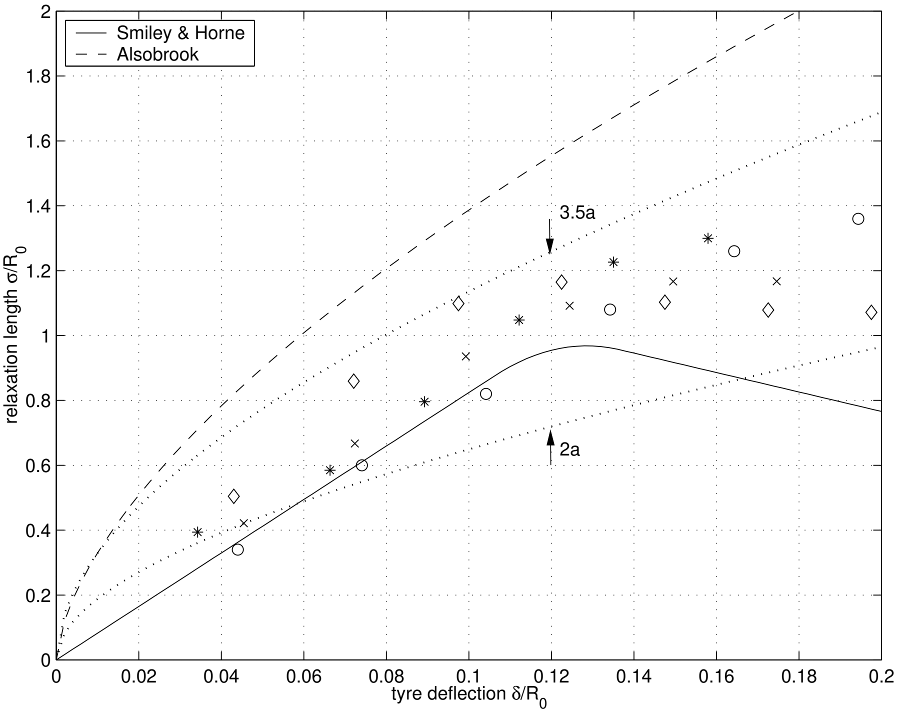

Fig. 4.37: Measurement and empirical formulas for the relaxation length, aircraft tyres.

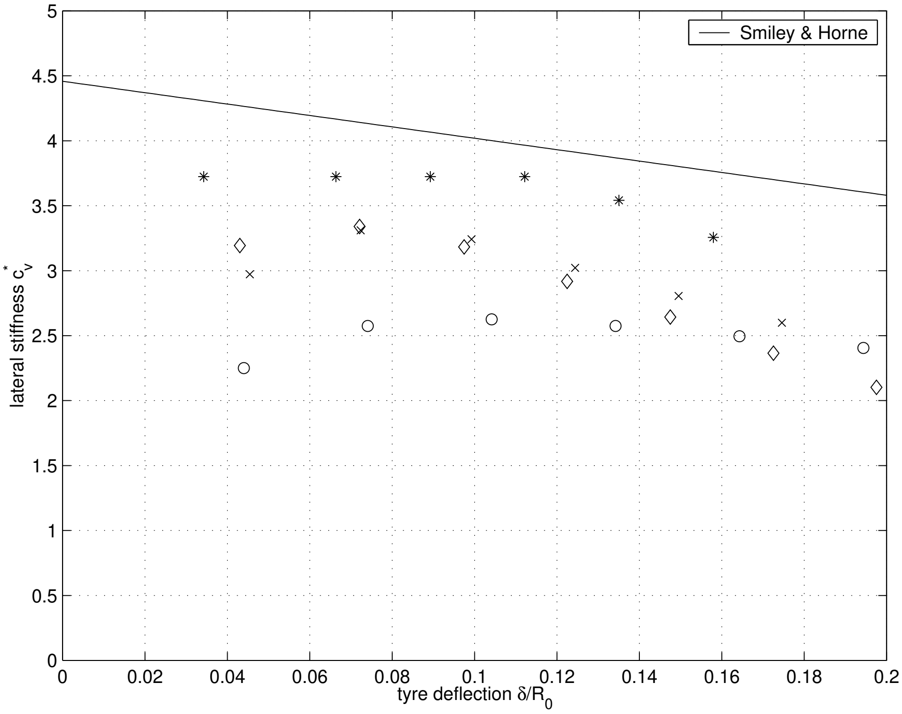

Fig. 4.38: Measurement and empirical formula for the tyre lateral stiffness, aircraft tyres.

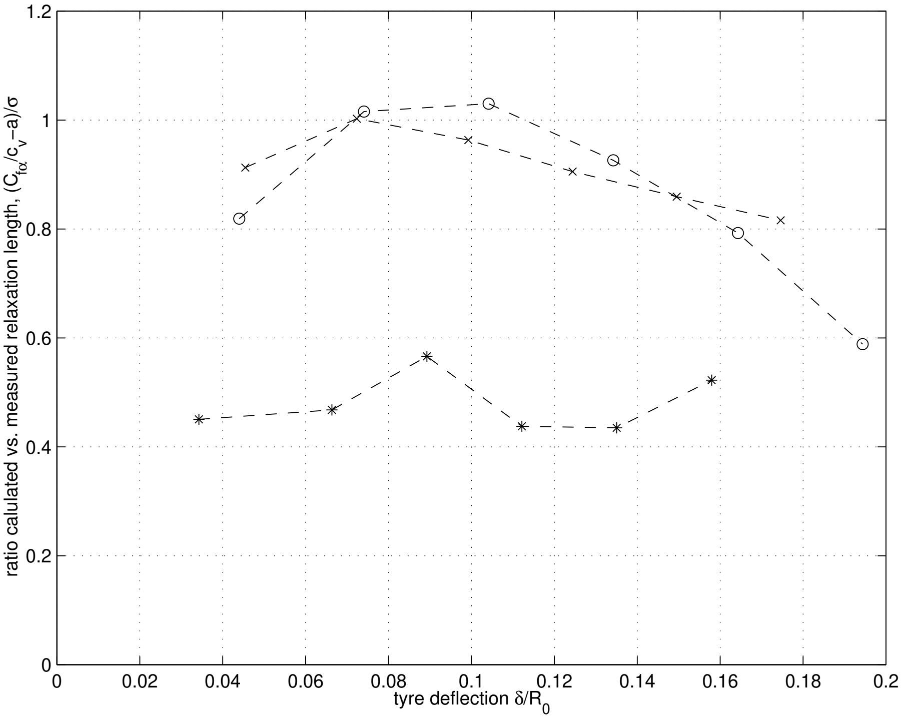

Fig. 4.39: Ratio of the calculated (using equation 4.90) and measured relaxation length, aircraft tyres.

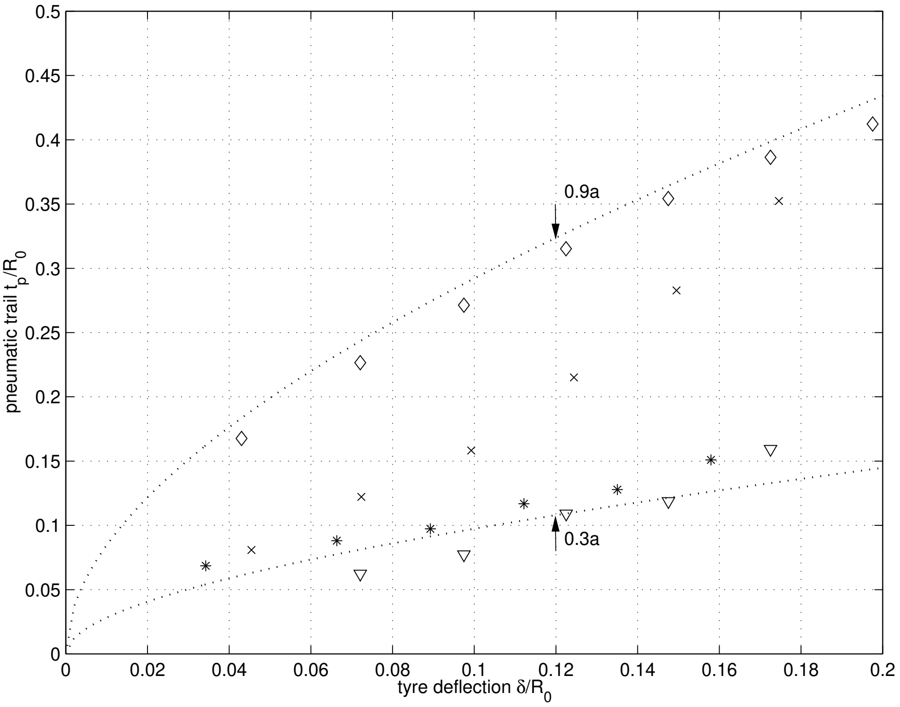

Fig. 4.40: Measured pneumatic trail as a function of tyre deflection, aircraft tyres.

Chapter 5

Detailed modelling and validation

This chapter describes the development of a detailed model, which was used to solve the shimmy problems occurring on an existing landing gear. In particular this chapter will focus on modelling the landing gear structure; tyre modelling has already been discussed in the previous chapter. Relatively simple models have been used to study the general trends in shimmy stability in the chapters 2 and 3; with respect to these models the deflection of the shock absorber has to be included.

The flexibility of the landing gear structure is a function of the shock absorber deflection. The normal load on the tyres will also depend on the shock absorber deflection and will result in changes of the tyre characteristics, as shown in section 4.6. Therefore the shimmy stability will become a function of the shock absorber deflection due to the changes in both structural stiffness and tyre properties. Other aspects which need to be considered in a detailed model are the non-linear behaviour due to free-play and friction. Also the shimmy damper may have a highly non-linear characteristic. Various tests are required to support and validate the model. Dedicated tests may be required to determine the characteristics of various components of the landing gear. Full-scale tests will also allow some validation of the model. Some practical information regarding these tests will be given and the ”lessons learned” will be discussed.

5.1 Shock absorber

A very important function of the landing gear is the energy absorption during landing impact. A shock absorber with a large stroke is required in order to limit the forces occurring in this process; typically the available travel is in the range of 0.3 to 0.6 meter. The shock absorber is an integral part of the load carrying structure for a cantilevered landing gear. Nitrogen (”air”) is used as the springing medium for nearly all aircraft and an oil flow through orifices provides the damping function. Figure 5.1 gives a schematic view of the internals of a shock absorber; this is an example of an *open* shock absorber, there are no provisions to separate the oil from the nitrogen. The metering pin is used to control the orifice area as a function of stroke.

Simple calculations on the shock absorber spring characteristics can be made assuming incompressible oil and polytropic compression of an ideal gas [31]. The resulting expression for the spring force F_s reads:

$$F_s = P_0 A_0 \left(\frac{V_0}{V_0 - A_0 \Delta l} \right)^n - P_b A_0 \tag{5.1}$$

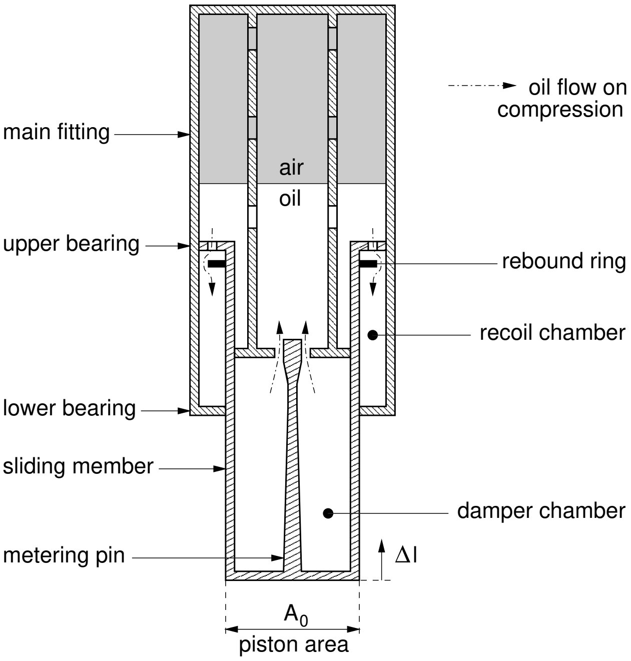
oil flow on compression
main fitting
air
oil
upper bearing
rebound ring
recoil chamber
lower bearing
sliding member
damper chamber
metering pin
Δl
A_0
piston area

Fig. 5.1: Internal lay-out of the shock absorber (not to scale).

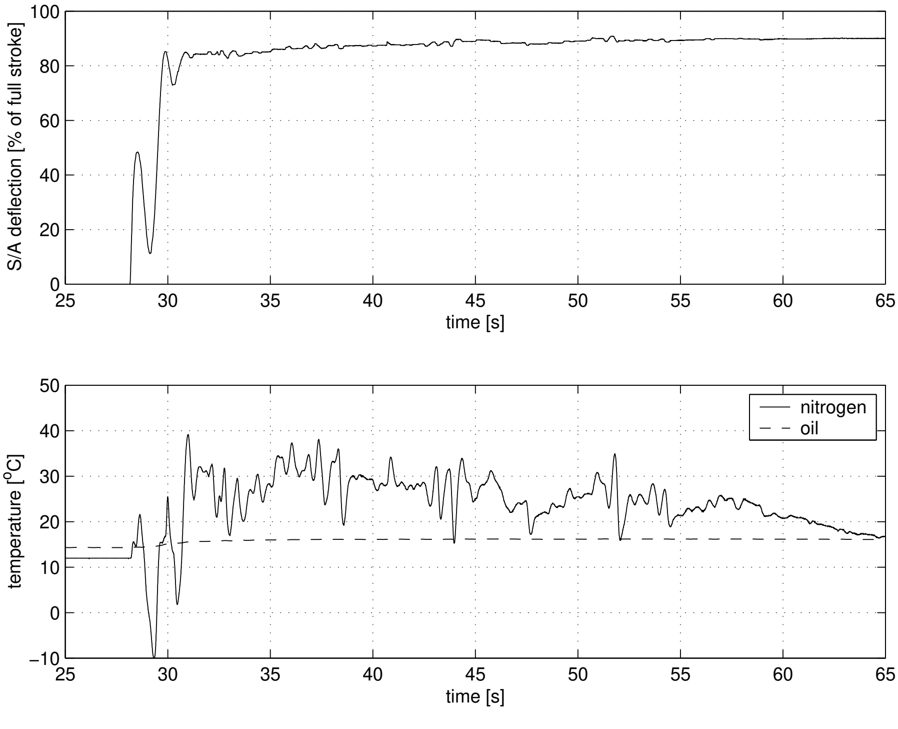

Fig. 5.2: Shock absorber (S/A) deflection and temperature during landing and roll-out (flight 7388 rec. 21, left hand gear).

where P_0 is the precharge pressure, P_b is the ambient pressure, A_0 the piston area, V_0 the initial air volume, Δl the shock absorber deflection and n the polytropic coefficient. For a slow, isothermal compression of the strut n equals one; in case of a rapid compression of the strut the polytropic coefficient n will be typically 1.1 for an open shock absorber. The polytropic coefficient n will be approximately 1.4 if a piston is present to separate the oil from the nitrogen (adiabatic process).

The oil flow Q through the orifices is turbulent and may be described by the next equation:

$$Q = C_d a \sqrt{\frac{2\Delta P}{\rho}} \tag{5.2}$$

where ΔP is the pressure drop across the orifice, C_d is the orifice discharge coefficient, a is the orifice area and ρ is the mass density of the hydraulic oil. The end result will be a quadratic damping coefficient which may be a function of the stroke due to the metering pin. A rebound ring reduces the orifice size on extension of the strut, so the damping coefficient will be much larger for this condition.

The shock absorber characteristics are validated by a drop test programme, which consists of landing tests in a laboratory environment. Generally the drop test programme focuses on the high descent velocity cases, which are important from a design loads point of view and for verification purposes of the energy absorption capability. The drop test results can generally be simulated with sufficient accuracy using the modelling approach as described above.

Nevertheless for average landing conditions the behaviour may be somewhat different. A number of tests have been performed with an instrumented landing gear, where the internal pressures and temperatures are recorded during landing impact and the consecutive roll-out of the aircraft. A typical test result is shown in figure 5.2. On touch-down the shock absorber is compressed and extends again, before the lift dumpers are activated and the static deflection is reached. The compression and expansion of the nitrogen is a thermodynamic process and the temperature responds accordingly, whereas the oil temperature remains nearly constant.

The internal pressures of the strut are shown in figure 5.3. It can be seen that the theoretical curve is quite accurate on initial compression of the strut, but the differences become much larger when the gear settles for a static position. Under these conditions it is clear that using the shock absorber deflection combined with the theoretical air spring curve will not be a reliable measure for the actual pressures inside the shock absorber. An explanation for the observed behaviour may be that under the increased pressure some of the nitrogen dissolves in the oil with a certain time constant [42]. A detailed model of the shock absorber was created, using some modelling aspects of the work of Verbeek [50], which proved to be fairly accurate in predicting the observed air spring behaviour. The discussion of this model is outside the scope of this thesis.

Figure 5.3 also shows the pressures of the damper and recoil chamber. It can be observed that the pressure drop across the orifices, which is a direct measure for the magnitude of the damping force, remains relatively small. The damping is tuned for high descent velocity cases and the damping forces will be small for normal landing conditions since they are quadratically dependent on velocity. This also implies that a metering pin will have little contribution to the reduction of loads under normal, average landing conditions.

In the shimmy analysis the shock absorber characteristics are important because they

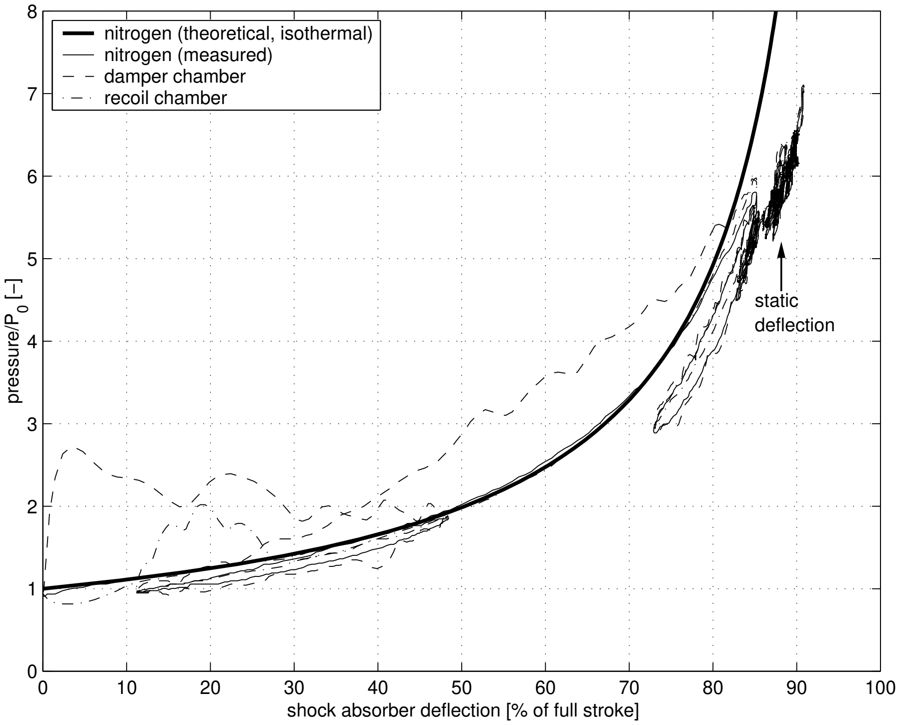

Fig. 5.3: Pressure as a function of shock absorber deflection during landing and roll-out (flight 7388 rec. 21, left hand gear).

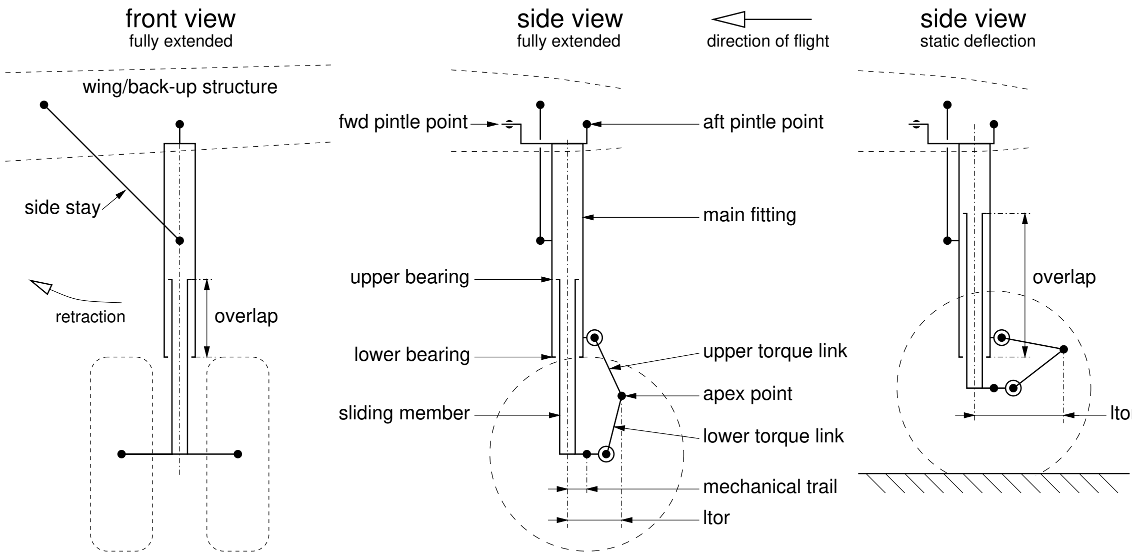
front view
fully extended
side view
fully extended
direction of flight
side view
static deflection
wing/back-up structure
side stay
retraction
overlap
fwd pintle point
aft pintle point
main fitting
upper bearing
lower bearing
sliding member
upper torque link
apex point
lower torque link
mechanical trail
ltor
overlap
ltor

Fig. 5.4: Landing gear in fully extended and static position.

relate the vertical load on the tyres with the shock absorber deflection. Tyre characteristics are a function of the vertical load, see section 4.6, and the stiffness of the landing gear is a function of the shock absorber deflection, as will be illustrated in the next section.

5.2 Landing gear flexibility

From the studies performed in chapters 2 and 3, it is obvious that the stiffness and geometrical lay-out of the landing gear may be decisive factors for shimmy stability. In the previous chapters simple, straightforward models have been used when analysing the shimmy fundamentals. For a detailed analysis of the landing gear stiffness a finite element model will be required. In order to understand and explain the results of the finite element model (or stiffness measurements) some important aspects, which determine the landing gear flexibility, will be discussed.

Figure 5.4 provides a schematic view of a landing gear. Since the aircraft and landing gear are designed for minimum weight, it is a good starting point to assume that all parts are flexible. The landing gear is attached to the wing via three spherical joints; the local reinforcement in the wing to support the landing gear is known as the back-up structure. The gear is retracted by folding the side-stay and a sideways rotation of the strut about the pintle points. Figure 5.4 also displays the changes in overlap and apex point location on compression of the strut. The assumption can be made that no bending moments are transferred between the main fitting and sliding member at the upper and lower bearing. Since the forward pintle point is not restricted in longitudinal direction it can be concluded that this landing gear may be considered as a statically determined structure: the reactions on the various components can be calculated from static equilibrium.

overlap

On compression of the strut the landing gear shortens and the distance between upper and lower bearing increases. This has a marked influence on the flexibility of the landing gear in the directions perpendicular to the strut centre line. This will be illustrated by considering a prismatic cantilever beam and a second prismatic beam, which are allowed to move with respect to each other, see figure 5.5. The deflection δ and rotation angle θ are considered as a function of the force F and moment M for varying shock absorber deflections.

For the geometry given in figure 5.5 and the assumption that the flexural rigidity of the cantilever beam is twice the value of the moving beam ($EI_m = 2EI_s$), the results of figure 5.6 can be obtained. Please note that the results have been normalised with respect to the fully closed condition. Figure 5.6 makes clear that the deformations may be over twice as large for a fully extended gear compared to the fully closed condition for a given load. The rotation angle under the influence of a moment M is less sensitive to the shock absorber deflection, but still an increase of 60% can be noted for a fully extended gear. The model as presented here typically reflects the fore/aft stiffness of a landing gear. In the lateral direction the situation is somewhat more complicated due to the presence of the lateral support via the side stay. It should be noted that the model presented here is just a conceptual model to illustrate the main effects; in a real landing gear the cross-sections may be non-prismatic and additional braces may be present.

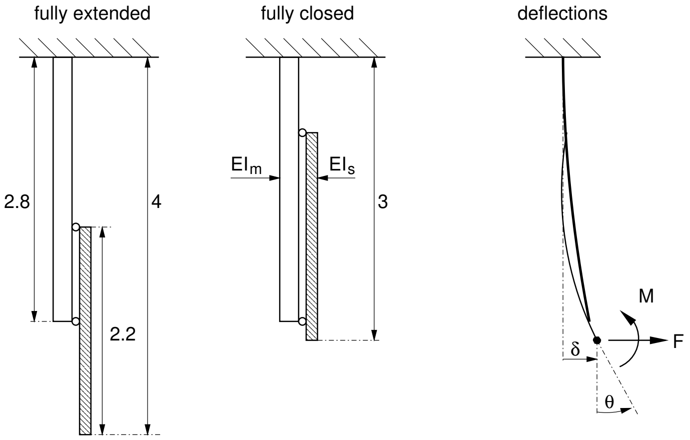
fully extended
fully closed
deflections
2.8
4
2.2
EIm
EIs
3
M
F
δ
θ

Fig. 5.5: Schematisation of main fitting and sliding member.

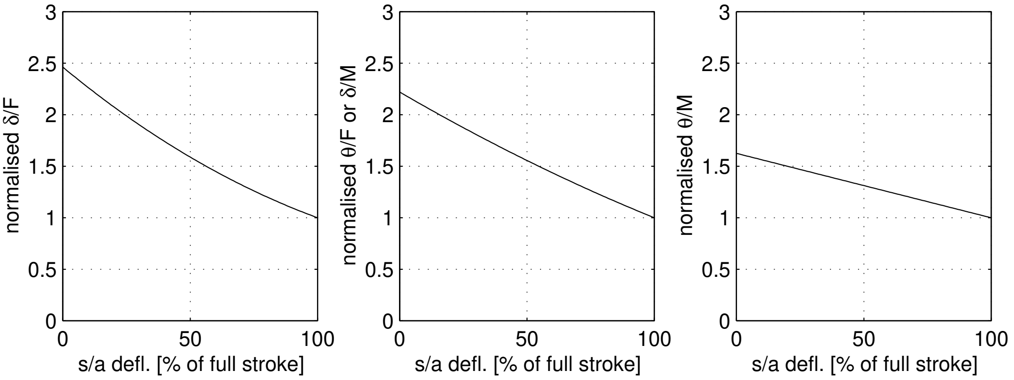

Fig. 5.6: Flexibility as a function of shock absorber deflection (=s/a defl.).

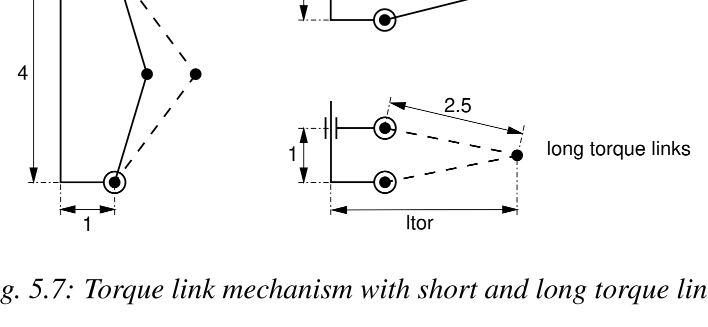
fully extended
fully closed
4
1
2.1
1
short torque links
2.5
1
long torque links
ltor

Fig. 5.7: Torque link mechanism with short and long torque links.

torque link geometry

The torque links prevent rotation of the sliding member with respect to the main fitting about the shock absorber centre line. If a yaw moment is applied the torque links will be loaded and the deflection of the torque links will contribute in the overall yaw flexibility of the landing gear. The upper and lower torque link are connected by a hinge with the main fitting and sliding member respectively; at the apex point they are connected by a spherical joint. In this mechanism the location of the apex joint will be a function of the shock absorber deflection.

A representative numerical example will be given to show the influence of the torque link geometry on the yaw stiffness. Two configurations are considered: short and long torque links, see figure 5.7. In this example it is assumed that only the torque links are flexible and that their bending stiffness is proportional to their length raised to the power three. Some results are given in figure 5.8. It is fairly obvious that the distance between the centreline of the strut and apex joint ($ltor$) will be larger if the long torque links are used. Combined with the reduced bending stiffness, the net result is still an increase in yaw stiffness for a fully extended gear. For the fully closed condition the long torque links lead to approximately 25% reduction of the yaw stiffness with respect to the short torque links in this numerical example. On a real landing gear this effect may be less pronounced due to the local flexibility of the lugs.

Figure 5.8 also illustrates that using short torque links will lead to a stronger dependency of the yaw stiffness on the shock absorber deflection; in this example a factor 3.4 is found between the fully extended and fully closed position. This dependency can be reduced to less than a factor 2 by introducing longer torque links, but this comes at the price of increased mass: just by its dimensions a longer torque link will be heavier. Furthermore the bending stiffness has to be increased in order to maintain the same yaw stiffness in the closed position, this will lead to an additional weight penalty.

effective trail

The mechanical trail e is a very important parameter for shimmy stability. From a flexibility point of view, the ratio between the lateral and yaw motion at the wheel axle centre upon application of a moment about the vertical axis, could be considered as an effective trail. For the models employed in chapter 2 and 3, the effective trail will always equal the mechanical trail. This may not be true for a landing gear as shown in figure 5.4, where an offset exists between the side stay attachment on the main fitting and strut centre line.

This can be illustrated by the following example, see figure 5.9. The main fitting can rotate in the lateral direction about the pintle points (or pintle axle); in this way the gear will be retracted. The support in the lateral direction is provided by the side stay attachment point. In this example we assume that no bending of the main fitting or sliding member occurs when a moment M_z is applied at the wheel axle centre. It is important to note that the moment M_z is only reacted in the pintle points and not at the side stay attachment point. This implies that the torsional deflection above the side stay attachment point will result in a lateral deflection of the strut.

The total lateral deflection at the wheel axle centre now consists of two contributions: the torsional deformation about the strut centre line multiplied with the mechanical trail plus the contribution of the strut lateral displacement. In this particular example the offset

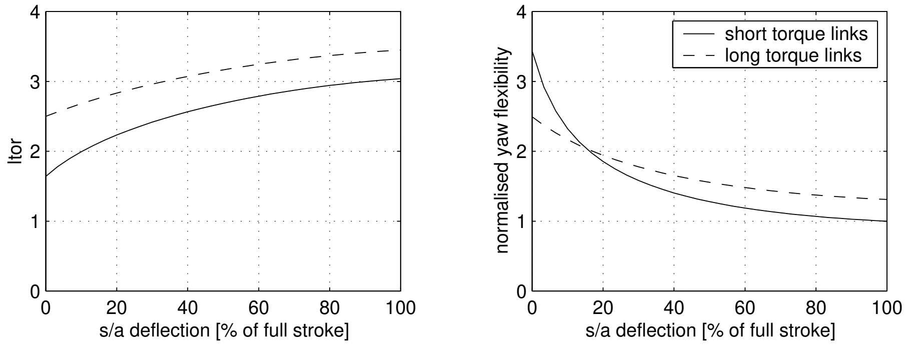

Fig. 5.8: Location of the apex point and yaw flexibility as a function of shock absorber deflection.

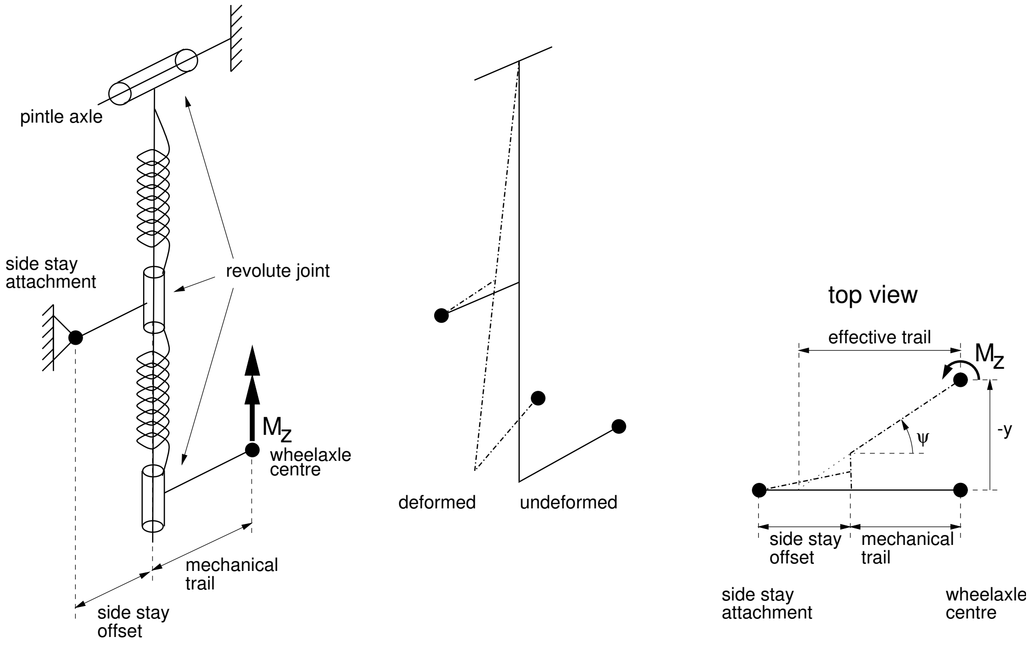
pintle axle
revolute joint
side stay
attachment
M_z
wheelaxle
centre
mechanical
trail
side stay
offset
deformed
undeformed
top view
effective trail
M_z
ψ
-y
side stay
offset
mechanical
trail
side stay
attachment
wheelaxle
centre

Fig. 5.9: Deformation of the landing gear under application of a moment M_z.

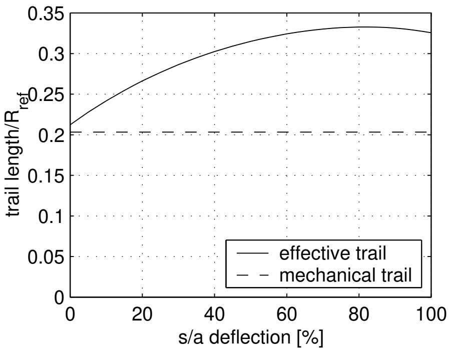

Fig. 5.10: Mechanical and effective trail as a function of shock absorber deflection.

of the side stay will result in the effective trail being larger than the mechanical trail. Due to changes in the torque link geometry large variations in torsional stiffness are to be expected for the part below the side stay attachment, as shown previously. This implies that the effective trail will be a function of the shock absorber deflection and will increase with increasing deflection. This is confirmed by figure 5.10, which is based on a validated finite element model of a landing gear.

Generally the location of the side stay is determined with packaging requirements in mind. It has been shown here that the location of the side stay will also affect the effective trail and therefore shimmy stability. In the available literature, Leve notes that having the side stay attachment point aft of the strut centreline may be beneficial, when trying to obtain a negative effective trail [28].

attachment stiffness

The stiffness at wheel axle level is not only determined by the landing gear, but also by the supporting structure (e.g. local back-up structure, wing and/or fuselage). For a specific aircraft Black notes that 24% of the lateral deflection is caused by fuselage motion [3]. Similarly Krabacher indicates that deflections of the back-up structure may result in a lateral stiffness decrease by a factor 1.5 to 3 [26].

Deflections of the supporting structure are not only present on the aircraft but also when the gear is mounted in a test rig to perform static stiffness tests. For a landing gear lay-out as shown in figure 5.4 it can be expected that the fore/aft motion may be particularly sensitive to deflections of the attachment structure: the distance between the pintle points is relatively small in comparison with the overall gear length. A drag load will result in high differential loading of both pintle points and small deflections of the pintle points may contribute significantly to the total deflection of the landing gear at wheel axle level. In order to obtain the ”true” stiffness of the gear, the test results have to be corrected for deflections of the test rig. This also implies that additional (accurate) instrumentation is required to measure these test rig deflections. Experience gained with one specific landing gear, indicates that the situation will be somewhat less critical for the lateral stiffness and that the test rig may be considered almost infinitely stiff in yaw.

To determine the overall lateral and yaw flexibility and to asses the contribution of the aircraft back-up structure and wing dedicated full-scale tests were performed. The results of these tests were used to validate and improve the FE model. In general, both the application of external forces and the support of the aircraft have to be selected with care in order to create a realistic loading case and not to damage the aircraft. In this particular stiffness test the aircraft was put on jacks and a hydraulic actuator was used to apply an opposite lateral load on both main landing gears at the wheel axle centre, see figure 5.11. In order to include the yaw stiffness an offset case was defined, whereby the lateral load was applied aft of the wheel axle. Wheels and brakes were removed and a special rig was constructed to facilitate this offset loading case. The maximum applied lateral load was approximately 25% of the static vertical load on one landing gear. Deformations of the landing gear were measured at wheel axle level and various other interesting locations.

Reviewing this test, there is some room for improvement. Application of the lateral load at the wheel axle ends may result in some geometrical stiffness effects due to the yaw motion of the wheel axle. Although these effects were taken into account in the model and found to be relatively small, it would be preferable to eliminate them by applying the load close to the centre of the wheel axle. Furthermore, to obtain a clearer distinction

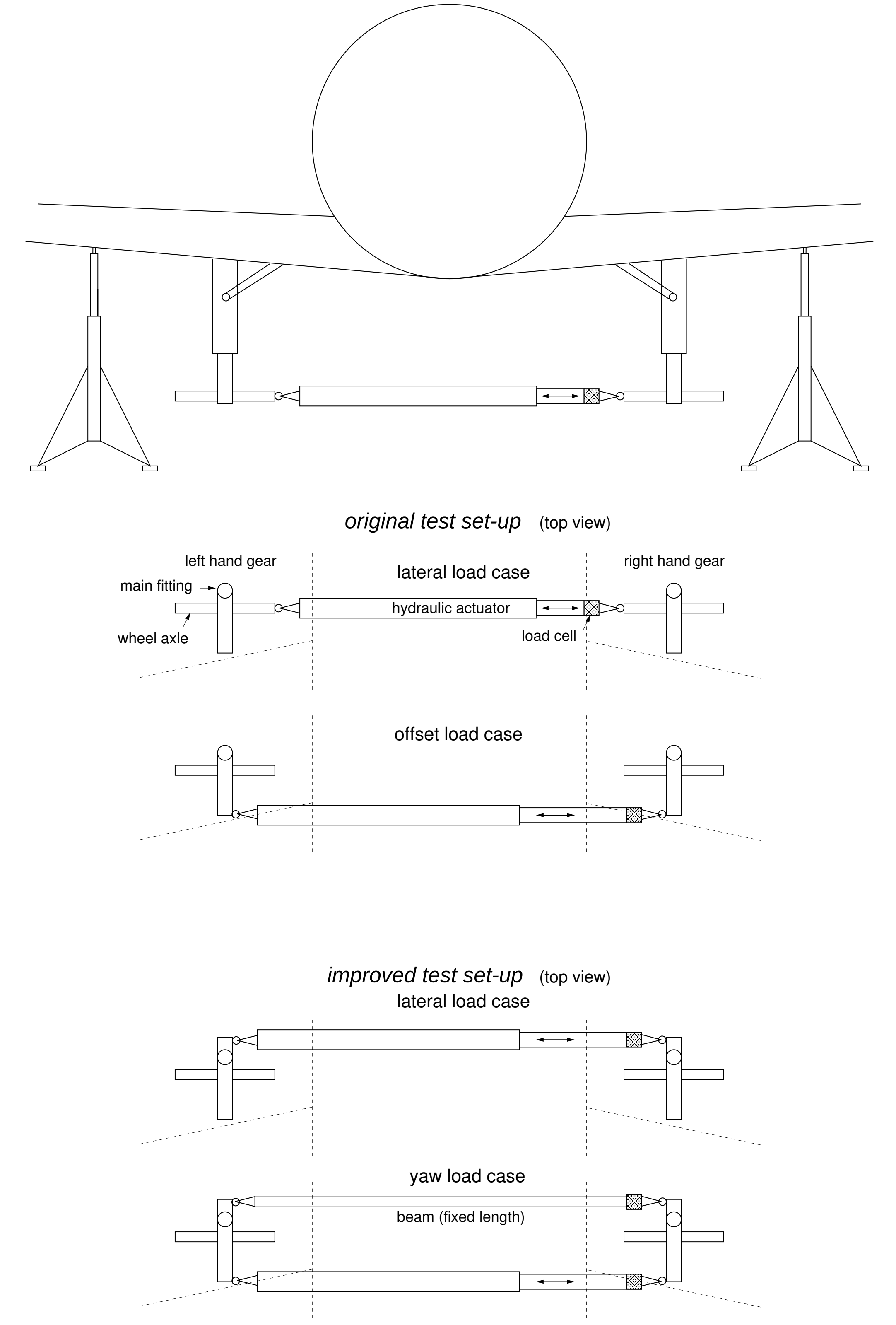
original test set-up (top view)
left hand gear
lateral load case
right hand gear
main fitting
hydraulic actuator
wheel axle
load cell
offset load case
improved test set-up (top view)
lateral load case
yaw load case
beam (fixed length)

Fig. 5.11: Set-up for landing gear stiffness testing on the aircraft (drawing not to scale).

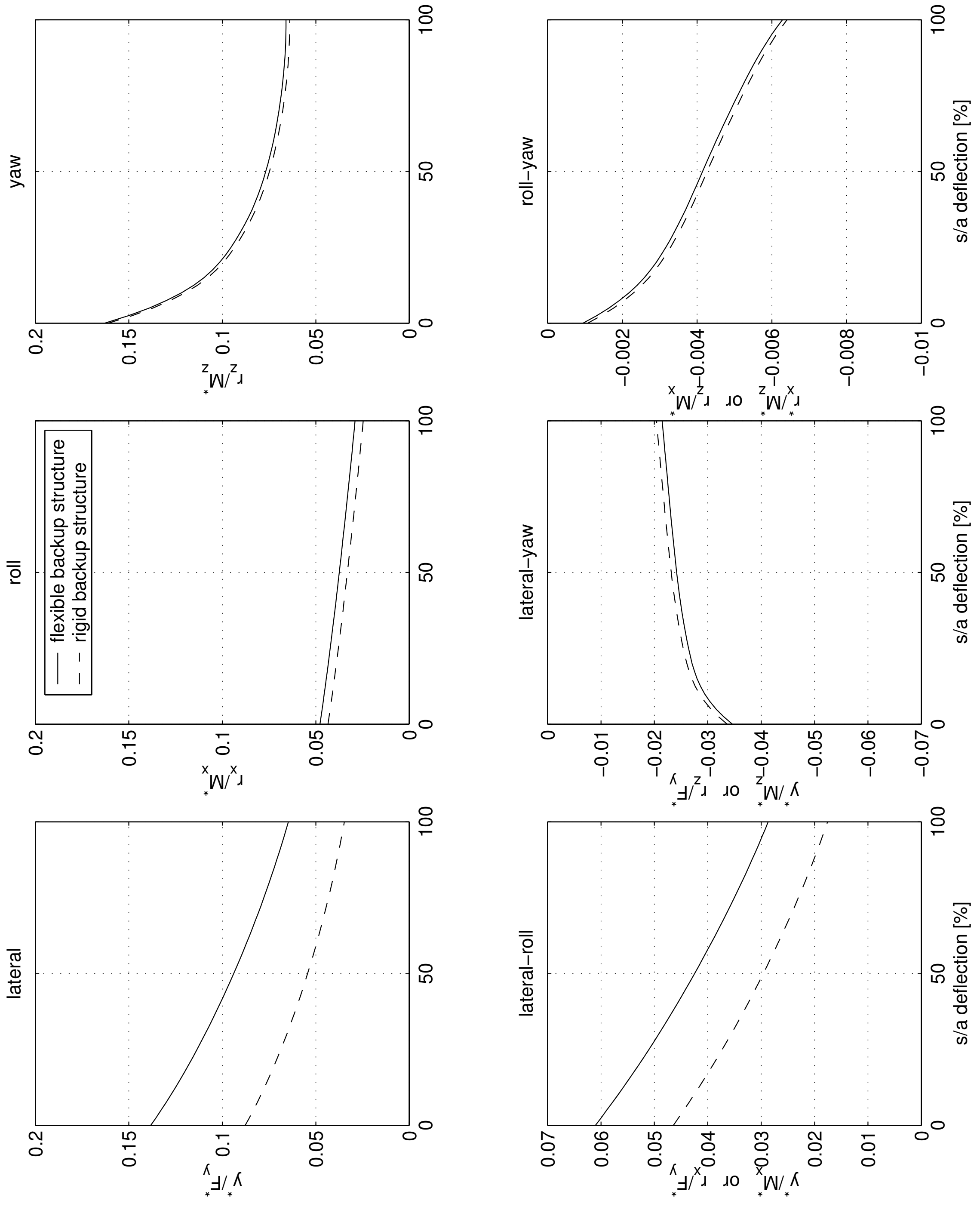

Fig. 5.12: Flexibility of the landing gear in lateral (y), roll (rx) and yaw (rz) direction at the wheel axle centre as a function of shock absorber deflection, excluding and including fuselage flexibility (validated FE model).

between the lateral and yaw load case one could decide to apply the lateral load at a point in front of the wheel axle in order to limit the yaw deflection. If this distance is close to the effective trail, the yaw rotation will be small to negligible. To enhance the yaw load case the actuator not only has to operate with an offset to the wheel axle, but a second beam (equipped with a load cell) connecting both landing gears could be introduced to restrict the lateral motion, see figure 5.11. By testing in this way more distinctive test results can be expected.

The influence of aircraft back-up structure deformations on the flexibility at the wheel axle centre is presented in figure 5.12. Note that this figure only shows the lateral (y), roll (rx) and yaw (rz) components, which are the most relevant for shimmy. It can be seen that the back-up structure flexibility mainly affects the lateral and roll motion of the gear under lateral loading (or vice versa: the lateral motion of the gear when a roll moment is applied). For yaw, the back-up structure is relatively stiff compared to the landing gear, so its contribution to the total gear deflection will be limited.

Furthermore figure 5.12 illustrates the dependency of the landing gear flexibility on shock absorber deflection. From the preceding analysis it is obvious that the flexibility decreases with increasing shock absorber deflection. The conceptual models introduced in this section may also be helpful in understanding the shape of the various curves.

5.3 Free-play

Various parts of the landing gear and back-up structure have to move with respect to each other; not only during landing impact but also when the gear is retracted in the wing and fuselage. Most connections are plain bearings, so some tolerances are required to allow a relative motion and assembly. Typical examples are the torque link assembly (torque link hinges, apex joint), upper and lower bearing between main fitting and sliding member, various hinges in the side stay assembly and pintle lugs. Summing the contributions of the various connections a fair amount of free-play can be expected at the wheel axle centre, typically in the order of millimetres in lateral and fore/aft direction and less than one degree in yaw.

Due to the changes in torque link geometry and overlap, it can be expected that the amount of free-play at the wheel axle centre in fore/aft, lateral and yaw direction will be a function of the shock absorber deflection. This has been verified experimentally by determining the amount of free-play from the stiffness measurements. For the simulation model development, it was found that the overall free-play as a function of shock absorber deflection can be represented fairly accurately by lumping the lateral free-play in the side-stay and the yaw free-play as a translational degree of freedom at the apex joint.

Free-play is modelled as a non-linear spring, see figure 5.13. Some deflection is possible before a force develops and if the amplitude remains within the free-play band the spring force will be zero. Grossmann suggests two different formulas to determine an equivalent linear stiffness c_{eq} as a function of amplitude outside the free-play band ($a_m > a_{fp}$) [15]:

$$c_{eq} = c\left(1 - \frac{a_{fp}}{a_m}\right) \tag{5.3}$$

$$c_{eq} = c\left(1 - \left(\frac{a_{fp}}{a_m}\right)^2\right) \tag{5.4}$$

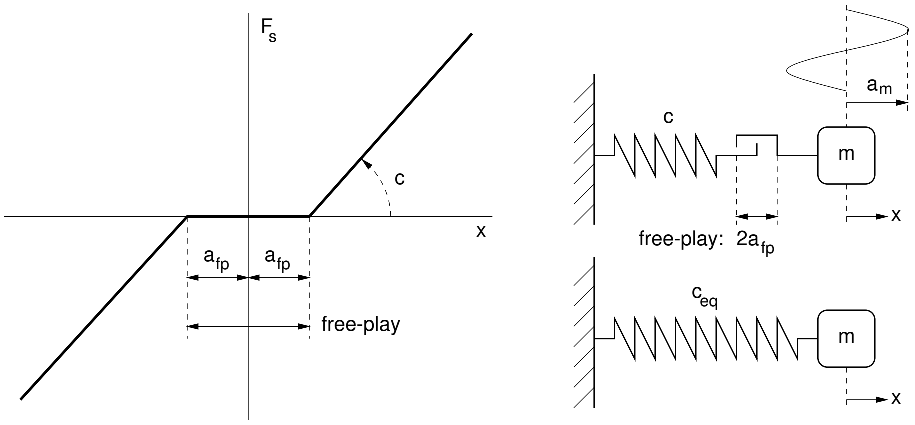

Fig. 5.13: Modelling free-play.

With a_m the amplitude of the motion and a_{fp} half of the free-play. Obviously the stiffness has become a function of the amplitude of the motion and will increase with the amplitude of the motion, see figure 5.14. In the shimmy analyses performed by Grossmann equation 5.3 gave a better correspondence with the non-linear simulations than equation 5.4. This is confirmed by simulations with a single degree of freedom mass-spring system with the free-play included, as shown in figure 5.13. The equivalent linear stiffness c_{eq} is defined as the stiffness which will result in the same resonance frequency as the non-linear simulation. These simulation results are also shown in figure 5.14 and suggest that the equivalent stiffness may even be lower than the estimated values using equation 5.3.

From the results presented in chapter 2 and 3 it will be clear that any change to the stiffness will affect shimmy stability. For example the equivalent yaw stiffness will be reduced by introducing yaw free-play; for a gear with a positive mechanical trail this may easily result in shimmy vibrations. This has been reported in the available literature various times, see e.g. references [2], [12], [15], [29], [51]. Less well known seems to be the fact that introducing lateral free-play may actually be beneficial for some landing gear configurations; this is illustrated by figure 5.15.

Free-play will increase with the number of flights due to wear. Though it may be possible to solve shimmy vibration problems in the prototype phase by applying tight tolerances, the problems will often reoccur after a certain number of flights on the aircraft in service. Furthermore it is possible that the balance between the lateral and yaw free-play is modified by replacing certain components, which potentially can make the gear more unstable.

5.4 Friction

The relative motion of the sliding member with respect to the main fitting will be opposed by friction forces at the upper and lower bearing. The main component of these friction forces originates from Coulomb friction on the bearing surface and will be proportional to the normal force on the bearing surface; a commonly used value for the friction coefficient μ is 0.05. The seals will also contribute to the total friction force. As shown in figure 5.1 the pressurised shock absorber is an integral part of the landing gear and various seals are present to prevent the loss of oil and to maintain the pressure differences across the bearings.

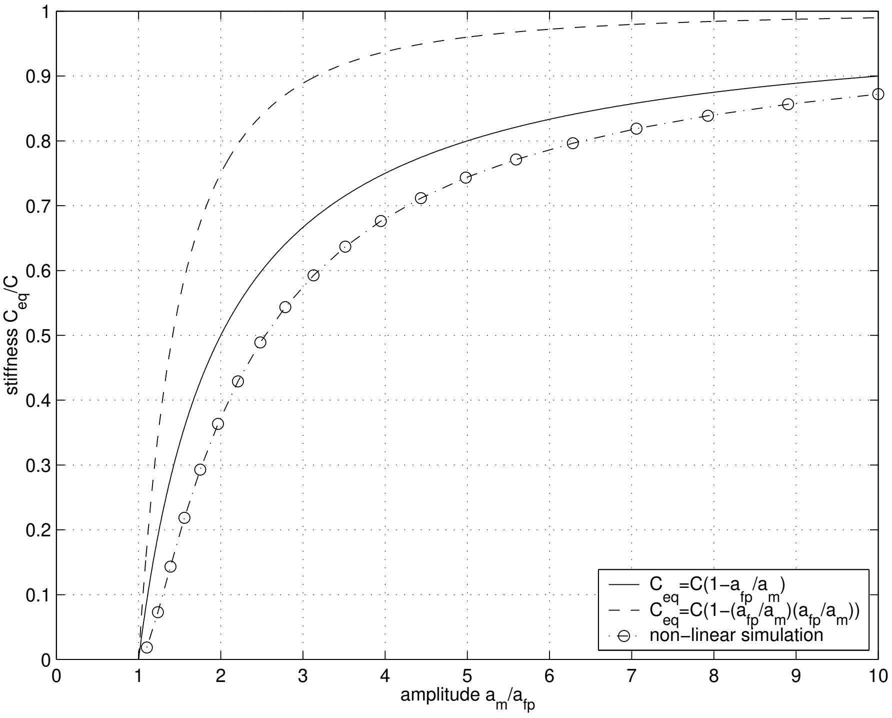

Fig. 5.14: Effective stiffness as a function of motion amplitude for a system with free-play.

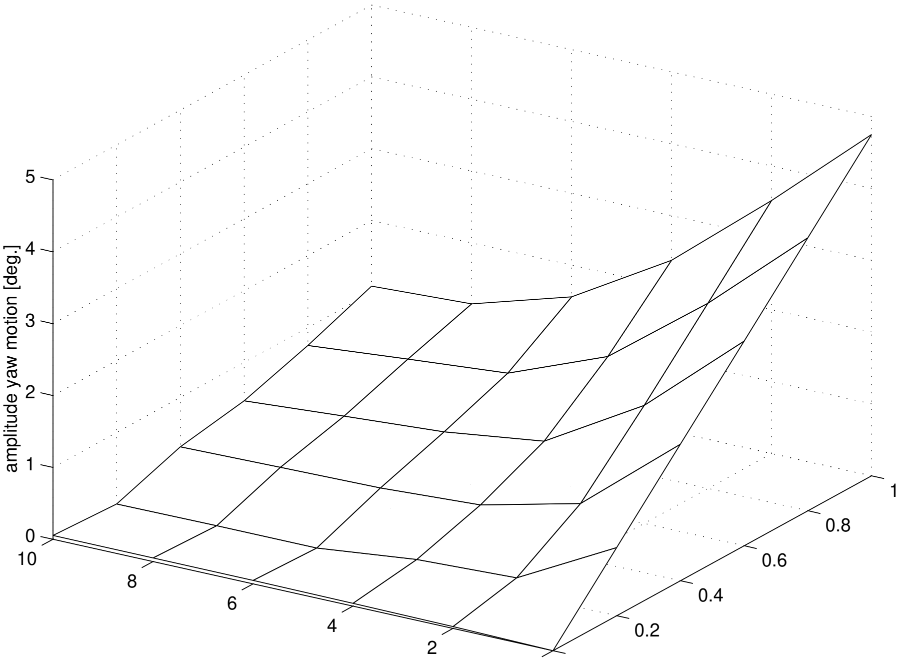

Fig. 5.15: Limit cycle amplitude as a function of yaw and lateral free-play.

Coulomb friction is a highly non-linear phenomenon. If the tangential forces in the contact area remain below the friction force F_w, both parts will be locked and the relative motion will be blocked. If a relative motion occurs, the friction force will be opposite to the relative velocity but the magnitude will be independent of this velocity. Friction may be approximated by an equivalent linear damping constant using linearisation techniques. A sinusoidal motion will be considered:

$$x(t) = a_m \sin \omega t \tag{5.5}$$

The energy dissipation during one cycle should be the same for the friction force and the equivalent damper:

$$W = \int_0^T F_w \operatorname{sgn}(\dot{x}(t))\, \dot{x}(t)\, dt = \int_0^T k_{eq} \dot{x}(t)\, \dot{x}(t)\, dt \tag{5.6}$$

Solving this integral gives the following result:

$$k_{eq} = \frac{4F_w}{\pi \omega a_m} = \frac{2F_w}{\pi^2 f a_m} \tag{5.7}$$

So the resulting equivalent damping k_{eq} is inversely proportional to the amplitude of the motion.

For normal rolling conditions, in the absence of e.g. spin-up or braking forces and the strut centre line perpendicular to the ground, the normal force F_n on the bearings will read (see also figure 5.16):

$$F_n = F_z \left(\frac{e}{l_b} \right) \tag{5.8}$$

The friction force F_w reads:

$$F_w = \mu F_n \tag{5.9}$$

So it is obvious that also the length of the mechanical trail e and overlap l_b will affect the magnitude of the friction forces. It can also be noted that the overlap increases with shock absorber deflection, see figure 5.4.

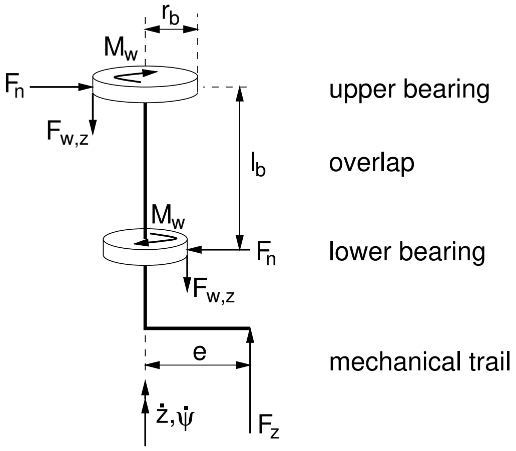

Fig. 5.16: Friction forces acting on the sliding member.

The Coulomb friction force will be opposite to the local, relative velocity on the bearing surfaces when the sliding member moves with respect to the main fitting. This is illustrated by figure 5.16. In case of a pure axial motion, $\dot{\psi} = 0$, the friction forces will be oriented parallel to the strut centre line. For a pure yaw motion, $\dot{z} = 0$, the friction forces are oriented tangentially and a friction moment M_w will be generated which opposes the yaw motion. Obviously, also combinations of axial and yaw motion are possible in which case the magnitude of the friction force F_w will remain constant, but the components in the different directions will depend on the relative magnitude of the velocity:

$$F_{w,z} = \mu F_n \left(\frac{\dot{z}}{\sqrt{\dot{z}^2 + (r_b \dot{\psi})^2}} \right) \tag{5.10}$$

$$M_w = \mu F_n \left(\frac{r_b^2 \dot{\psi}}{\sqrt{\dot{z}^2 + (r_b \dot{\psi})^2}} \right) \tag{5.11}$$

In these equations r_b is the radius of the bearing. As indicated in figure 5.16 the radius of the upper bearing will be larger than the lower bearing radius; for a real landing gear this difference will be about 15%. It seems permissible to use an average value for the bearing radius considering the relative inaccuracy of the friction coefficient.

From equation 5.11 it can be seen that by increasing the axial velocity component $\dot{z}$, it is possible to reduce the friction moment in yaw M_w. This result has a rather important implication: in the first seconds after landing impact the shock absorber deflection will vary in a dynamic way, before settling for a static position as is illustrated by figure 5.2. This also implies that the friction moment M_w will be relatively small and the (equivalent) damping of the yaw motion will be reduced under these conditions. This mechanism has also been described in reference [16].

The importance of friction on the shimmy stability should not be under estimated. For a certain landing gear instrumented taxi tests were performed up to very high forward velocities, without any indication of a possible shimmy instability. Nevertheless the same gear experienced a very severe shimmy instability just shortly after landing impact. The forward velocity during this particular landing was well within the range covered by the taxi tests. Apparently the reduced friction in yaw in the first seconds after landing impact, combined with a yaw disturbance due to asymmetrical spin-up of the wheels, see section 5.8, may have triggered the shimmy instability.

5.5 Eigenfrequencies and mode shapes

Modal testing can be performed on the landing gear with the aim of identifying eigenfrequencies and the accompanying mode shapes. These results can be used again in the process of validation of the landing gear structural model; the underlying idea is that the static stiffness tests are used to verify the flexibility and the modal tests can be used to verify the mass and inertia properties of the landing gear. Modal tests on the landing gear were performed both on the aircraft and test rig.

The main problem with modal testing of the landing gear is the strong dependency of the results on the excitation level. Some experimental results to illustrate this are presented in figure 5.17. In particular the yaw resonance frequency is highly dependent on the excitation level: the experimentally determined resonance frequency varies between 14 and 24 Hz. Obviously the mass and inertia of the gear are independent of the amplitude, so this behaviour has to be caused by non-linear stiffness characteristics of the gear.

In particular for the yaw resonance frequency different stages can be identified. Friction forces at the upper and lower bearing will lock the relative motion between sliding member and main fitting for small amplitude excitation. The yaw stiffness obtained in this way will be about a factor 2 to 3 higher compared to the normal condition, when the entire load is transferred through the torque links; this results in a high resonance frequency. As the amplitude is increased the friction forces will not be able to lock the sliding member and main fitting and gradually the load will be passed though the torque links. Since a large portion of the free-play will be located in the torque link assembly, the effective stiffness will again be a function of the amplitude (see figure 5.14). The effective stiffness increases with increasing amplitude and this will again result in an increase of the resonance frequency as can be seen in figure 5.17. These phenomena have also been reported independently by Woerner [51].

Despite understanding the experimental results, the question remains how to utilise them for validation of the FE model of the landing gear. Since the majority of the test results were available for a low level excitation it was decided to lock the sliding member and main fitting in the FE model and make a comparison between the calculated and experimental results. At that stage the stiffness of the model had already been tuned to give the best match with the experimental results and the mass and inertia properties of various components had already been assessed. It was found that the results (both frequency and mode shapes) matched quite well, so no modifications were made to improve the model. This means that the modal tests were only used to gain additional confidence in the model, but may not be strictly necessary in the development of the landing gear model.

For the large amplitude excitation results, also a comparison can be made between test and model; in this case without locking sliding member and main fitting in the FE model, obviously. It appeared that in the modal tests the amplitude was not large enough in comparison to the free-play; the measured resonance frequencies tended to be too low compared to model results. This could have been prevented by either increasing the amplitude further, which was impossible for actuators in use, or by eliminating free-play. Despite the logic of testing the landing gear ”as is”, it can be argued that more useful results could have been obtained for model validation purposes by eliminating free-play as much as reasonably possible.

The four lowest eigenfrequencies of the landing gear model are shown in figure 5.18; these eigenfrequencies will again be a function of the shock absorber deflection due to the varying stiffness. The accompanying mode shapes are shown in figure 5.19 up to figure 5.22, they apply to 87.5% shock absorber deflection. These results have been calculated including the aircraft back-up structure, the wheels locked on the wheel axle and no locking of the main fitting with respect to the sliding member.

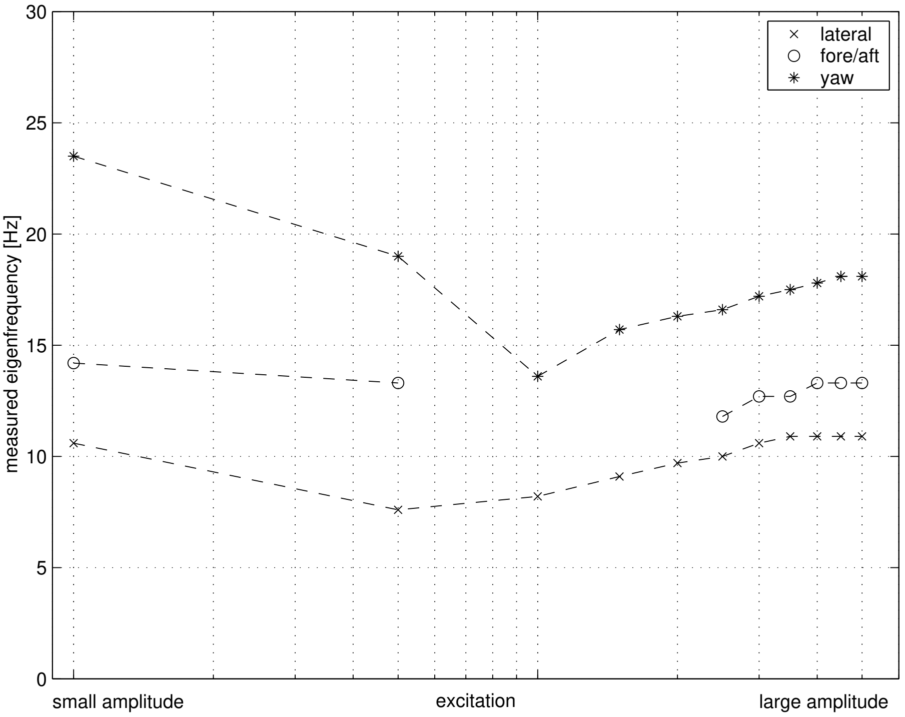

Fig. 5.17: Measured eigenfrequencies measured as a function of excitation amplitude.

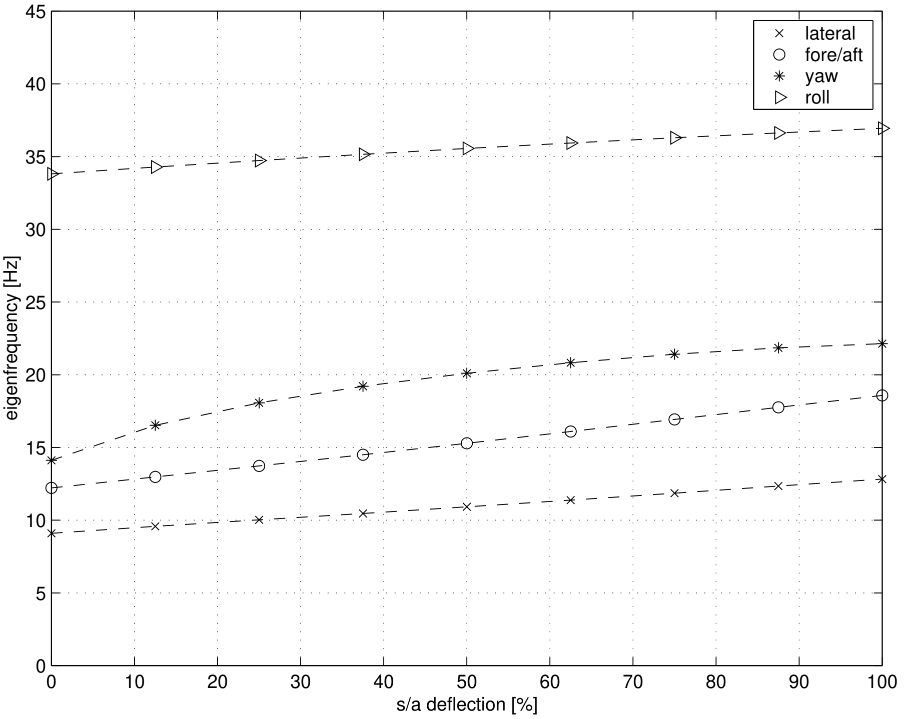

Fig. 5.18: Eigenfrequencies as a function of shock absorber deflection.

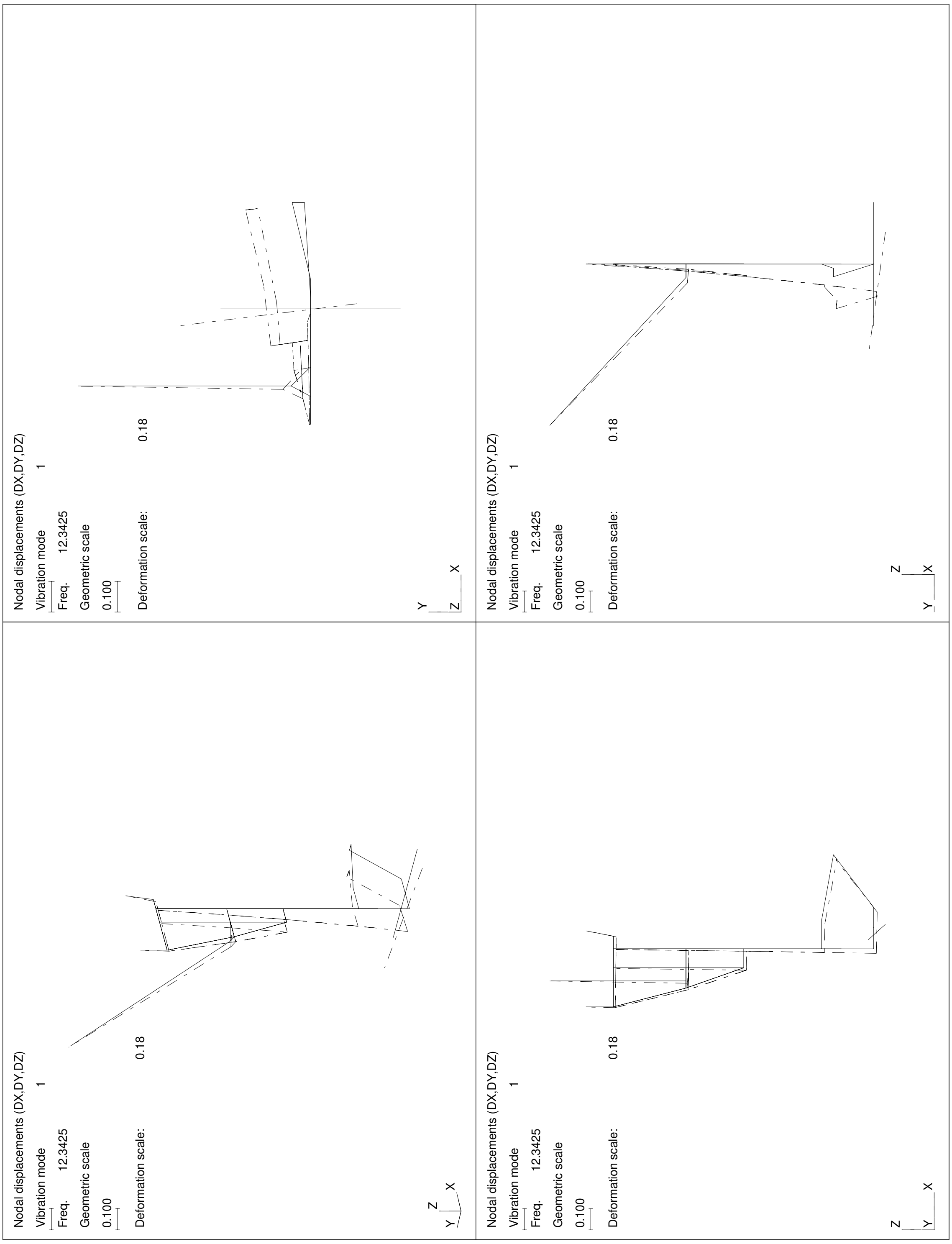
Nodal displacements (DX,DY,DZ)
Vibration mode 1
Freq. 12.3425
Geometric scale
0.100
Deformation scale: 0.18
Y
Z
X
Nodal displacements (DX,DY,DZ)
Vibration mode 1
Freq. 12.3425
Geometric scale
0.100
Deformation scale: 0.18
Z
Y
X
Nodal displacements (DX,DY,DZ)
Vibration mode 1
Freq. 12.3425
Geometric scale
0.100
Deformation scale: 0.18
Y
Z
X
Nodal displacements (DX,DY,DZ)
Vibration mode 1
Freq. 12.3425
Geometric scale
0.100
Deformation scale: 0.18
Z
Y
X

Fig. 5.19: Lateral mode of the landing gear.

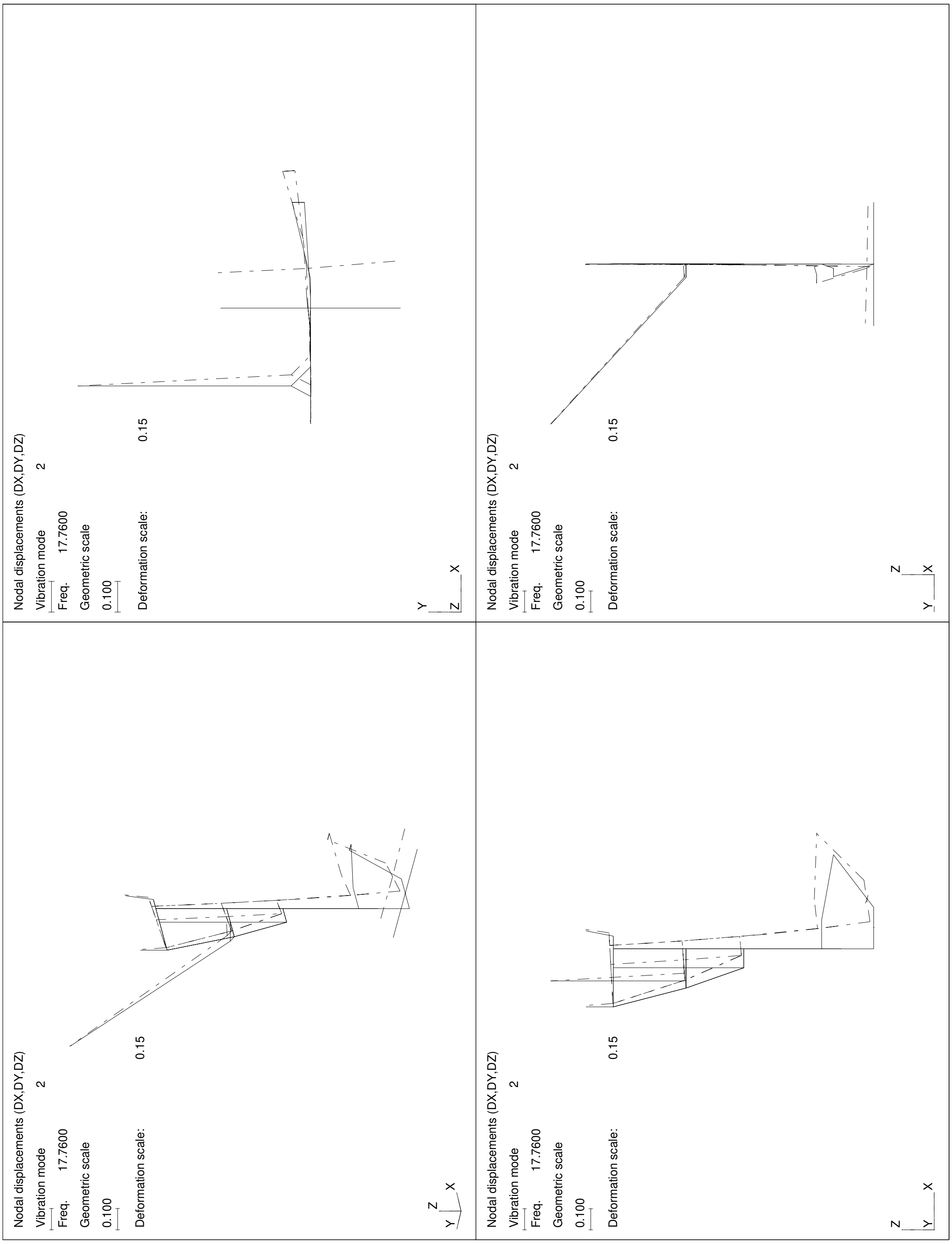
Nodal displacements (DX,DY,DZ)
Vibration mode 2
Freq. 17.7600
Geometric scale
0.100
Deformation scale: 0.15
Y
Z
X
Nodal displacements (DX,DY,DZ)
Vibration mode 2
Freq. 17.7600
Geometric scale
0.100
Deformation scale: 0.15
Z
Y
X
Nodal displacements (DX,DY,DZ)
Vibration mode 2
Freq. 17.7600
Geometric scale
0.100
Deformation scale: 0.15
Y
Z
X
Nodal displacements (DX,DY,DZ)
Vibration mode 2
Freq. 17.7600
Geometric scale
0.100
Deformation scale: 0.15
Z
Y
X

Fig. 5.20: Fore/aft mode of the landing gear.

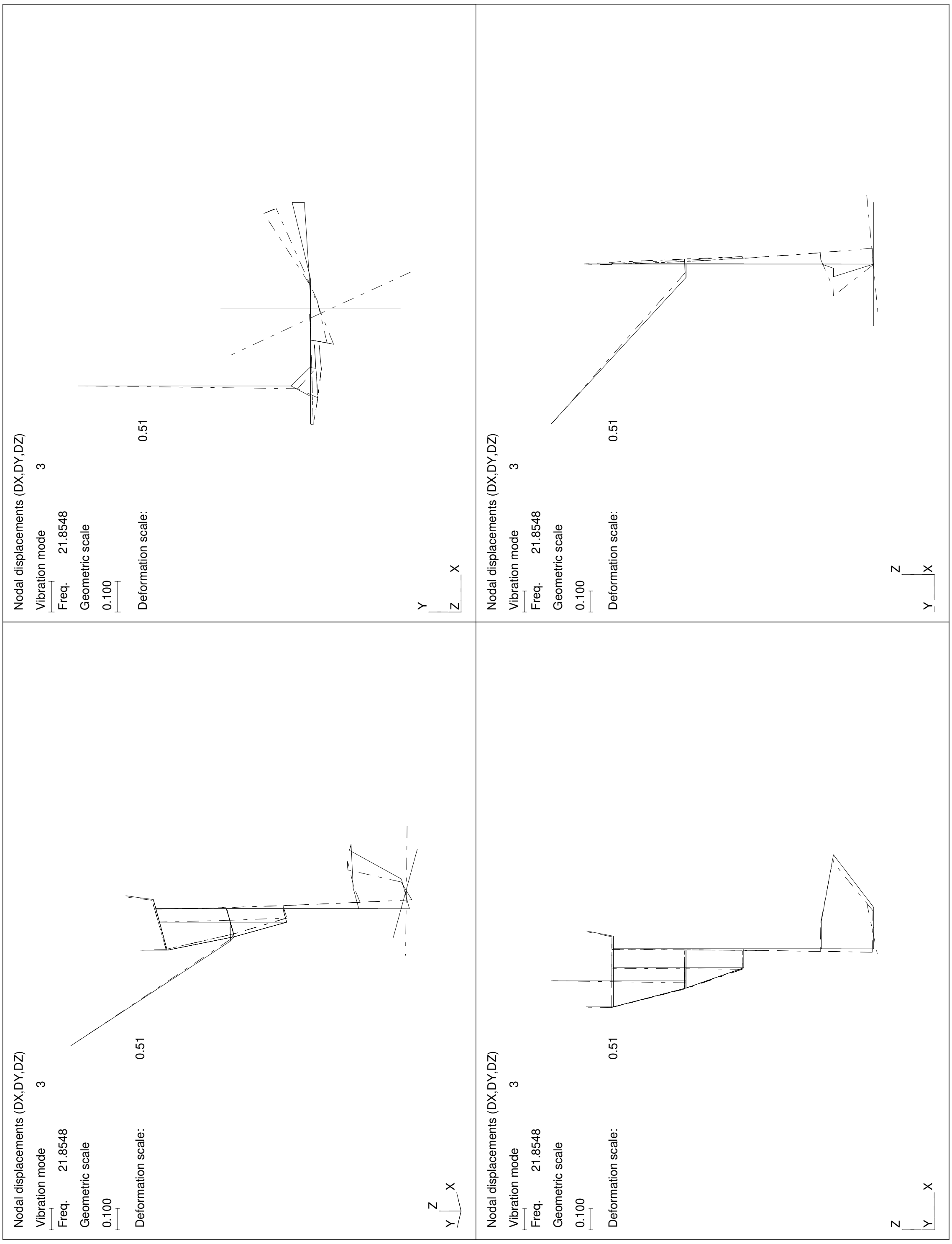
Nodal displacements (DX,DY,DZ)
Vibration mode 3
Freq. 21.8548
Geometric scale
0.100
Deformation scale: 0.51
Y
Z
X
Nodal displacements (DX,DY,DZ)
Vibration mode 3
Freq. 21.8548
Geometric scale
0.100
Deformation scale: 0.51
Z
Y
X
Nodal displacements (DX,DY,DZ)
Vibration mode 3
Freq. 21.8548
Geometric scale
0.100
Deformation scale: 0.51
Y
Z
X
Nodal displacements (DX,DY,DZ)
Vibration mode 3
Freq. 21.8548
Geometric scale
0.100
Deformation scale: 0.51
Z
Y
X

Fig. 5.21: Yaw mode of the landing gear.

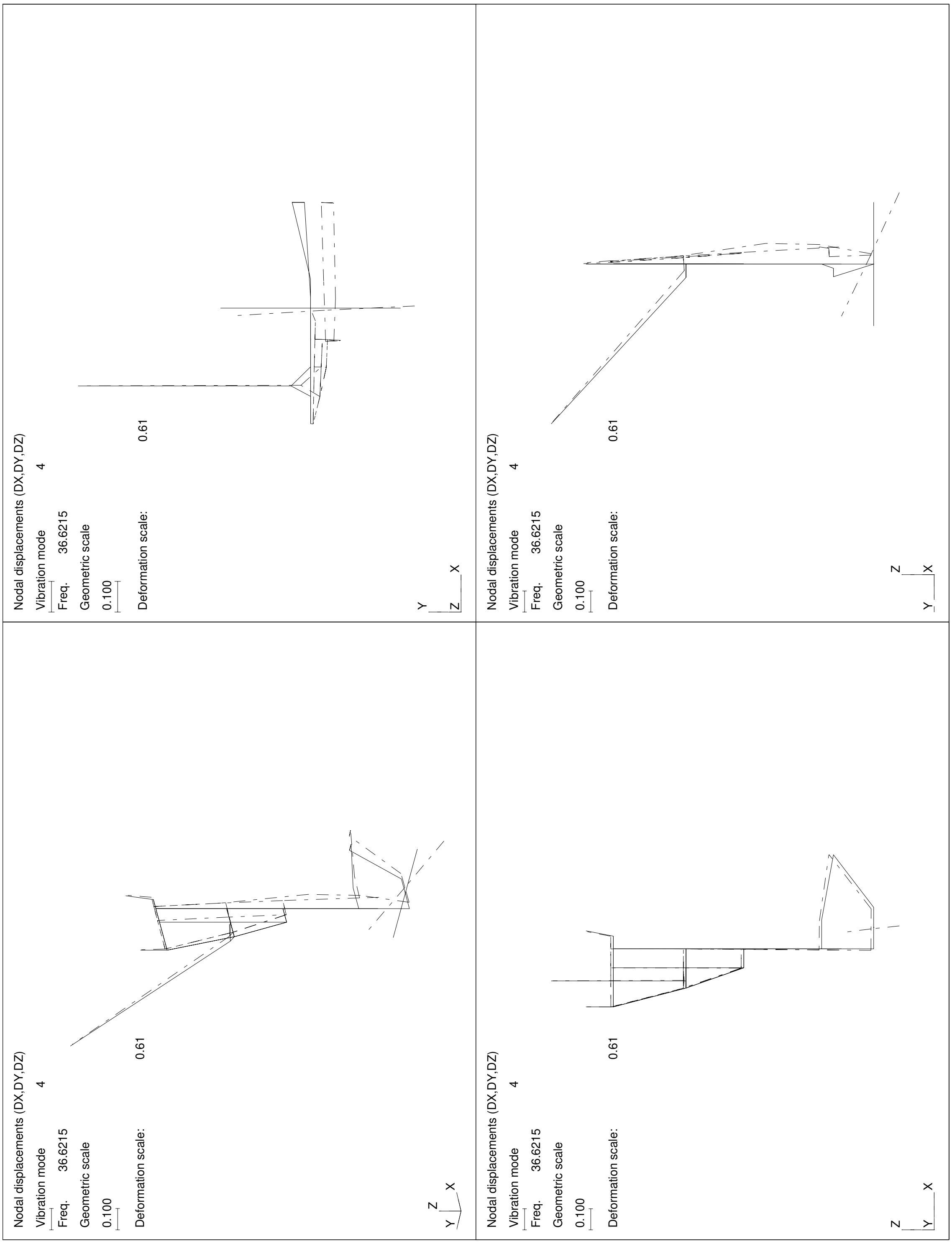
Nodal displacements (DX,DY,DZ)
Vibration mode 4
Freq. 36.6215
Geometric scale
0.100
Deformation scale: 0.61
Y
Z
X
Nodal displacements (DX,DY,DZ)
Vibration mode 4
Freq. 36.6215
Geometric scale
0.100
Deformation scale: 0.61
Y
Z
X
Nodal displacements (DX,DY,DZ)
Vibration mode 4
Freq. 36.6215
Geometric scale
0.100
Deformation scale: 0.61
Z
Y
X
Nodal displacements (DX,DY,DZ)
Vibration mode 4
Freq. 36.6215
Geometric scale
0.100
Deformation scale: 0.61
Y
Z
X

Fig. 5.22: Roll mode of the landing gear.

5.6 Non-linear behaviour of the shimmy damper

In section 3.6 the introduction of a *linear* shimmy damper to improve shimmy stability was discussed. Shimmy dampers can be found on the main landing gears of e.g. the Boeing 737, Airbus A-320, McDonnell Douglas MD-80 and Fokker 100. The shimmy damper is installed at the apex joint, see figure 1.2, and operates in series with the torque links.

The shimmy dampers in use on various aircraft have a non-linear spring and damping characteristic. The internal lay-out of the shimmy damper is illustrated by figure 5.23. The centring springs combined with the spring cage will result in a preload, see figure 5.24. Flexibility of the spring cage will mainly attribute to the high stiffness about the centre position. Furthermore the overall stroke of the damper is limited. The damping force is generated by a turbulent oil flow through an orifice with constant dimensions, which will result in a velocity squared damping force. This is identical to the operation of the shock absorber as discussed in section 5.1.

The non-linear shimmy damper characteristics may be linearised using a harmonic balance. A sinusoidal input signal will be assumed:

$$x(t) = a_m \sin \omega t \tag{5.12}$$

The expression for the equivalent stiffness using the harmonic balance:

$$c_{eq} = \frac{\displaystyle\int_0^T F_s(t)x(t)dt}{\displaystyle\int_0^T x(t)^2 dt} \tag{5.13}$$

The spring is assumed to be a piecewise linear function as indicated in figure 5.24, with c_1 the stiffness near the centre position, c_2 the off-centre stiffness and F_p the preload force. We will now consider motions about the centre position within the maximum damper stroke but outside the preload, $x_p < a_m < x_m$. Solving equation 5.13 results in:

$$c_{eq} = \frac{a_m^2 c_1 (2\theta_p - \sin 2\theta_p) + a_m^2 c_2 (\pi - 2\theta_p + \sin 2\theta_p) + 4F_p a_m cos\theta_p \left(1 - \dfrac{c_2}{c_1}\right)}{a_m^2 \pi} \tag{5.14}$$

with:

$$\theta_p = \arcsin\left(\frac{F_p}{a_m c_1}\right) \tag{5.15}$$

The damping force is quadratically dependent on velocity:

$$F_d = k_{sd,q}\dot{x}|\dot{x}| \tag{5.16}$$

Again the harmonic balance can be applied:

$$k_{eq} = \frac{\displaystyle\int_0^T F_d(t)\dot{x}(t)dt}{\displaystyle\int_0^T \dot{x}(t)^2 dt} \tag{5.17}$$

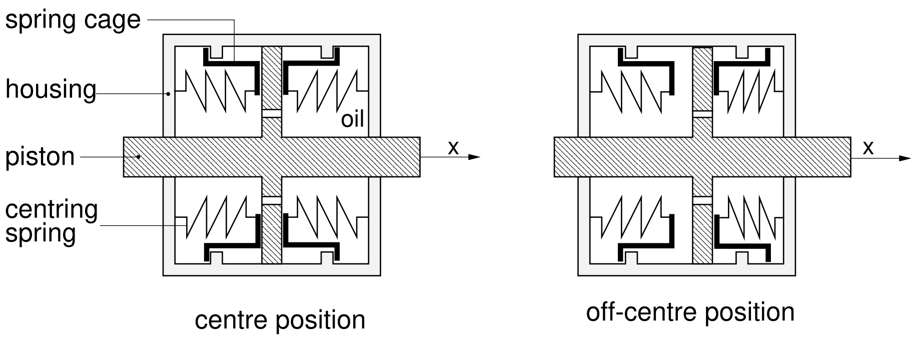
spring cage
housing
piston
centring spring
oil
x
x
centre position
off-centre position

Fig. 5.23: Schematic lay-out of the shimmy damper.

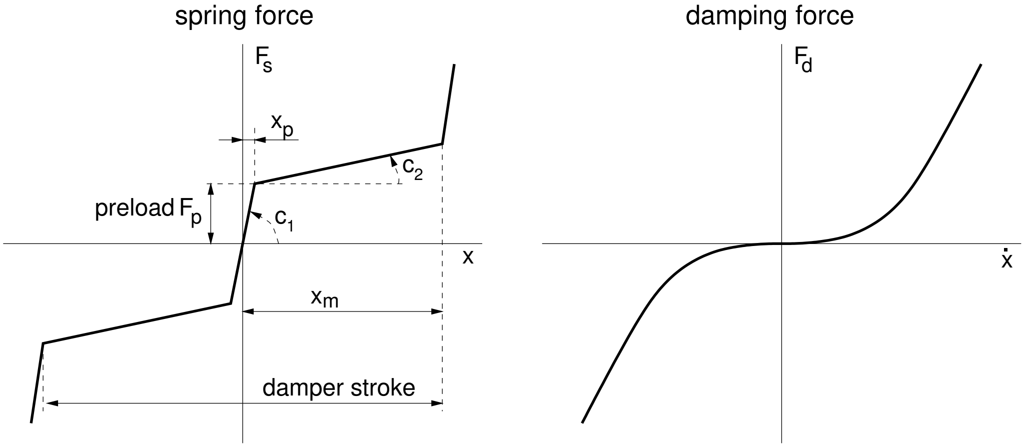

Fig. 5.24: Non-linear characteristics of the shimmy damper.

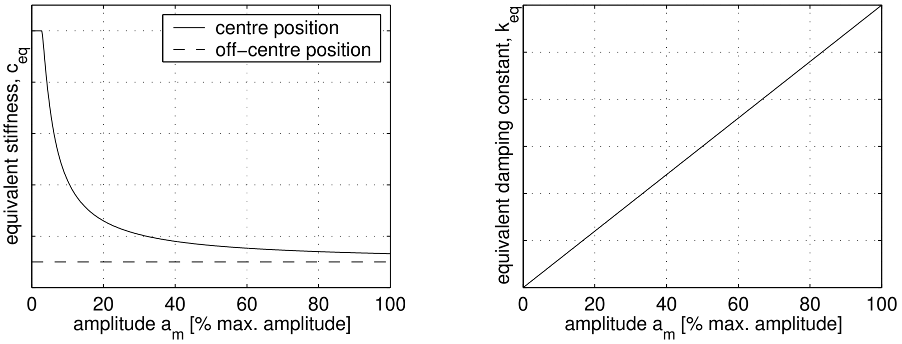

Fig. 5.25: Equivalent stiffness and damping constant as a function of damper amplitude.

It may be noted that in this particular case the harmonic balance is identical to requiring that the work done in one cycle is equal for the non-linear and the equivalent linear damper:

$$W = \int_0^T F_d(t)\,\dot{x}(t)\,dt = \int_0^T k_{eq}\dot{x}(t)\,\dot{x}(t)\,dt \tag{5.18}$$

Solving equation 5.17, the next expression for the equivalent linear damping constant can be obtained:

$$k_{eq} = \frac{8}{3\pi} a_m k_{sd,q}\,\omega = \frac{16}{3} a_m k_{sd,q} f \tag{5.19}$$

From equations 5.14 and 5.19 it can be concluded that both the equivalent stiffness and damping will be a function of the amplitude of the motion of the shimmy damper a_m. A representative example is shown in figure 5.25, which also illustrates the difference in equivalent stiffness when the damper motion is off-centre and does not encounter the preload.

In section 3.6 a *linear* shimmy damper was investigated. Summarising the results it can be observed that the damping constant k_{sd} requires tuning (figure 3.31) and that the stiffness of the shimmy damper c_{sd} should be sufficiently low to allow the damper to work (figure 3.37). In this section it is shown that the behaviour of a real shimmy damper may be highly amplitude dependent. In particular for small amplitudes this may become apparent: the equivalent damping constant will be low and the stiffness will be high, so despite the presence of a shimmy damper, the system could still be unstable. But as the amplitude grows, due to the instability, the equivalent stiffness will drop and the damping constant increases and a stable limit cycle may be encountered.

The existence of this limit cycle has been confirmed by simulations; in these particular simulations the shimmy damper is the only non-linear element. Two typical time histories are shown in figure 5.26, using either a small or large initial disturbance. The validity of the linearisation techniques as described in this section is illustrated by figure 5.27. For each damper amplitude the system can be linearised and damping of the least damped mode can be calculated. As shown in figure 5.27 the amplitude where the damping equals zero corresponds fairly well to the limit cycle amplitude in the non-linear simulation.

A final note is that coulomb friction in the yaw direction may prevent the development of a limit cycle. Friction may be approximated by an equivalent damping constant as was shown in section 5.4. This equivalent damping constant is inversely proportional to the amplitude of the motion, see equation 5.7 and may stabilise the system for small amplitudes.

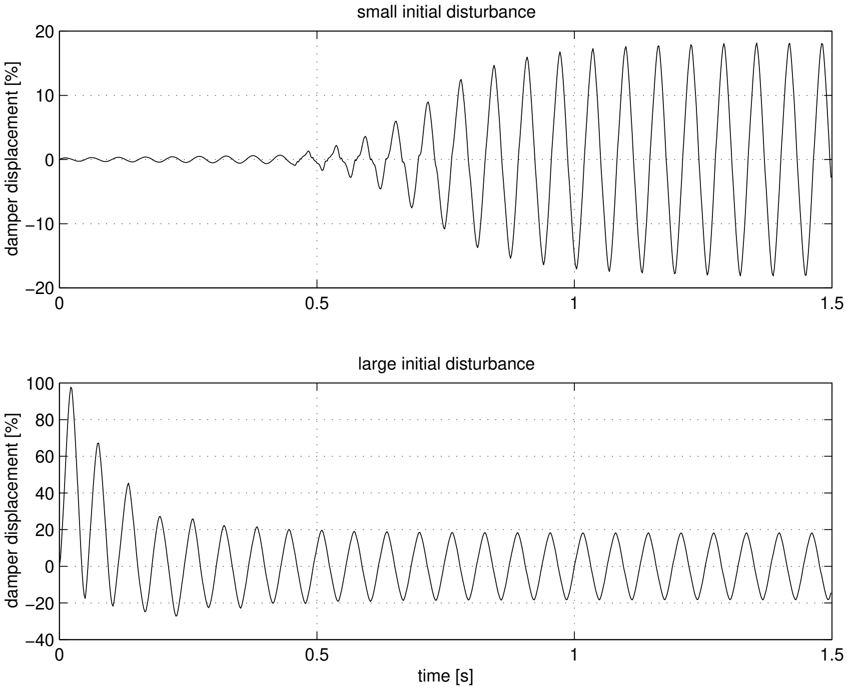

Fig. 5.26: Simulation results with non-linear shimmy damper model showing a limit cycle.

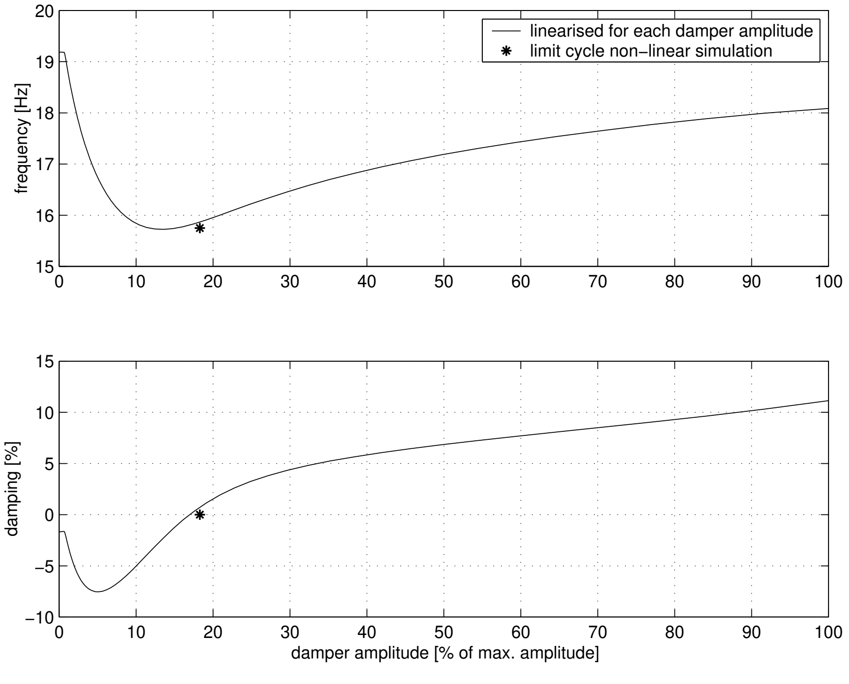

Fig. 5.27: Stability as function of damper amplitude using linearised shimmy damper characteristics.

5.7 Model development

Traditionally, the equations of motion of landing gear and tyre are derived by hand. The next step is translating these equations into software in order to perform time-domain simulations or to calculate the eigenvalues. Generally, these in-house developed software programmes are written in FORTRAN, possibly using a numerical library in addition (e.g. NAG-library). Nowadays, the MATLAB/Simulink environment (or equivalent software packages) is a more natural choice; much of the required functionality is readily available: integrators, eigenvalue analysis, plotting facilities, etc. Furthermore this environment tends to be more flexible compared to in-house developed software. It should be noted however, that these new tools do not provide support for the derivation of the equations of motion.

In the design of a landing gear, finite element models are used primarily for the stress analysis, but these models may also be used for the assessment of the landing gear stiffness. The origin of the finite element model used in this thesis dates back about ten years. The model may be classified as a ”beam” model: the various parts of the landing gear are almost exclusively represented by beam elements. At a later stage in the design process more detailed ”volume” FE models were introduced in the stress analysis to study details of the torque link attachment lug on the main fitting. The varying shock absorber deflection, which results in changes of the overlap and torque link geometry as shown before, poses a special challenge for classical finite element packages, like e.g. NASTRAN. Generally, these packages cannot cope with mechanisms and would only allow to create a model for one fixed shock absorber deflection; multiple models have to be created when analysing a number of different shock absorber deflections. Reference [21] reports on the development of a truck model in NASTRAN, which would be suitable for shimmy analyses. The equations of the straight tangent tyre model were introduced by modifying the mass, damping and stiffness matrix.

Multi-body software packages, with ADAMS being the most well known example, are used for the analysis of mechanisms and vehicle dynamics studies, to name a few applications. In a multi-body package the simulated system consists of rigid bodies, which are interconnected by springs and/or joints (e.g. revolute joint, spherical joint, translational joint, etc.). When modelling the landing gear the main problem would be to accurately incorporate the changing overlap and resulting variations in stiffness. Although the majority of the multi-body packages allows the introduction of flexible bodies, the flexible characteristics generally have to be constant and does not allow large changes in geometry.

The SAMCEF MECANO software package, reference [5], provides an interesting mix of multi-body and finite element techniques to overcome the problems noted above. The key element is the so-called ”flexible slider” which consists of a regular beam element, extended with a third node which is allowed to move along the deformable beam, see figure 5.28. The third node may also move from one beam element to another; so e.g. a multiple supported flexible rail can be modelled with a contact point moving along it. The sliding node only transfers forces, not moments. A friction force F_w can be introduced along the deformable trajectory, using the normal force F_n of the sliding node and a constant friction coefficient, see figure 5.28.

The flexible slider element allows a convenient modelling of the sliding member, main fitting and the continuously varying overlap, see figure 5.29. Since MECANO can be used to analyse mechanisms, the varying torque link geometry does not pose any particular

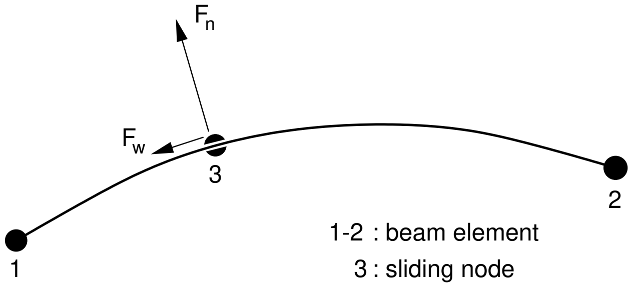
Fn
Fw
3
2
1
1-2 : beam element
3 : sliding node

Fig. 5.28: The MECANO flexible slider element.

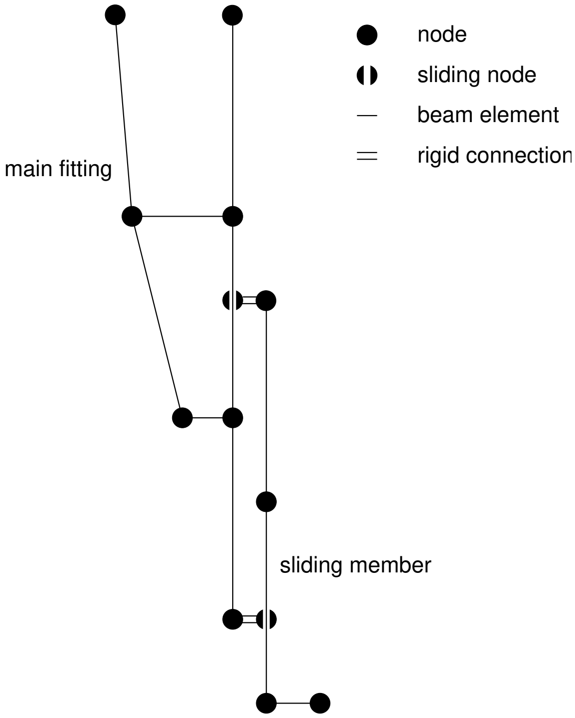
node
sliding node
beam element
rigid connection
main fitting
sliding member

Fig. 5.29: Schematic view of the usage of the flexible slider to model the main fitting and sliding member.

problem. Based on a detailed NASTRAN model a simplified beam model was developed for usage with MECANO, aiming at the same overall stiffness at wheel axle level. The motivation for reducing the number of beams is that the MECANO model was also used for the dynamic simulation of landing events; this requires some limitation on the number of degrees of freedom in order to maintain acceptable calculation times. The tyre model and shock absorber were introduced as ”user” elements; they were programmed in FORTRAN and linked to the MECANO solver.

Summarising the implementation of the various items, as discussed in the previous sections, in the MECANO model:

- *tyres (chapter 4)*
  The non-linear vertical spring characteristic is implemented using a look-up table and includes bottoming of the tyre. The longitudinal slip characteristic is introduced using a non-linear function, similar to the Magic Formula, describing the friction coefficient μ_x as a function of the longitudinal slip κ. The straight tangent model is used to include the lateral behaviour of the tyre. Various look-up tables are required to describe the tyre characteristics as a function of the vertical force on the tyre. The straight tangent model was selected because of the ease of implementation in the MECANO program. Furthermore it was shown in chapter 4, that it is conservative with respect to detecting shimmy compared to other tyre models as e.g. the Von Schlippe model. The interaction between lateral and longitudinal tyre behaviour is not considered.

- *shock absorber (section 5.1)*
  The non-linear air spring behaviour as described in section 5.1 is taken into account, including the mechanical stops both on compression and extension. Also the compressibility of the oil and expansion of the main fitting is taken into account, but the discussion of these phenomena is outside the scope of this thesis. The metering pin profile is included using a look-up table describing the orifice area as a function of shock absorber deflection.

- *flexibility (section 5.2)*
  The landing gear structure is modelled using beam and flexible slider elements, see figure 5.29. The continuously changing torque link geometry and varying overlap can be described quite satisfactory using MECANO. Flexibility of the back-up structure is included by introducing a stiffness matrix at the landing gear attachment points, which was derived from a detailed FE model of the fuselage and wing. It should be noted that various cross coupling terms exist, in particular between the forward and aft pintle point.

- *free-play (section 5.3)*
  The free-play present at wheel axle level is ”lumped” at two locations: the lateral free-play is included by introducing a non-linear normal stiffness of the side stay, free-play in yaw is included at the apex joint. Following this approach the free-play at wheel axle level becomes a function of shock absorber deflection; the validity of this approach was confirmed by experimental results.

- *friction (section 5.4)*
  Though the flexible slider is very convenient for modelling the varying overlap,

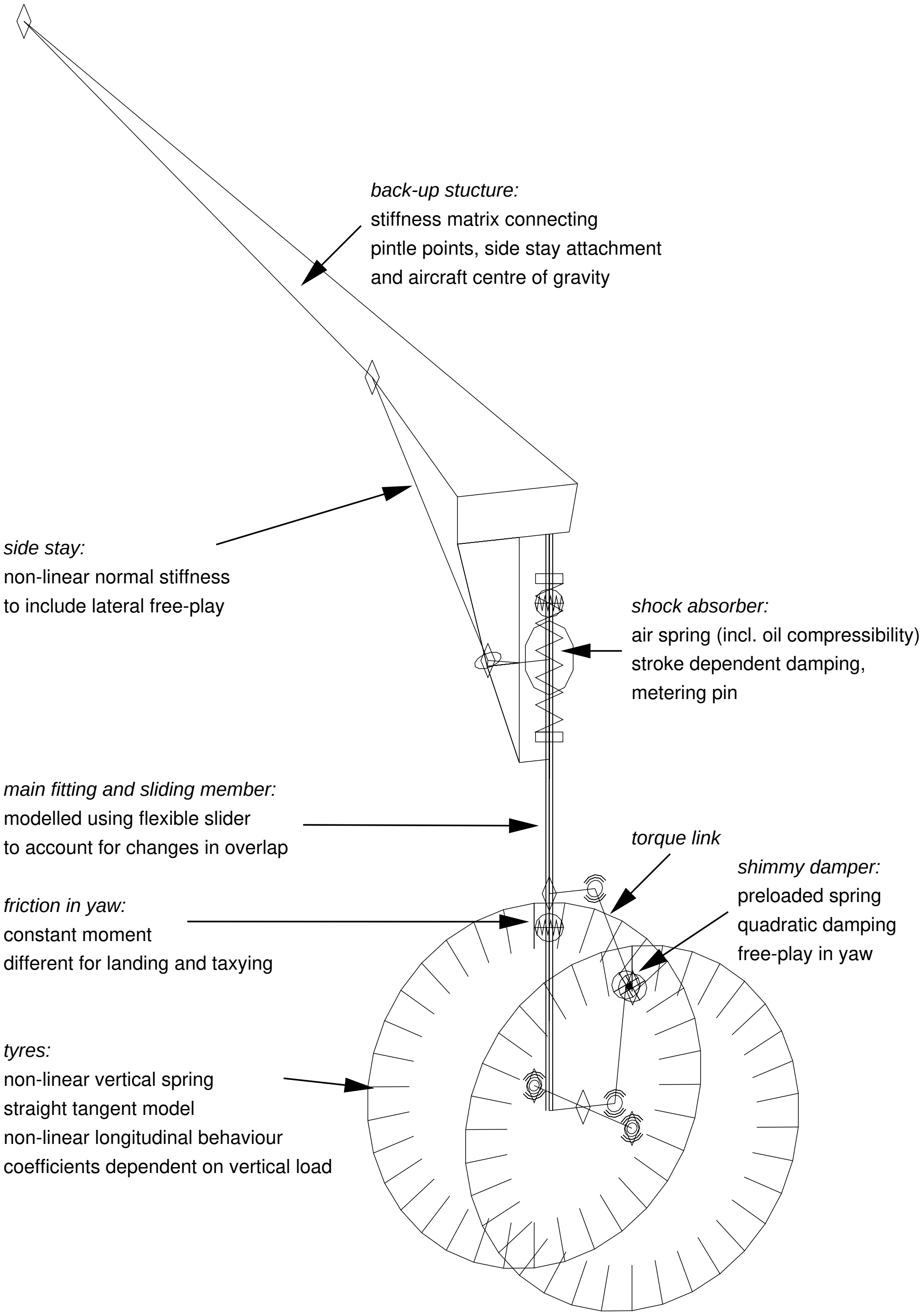

back-up stucture:
stiffness matrix connecting
pintle points, side stay attachment
and aircraft centre of gravity

side stay:
non-linear normal stiffness
to include lateral free-play

shock absorber:
air spring (incl. oil compressibility)
stroke dependent damping,
metering pin

main fitting and sliding member:
modelled using flexible slider
to account for changes in overlap

torque link

shimmy damper:
preloaded spring
quadratic damping
free-play in yaw

friction in yaw:
constant moment
different for landing and taxying

tyres:
non-linear vertical spring
straight tangent model
non-linear longitudinal behaviour
coefficients dependent on vertical load

Fig. 5.30: Full MECANO model of the landing gear.

simplifications with respect to section 5.4 are required, when including friction. The main problem is that the flexible slider does not allow to transfer moments, so it is not possible to directly include the friction moment in yaw M_w depending of the normal load F_n. Also the interaction with the axial friction force cannot be modelled. An approximation was found by using a non-linear damper element to account for the friction in yaw. In the landing simulations a small, constant value for the friction in yaw is used and a high constant value during taxiing.

- *shimmy damper (section 5.6)*
  The non-linear behaviour of the shimmy damper, as shown in figure 5.24, is included using a non-linear spring and damper element.

An impression of the MECANO model and a summary of the various modelling issues can be found in figure 5.30.

5.8 Test programme and parameter assessment

Various aspects of the development of a landing gear model suitable for a shimmy analysis have been discussed. We may distinguish between questions regarding modelling issues (e.g. which tyre model is to be used, how to model the varying overlap?) and the assessment of parameters for the model (e.g. obtaining realistic values for the relaxation length, friction values, etc.). Obviously these aspects are related: a very detailed model will require many parameters. On the other hand, if the problem is governed by a limited set of parameters which cannot be determined very accurately, it can be questioned if the development of a very detailed and complicated model can be justified.

Also the scope and application of the model are important when determining the required level of detail. The shimmy incidents occurred very shortly after landing impact; the aim of the MECANO model is to simulate the complete landing event starting from the first contact between tyre and runway. This implies that it also has to be possible to simulate spin-up of the wheels and the fore/aft dynamics of the landing gear have to be included.

Various tests have been performed (or were already available) to determine parameters for the MECANO model or to validate its characteristics. We may distinguish between component and full-scale testing.

component tests

- *tyre characteristics*
  Tyre parameters are supplied by the tyre manufactures and generally consist of a load-deflection curve, the cornering stiffness, self aligning stiffness, relaxation length and contact length for the entire vertical load range. Accurate assessment of tyre parameters is difficult. Since the tyre dimensions and inflation pressure remain unchanged, various cross checks can been made between the data from different sources to identify extreme or unusual behaviour. The data can also be checked against the empirical formulae developed by Smiley and Horne [47]. More details are given section 4.6.

- *shock absorber characteristics*
  The spring and damping characteristics are validated using the results from the

regular drop test programme and free extension tests. When performing full-scale aircraft tests, additional instrumentation was installed to record pressures and temperatures inside the strut. This information can also be used to validate the shock absorber characteristics, see e.g. figure 5.3.

- *flexibility*
  Initial estimates for the stiffness of the landing gear were based on a FE model. At a later stage dedicated stiffness tests were performed in a test rig to check these results, and modify the model to improve its accuracy. Up to four different shock absorber deflections were considered in this measurement programme. Furthermore, stiffness tests were performed on the aircraft, to determine the overall flexibility of the landing gear including the flexibility of back-up structure and wing, see figure 5.11.

- *modal testing*
  Following the stiffness tests, modal tests were performed on the landing gear in the stiffness test rig. Due to the problems described in section 5.5, the results were only used to gain additional confidence in the model.

- *free-play*
  The stiffness tests may be used to extract some numbers on free-play, but these are unlikely to represent the most extreme case since the gear under study was new. The landing gear manufacturer has provided the tolerances on the various components for a fully worn condition, and using this information the ”overall” free-play at wheel axle level can be estimated.

- *friction*
  Numbers on friction are rather hard to obtain. A limited number of tests was performed on an unpressurised landing gear, but this gave only a crude indication of magnitude of the friction forces to be expected. Assuming the friction to be zero will generally be conservative in detecting shimmy, but on the other hand this will not allow an accurate simulation of the landing gear behaviour under various conditions.

- *shimmy damper*
  The spring and damping characteristics of the shimmy damper were determined using a dedicated hydraulic test rig.

full-scale tests

By performing tests on various subsystems of the landing gear, confidence will be gained that various aspects of the landing gear behaviour are modelled accurately. But the all important question will be if the full model also behaves as the real landing gear and how will this be shown?

Full-scale tests on the landing gear can be performed in a laboratory environment on a dynamometer. There may exist a number of reasons for discrepancies between the laboratory tests and the results obtained on the actual aircraft. Firstly, the curvature of the drum will affect various aspects of the tyre behaviour and may result in a configuration which is more stable. Also attention should be paid to the attachment stiffness and friction levels. An advantage of laboratory testing is that the excitation of the landing gear can be closely controlled and repeated for runs with different configurations. In addition, no aircraft is needed which clearly reduces safety risks and possible damage in case of a shimmy event. The past experience for one particular landing gear showed that it was not possible to provoke shimmy in the laboratory environment, although the gear experienced a torque link failure on the aircraft due to shimmy instability.

When performing full-scale aircraft tests, it will be necessary to introduce some (external) disturbances to excite the landing gear in order to obtain a dynamic response. A yaw pulse can be obtained by taxiing over a plank, which is diagonally placed and fastened to the runway, see reference [33]. Another way of exciting the landing gear is by introducing a relatively large unbalance mass on one of the wheels and performing taxi-runs with a sweep in forward velocity; the excitation frequency will correspond with the angular velocity of the wheels. Reference [49] describes how this method was used to validate the operation of a shimmy damper.

Asymmetrical braking of the landing gear is yet another possibility to generate a yaw input to the landing gear. This was achieved by modifying the braking system so that only the inboard brake is used. The pilot applies full brakes for a very short period by briefly kicking on the brake pedal; this may provoke a deep-skid on the braked wheel. When the anti-skid system detects the rapid deceleration of the braked wheel, the locked wheel protection will momentarily dump the brake pressure and the wheel will spin-up again. Using this technique it was possible to obtain some limited dynamic response from landing gear as shown in figure 5.31. This particular measurement was also simulated using the MECANO model, see figure 5.32. In this simulation it is assumed that the measured brake pressure can be translated directly into a brake torque. Considering the rather rough conversion of the brake pressure into a brake moment the results are fairly good, in particular the sequencing of the various events.

Instrumented landings were also part of the test programme and may also be used for model validation purposes. Under these conditions the yaw excitation originates from asymmetrical spin-up of the wheels. The asymmetrical spin-up is again a result of roll of the aircraft and/or crown (transverse slope) of the runway. Figure 5.33 shows the recordings for a soft landing at a relatively low forward velocity. The largest dynamic response is seen immediately after touch-down; figure 5.34 zooms in on the first 0.5 seconds of the landing event. It can be seen that the inboard wheel spins up more quickly than the outboard wheel. This also results in a difference in longitudinal acceleration between the inboard and outboard wheel, and consequently some yaw motion and shimmy damper displacement. The MECANO simulation results for this particular landing are shown in figure 5.35. The asymmetrical spin-up is represented with a reasonable accuracy, but some of the lateral and yaw dynamic behaviour appears to be missing in the MECANO model when the wheels have spun-up. The asymmetrical spin-up was achieved by introducing a transversely sloped runway in the simulation model. This example also illustrates that it may be very difficult to exactly recalculate a landing event.

A final remark is that it will be very difficult to get a rigorous proof of shimmy stability from full-scale testing; this is also an important driver for the development of simulation models.

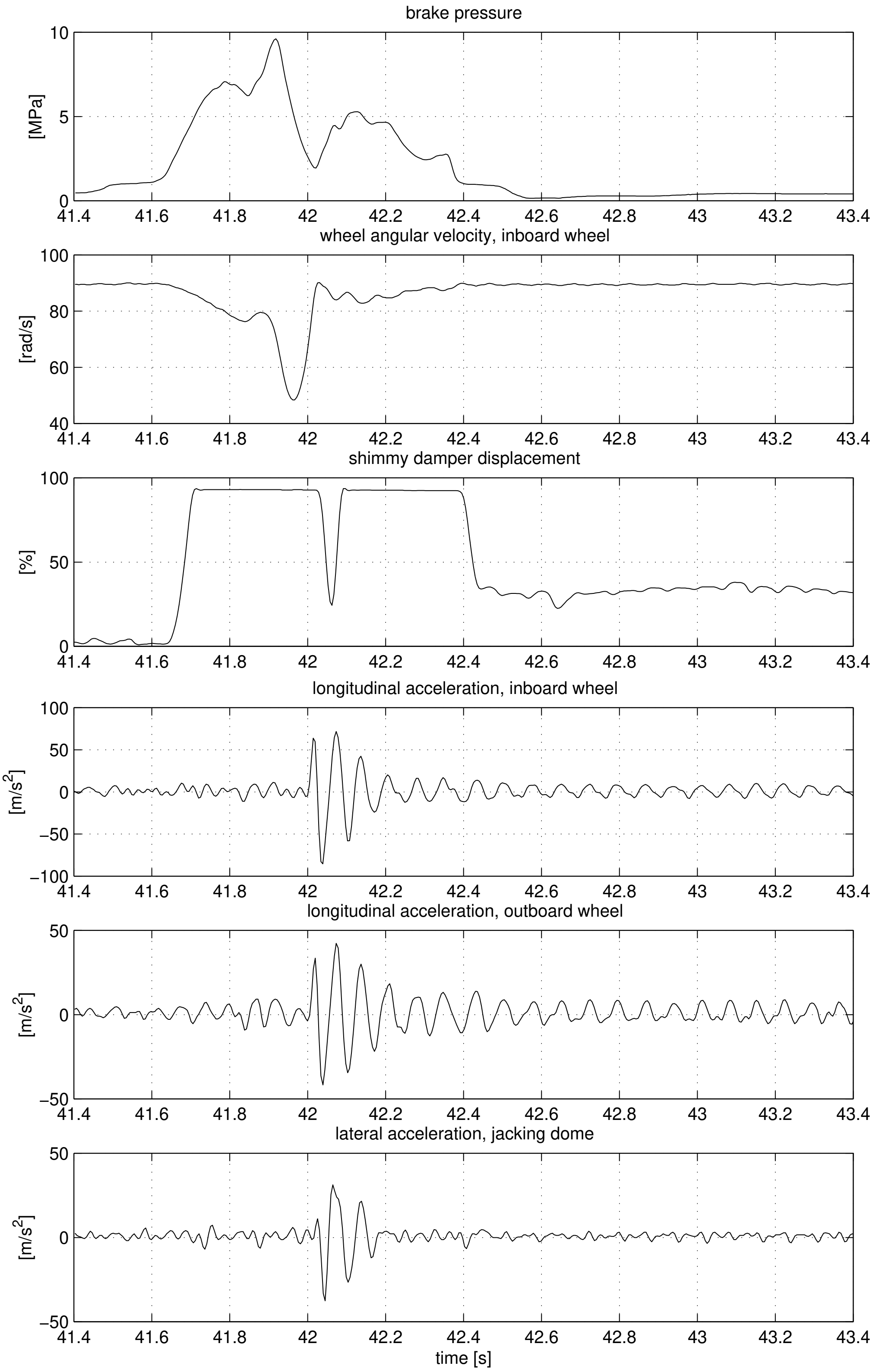

Fig. 5.31: Measured landing gear response during an asymmetrical braking event (flight 853 rec. 45, left hand gear).

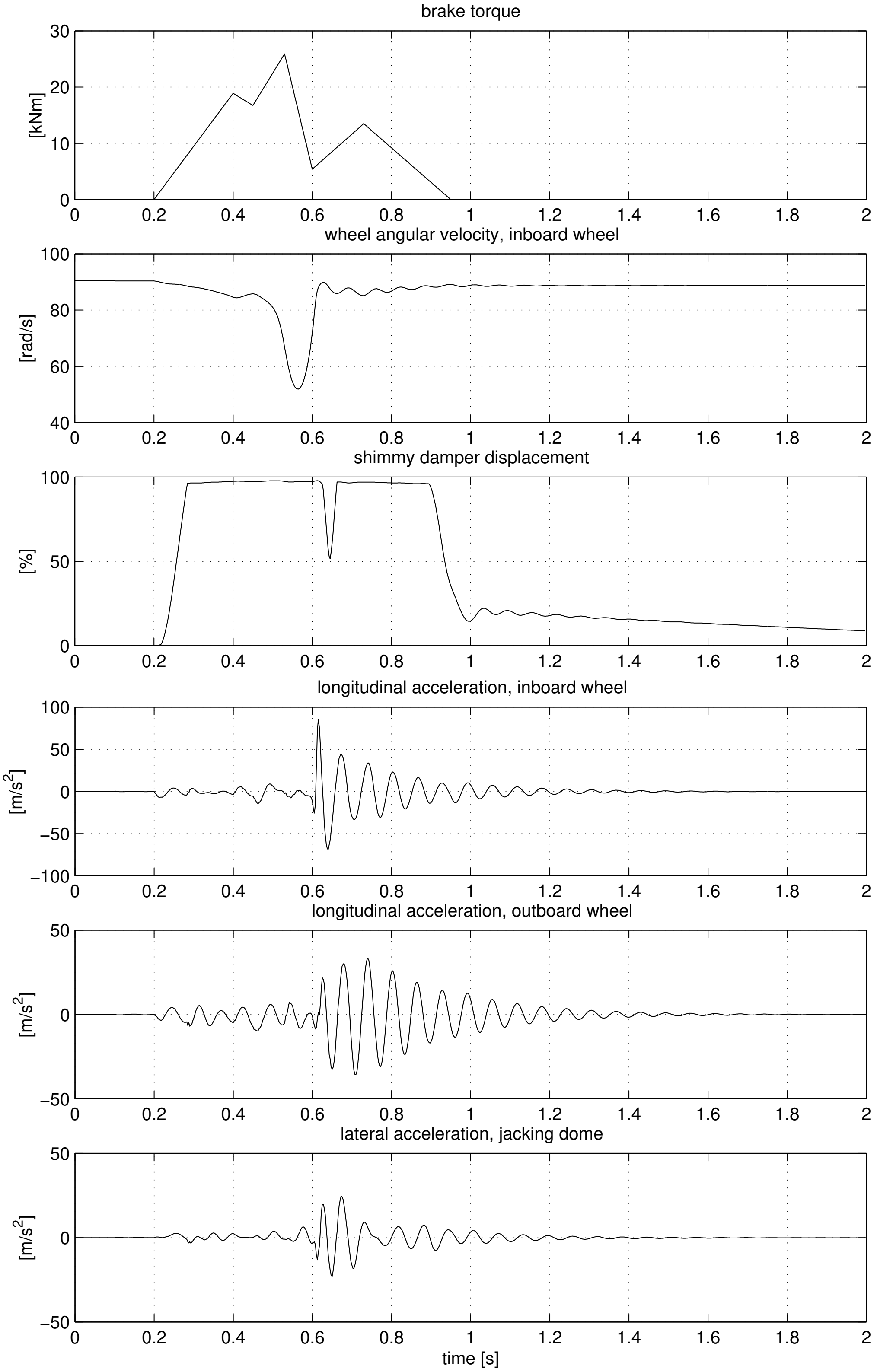

Fig. 5.32: Simulated landing gear response during an asymmetrical braking event.

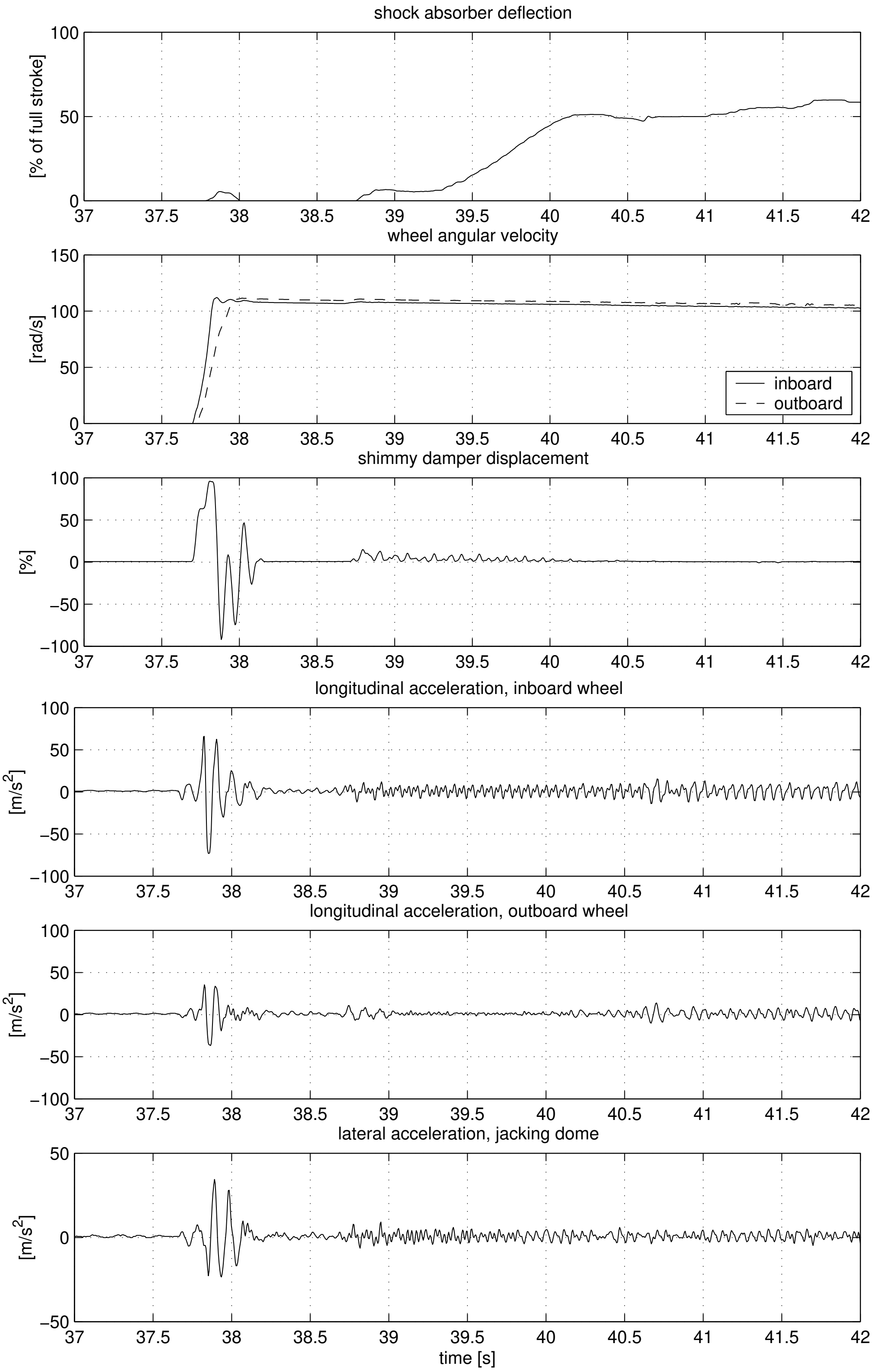

Fig. 5.33: Measured landing gear response during landing impact (flight 856 rec. 29, left hand gear).

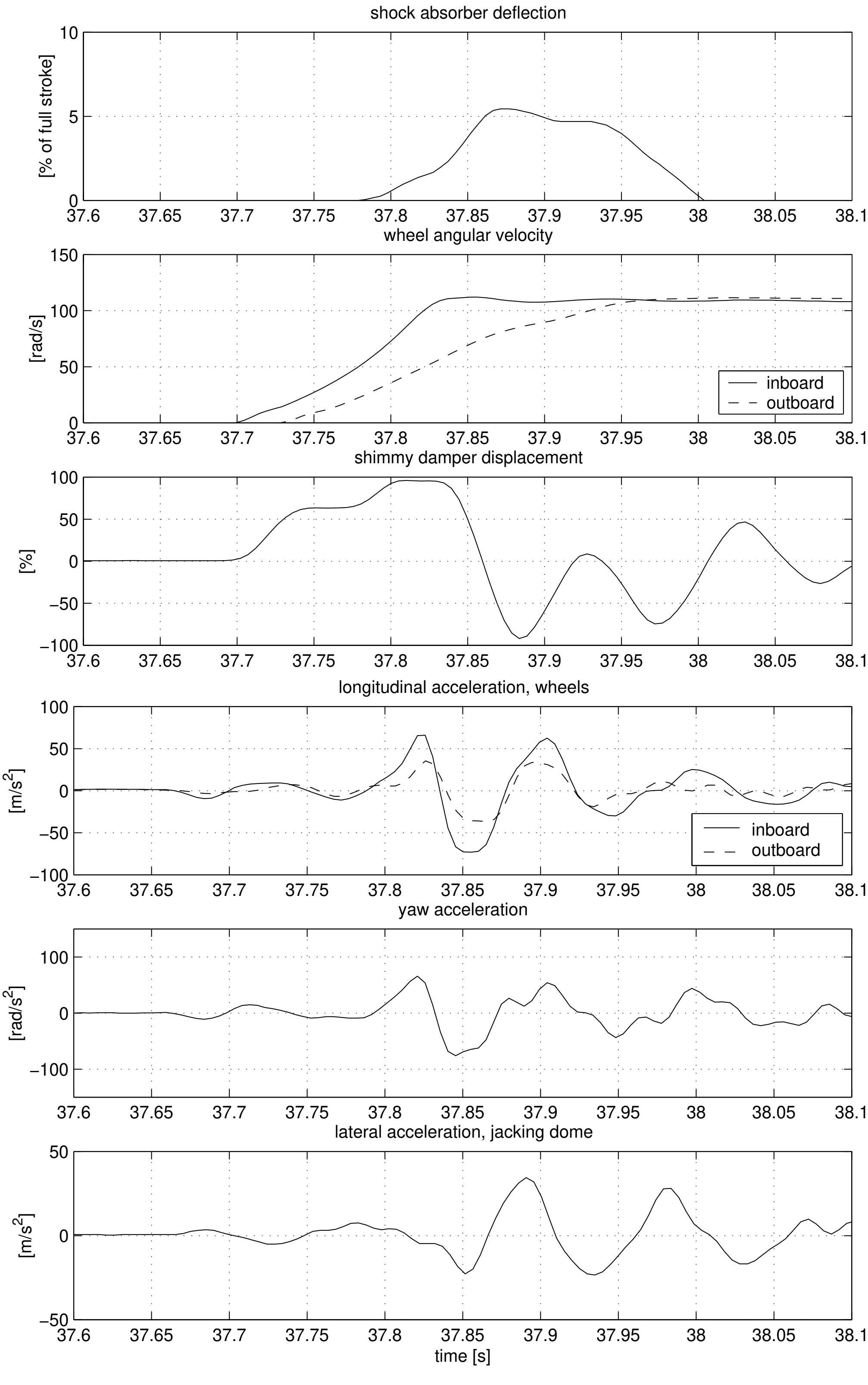

Fig. 5.34: Measured landing gear response, zooming in on initial phase (flight 856 rec. 29, left hand gear).

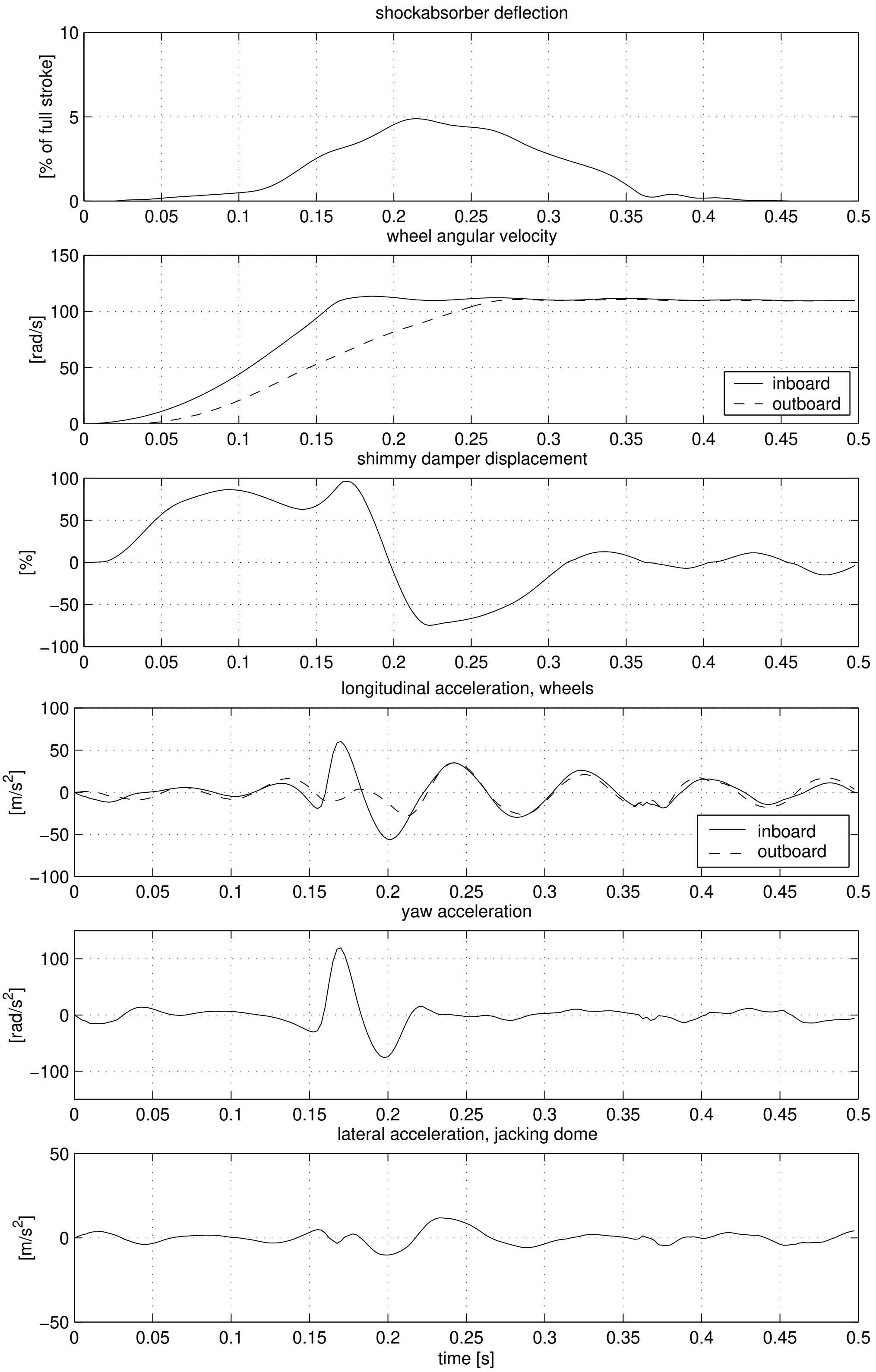

Fig. 5.35: Simulated landing gear response during initial phase of landing impact.

Chapter 6

Evaluation of a shimmy event

In this chapter a shimmy event will be analysed, which occurred on a test aircraft. In this particular case some instrumentation was available, which recorded the unstable shimmy vibration. This information allows a much more detailed analysis of the unstable motion than normally possible. In chapter 5 the development and validation of a detailed landing gear model is described. The MECANO model will be used to evaluate shimmy stability of this particular landing gear. In addition a linear derivative of the MECANO model has been developed, which allows scanning the various operating conditions of the aircraft more quickly.

6.1 Analysis of recorded data

Experience indicates that main landing gear shimmy is most likely to develop very shortly after landing impact. Under these conditions the friction in yaw direction will be reduced and asymmetrical spin-up of the wheels may serve as an initial disturbance. The pilot may notice a landing gear vibration, which can develop from many sources and does not necessarily have to be caused by shimmy. In severe cases, shimmy may result in structural damage; in particular a torque link failure is likely to happen. Generally the torque links will be designed to include a break spot, which fails in case of an overload condition. In this way the main fitting and sliding member remain undamaged and will still be able to carry the weight of the aircraft. In addition the replacement of a torque link is a minor task compared to replacing a sliding member and/or main fitting.

In case of a shimmy event only limited data will be available to investigate the vibration and establish the boundary conditions (e.g. forward velocity, shock absorber deflection, etc.). The flight data recorder may be used to determine the indicated air speed and vertical acceleration on touch down. The velocity with respect to the ground (”ground speed”) may be different from the air speed, but normally this difference can be ignored. Furthermore the mass of the aircraft and flap settings will be known. Nevertheless this information can only give a crude idea of the type of landing which is performed, details on the shimmy vibration itself can be even harder to obtain. The tyres may leave sinusoidal marks on the runway which are very characteristic for a shimmy instability, see figures 6.1, 6.2 and 6.3. The wavelength of these marks will be several meters. In some cases, data from the cockpit voice recorder can be used to establish the frequency of the vibration. So normally only very limited data is available, which makes a detailed assessment difficult.

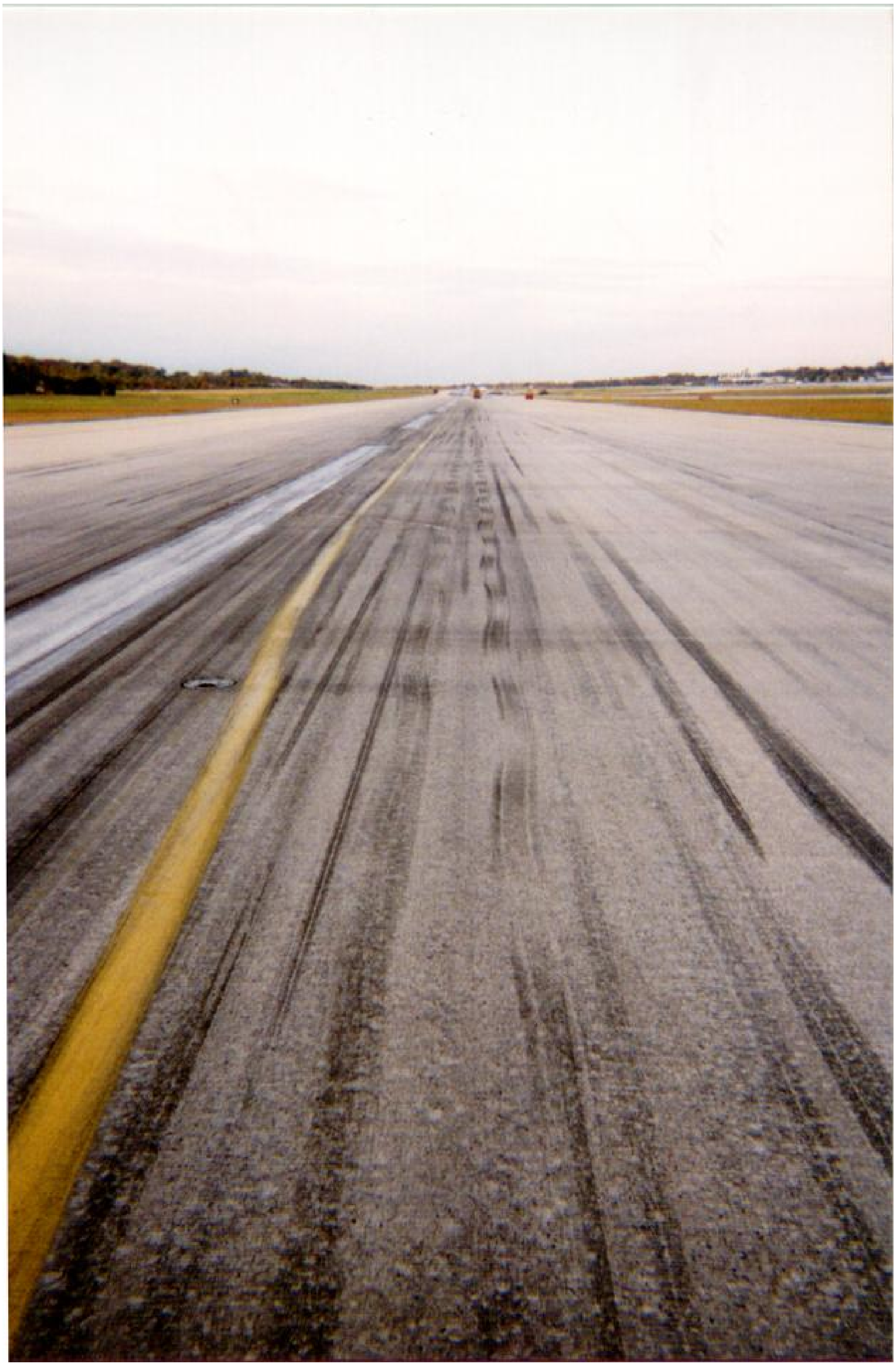

Fig. 6.1: Tyre marks on the runway (1).

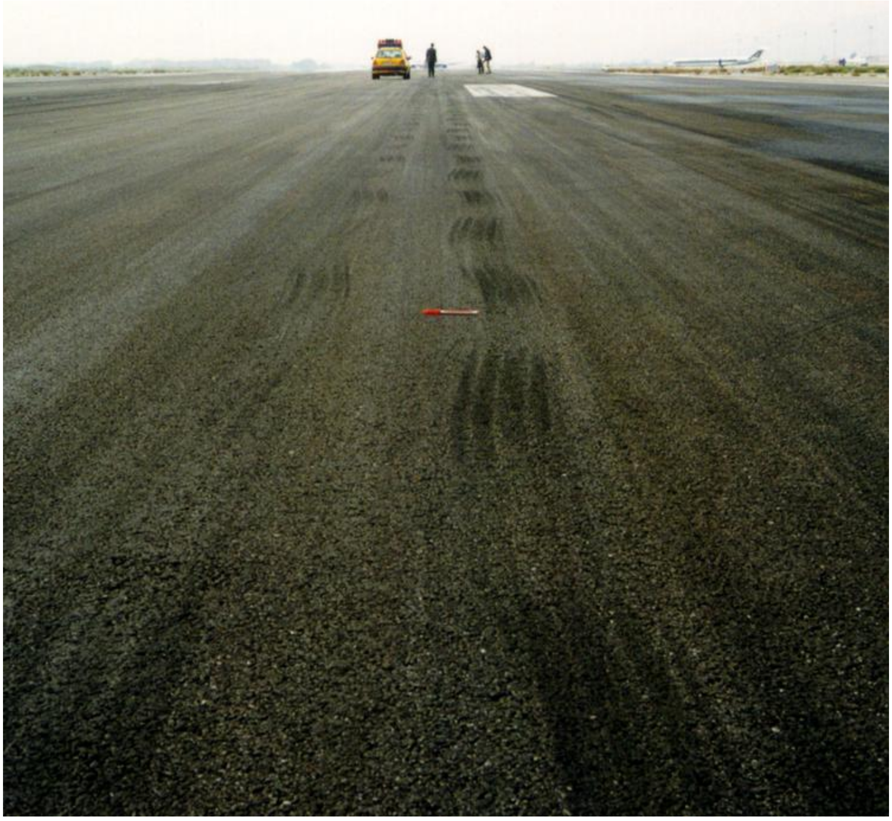

Fig. 6.2: Tyre marks on the runway (2).

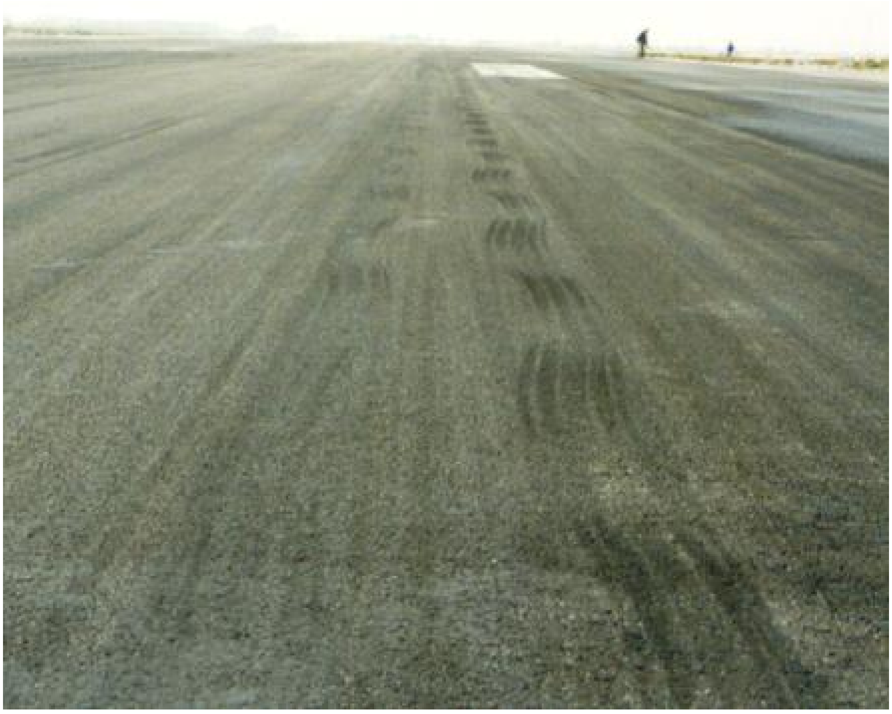

Fig. 6.3: Tyre marks on the runway (3).

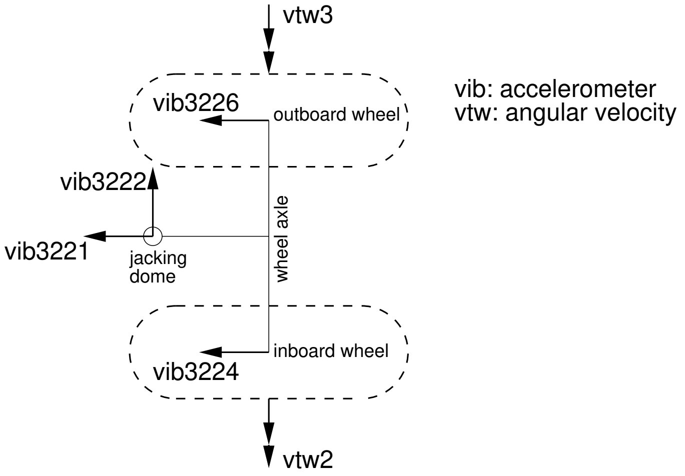

Fig. 6.4: Instrumentation of the right hand main landing gear (flight 228, rec. 23).

We will now discuss a shimmy event which occurred on a test aircraft and resulted in a torque link failure. This event is particularly interesting because the landing gear was instrumented with several accelerometers and other measurement equipment, thus revealing more details of the shimmy instability. Details on the instrumentation are given in figure 6.4. It should be noted that this configuration of the landing gear was never taken into production and never used by any airline.

The aircraft ground speed and shock absorber deflection are shown in figure 6.5. The forward velocity of 60 m/s at touch-down is relatively low and the landing is a bit bumpy considering the shock absorber deflection. Furthermore, it can be noted that the shock absorber remains almost fully extended for about 5 seconds. At approximately t=22 seconds the lift dumpers and thrust reversers are activated, resulting in an increased deceleration of the aircraft and increasing shock absorber deflection.

The angular velocity of the wheels is shown in figure 6.6. It can be seen that this particular landing represents a rather extreme case of asymmetrical spin-up. On the first touch, the inboard wheel spins up completely, but the outboard wheel reaches only 35% of the angular velocity corresponding to aircraft forward velocity. Then the aircraft becomes fully airborne for almost two seconds before the second ground contact. At that stage the outboard wheel also spins up completely. Recorded accelerations are shown in figure 6.7 and 6.8. The unstable vibration starts at about t=16 seconds and continues until the torque link fails at t=23.5 seconds, the frequency of the vibration ranges from 12.5 to 14 Hz. Some of the signals may show a discontinuity, either due to a failure of the transducer or clipping of the measurement amplifier.

The lateral acceleration signal is unusable after t=18 seconds. We will focus now on the time interval from 16 to 17.6 seconds: in this period the amplitude grows about a factor seven and there are no particular external disturbances to the landing gear. The accelerations of the jacking dome and wheels are shown in figure 6.9. The longitudinal accelerations of the wheel centres are in counter phase indicating a yaw motion of the axle; the outboard longitudinal acceleration being slightly larger compared to the inboard acceleration. This is confirmed by the fact that the longitudinal acceleration of the jacking dome remains limited. The lateral acceleration of the jacking dome increases at nearly the same rate as the longitudinal accelerations of the wheels, though it differs in phase.

The acceleration signals may be integrated twice with respect to time in order to get an impression of the amplitude of the motion. This process also suppresses some of the higher frequency noise present in the acceleration signal. A high pass filter is applied on the integrated signals in order to eliminate static drift. The lateral position of the wheel axle centre is calculated using the various acceleration signals and their locations. The sign of the lateral displacement is reversed in order to agree with the sign convention adopted in this thesis. The result is shown in figure 6.10, which clearly illustrates the phase difference between the lateral and yaw motion. In the time interval considered, the amplitude reaches already more than 5 degrees in yaw and 35 mm in lateral direction. Taking into account the growth of the longitudinal wheel accelerations, it can be expected that the peak amplitudes reached during this shimmy event will be more than twice these values.

The motion shown in figure 6.10 can be analysed in more detail; figure 6.11 lists a number of results. The frequency varies between 12.2 and 13.5 Hz; the changes in frequency correspond fairly well with differences in the shock absorber deflection. Similarly, the wavelength varies between 4.2 and 4.7 meter. Figure 6.10 clearly indicates that the lateral motion lags the yaw motion; this phase lag is in the order of 140 degrees (or equivalently a phase lead of 220 degrees). The amplitude ratio between lateral and yaw motion decreases somewhat when the overall amplitude grows; the order of magnitude of this ratio is 0.45 meter. Taking into account the factor seven increase in magnitude, it can be concluded that the ratio between lateral and yaw amplitude remains fairly constant.

In section 2.3 various combinations of lateral and yaw input to the tyre contact centre at road level were studied. It was found that instability may occur for certain combinations of the amplitude ratio η and relative phase angle ξ for a particular wavelength λ, see figure 2.15 on page 35. In this figure the various parameters have been made dimensionless using half of the contact length a. For the shimmy event studied in this chapter, a may be calculated using the measured (oil) pressure in the strut and the characteristics supplied by the tyre manufacturer. For the time interval under consideration, half of the contact length is on average 85 mm. Combining the data available in figure 6.11 we get: $50a < \lambda < 60a$, $5a < \eta < 6a$ and $215 < \xi < 235$ degrees. Plotting these combinations of η and ξ in figure 2.15 it is clear that they will always reside inside the $\lambda = 50a$ or $\lambda = 60a$ circle; thus indicating that this particular gear motion is potentially unstable.

Two remarks can be made regarding this analysis. Firstly, some assumptions have been made regarding the tyre parameters in figure 2.15: $\sigma = 3a$ and $t_p = 0.5a$. Considering the experimental data shown in section 4.6, this seems to be a reasonable approach. Secondly, figure 2.15 applies to input at the *tyre contact centre at road level*, whereas the data shown in figure 6.11 is determined for the *wheel axle centre*. So the contribution of roll of the wheel axle is not taken into account: no measurement data is available to determine the amount of roll of the wheel axle during the shimmy event, but the simulation results presented in the next section indicate that the contribution of roll will be relatively small in this particular case.

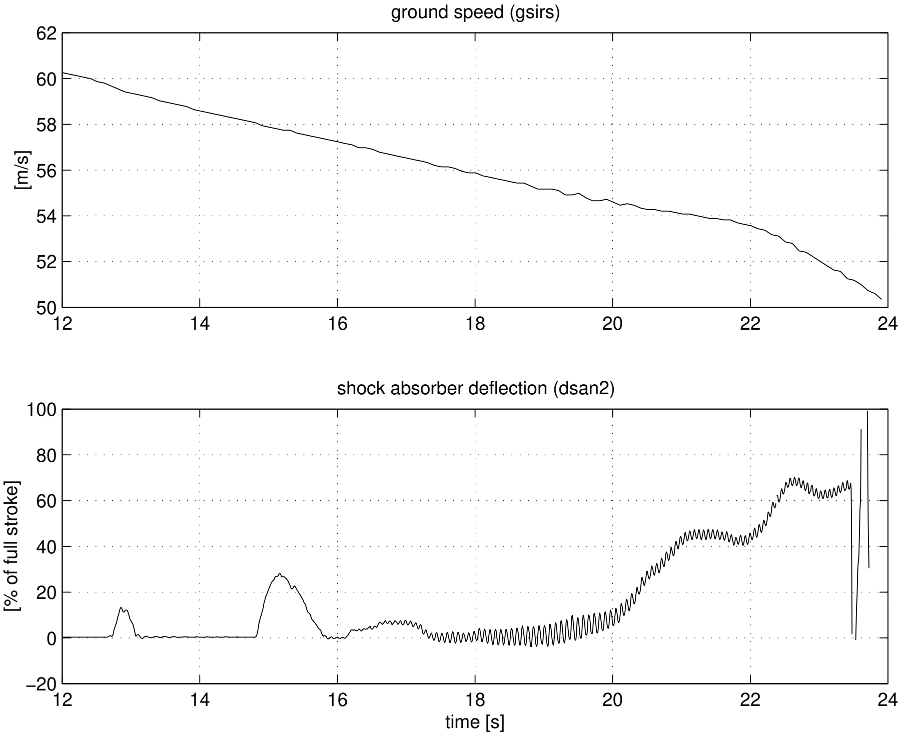

Fig. 6.5: Forward velocity and shock absorber deflection (flight 228, rec. 23).

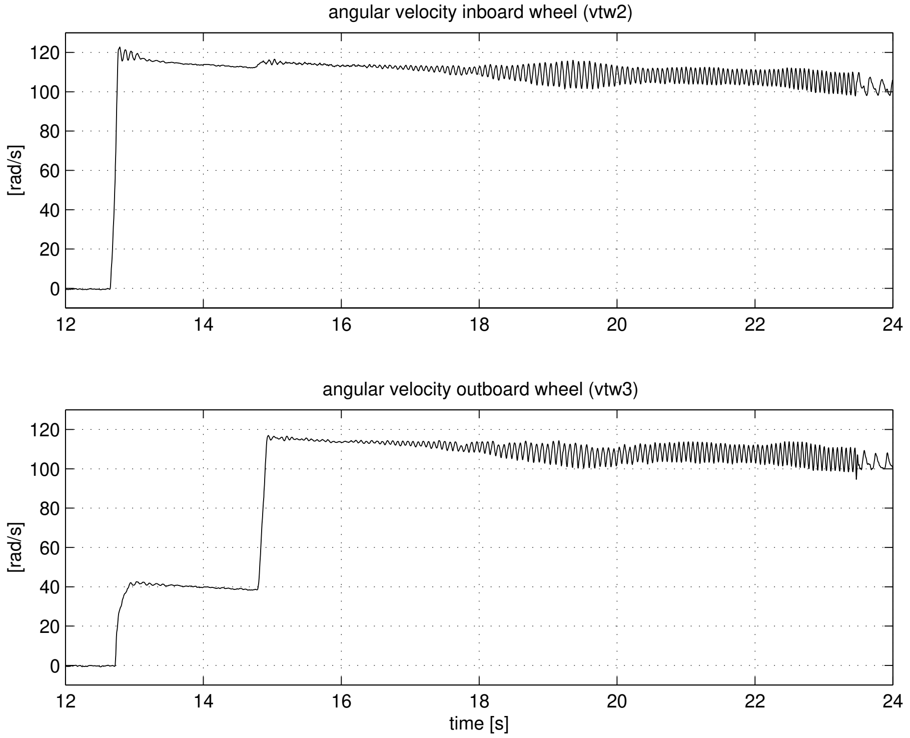

Fig. 6.6: Angular velocity of the inboard and outboard wheels (flight 228, rec. 23).

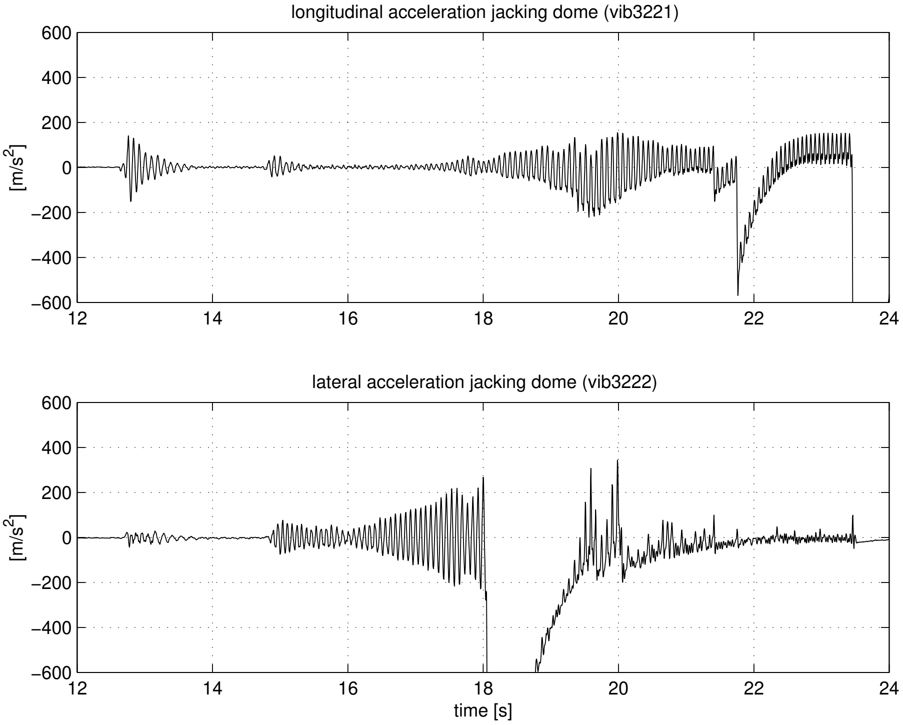

Fig. 6.7: Longitudinal and lateral acceleration of the jacking dome (flight 228, rec. 23).

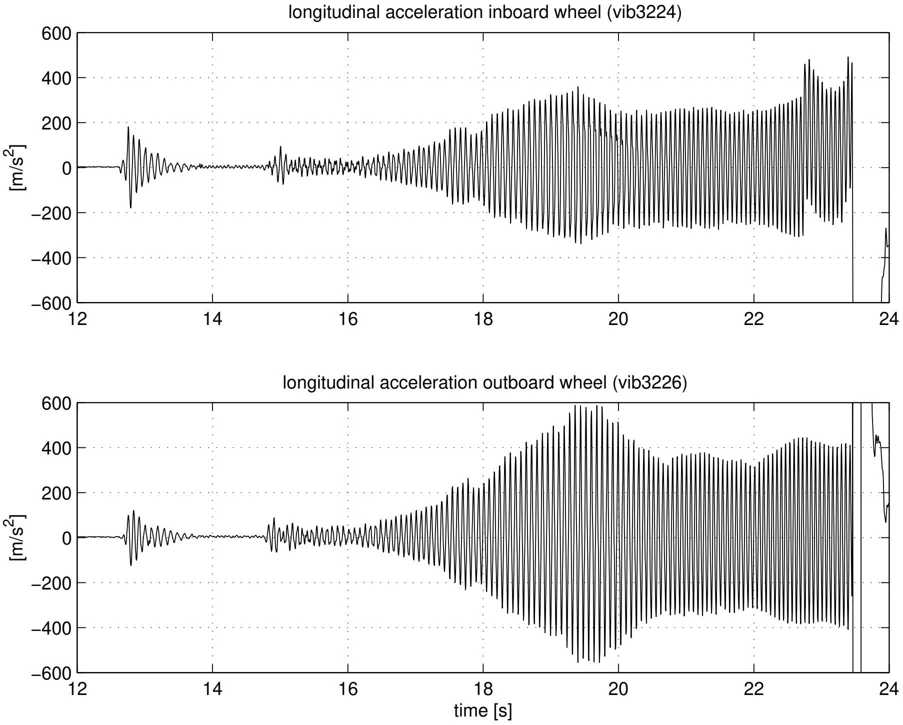

Fig. 6.8: Longitudinal acceleration of the wheel centre (flight 228, rec. 23).

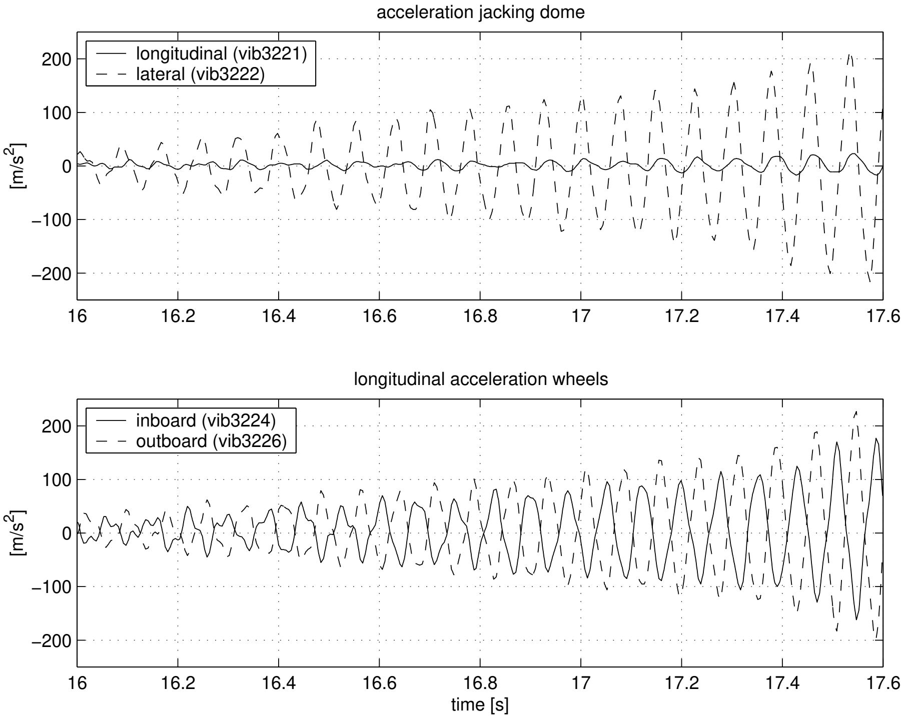

Fig. 6.9: Acceleration of the jacking dome and wheel centre (flight 228, rec. 23).

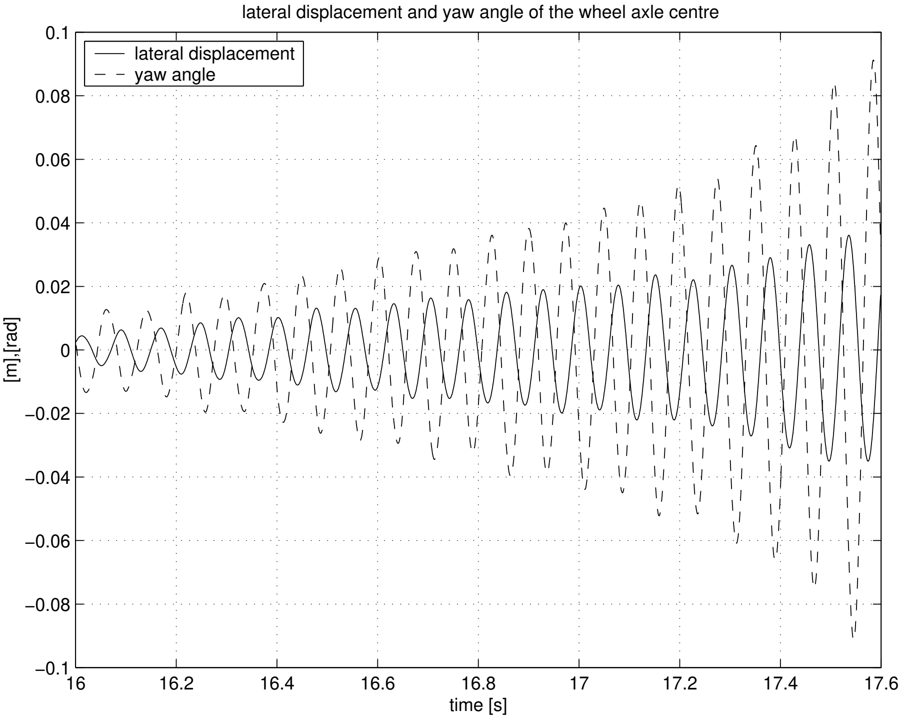

Fig. 6.10: Motion of the wheel axle centre (based on flight 228, rec. 23).

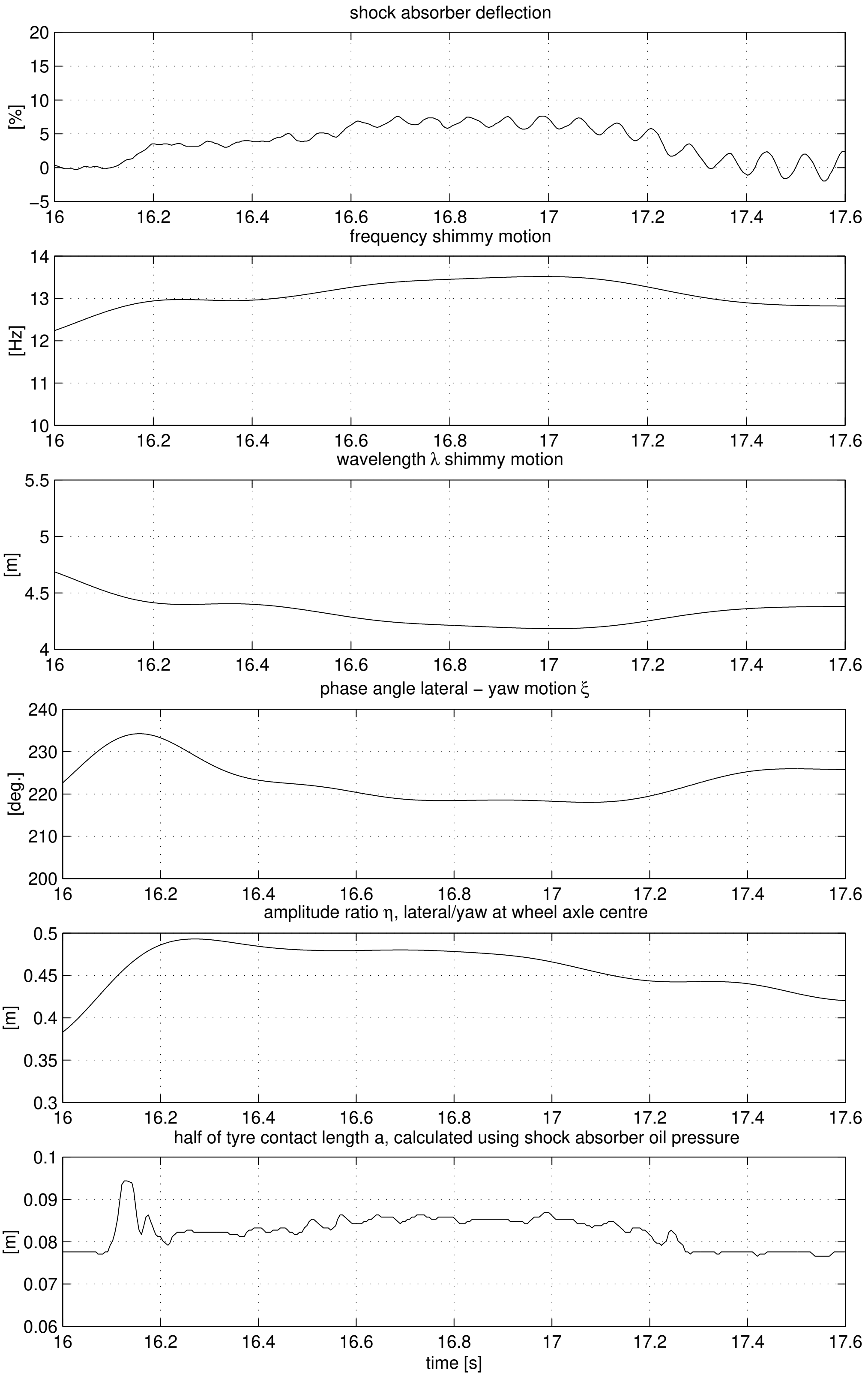

Fig. 6.11: Various characteristics of the shimmy vibration (based on flight 228, rec. 23).

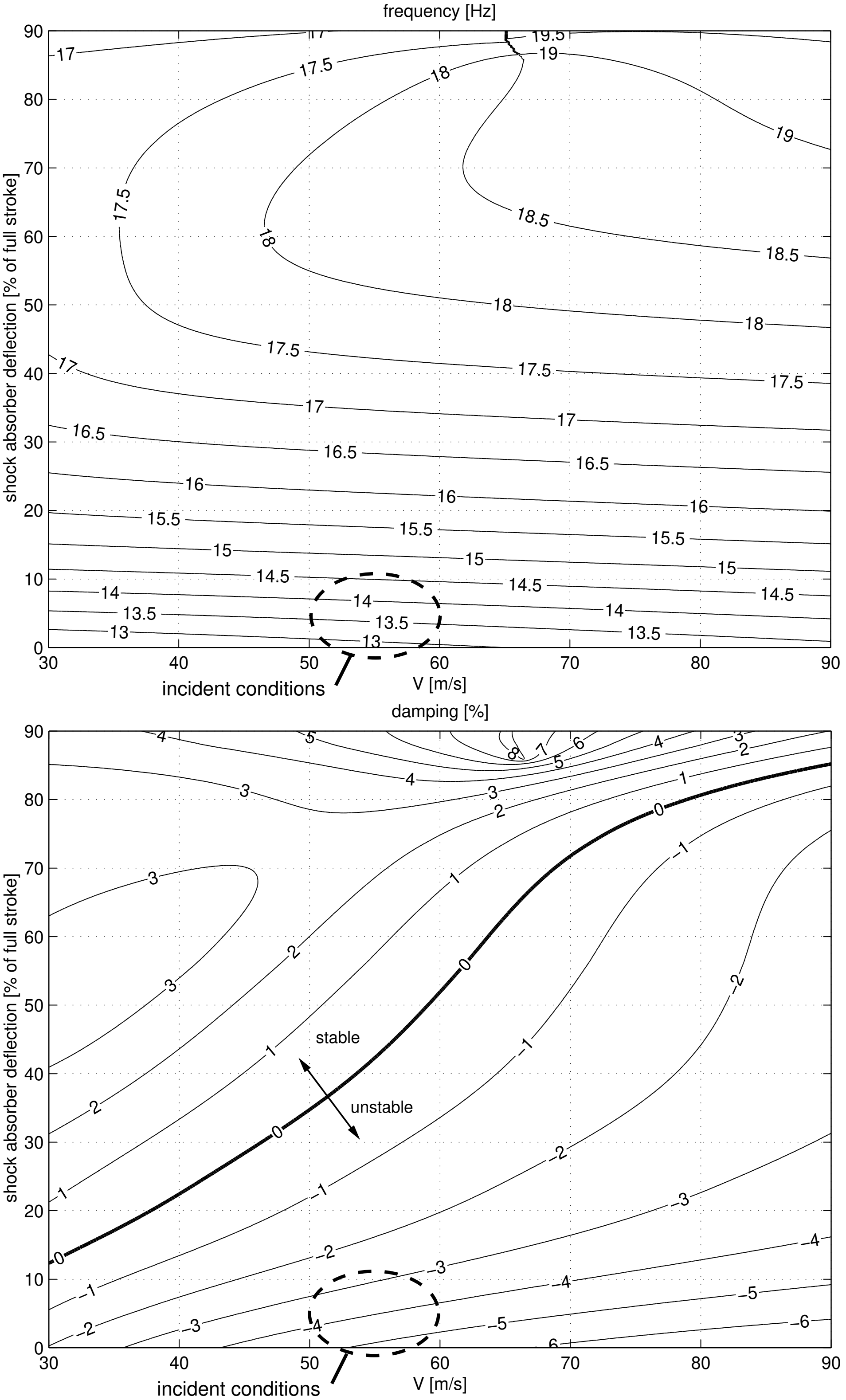

Fig. 6.12: Results of the linear shimmy analysis model.

6.2 Model results

Apart from the MECANO simulation model, a linear model was developed to quickly assess system stability for different shock absorber deflections and forward velocities. This linear model follows a similar modelling approach as the model discussed in section 3.1 and uses three mechanical degrees of freedom: a lateral, yaw and roll motion of the wheel axle centre. To improve the accuracy, the stiffness properties of the MECANO model are incorporated using look-up tables (see figure 5.12). The vertical load on the tyres is calculated using the theoretical air spring curve (see equation 5.1) and the tyre parameters are a function of the vertical load (see section 4.6). For each combination of forward velocity and shock absorber deflection the eigenvalues are calculated; the frequency and damping of the least damped mode below 30 Hz will be plotted.

For the shimmy event the forward velocity V is in the range of 50 to 60 m/s and the shock absorber deflection is less than 10%. The linear model indicates an unstable gear, as shown in figure 6.12: the frequency will be in the range of 13 to 14.5 Hz and damping will be 3 to 5% negative. Furthermore it can be observed that the gear would become stable again when the shock absorber deflection is sufficiently large. Therefore, it is possible that during a normal landing the instability does not reach a level where structural damage occurs, because the shock absorber will enter a stable area again when settling for the static deflection. The landing event described in section 6.1 is rather special, because the landing gear remained almost fully extended for about five seconds. Combined with the extreme asymmetrical spin-up this may have triggered the shimmy instability.

The MECANO model is used to recalculate the shimmy event. The simulation is started on the second ground contact, when the outboard wheel also spins up ($t \approx 14.8$ seconds in the measurement data). A number of time histories are shown in figures 6.13 to 6.16, which may be compared with the measurements shown in figures 6.5 to 6.8. Obviously, the MECANO simulation also shows the instability. The lateral load at the apex joint is shown in figure 6.17. The maximum value of 300 kN occurring in the simulation, is well above the static strength design load. So it can be expected that a torque link failure occurs due to a static overload condition.

A more detailed view on the unstable motion is shown in figure 6.18, which can be compared to figure 6.10. In figure 6.18 the roll angle of the wheel axle is also shown; this angle remains relatively small. In the simulation the instability has an exponential growth, whereas the measurements show a more or less linear increase in vibration amplitude. Similar to figure 6.11, the unstable shimmy vibration has been analysed in detail, see figure 6.19. When comparing the results it can be noted that, at least initially, the frequency tends to be too low and the wavelength is somewhat too large, but this error is reduced as the amplitude grows. The phase relation between lateral and yaw motion of the simulation appears to be quite accurate when compared to the measured results. The largest error can be found in the amplitude ratio at the wheel axle centre: in the simulation the lateral motion is too small relative to the yaw angle.

It should be noted that the results presented here cover just one specific condition. The simulation results appear to be quite sensitive to e.g. the amount of free-play, but the actual values are unknown. Within reasonable free-play limits, it is possible to select a combination of lateral and yaw free-play which would result in a far more unstable landing gear. It is also possible to select a combination which maintains stability during this landing event; the trends are similar as discussed in section 5.3 (figure 5.15).

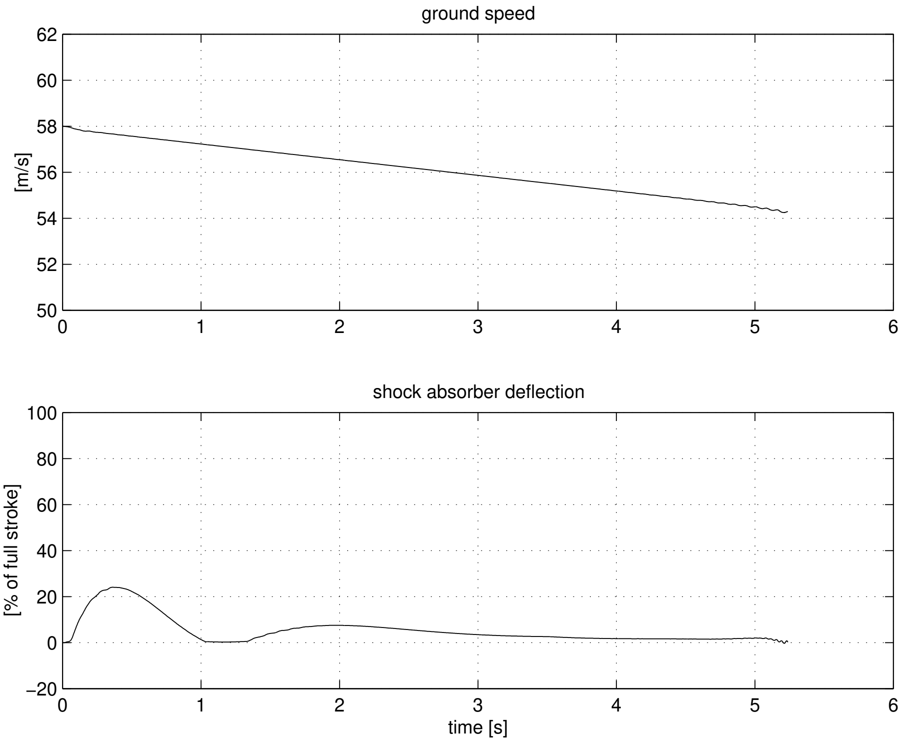

Fig. 6.13: Forward velocity and shock absorber deflection (simulation).

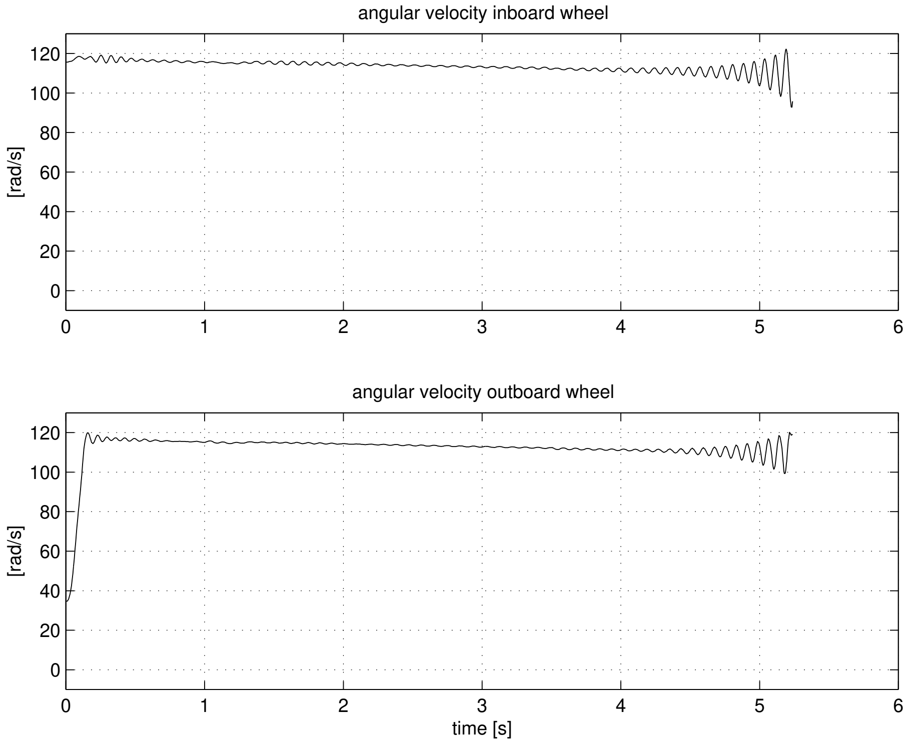

Fig. 6.14: Angular velocity of the inboard and outboard wheels (simulation).

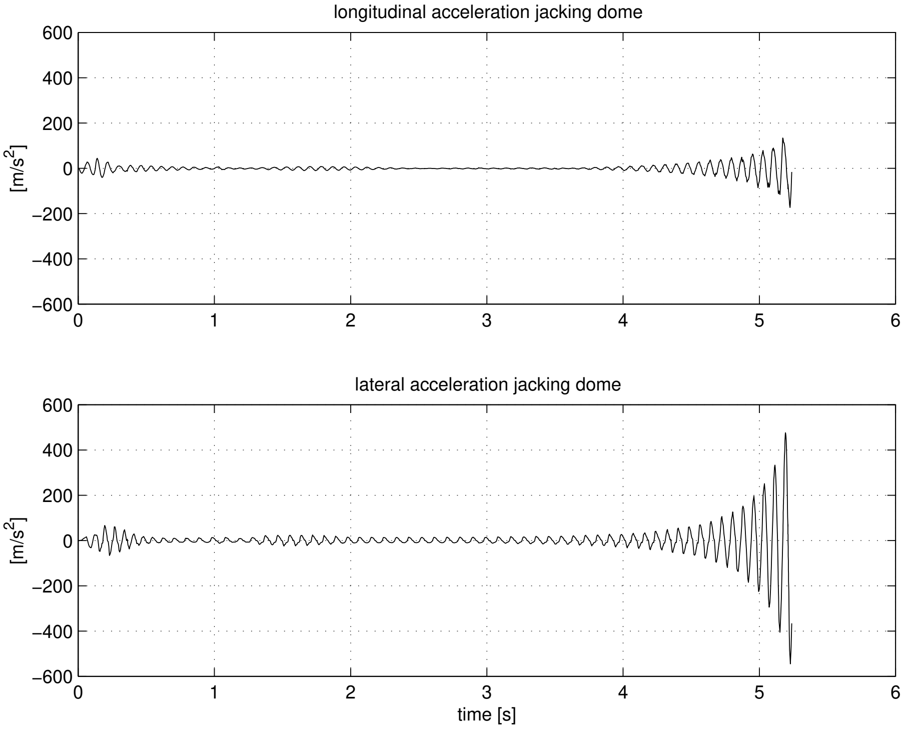

Fig. 6.15: Longitudinal and lateral acceleration of the jacking dome (simulation).

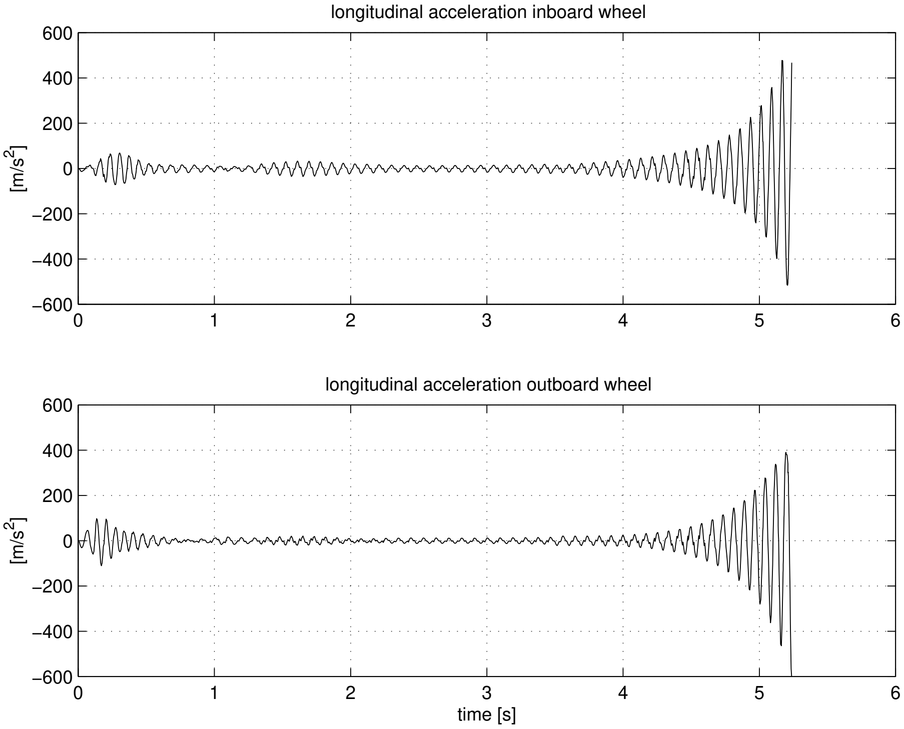

Fig. 6.16: Longitudinal acceleration of the wheel centres (simulation).

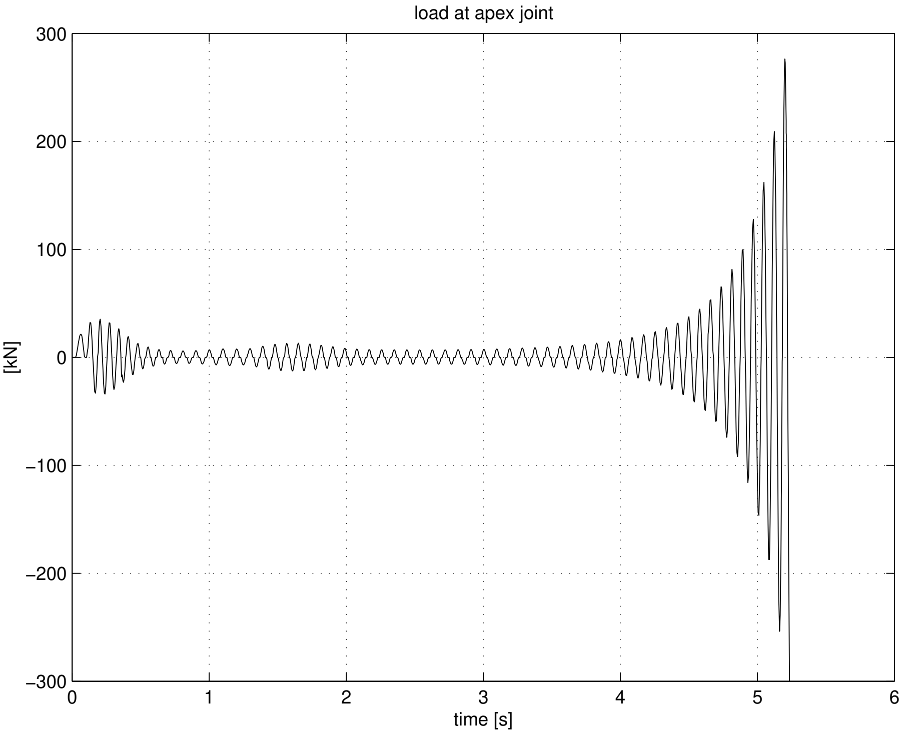

Fig. 6.17: Lateral load at the apex joint (simulation).

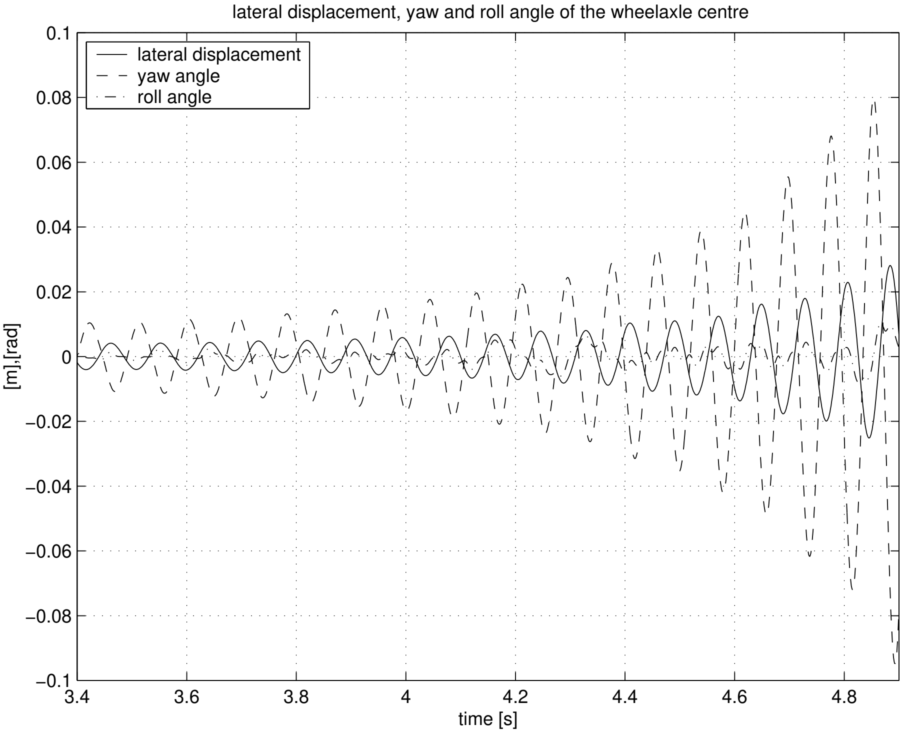

Fig. 6.18: Motion of the wheel axle centre (simulation).

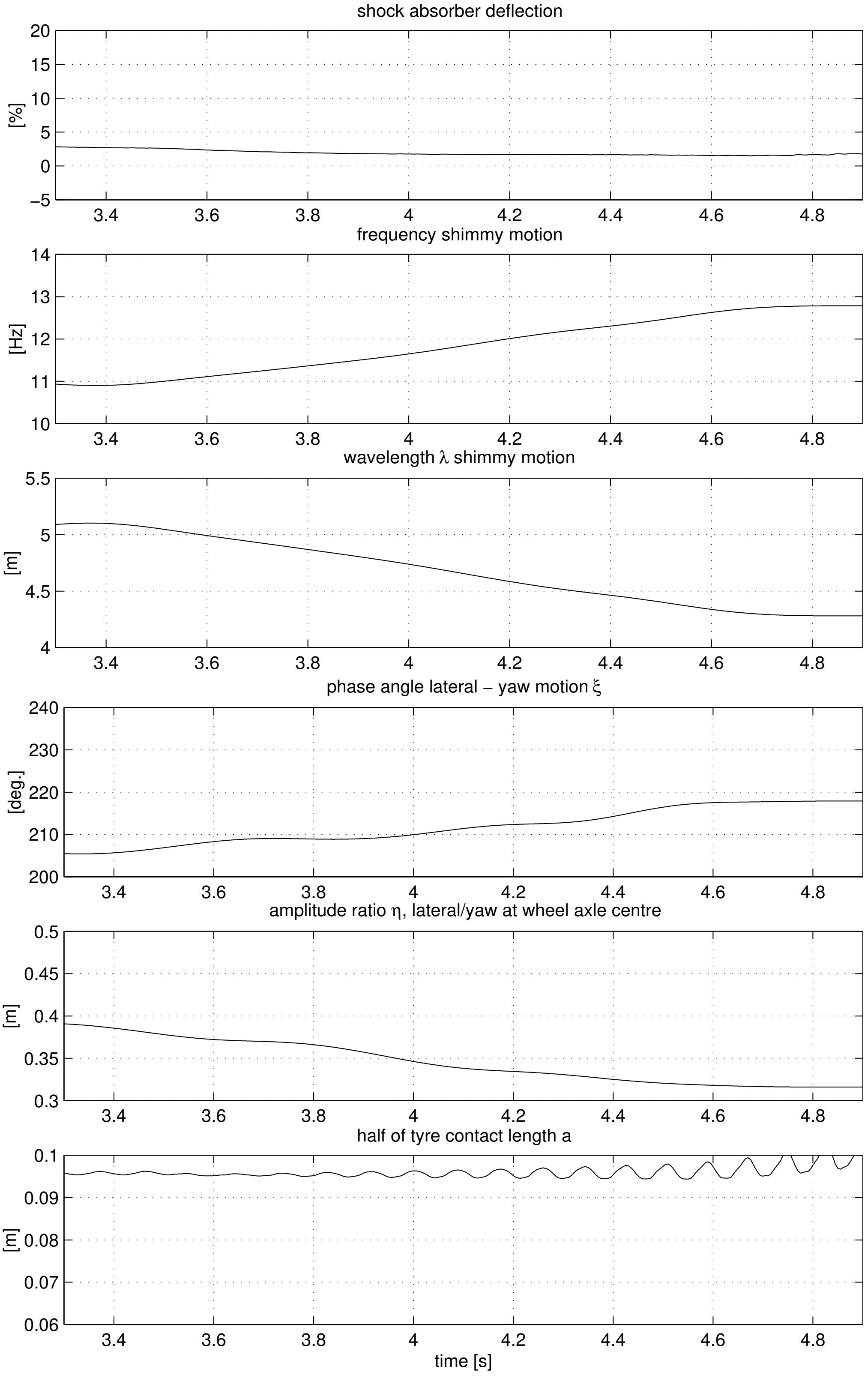

Fig. 6.19: Various characteristics of the shimmy vibration (simulation).

Chapter 7

Conclusions and recommendations

7.1 Conclusions

Shimmy of landing gears is potentially dangerous and may result in severe damage to the aircraft. Therefore, it should be an important consideration in the design of a landing gear. Experience has shown that it is difficult to reliably demonstrate shimmy stability from laboratory or flight tests. For that reason much effort has to be put in the development of computer simulation models in order to make reliable stability predictions and to understand the mechanisms governing shimmy.

The shimmy stability of a main landing gear is a function of many design variables and involves both the dynamic behaviour of the tyre and landing gear structure. The approach followed in this thesis is to start with relatively simple models to understand the phenomenon and gradually increase their complexity for a more detailed analysis. Analytical expressions for the shimmy stability can be derived for the trailing wheel system with lateral flexibility of the support. Essentially two stable areas exist:

- small negative trail combined with a low yaw stiffness and high lateral stiffness.
- large positive trail combined with a high yaw stiffness and low lateral stiffness.

A lower boundary on the yaw moment of inertia exists for both configurations to maintain shimmy stability. These results have also been confirmed when using a more detailed twin-wheeled landing gear model. Gyroscopic effects, caused by the rotating wheels and tyres, and structural damping make the stability boundaries velocity dependent. The gyroscopic effects tend to increase the instability for small positive trail values at higher forward velocities.

Apart from optimising the gear stiffness and geometry, various other methods exist to solve shimmy instability; the shimmy damper and a tuned mass being the most promising options. Since a shimmy damper will operate in series with the yaw stiffness of the gear, this stiffness has to be sufficiently high in order to allow the damper to function properly. Furthermore it is shown that a bogie configuration is inherently more stable than a cantilevered design.

The Nyquist criterion can be applied to investigate shimmy stability in the frequency domain by considering the gear structure and tyre as a feedback system. The shimmy frequency may be quite different from the eigenfrequencies of the gear structure. An important advantage of the Nyquist criterion is that it allows a better physical interpretation of the cause of the shimmy phenomenon compared to e.g. the calculation of eigenvalues or Hurwitz criterion.

A comparison between various linear dynamic tyre models has been made. It is shown that the different approaches are closely related and that in some cases equivalence conditions can be established. For the wavelengths normally encountered in aircraft main landing gear shimmy, the straight tangent tyre model is conservative with respect to detecting instability. It appears that the results obtained using the models of Von Schlippe, Rogers, Keldysh and Smiley are quite similar. The Moreland tyre model may be notably different, depending on the choice of the tyre time constant. An expression has been derived for the tyre time constant, which will result in more physically plausible path dependent behaviour for the Moreland model. Based on an energy balance, it can be shown that shimmy will only occur for certain combinations of lateral and yaw input to the wheel plane at road level.

In the design process a detailed landing gear model is required to evaluate and ensure shimmy stability. This model should have the following features:

- a load (or deflection) dependent set of tyre characteristics
- an accurate representation of the gear stiffnesses as a function of shock absorber deflection
- account for the flexibility of the attachment structure
- inclusion of the gyroscopic effects of the rotating wheels/tyres
- possibility to introduce free-play in lateral and yaw direction
- consideration of Coulomb friction on the bearings, including the interaction between axial and yaw motion

Apart from full-scale aircraft tests, various component tests, most notably the measurement of tyre characteristics and structural stiffness, are required to establish a quantitatively correct model.

7.2 Recommendations for future research

Though the modelling approach presented in this thesis has been applied successfully in explaining and solving shimmy problems on a particular landing gear, various items require further attention:

- *tyre parameters*
  Shimmy stability is dependent on tyre characteristics and reliable tyre data is required to make accurate predictions. Though the work of Smiley and Horne (reference [47]) and section 4.6 of this thesis may provide some guidelines, more data is required; in particular radial and retreaded aircraft tyres should be evaluated. In addition, the effects of inflation pressure, wear and road surface texture should be addressed.

- *tyre modelling*
  In this thesis the discussion of various tyre models to describe dynamic tyre behaviour is limited to linear models. As already shown in figure 4.3, the forces generated by the tyre will be a non-linear function of the side slip angle. The Magic Formula is a generally accepted method of describing the steady-state tyre behaviour. In recent years extensions have been made towards dynamic behaviour using a rigid ring approach (references [53] and [30]). Following this modelling approach, the gyroscopic moment generated by the tyre belt and the reduction of the relaxation length with increasing side slip angle can be incorporated in a very natural way. Nevertheless turn slip is not yet fully included and subject of on-going research. These enhanced tyre models will also require additional data, which may currently not be available for aircraft tyres.

- *friction*
  The friction between sliding member and main fitting is important for shimmy stability. In section 5.4 the basic mechanism is explained, but no experimental data is available to substantiate this. Differences between break-out and sliding friction may need to be addressed. Also the influence of external disturbances, e.g. tyre unbalance or road irregularities, may prove to be of importance.

- *brakes*
  The possible impact of the brakes on shimmy stability has not been touched in this thesis. The main landing gear is equipped with disk brakes, consisting of a stack of rotors (connected to the wheel) and stators (connected to the axle) which are compressed by the brake cylinders upon application of the brakes. As shown in figure 6.7 very high lateral accelerations are to be expected in case of a shimmy instability, which could potentially result in a cyclic brake excitation due to the lateral vibration of the landing gear. Nevertheless it is believed that this mechanism is unimportant for the *initiation* of shimmy, but research needs to be performed to positively confirm this.

- *dynamic behaviour of the wing and fuselage*
  In the detailed landing gear model, as described in chapter 5, only the static stiffness of the back-up structure is considered. As already pointed out by Black (reference [3]) it may be necessary to include the dynamic behaviour of the supporting structure. Depending on the general configuration, the bending modes of the wing could have some impact on the shimmy stability of the main landing gear; the resonance frequency of the lowest bending modes of the wing are typically below the frequency of the shimmy vibration.

As already pointed out in the introduction, section 1.2, there is a general need for guidelines to design a shimmy-free landing gear. Though this thesis may contribute to the understanding of the shimmy phenomenon, more work needs to be done to achieve this goal. In particular it would be important to evaluate various existing landing gear designs for shimmy stability. Though the trend in the industry is to only start developing shimmy models once problems occur, it will be very useful to develop models of landing gears which are known to have no shimmy problems. This will improve the general understanding of the shimmy phenomenon and may also provide additional confidence in the simulation techniques.

References

[1] C.B. Alsobrook and M.G. Vogel, Relaxation behavior of aircraft tires, SAE technical paper 961300, 1996

[2] J. Baumann, C.R. Barker and L.R. Koval, A nonlinear model for landing gear shimmy, ASME 91-WA-DSC-14, 1991

[3] R.J. Black, Realistic evaluation of landing gear shimmy stabilization by test analysis, SAE technical paper 760496, 1976

[4] R.J. Black, Application of tire dynamics to aircraft landing gear design analysis, NASA Tire Modelling Workshop, Langley Research Center, September 1982

[5] A. Cardona, An integrated approach to mechanism analysis, PhD thesis, University of Liege (Belgium), February 1989

[6] S.K. Clark, R.N. Dodge and G.H. Nybakken, Dynamic properties of aircraft tires, AIAA Journal of Aircraft, Vol. 11, Nr 3, 1974, pp. 166-172

[7] R.L. Collins and R.J. Black, Experimental determination of tire parameters for aircraft landing gear shimmy studies, AIAA Paper 68-311, April 1968

[8] R.L. Collins and R.J. Black, Tire parameters for landing gear shimmy studies, AIAA Journal of Aircraft, May-June 1969, pp. 252-258

[9] P.A. Davis et al., 26x6.6 radial-belted aircraft tire performance, SAE technical paper 912157, 1991

[10] P.A. Davis, Comparison of 30x11.5-14.5 bias-ply and radial-belted tire characteristics, SAE technical paper 922012, 1992

[11] Editorial staff, Landing gear topped list of aircraft systems involved in accidents during 35-year period, Flight Safety Foundation, Flight Safety Digest, December 1994, pp. 13-16

[12] J. Glaser and G. Hrycko, Landing gear shimmy - De Havilland's experience, AGARD Meeting 1995

[13] V.I. Goncharenko, L.G. Lobas and N.V. Nikitina, Wobble in guide wheels, Soviet Applied Mechanics vol. 17 no. 8, 1981, pp. 765-769

[14] V.I. Goncharenko, Shimmy of nose gear on an asymmetric suspension, International Applied Mechanics vol. 33 no. 2, 1997, pp. 168-173

[15] D.T. Grossman, F-15 nose landing gear shimmy, taxi test and corrective analyses, SAE technical paper 801239, 1980

[16] D.J. Feld, An analytical investigation of damping of landing gear shimmy, SAE technical paper 902015, 1990

[17] Hagedorn, Nicht-lineare Schwingungen, 1978, pp. 97-99

[18] A. Higuchi, Transient response of tyres at large wheel slip and camber, PhD thesis, Delft University of Technology, December 1997

[19] H.P.Y. Hitch, Aircraft ground dynamics, Vehicle System Dynamics (10), 1981, pp. 319-332

[20] F.H. Ho and M.F. Hall, An experimental study of the pure-yaw frequency response of the 18x5.5 type VII aircraft tyres, AFFDL-TR-73-79, 1973

[21] I. Johansson and S. Edlund, Optimization of vehicle dynamics in trucks by use of full FE-models, IMechE C466/016/93, 1993

[22] M.V. Keldysh, Shimmy of the front wheel of a three-wheeled landing gear, Tr. Tsentr. Aerogidrodinamicheskogo Inst., No. 564, 1945

[23] M.A.M. Kluiters, An investigation into F-28 main gear vibrations, Fokker report X-28-430, September 1969

[24] K. Koenig, Unsteady tire dynamics and the application thereof to shimmy and landing load computations, AGARD Meeting 1995

[25] W.E. Krabacher, Aircraft landing gear dynamics present and future, SAE technical paper 931400, 1993

[26] W.E. Krabacher, A review of aircraft landing gear dynamics, AGARD Meeting 1995

[27] W. Krüger, I. Besselink, D. Cowling, D.B. Doan, W. Kortüm and W. Krabacher, Aircraft landing gear dynamics: simulation and control, Vehicle System Dynamics 28, 1997, pp. 119-158

[28] H.L. Leve, Designing stable dual wheel gears, AIAA Paper No. 69-769, July 1969

[29] G.X. Li, Modelling and analysis of a dual-wheel nose gear: shimmy instability and impact motions, SAE technical paper 931402, 1993

[30] J.P. Maurice, Short wavelength and dynamic tyre behaviour under lateral and combined slip conditions, PhD thesis, Delft University of Technology, January 2000

[31] B. Milwitzky and F.E. Cook, Analysis of landing gear behavior, NACA TN 2755, 1952

[32] W.J. Moreland, The story of shimmy, Journal of the Aeronautical Sciences, December 1954

[33] W.J. Norton, C-17A landing gear shimmy testing, 1993

[34] J.J.M. van Oosten, C. Savi, M. Augustin, O. Bouhet, J. Sommer, J.P. Colinot, Time - tire measurements forces and moments - A new standard for steady state cornering tyre testing, presented at EAEC, June 30-July 3, 1999

[35] H.B. Pacejka, The wheel shimmy phenomenon, Doctoral Thesis, Delft University of Technology, December 1966

[36] H.B. Pacejka, Analysis of the shimmy phenomenon, Automobile Division Institution of Mechanical Engineers, Proceedings 1965-1966 Volume 180 Part 2A

[37] H.B. Pacejka, Yaw and camber analysis, Chapter 7.5 of ”Mechanics of Pneumatic Tires”, editor S.K. Clark, NBS monograph 122, Washington D.C., November 1971

[38] H.B. Pacejka and I.J.M. Besselink, Magic Formula tyre model with transient properties, Vehicle System Dynamics Supplement 27, 1997, pp. 234-249

[39] L.C. Rogers and H.K. Brewer, Synthesis of tire equations for shimmy and other dynamic studies, AIAA Journal of Aircraft, September 1971, pp. 689-697

[40] L.C. Rogers, Theoretical tire equations for shimmy and other dynamic studies, AIAA Journal of Aircraft, August 1972, pp. 585-589

[41] Society of Automotive engineers, Surface vehicle recommended practice - vehicle dynamics terminology, SAE-J670e, 1976

[42] P.H. Schweitzer and V.G. Szebehely, Gas evolution in liquids and cavitation, Journal of Applied Physics, volume 21, December 1950, pp. 1218-1224

[43] L. Segel, Force and moment response of pneumatic tyres to lateral motion inputs, Transactions of ASME, Journal of Engineering for Industry, 88B, 1966

[44] R.S. Sharp and C.J. Jones, A comparison of tyre representations in a simple wheel shimmy problem, Vehicle System Dynamics 9, 1980, pp. 45-57

[45] B. von Schlippe and R. Dietrich, Das Flattern eines bepneuten Rades, Bericht 140 der Lilienthal Gesellschaft (1941), English translation: NACA TM 1365, 1954, pp. 125-147

[46] R.F. Smiley, Correlation and extension of linearized theories for tire motion and wheel shimmy, NACA report 1299, 1957

[47] R.F. Smiley and W.B. Horne, Mechanical properties of pneumatic tires with special reference to modern aircraft tires, NACA TR-R-64, 1960

[48] J.E. Stevens, Shimmy of a nose gear with dual co-rotating wheels, Journal of the Aerospace Sciences, August 1961

[49] R. van der Valk and H.B. Pacejka, An analysis of a civil aircraft main landing gear shimmy failure, Vehicle System Dynamics (22) 1993, pp. 97-121

[50] B. Verbeek, Nonlinear parametric identification using periodic equilibrium states with application to an aircraft landing gear damper, PhD thesis, Eindhoven University of Technology, July 1993

[51] P. Woerner and O. Noel, Influence of nonlinearity on the shimmy behaviour of landing gear, AGARD Meeting 1995

[52] T.J. Yager, S.M. Stubbs and P.A. Davis, Aircraft radial-belted tire evaluation, SAE technical paper 901913, 1990

[53] P.W.A. Zegelaar, The dynamic response of tyres to brake torque variations and road unevennesses, PhD thesis, Delft University of Technology, March 1998

Summary

Shimmy of Aircraft Main Landing Gears - I.J.M. Besselink

The landing gear is an important aircraft system, which has to meet many different design requirements. It is a highly loaded structure, which is designed for minimum weight. Shimmy is a dynamic instability of the landing gear, which is caused by the interaction of the dynamic behaviour of the landing gear structure and tyres. The unstable lateral and yaw vibration of the landing gear can reach considerable amplitudes and may even result in severe damage to the aircraft. Shimmy is easily ignored in the design process, which may be caused by a of lack of knowledge on the shimmy phenomenon, absence of suitable analysis tools or the non-availability of e.g. tyre characteristics. Computer simulations are very important to evaluate the shimmy stability of a landing gear. Experience has shown that it will be very difficult to rigorously prove shimmy stability from experiments, e.g. full-scale flight tests or laboratory tests using a drum.

Three fields of research are covered in this thesis:

- shimmy fundamentals
- modelling of the tyre dynamic behaviour
- the development and validation of a detailed landing gear model

Analytical expressions for the shimmy stability have been derived for a number of relatively simple systems using the Hurwitz criterion. In particular, an analytical solution has been found for a system where the wheel has a mechanical trail and both the yaw and lateral stiffness of the hinge point are taken into account. The stability boundaries can be represented by two shifted parabolas in the mechanical trail versus yaw stiffness plane; this analytical result is very important to understand the interaction between the different variables. The model may be enhanced by including the gyroscopic behaviour of the rotating wheel and structural damping. The shimmy stability can also be analysed in the frequency domain by considering the landing gear structure and tyre as a feedback system and applying the Nyquist criterion.

A design study is performed using a twin wheeled landing gear, having three mechanical degrees of freedom (lateral, roll and yaw). The stability of the baseline configuration can be improved considerably by modifying the length of the mechanical trail, lateral stiffness, yaw stiffness and wheel track. It appears that a small positive mechanical trail is better avoided; this is substantiated by the analytical results. Other methods to improve the stability have been investigated: modification of the cant angle, the introduction of a bob mass, tuned mass, shimmy damper or co-rotating wheels. Furthermore the stability of a bogie landing gear has been evaluated both analytically and using a more complex model; the results indicate that this configuration is far less susceptible to shimmy.

Different linear tyre models have been developed for application in a shimmy analysis; in particular the models of Von Schlippe, Smiley, Pacejka (straight tangent and parabolic approximation), Kluiters, Rogers, Keldysh and Moreland are discussed. Expressions for the transfer functions with respect to side and turn slip are derived and equivalence conditions can be established between some of the tyre models. A comparison is made using transfer functions, step response and energy considerations. In addition, the impact of the tyre model on system stability is studied for a number of simple mechanical systems. Some guidelines regarding the values of different tyre parameters are given using measurement data and literature.

A detailed model will be required to assess shimmy stability in the design stage or when solving actual shimmy problems. The stiffness of a landing gear is dependent on the shock absorber deflection due to changes in torque link geometry and distance between upper and lower bearing. The flexibility of the back-up structure and wing results in a significant reduction of the lateral stiffness of the landing gear at wheel axle level. Modal testing can be performed to assess eigenfrequencies and mode shapes of the landing gear, but measurements show that the results may be highly amplitude dependent due to free-play and friction. Free-play and friction are also important for the shimmy stability and will have to be included in a detailed model. The shimmy damper may have a non-linear characteristic consisting of a preloaded spring and velocity squared damping force. Various component tests will be required to determine parameters or to validate the characteristics of the model. A detailed simulation model was developed using the MECANO multi-body software package. The flexible slider element proved to be very convenient for modelling the landing gear structure.

Full-scale tests on the aircraft may be used to perform a limited validation of the simulation model. During taxi runs an external disturbance is required to provoke a dynamic response of the landing gear. This may be achieved by running over a diagonally positioned plank, introducing an unbalance mass or asymmetrical braking. In a landing event the asymmetrical spin-up of the wheels is the main excitation source. Generally, only limited data will be available when a shimmy event occurs, which makes it difficult to perform a detailed assessment. An interesting exception is a shimmy vibration which occurred on a test aircraft, equipped with an instrumented landing gear. The unstable motion is analysed in detail. This event has also been simulated using the MECANO model, aiming to match the landing conditions as closely as possible. A reasonable agreement can be obtained between simulation model and measurement.

Future research may aim at an accurate determination of tyre characteristics and correlation between different tyres. The dynamic tyre model can be extended to describe the non-linear tyre behaviour at large side slip angles more accurately. Also some enhancements of the landing gear and airframe model are possible, in particular the dynamic behaviour of the wing and brakes may be included. Friction may be rather important for an accurate simulation of the landing gear behaviour; in this field both additional experimental data and improved modelling techniques may be required.

Curriculum vitae

Igo Besselink was born on the 18th of October 1966 in Hengelo (Gelderland), the Netherlands. After graduation from pre-university education (VWO) at the Ludgercollege in Doetinchem in June 1985, he started studying Mechanical Engineering at the Delft University of Technology. In the final years of this study he specialised in vehicle dynamics at the section of professor Pacejka. A practical traineeship on dynamic tyre loads was performed at the Volvo Truck Company in Göteborg, Sweden. The graduation project was done at DAF Trucks in Eindhoven and concerned the numerical optimisation of vehicle suspension components with respect to ride comfort. Igo graduated with distinction in December 1990.

In February 1991 he joined Fokker Aircraft B.V., located near Schiphol. During the first years, work consisted of the calculation of landing gear design loads and development of computer simulation models. A landing gear shimmy event with a test aircraft in 1993 marked the starting point of this PhD study and became the main focal point for the years to come. Together with colleagues and support from professor Pacejka, much effort was put in the development and validation of dedicated simulation models to describe and analyse the shimmy phenomenon.

Igo joined the Vehicle Dynamics Department of the TNO Road-Vehicles Research Institute in Delft in March 1996. There he works as a research engineer in the field of vehicle and tyre simulation model development; this includes the implementation and testing of the ”Delft Tyre” Magic Formula tyre model in various multi-body environments and consultancy activities for vehicle manufacturers. The PhD study on aircraft landing gear shimmy was continued, but the emphasis was shifted towards fundamental research in the field of the tyre - gear structure interaction and comparison of various theories to describe dynamic tyre behaviour.

Document history

September 2000: paper version

January 2007: pdf file created

- Minor formatting changes due to the usage of postscript fonts
- Page numbering modified (a shift of 10 pages with respect to the paper version)
- Two chapters with dutch text have been removed (”Samenvatting” and ”Nawoord”)
- Equation 3.4 corrected, expression in the original document:
  $\mathbf{C}(3,3) = c_\psi + 2c_z w^2 sin^2\theta + 2F_z(e - R\cos\theta)\sin\theta$
  $R\cos\theta$ is replaced by $R\sin\theta$